DESIGN AND CHARACTERIZATION OF AROMATIC THERMOSETTING COPOLYESTER RESIN FOR POLYMER MATRIX NANOCOMPOSITES

BY

METE BAKIR

DISSERTATION

Submitted in partial fulfillment of the requirements
for the degree of Doctor of Philosophy in Mechanical Engineering
in the Graduate College of the
University of Illinois at Urbana-Champaign, 2019

Urbana, Illinois

Doctoral Committee:

Professor Iwona Jasiuk, Chair and Director of Research
Professor James Economy, Co-Director of Research
Professor Munir Nayfeh
Assistant Professor Kyle Smith
Assistant Professor Seok Kim

ABSTRACT

This study presents the development of multifunctional polymer nanocomposite systems utilizing aromatic thermosetting copolyester resin enriched with various forms of nanofiller particles. The molecular weight and crosslinking functionality of precursor oligomers during condensation polymerization reaction regulate thermal-mechanical properties of self-generated foam morphologies. Aluminum foam layered aromatic thermosetting copolyester foam sandwich structures demonstrate outstanding impact energy absorption characteristics. High-performance nanocomposite foams, incorporating homogenously distributed carbonaceous nanoparticles, display significantly improved thermophysical properties that outperform state-of-the-art configurations. Periodically-functionalized self-assembled shish-kebab structures develop within an aromatic resin dip-coated graphene fiber system through an epitaxial step-growth polymerization process. Graphene nanoplatelet particles conjugate with precursor oligomers during *in situ* polymerization process forming electrically percolated network domains which enable controllable conductivity for nanocomposite structures. The interfacial attachment mechanism between carbonaceous particles occurs via oxygen-bearing functional groups, which establishes covalent bonding with cure advancing crosslinking polymer network and modifies the glass transition region characteristics. The aromatic resin forms an interfacial liquid crystalline mesophase domain around graphene nanoplatelets, which uniquely displays a thermally reversible characteristic with shape memory effect. Self-luminescent dielectric silicon nanoparticles homogenously disperse into the aromatic matrix without neither losing their luminescent properties nor deteriorating chemical configuration of the polymer network. The neat and nanocomposite structures preserve their physical and chemical properties following

direct exposure to aggressive environmental aging conditions. Bioactive nanofiller particles reinforced bionanocomposites hold a promise as a reconfigurable bone replacement material, for which interfacial coupling with nanoparticles enables more deformation tolerant nanocomposite matrix.

The aromatic resin can afford high-temperature enabled solid-state dynamic covalent bond exchange reaction between two similar surfaces, which enables a reversible bonding scheme to develop multifunctional reconfigurable in-space architectures for deep-space missions. The bonding/debonding mechanism displays >50 times repeated cycles through predominantly cohesive failure along with high glass transition temperature and bonding strength required for relevant application requirements. The solid-state bonding concept can also be utilized to join similar/dissimilar polymer composites and metal articles permanently. Via controlled process time, temperature and pressure, aromatic resin displays relatively high bonding strengths viable from cryogenic temperatures to elevated temperatures. The bonding approach can be utilized to produce lightweight fuselage structures for spacecraft without necessitating additional joining mechanisms.

Covetics are a novel class of carbon-metal nanomaterials for which *in situ* generated arc discharge during fabrication induces a chemical conversion reaction converting amorphous carbon to a crystalline graphitic structure which forms an intermetallic covalent bonding with host metal matrix. The covetics exhibit improved thermophysical properties as compared to their parent metals. We provide a comprehensive literature review on the covetics. Aluminum covetics demonstrate significantly improved corrosion potential relative to parent material with no carbon added. Both the hardness and the compressive strength of the aluminum covetic with carbon added are also improved. The carbon particles during covetics fabrication conditions induce

structural modifications on intrinsic secondary phases which contribute to the observed changes in corrosion behavior and improvement in mechanical properties.

ACKNOWLEDGEMENTS

I foremost express my sincere gratitude to my advisor, Dr. Iwona Jasiuk, for granting me liberty to explore new grounds in my research projects.

I would like to thank Jacob Meyer for introducing me to aromatic thermosetting copolyester, by which I have learned much about polymer technologies.

I would like to thank Dr. Munir Nayfeh, Ersin Bahceci, and Adem Kocyigit for their invaluable guidance and fruitful research discussions.

I would like to thank Dr. Andre Sutrisno for introducing me to NMR and his invaluable help with NMR analysis.

I would like to thank Dr. Irina Hussainova for help with the development of nanofiber composite structures, Chrissy Henderson for invaluable contributions to polymer aging project, Mohamed Elhebeary for the help with SEM imaging, and Jason Varnell for help with the corrosion project.

I would like to thank Lee Booher and Gregory Milner for their invaluable help with sample machining at their shop.

I acknowledge funding from the National Science Foundation I/UCRC grant (IIP-1362146) and Air Conditioning and Refrigeration Center at the University of Illinois at Urbana-Champaign grant. The findings, conclusions, and recommendations expressed in this dissertation are those of the authors and do not necessarily reflect their views.

I dedicate this dissertation to my dad who truly inspired me to be a mechanical engineer, my grandmother who raised me to be a strong person, and my mom and my sister who have always been there for me with their true love.

To my dad, grandmother, mom, and sister

TABLE OF CONTENTS

LIST OF FIGURES

LIST OF TABLES

CHAPTER 1: INTRODUCTION

1.1 Background

The technological evolution of structural materials for automotive, aerospace, and defense industries currently depends on the introduction of alternative lightweight material solutions which ensure materials performance commensurate with conventional systems as well as enabling cost-effective and industrially scalable high throughput production methodologies. Polymers, also known as plastics, provide immense advantages over metals by offering weight reduction up to 80% along with lower production costs. However, polymers mainly suffer poor physical properties due in part to inherently weak chemical structures. Carbon-fiber reinforced polymer composites provide material performance akin to the conventional metal articles as much as complying with industrially scalable production routines. Hence, at present, carbon fiber-reinforced polymer composites are actively adopted in aerospace and automotive industries, which mainly aims at reducing vehicles weight to improve fuel efficiency. However, metals are intrinsically forgiving materials due to their ductility, and thus tolerant to damage under cyclic loads. Thus, the pivotal shortcoming with the use of polymer composites is that their brittle nature can cause fracture under minor out-of-plane shear loads, which may even lead to catastrophical failures.

As a relatively new paradigm in polymer science, polymer nanocomposites are combinations of nanofiller reinforcement particles and host polymer matrix, which uniquely embody multifunctional properties within low-density morphologies. Polymer nanocomposites bear a great potential to address a broad range of cutting-edge technological applications. Yet, contemporary polymer nanocomposite configurations are deficient in mechanical strength and thermal stability due in part to inherently weak chemical-physical properties of host matrices. As

well, conventional shear-based mixing techniques impede homogenous and intact dispersion of nanofiller particles within polymer matrix. As a result, polymer nanocomposites do not fully benefit from the use of nanofillers as reflected in limited global physical properties. In the realm of realizing the polymer nanocomposites a practical reality in engineering systems, three significant challenges that have not met to unlock their practical potential; facile fabrication methods, controllable structure-property relations, and flexible structural integration strategies.

Aromatic thermosetting copolyester (ATSP) was developed in the 1990s utilizing low cost, easily processable and readily crosslinkable oligomers to form a new high-performance polymer system. The ATSP morphology comprises a crosslinked network of aromatic polyester backbone interconnected via covalent oxygen bonds, which hence enables superior physical properties. Carbon fiber reinforced ATSP composites demonstrate superior shear strength, modulus, and fracture toughness comparable or superior to industrial gold-standard of epoxy and polyimide carbon fiber composites. Additionally, chemistry-favored tailorable macromolecular architectures along with convenient reconfigurability into different physical forms (e.g., foam, coating, and adhesive) makes ATSP available for various nanocomposite applications. Besides, ATSP resin is resistant to microcracking, due to its tendency of the locally matching coefficient of thermal expansion (CTE) around the carbon fiber and are capable of withstanding extreme hot and cold temperature cycles via cryogenic thermal cycling. Additionally, the ATSP composites are durable, *in-situ* self-repairable, and maintain mechanical properties at elevated temperatures.

1.2 Dissertation Statement

This dissertation presents the development of novel multifunctional polymer nanocomposites utilizing aromatic thermosetting copolyester resin and various types of nanofiller particles with unique characteristics. It provides a comprehensive approach combining

synthesis, fabrication, multiscale experimental characterization, structure-process-property relations, and structural integration methodologies to address the aforementioned significant challenges.

1.3 Dissertation Overview

In Chapter 2, chemical strategy and fabrication approach are presented for the development of novel aromatic thermosetting copolyester foams. Fundamental phase transformation stages emerge during heat-induced condensation polymerization reaction between precursor oligomer groups are investigated. Cure and post-cure characteristics are analyzed to design an optimum cure cycle with most favorable pair of cure time and cure temperature. The effect of crosslinking density and molecular weight on global physical properties are characterized on reaction final products of aromatic thermosetting copolyester foams.

In Chapter 3, aluminum foam face layered aromatic thermosetting copolyester foam core sandwich composite structures are demonstrated. Obtained via *in situ* polymerization-driven foaming mechanism, polymer foam core exhibits robust interlayer adhesive strength, as characterized with lap shear experiments. The sandwich structure yield four-time higher impact energy absorption in comparison to bare aluminum foam of overall same thickness.

In Chapter 4, aromatic thermosetting copolyester nanocomposite foams are presented. A facile solid-state mixing method is introduced to combine various nanofiller particles and precursor oligomers. The nanocomposites demonstrate near-homogenous and intact dispersion of nanofillers within matrix. Due in part to facilitated distribution of nanofillers, the nanocomposites demonstrate significantly improved physical properties.

In Chapter 5, *in situ* epitaxial step-growth polymerization reaction driven interfacial functionalization of aromatic thermosetting copolyester with multilayered graphene wrapped

alumina fiber surface is demonstrated. Polymer resin-coated fiber strands develop a nanohybrid shish-kebab structure with periodically assembled and off-surface grown mesomorphic polymer lamella. Fiber surfaces and polymer matrix develop robust interfacial coupling.

In Chapter 6, the effects of cyclic water immersion and salt spray aging tests on the physical properties of aromatic thermosetting copolyester neat and nanocomposite matrix is demonstrated. The polymer matrix exhibits an adsorption-regulated mass uptake mechanism. Contact angle measurements reveal nanofiller-neutral and hydrophobic characteristics. Only minute physical and chemical degeneration occurs in the matrix due in part to hygroscopic swelling, which lie within the regime of their virgin (not exposed to the aging conditions) counterparts.

In Chapter 7, physicochemical effects induced by nanofillers on condensation polymerization reaction of aromatic thermosetting copolyester through the formation of electrically conductive percolating network is demonstrated. The controlled nanofiller particle size promotes different percolation thresholds and ultimate electrical conductivities. Microstructural analysis and cure process characteristics reveal thermochemical changes by nanofillers. Chemical spectroscopy exhibits the formation of interfacial coupling between nanofillers and polymer matrix.

In Chapter 8, the formation process and thermophysical characteristics of preferentially oriented interfacial liquid crystalline mesophase domain emerging around nanofillers within amorphous aromatic thermosetting copolyester matrix is demonstrated. A nematic liquid crystalline network develops via crystalline nanofiller surface induced local ordering effects. The liquid crystalline network exhibits thermally reversible phase transition characteristics. The

liquid crystalline network enables strong coupling with nanofillers, which subsequently alters chain relaxation characteristics of nanocomposite matrix.

In Chapter 9, imparting strong photoluminescence to otherwise weak luminescent aromatic thermosetting copolyester matrix by incorporating self-luminescent nanoparticles is demonstrated. Pre-polymerization stage develops a convention-like motion forming 2-D nanosheets decorated with nanoparticles and oligomer particles. Post-polymerization analysis shows homogenous incorporation of nanoparticles into polymerization process as a secondary crosslinker neither losing their luminescence functionality nor deteriorating physical properties of matrix. Chain relaxation characteristic indicate effective conjugation of nanoparticles with crosslinked polymer backbone.

In Chapter 10, bioactive nanoparticle reinforced aromatic thermosetting copolyester matrix bionanocomposites as a potential reconfigurable bone replacement material is demonstrated. Morphological analysis exhibit near-homogenous distribution of nanoparticles within the matrix. Due in part to robust interfacial coupling, nanoparticles behave as a crack-arrester promoting deformation-tolerant structure with enhanced material toughness. Chemical characterization of backbone chain composition of nanocomposites reveals the presence of hydrogen-advanced covalent interfacial coupling between nanofiller particles and polymer matrix. Chain relaxation dynamics of nanocomposite matrix during glass transition is modified via nanoparticle-induced segmental immobilization.

In Chapter 11, nanofiller-contiguous polymer network with aromatic thermosetting copolyester nanocomposites in which chemically pristine carbon nanofillers covalently conjugate with cure advancing crosslinked backbone chains through functional end-groups of constituent precursor oligomers upon an in situ polymerization reaction is demonstrated. Via thoroughly

transformed backbone chain configuration, the polymer nanocomposites demonstrate unprecedented glass transition peak broadening by about 100 °C along with significant temperature upshift of around 80 °C.

In Chapter 12, a conveniently reconfigurable joining approach to connect highly scalable multifunctional architectures with fiber-reinforced polymer composite links. A reversible solid-state bonding mechanism is enabled using a novel high-performance polymer resin, for which only physical contact and application of heat is required. Optimum operational bonding parameters are systematically studied.

In Chapter 13, a solid-state bonding approach for carbon fiber reinforced high performance aromatic thermosetting copolyester resin composites with primary metal spacecraft structures is demonstrated that enables building lightweight elements with tailorable structural properties without necessitating additional uses of adhesives or mechanical joints. Optimum operational bonding parameters are systematically studied. Physical properties of bonded specimens are investigated. Novel fabrication concepts for the development of multilayer composite materials are introduced.

In Chapter 14, a review of literature on carbon-metal covetic nanomaterials is demonstrated. The covetic materials are introduced followed by a brief overview of carbon-metal matrix nanocomposites. Experimental results obtained on various covetic material configurations are demonstrated. Current challenges and future directions in the covetics research are provided.

In Chapter 15, the origin of the increased corrosion potential of an aluminum-carbon covetic material is investigated. The covetic sample with carbon added exhibits a higher corrosion potential. Both the hardness and the compressive strength of the covetic with carbon added are also improved. Physical characterization using chemical spectroscopy reveal changes

in surface composition within the covetic after carbon addition. After corrosion, the surface is enriched in some elements present in the parent alloy and exhibits a reduced grain size both of which contribute to the observed changes in corrosion behavior and improvement in mechanical properties.

CHAPTER 2: HEAT-INDUCED POLYCONDENSATION REACTION WITH SELF-GENERATED BLOWING AGENT FORMING AROMATIC THERMOSETTING COPOLYESTER FOAMS

2.1 Introduction

Starting with the invention of the first polystyrene foam back in the early 20th century, polymer foam literature has been expanded along with the development of other well-known systems of polyurethane, polyvinyl chloride, polypropylene, and others [1-4]. Having promptly been implemented and refined processing conditions by the polymer industry, low-cost and high-throughput polymer foams have been performed via conventional techniques of foam extrusion, molded bead, and injection molding. Ultimately, they have found broad applications in automobile, aeronautic, packaging and construction industries [5]. Furthermore, current research interests driven for lightweight materials have accelerated advancement in other naturally-occurring cellular materials fabricated via more sophisticated foaming processes bringing more flexibility into materials selection in order to utilize ultimate enhancements in physical properties of final products [6-8]. Drawing substantial interest within the given framework, the polymer foams generally are more pronounced with the highlighted aspects of low structural density, good thermal insulation, low dielectric constant, superior acoustic properties and cost-effective manufacturing schemes [9-12]. More recently, polymer foams have also been shown as synthetic bone tissue scaffolds, biodegradable and recyclable raw materials, antibacterial water filters, and nanocomposite structures incorporating carbonaceous nanofillers [13-19].

This work was previously published: Bakir, M., Meyer, J.L., Economy, J., and Jasiuk, I., Heat-induced polycondensation reaction with self-generated blowing agent forming aromatic thermosetting copolyester foams, Macromolecules, 49 (17), 6489-6496 (2016).

That overall perspective being given, state-of-the-art polymer foams can be viewed from the benchmarking aspects of foaming methodologies, material systems and foam formation, and pore architectures. In the processes that use an externally introduced blowing agent to produce porous structure, two foaming methodologies have been extensively utilized; physical foaming and chemical foaming [20-23]. As a physical foaming agent, CO_2 has attracted much attention by simply being inexpensive, environmentally benign and non-toxic substance when compared to its counterparts of chlorofluorocarbon, hydrocarbons and other inert gases [24-25]. Specifically, CO_2 can take the form of a supercritical fluid (sCO_2) at relatively low pressures and temperatures that facilitates preserving pore cell geometries during the foaming processes by saturating the polymer matrices in their glassy states at reduced processing temperatures, down to below the glass transition temperatures of polymers [26-31]. However, use of sCO_2 has come along with several production-oriented issues such as low solubility in most polymer systems, especially high molecular weight polymers, due to lack of polar groups or higher degree of crystallinity in polymers which overall affect physical properties such as pore size, structural density, and mechanical strength.

Among the polymer systems forming cellular morphologies, thermoplastics have upstream advantages of material recyclability, structural conformality, relatively reduced processing periods, and so readily implementation into existing processing techniques. In general, thermoplastics have three primary foaming stages; introduction of blowing agent, bubble expansion, and bubble stabilization. Hence, the solubility of the blowing agent stands out to be a crucial processing parameter to initialize bubble nucleation phase as well as surface tension, viscosity and solidification being other essential factors for maximized bubble homogeneity and controlled pore sizes within the structures. On the other hand, thermosets

foams come along with conventionally complex processing conditions requiring an additional cure process to be performed at relatively high temperatures for considerably long durations. Hence, the conventional thermoplastic foam fabrication frameworks give rise to the aforementioned issues with the blowing agent considering bubble expansion and bubble stabilization stages, which are to be strictly affected by the concurrent formation of cross-linked morphology during extended cure periods. In terms of structural architecture, foamed polymers generally exhibit fully closed, fully open or combined morphologies with either microcellular or macrocellular pore structures which ultimately alter materials properties as well as functionalities of the structures [32-36].

All in all, the state-of-art polymer foams possess relatively poor strength-to-weight ratio, low thermomechanical stability, blowing agent solubility issues, and intricate fabrication conditions which overall have limited their implementations into high-performance applications [37-39]. Herein, we introduce aromatic thermosetting copolyester foams fabricated via facile heat-induced polycondensation between the carboxylic acid and acetoxy-capped oligomer groups. The aromatic thermosetting copolyester foams demonstrate high glass transition temperature, exceptional thermal stability, quite low thermal expansion coefficient and outstanding compressive mechanical strength.

As seen in Figure 2.1.a, the proposed cure mechanism is an acidolysis-type interchange condensation reaction (that can be classed as a transesterification) wherein the hydroxyl group of the carboxylic acid is replaced by the ether oxygen of the acetoxy producing cross-linked ester backbone polymer matrix along with releasing acetic acid as the reaction by-product by combination of the hydroxyl of the carboxylic acid and the acetoxy unit [40-41]. Being synthesized from a set of benzene derivative monomers, the constituent oligomers are comprised

of aromatic rings including carboxylic acid and aromatic acetoxy functional groups, which are connected together via covalent single and-double oxygen bonds (Figure 2.2). Due to high thermal stability and unique chemical inertness of the aromatic rings, and intramolecular cohesive binding energies of oxygen bonds along with comparable electronegativities of the constituent oligomer groups, the designed chemical structures and aromatic natures of the oligomers were retained through the course of the polymerization reaction. Hence, only chemically reactive acetoxy and carboxylic acid functional groups took part in the condensation polymerization reaction releasing acetic acid as the main side product of the reaction, which prevails in the gas form favorably acting as blowing agent to nucleate bubbles within oligomer compounding medium. Also, the acetic acid emerges in the gas form *in situ* due to polycondensation reaction temperature exceeding 117.9 °C boiling point of acetic acid. Hence, the acetic acid performs as a self-generated internal blowing-agent forming three-dimensionally porous polymer matrix. In the meantime, the constituent oligomer groups were conjugated through these functional groups establishing the ester backbone of the polymers.

Figure 2.1.b-e show schematics defining fundamental phase transformation stages took place during the formation of the foams. First, acetoxy (-CH_3COO) and carboxylic acid (-COOH) end group oligomers are mixed together in powder form at 1:1 weight ratio, which enabled molecular weight balanced polycondensation reaction between the oligomer groups (b). Second, under isothermal heating, micron-sized oligomer powder particles physically relaxed and then melted blending together driven via thermodynamical effects, and completely filled cavity of a container (c). Third, bubble nucleation started due to acetic acid discharge at sufficient polymerization reaction temperature along with bubble growth generating porous polymer matrix (d). Finally, the polymer matrix with internal pores was cured for pre-defined

durations at select temperatures to obtain the final physical products (e). We studied high cross-link density/low molecular weight and low cross-linking density/high molecular weight grades of the aromatic thermosetting copolyester foams. We initially demonstrate hot-stage assisted optical microscope images of the phase transformation stages along with associated temperatures, and then use Differential Scanning Calorimetry (DSC) and Thermogravimetric Analysis (TGA) to determine optimum cure temperature of the polymer foams. Ultimately, we design a rational cure cycle on the basis of these outcomes. Furthermore, we characterize and evaluate thermophysical properties of the foams on the basis of cross-linking density and molecular weights of the polymer foams.

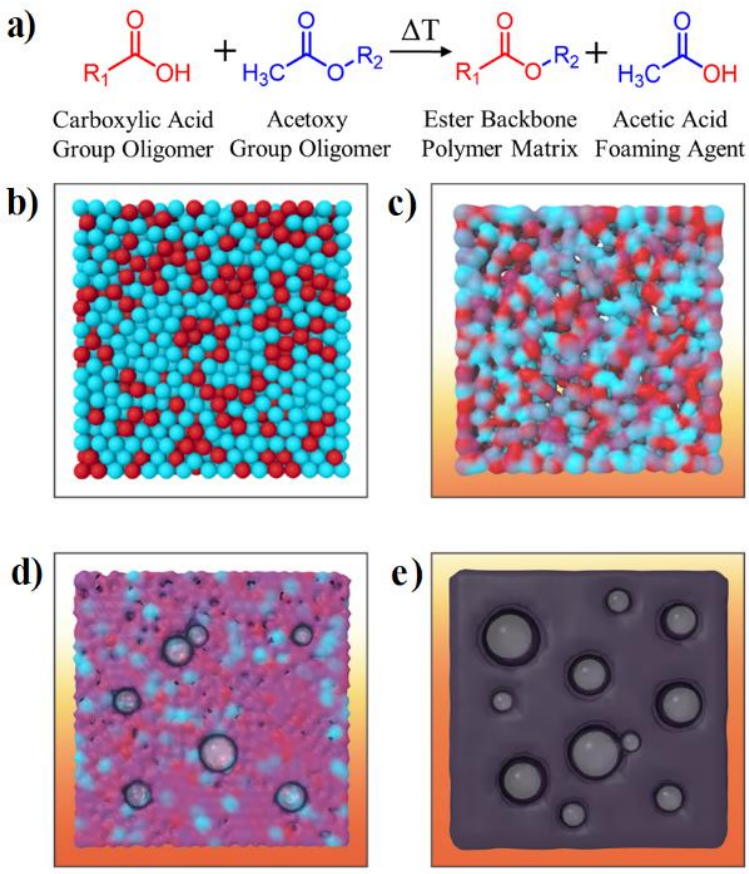

Figure 2.1 a) Heat-induced foaming reaction; giving off the acetic acid foaming agent. b-e) Schematics of fundamental phase transformations during the endothermic foaming process; (b) loosely packed oligomers, (c) melt-state oligomers, (d) bubble nucleation/growth, and (e) cured polymer foam product.

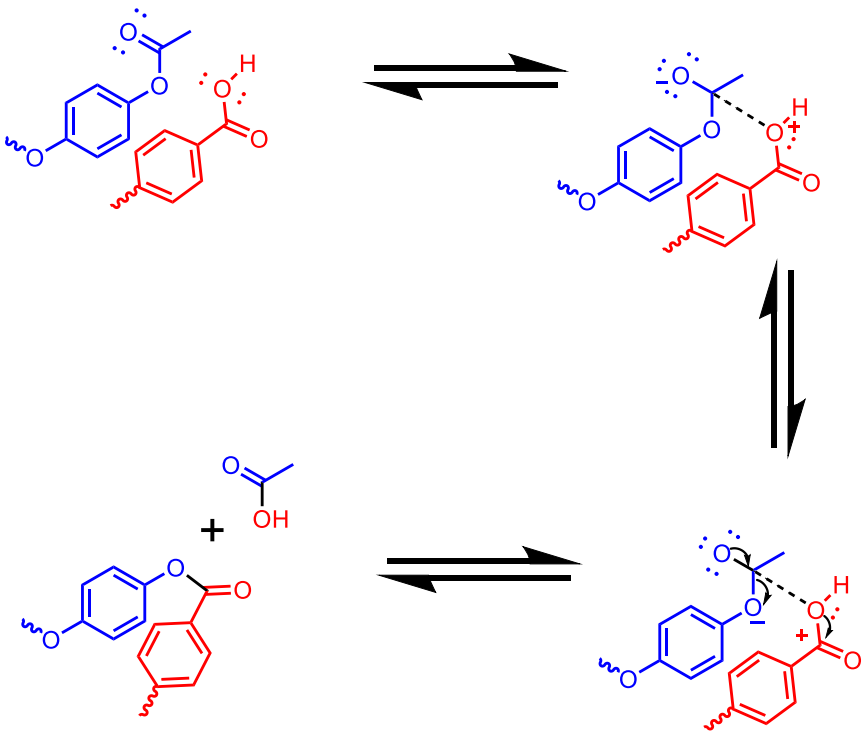

Figure 2.2 Cure mechanism via interchain transesterification reaction.

2.2 Materials and Methods

Carboxylic acid-capped oligomer using biphenol diacetate (CB and CB2) and Acetoxy-capped oligomer using biphenol diacetate (AB and AB2) ("2" denotes numeration) oligomers were utilized to produce the aromatic thermosetting copolyester foams. Both aromatic oligomer groups were synthesized using biphenol diacetate (BPDA), 4-acetoxybenzoic acid (ABA), isophthalic acid (IPA), and trimesic acid (TMA) at peculiar molar feed ratios, as given in Table 2.1 [42-43]. Also, Figure 2.3 shows chemical structures of the monomers used to synthesize the oligomers.

Table 2.1 Molar fractions of monomers used in the synthesis, and molecular weights of the acetoxy and carboxylic acid-capped oligomers.

Oligomer	ABA	BPDA	TMA	IPA	M_w (g/mol)
AB	3	3	1	0	1201
CB	3	2	1	2	1203
AB2	5	4	1	1	1758
CB2	5	3	1	3	1760

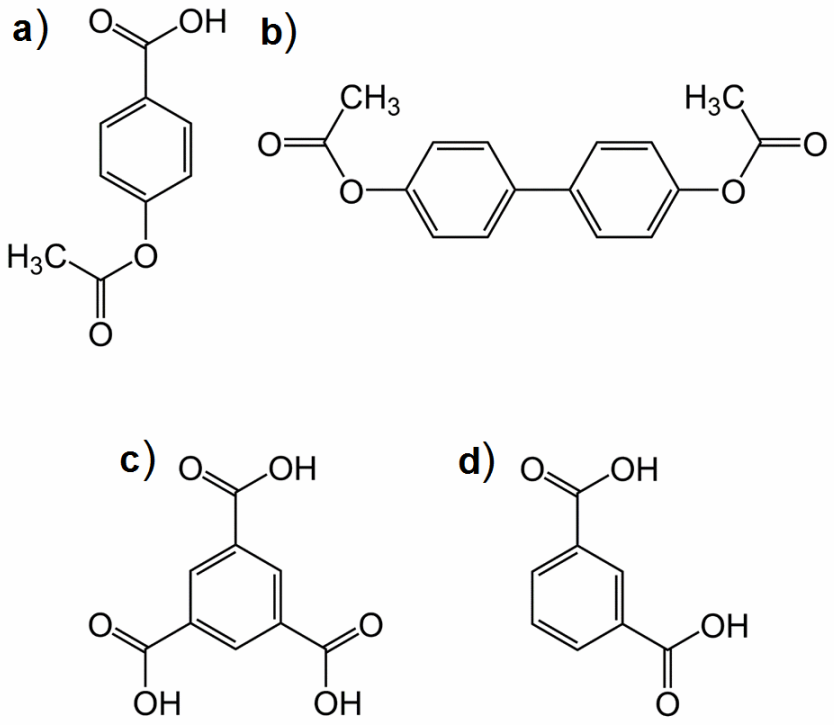

Figure 2.3 Chemical structures of the monomers a) 4-acetoxybenzoic acid (ABA), b) biphenol diacetate (BDPA), c) trimesic acid (TMA) and d) isophthalic acid (IPA).

The matched oligomer sets, when reacted together, are labeled as CBAB and CB2AB2 as their naming convention. The aromatic thermosetting copolyester foams CBAB and CB2AB2 were fabricated by mixing one set aromatic acetoxy end-group oligomer with another set of aromatic carboxylic acid end-group oligomer, both in powder-form, at 1:1 weight ratio, and by

operating the pre-designed cure-cycle under vacuum to induce condensation polymerization reaction between the two oligomer groups. CBAB was designed to have high cross-linking density/low molecular weight, and so was CB2AB2 low cross-linking density/high molecular weight.

The powder-form uncured oligomer combinations were sandwiched between two coverslips and placed onto a heating stage (TMS 91 Linkam Scientific Instruments Ltd.). The heating stage was then separately set to an upright bright-field optical microscope, and the oligomer combinations were run through a temperature-ramp cycle with constant 40°C/min heating rate. The images were captured with a megapixel resolution color digital camera mounted on the optical microscope setup.

The cure characteristics of the aromatic thermosetting copolyester foams were analyzed using a Differential Scanning Calorimetry (DSC) (TA Instruments TGA 2910) and Thermogravimetric Analysis (TGA) (TA Instruments TGA 2950). Both instruments were operated at 30 °C/min constant heating rate temperature-ramp cycles. The tests were performed under an inert atmosphere of nitrogen. The DSC analyses were performed on sets of the oligomer combinations, carboxylic-acid, and acetoxy-capped oligomer groups. The first cycle denotes the curing cycle of the oligomer combinations and does the second cycle post-curing following the first cycle. The TGA analyses were applied only to the oligomer combinations. Similarly, the first cycle and the second cycle stand for the curing and post-curing cycles, respectively.

3D microstructural images of the aromatic thermosetting copolyester foams were visualized using a high-resolution 3D X-ray micro-computed tomography (Micro-CT) (Xradia MicroXCT-400). The 3D image was reconstructed utilizing total 1441 images taken at every

0.25° corresponding to sample rotation during the imaging process. The samples were in 10 mm x 20 mm cross-section with 4 mm thickness, as fabricated through the cure-cycle.

The thermomechanical properties of the aromatic thermosetting copolyester foams were characterized using a Dynamic Mechanical Analysis (DMA) (TA Instruments Q800 DMA). The DMA was operated in dual-cantilever beam (DCB) bending mode in the room atmosphere. The temperature-ramp cycle was run at a constant heating rate of 3 °C/min on the samples. The samples were in 10 mm x 5 mm cross-section with 35 mm length, as fabricated through the cure-cycle.

The thermal stability of the aromatic thermosetting copolyester foams at elevated temperatures was characterized using Thermogravimetric Analysis (TA Instruments TGA 2950). A temperature cycle combining constant 30 °C/min heating rate temperature-ramp cycle and 120 min temperature-hold cycle was performed on the samples. Smaller samples of 15-20 mg weight were cut from the foams as fabricated through the cure cycle. The tests were performed under atmospheres of air and nitrogen.

Thermal expansions of the aromatic thermosetting copolyester foams as a function of temperature were measured using a horizontal, digital dilatometer (Edward Orton Jr Ceramic Foundation Model 2010 B). The tests were performed in the room atmosphere. The temperature-ramp cycle was run at a constant heating rate of 3 °C/min on the samples. The samples were in 12.7 mm diameter with 25.4 mm length, as fabricated through the cure-cycle described below.

The compressive mechanical strength of the aromatic thermosetting copolyester foams was measured using compressive loading frames (Instron Testing Systems 4483 Load Frame). A constant crosshead speed of 6 mm/min was performed on the samples. The samples were in 1.27 cm diameter having 2.54 cm length, as fabricated through the cure-cycle. Densities were

calculated using a ratio of volume and weight measured on the samples. Relative densities were calculated with respect to densities of 1.27 Mg/m^3 and 1.30 Mg/m^3 of fully dense CBAB and CB2AB2, respectively. The results were obtained on five samples for both CBAB and CB2AB2.

2.3 Results and Discussion

Phase transformation stages developed during the heat-induced condensation polymerization reaction between the aromatic acetoxy and carboxylic acid-capped oligomers were visually studied. Besides, effective reaction temperatures emerged during these phases were successfully determined. Figures 2.4-2.5 exhibit optical micrographs captured during the foaming processes of CBAB and CB2AB2 curing polymers, respectively. As observed in Figures 2.4.a and 2.5.a, the darker regions are oligomer powder mixtures, and the brighter regions are merely optical microscopy reflections of glass substrates. As the heating processes started at 30°C, no morphology changes were observed until the softening points of the curing polymers. At the beginning of softening stages, around 120°C, both CBAB and CB2AB2 curing polymers lightly wetted the coverslip surfaces, which were not easily distinguishable to eye until melting took place. We discerned the melt-states from the softened-states by virtue of the melt-flow occurred during the latter process. Afterward, the curing polymers entered into the melting stages at 170 °C as for CBAB and 180°C as for CB2AB2; melt-compounding curing polymers were observed as the darker islands in Figures 2.4.b and 2.5.b. Hence, as the temperature was progressively increased, the melt-states blanketed coverslip surfaces, and then bubble nucleation stages started at 225 °C and 230 °C for CBAB and CB2AB2, respectively (Figures 2.4.c and 2.5.c). Note that in Figure 2.5.c, the brighter regions formed in the melt-compounding state represent regions of increasing amorphosuity in the thermoset based on the development of the polymerization cross-linking of CBAB being concurrently initiated with the bubble nucleation.

CBAB was designed to have higher cross-linking density/lower molecular weight as compared to CB2AB2 by virtue of selection of monomer feed ratios. The primary means of adjusting crosslink density is by adjustment of the ratio of TMA (the crosslinking agent) versus other constituents. If we assume a complete yield of acetic acid from the cross-linking reaction, the crosslink density can then be parameterized by the branch coefficient χ_c, which is 0.133 for CBAB and 0.087 for CB2AB2, as well as the mass between crosslinks $(M_c)_N$ of 1123 g/mol for CBAB and for 1668 g/mol for CB2AB2 [43]. Following the initial bubble nucleations, rather more bubbles were generated as the temperature rose above the melt-state, and consecutively bubble sizes subtantially enlarged at elevated temperatures of 260 °C for CBAB and 270 °C for CB2AB2 (Figures 2.4.d and 2.5.d). It is worth highlighting that CBAB curing polymer, in addition to the priorly initiated cross-linking formation, yielded lower phase transformation temperatures than those of CB2AB2 due to its designed lower molecular weight. Table 2.2 summarizes the phase transformation temperatures associated with both CBAB and CB2AB2.

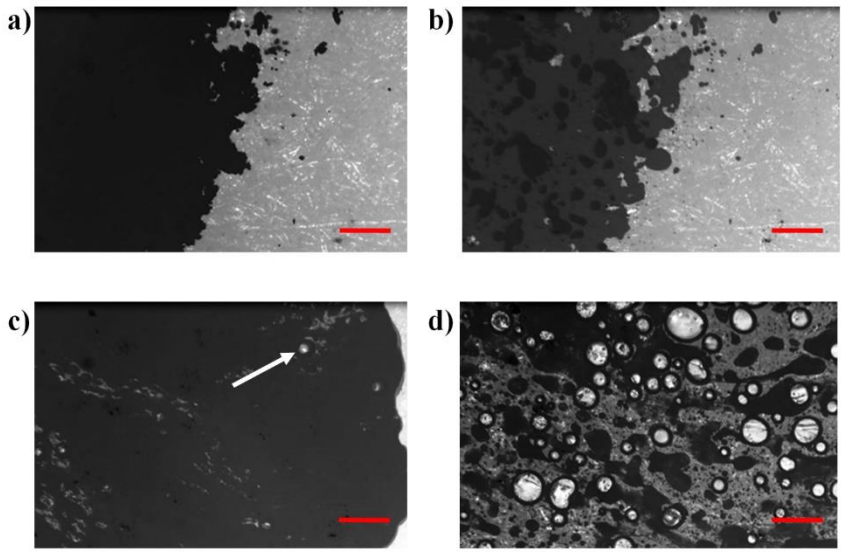

Figure 2.4 Phase transformations during the foaming process of CBAB. a) Curing polymer at 30°C, b) melting starts at 170°C, c) reaction by-product acetic acid releases nucleating bubbles at 225°C, d) cross-linking formation and bubble growth at 260°C. The scale is 5 mm.

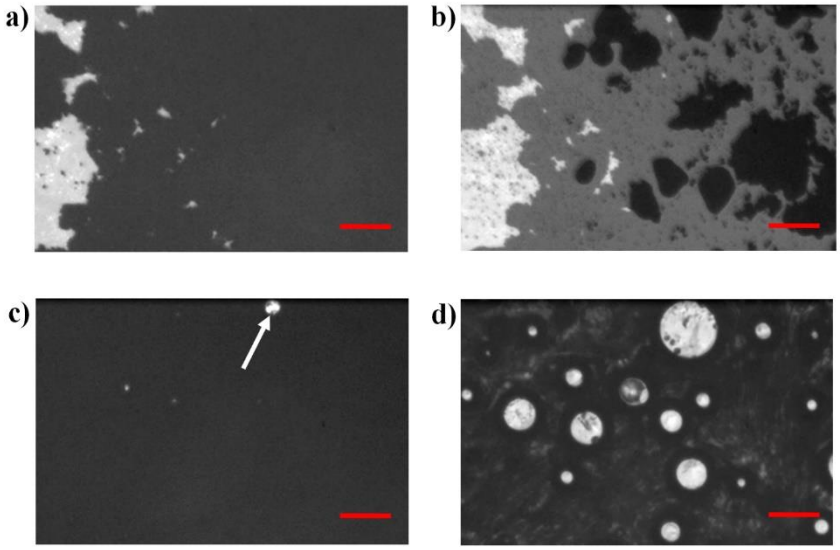

Figure 2.5 Phase transformations during the foaming process of CB2AB2. a) Curing polymer at 30°C, b) melting starts at 180°C, c) reaction by-product acetic acid releases nucleating bubbles at 230°C, d) cross-linking formation and bubble growth at 270°C. The scale is 5 mm.

Table 2.2 Fundamental phase transformation and cure temperatures of CBAB and CB2AB2 foams**.**

	Softening	**Melting**	**Bubble Nucleation**	**Bubble Growth**	**Final Cure**
			Curing Process		
CBAB	120 ºC	170 ºC	225 ºC	260 ºC	330 ºC
CB2AB2	120 ºC	180 ºC	230 ºC	270 ºC	330 ºC

Having the phase transformation temperatures detected, the necessary cure temperature for the thermosetting foams is still yet to be determined. Figure 2.6 shows cure and post-cure characteristics of the curing polymers and their constituent oligomers studied using DSC. Herein, the curing polymer curves, as denoted 1st cycle, displayed dimples taking heat up between 290 °C and 330 °C temperature ranges (Figures 2.6.a and 2.6.b) which correspond to their curing regions – also indicating that the condensation polymerization reaction was weakly endothermic. The endothermic reaction energies for CBAB and CB2AB2 were determined to be 3.55 mJ/mg and 1.41 mJ/mg, respectively. As well, the very same curing curves progressed in the exothermic direction as cure regions were crossed through, which clearly indicated completion of the cure reaction. In this manner, when the 2nd cycles were run on the same particular cured polymers, the cure regions, as well as other minima along the curing curves, disappeared validating fully-cured states of the polymers. Besides, the constituent oligomers had cure regions took place at either lower or higher temperatures than the curing polymers per se, so it was concluded that the curing polymers had different cure behaviors than their building blocks. All in all, three distinct and potentially applicable cure temperatures, 290 °C, 310 °C and 330 °C, were selected within the cure regions to be optimized through the use of TGA.

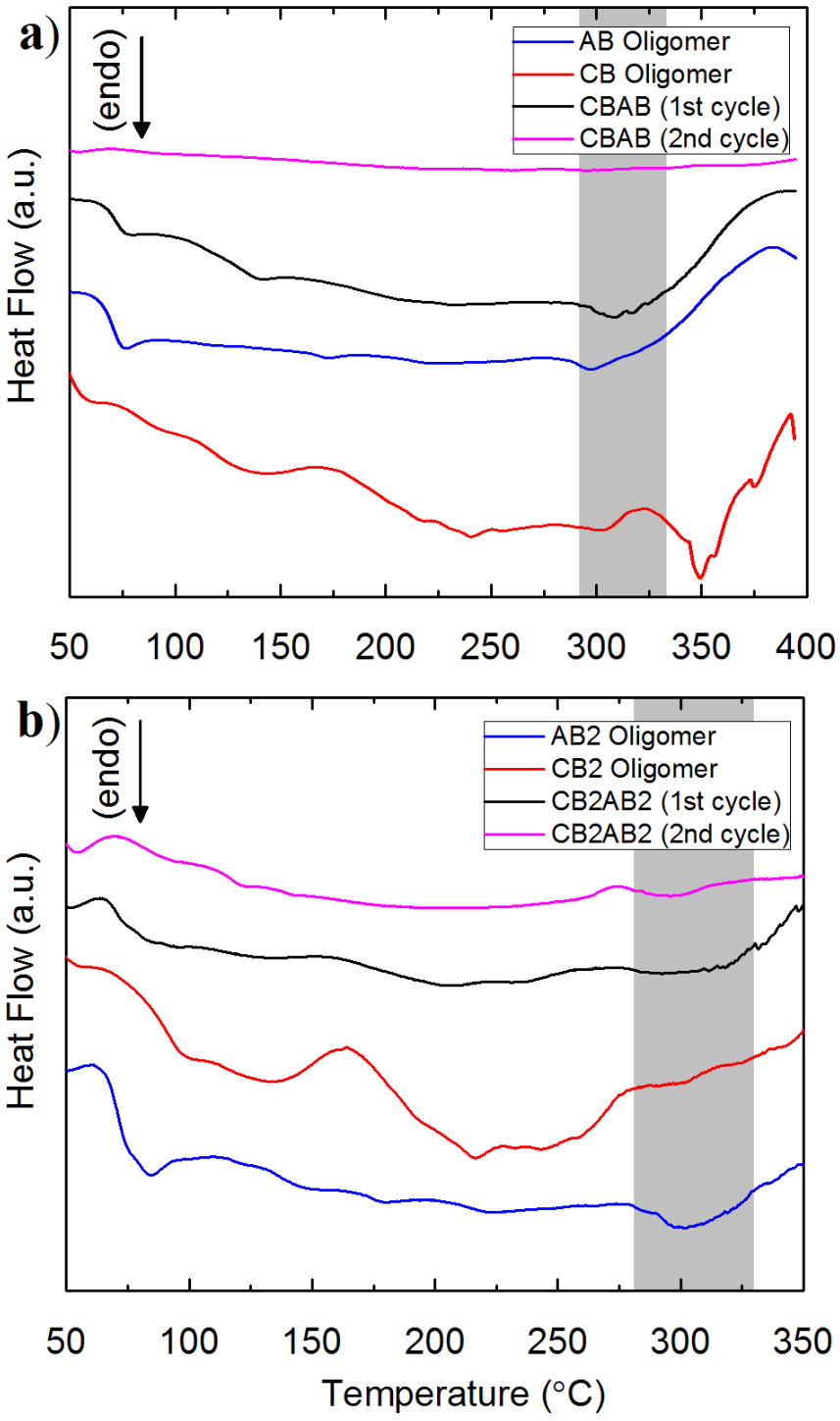

Figure 2.6 Analyses of cure and post-cure characteristics of the curing polymers and constituent oligomers in DSC. 1st and 2nd cycles denote cure process and post-cure processes of CBAB (a) and CB2AB2 (b), respectively. Tests were performed under nitrogen.

Figure 2.7 shows cure and post-cure characteristics of the curing polymers analyzed with TGA at the three pre-determined temperatures. The curing polymers yielded substantial weight losses within first 20 minutes of the curing cycle, yet almost-zero weight changes occurred during the post-curing cycles. The progressively occurred weight reductions illustrated real-time emission of acetic acid blowing agent indicating the initiation of the polymerization reaction at given select temperature. Also, the gentle decays took place in the post-cured polymer curves depicted that the select temperatures had provided sufficient curing environment during the first cycle, yet the cured polymers thermally degraded at those considerably high operational temperatures. Additionally, the measure of the weight loss, or the acetic acid release, undoubtedly increased as the pre-defined cure temperatures enlarged due to increased rates of the polymerization reaction. Hence, it was deduced that all three temperatures could practically initiate the foaming reaction, yet 330 °C was preferred to allow most sufficient cure conditions for the foams.

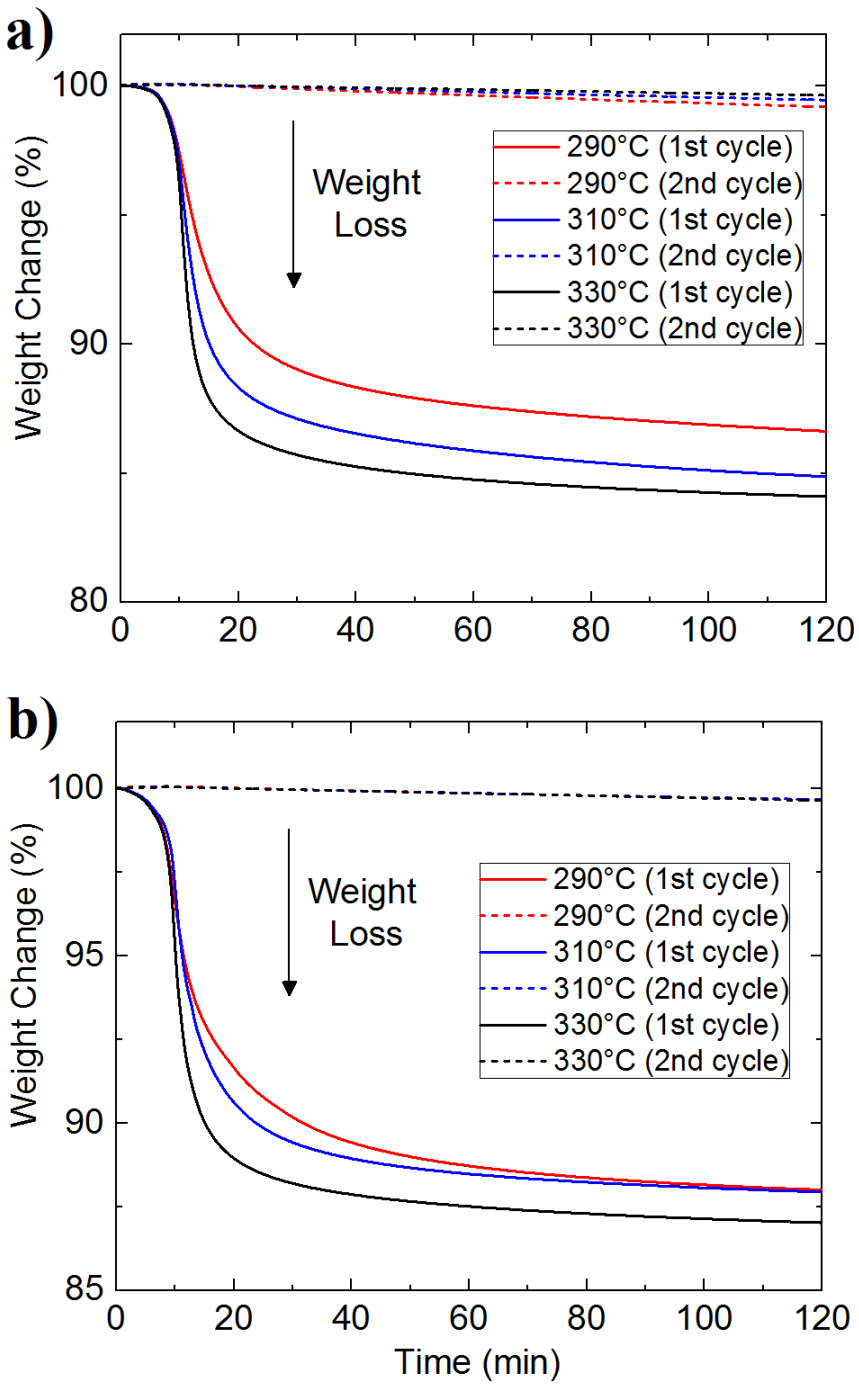

Figure 2.7 Analyses of cure and post-cure characteristics of curing polymers and constituent oligomers in TGA. 1st and 2nd cycles denote cure process and post-cure processes of CBAB (a) and CB2AB2 (b), respectively. Tests were performed at three temperatures 290 °C, 310 °C and 330 °C under nitrogen.

We designed a rational cure cycle based on the thermal cure characteristics of the curing polymers. The cure cycle with three temperature-hold steps at 202 °C for 90 min, 270 °C for 150 min and 330 °C for 180 min, which corresponded to the melting, the bubble growth and the cure temperatures of the foaming process, respectively. As well, the extended phase transformation periods, compared to hot-stage experiments (~6-8 min) and TGA analyses (~ 2 hours), were aimed to hold the phase transformation stages effectively develop in equilibrium conditions, so homogenously cured polymer structures were obtained. Aromatic thermosetting copolyester foam physical products were successfully fabricated through the pre-designed cure cycle and then subjected to thermo-mechanical material property characterization tests. As a visual observation, three-dimensional (3D) images of foam microstructures were taken using X-ray Micro-CT (Figure 2.8.a). As previously observed in Figures 2.4 and 2.5, the foaming reaction did not generate equal-sized bubbles, and it caused the foams have randomly distributed pores through the material structures. This characteristic phenomenon can also be observed in naturally-occurring materials systems, such as bone. With regard to cell architecture of the polymer foams, the weight losses observed during the course of TGA measurements showed that blowing agent was not trapped within the pores meaning that open cell morphologies were generated within the polymer foams. Also, there were other cells visually observed to be surrounded by the solid constituent material which could be defined as closed cells. Hence, the foams were defined to have combined forms of both closed cell and open cell pore structures. (Figure 2.8.b).

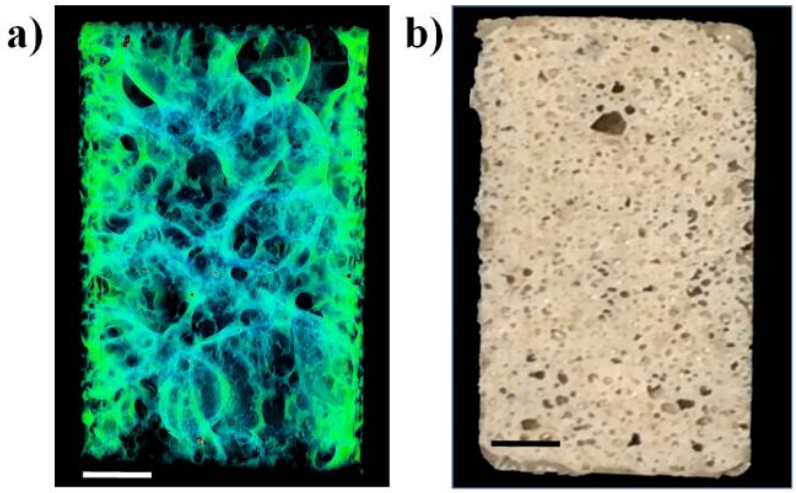

Figure 2.8 3D microstructural image of CBAB foam obtained using Micro-CT scanning (a) and a photo of the physical product (b). The scale is 2.5 mm.

Figure 2.9 shows thermomechanical properties of the foams obtained using DMA. In Figure 2.9.a, CBAB showed a shoulder peaking at 79 °C which corresponded to sub-T_g relaxation associated with segmental mobility in the structure. The succeeding peak at 191 °C defined the glass transition temperature of CBAB. On the other hand, CB2AB2 did not reveal any sub-T_g chain relaxation characteristics within the given temperature window, which would be possibly observed below at cryogenic temperatures, yet its glass transition temperature was detected at 172 °C, as shown in Figure 2.9.b. In addition to detection of the glass transition temperatures, DMA results demonstrated that the foams behaved in the elastic manner rather than the viscoelastic, as the storage modulus was one order of magnitude larger than loss modulus. Also, considerably low values of the loss moduli, on the order of 10-20 MPa, illustrated relatively brittle nature of the polymer foams. As well, number average molar mass between crosslinks ($M_{C,N}$) of CB2AB2 was calculated as 1669 g/mol, which is much larger than 1112 g/mol of CBAB, which essentially introduced longer polymer chains and afforded more

degree of freedom for chain motion allowing a transition at a lower temperature (a 19 °C difference) [43].

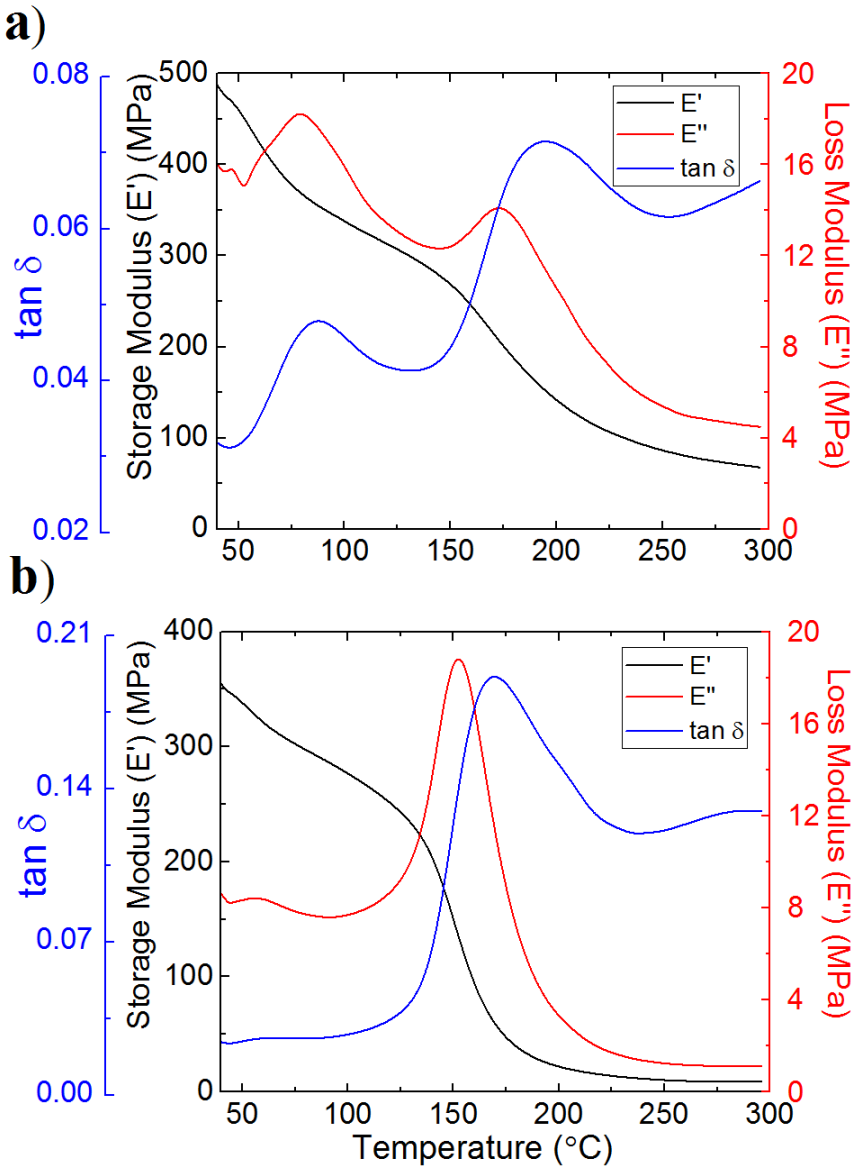

Figure 2.9 Characterization of thermomechanical properties, and detection of glass transition temperature of CBAB (a) and CB2AB2 (b) foams using DMA.

Figure 2.10 shows thermal stability performances of the foams characterized using TGA. In Figure 2.10.a, CBAB demonstrated only 5% weight loss at 537 °C in N_2 and 527°C in air. As well, the first derivative curve peaked at 572 °C denoting maximum degradation rate of CBAB.

Similarly, CB2AB2 demonstrated only 5% weight loss at 515°C in N_2 and 512 °C in air (Figure 2.10.b). In addition, the first derivative curve peaked at 567 °C in N_2 and 560 °C in air denoting maximum degradation rates of CB2AB2. First, no rather sudden decreases in the sample weights were observed, as those of the cure curves, which denoted fully-cured states of the polymer foams. The high cross-linked CBAB morphology introduced relatively superior thermal performance than the low cross-linked counterpart CB2AB2 which was attributed to improved the extent of bond scissions during the chemical decomposition. Also, use of air atmosphere in the course of TGA experiments overall resulted in lower degradation rates than the inert atmosphere of N_2 which was attributed to adsorptions of molecules on the decomposing surfaces suppressing the degradations rates. This effect was more pronounced with the high cross-linked morphology of CBAB due to enhanced interaction area exposed to the air.

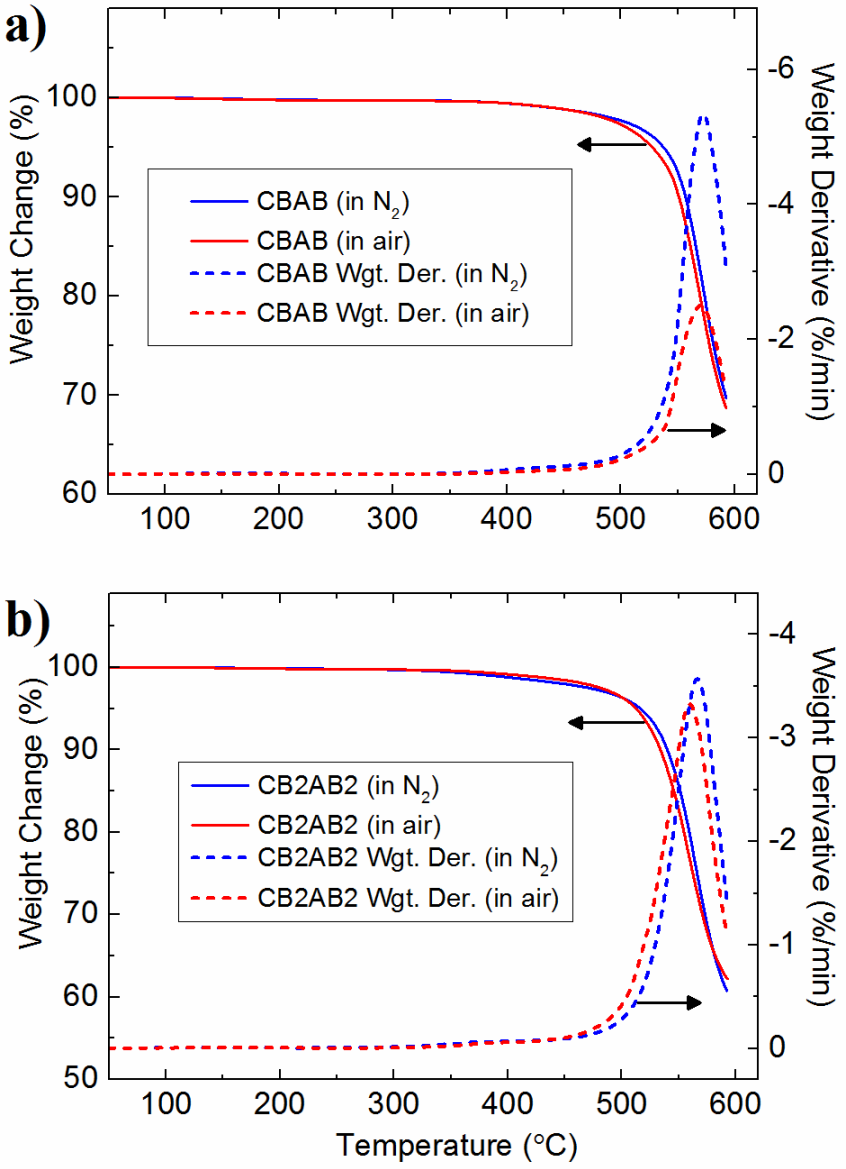

Figure 2.10 Characterization of thermal stability of CBAB (a) and CB2AB2 (b) foams in TGA. Tests were performed under air and nitrogen.

Figure 2.11 shows thermal expansion characteristics of the foams as a function of temperature measured using dilatometer. Linear thermal expansion trends were obtained in both CBAB and CB2AB2 yielding maximum longitudinal extensions of %1.53 and %1.19 at 200 °C, respectively. Also, the coefficients of thermal expansion of the foams were calculated as 96 x 10^{-6} /C and 76 x 10^{-6}/C for CBAB and CB2AB2, respectively. As results showed, CB2AB2

generated more confined structure due to its higher molecular weight morphology. This result was attributed to the increased density of the resultant CB2AB2 foam, which in turn was understood to be a result of the lower number of moles of acetic acid available to evolve during the cure reaction and serve as the blowing agent.

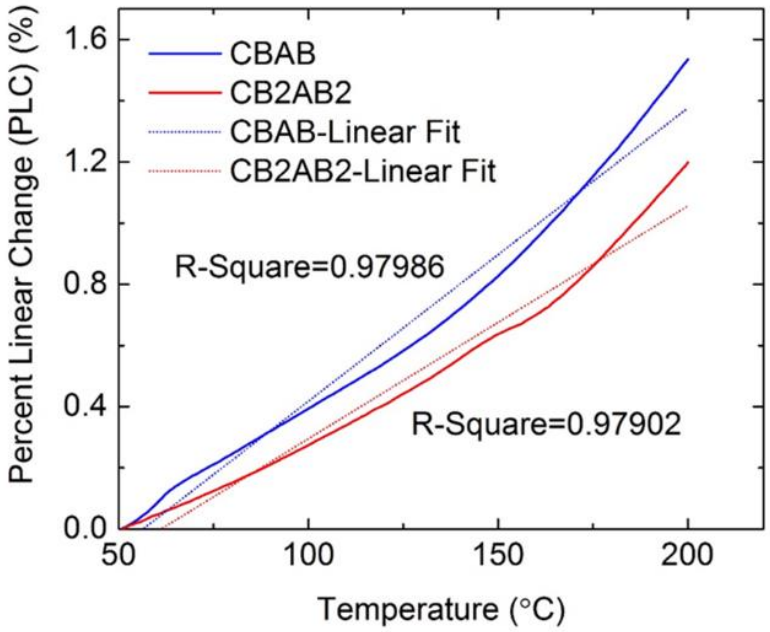

Figure 2.11 Characteristics of thermal expansion of CBAB and CB2AB2 foams.

Figure 2.12 demonstrates mechanical characteristics of the foams under compressive loads. CB2AB2 delivered a stronger structure over 10.5 MPa strength compared to that of 7.6 MPa with CBAB (Table 2.3). As well, CB2AB2 was stiffer up to 0.30 GPa Young's modulus, yet less dense around 0.62 Mg/m^3 density, in comparison to those of 0.27 GPa and 0.54 Mg/m^3, respectively, of CB2AB2. Similarly, relative densities of CBAB and CB2AB2 are 0.42 Mg/m^3 and 0.48 Mg/m^3, respectively. Based on the mechanical testing results, we concluded that higher molecular weight of CBAB2 embodied polymers with higher structural density, which eventually gave rise to the enhanced mechanical properties.

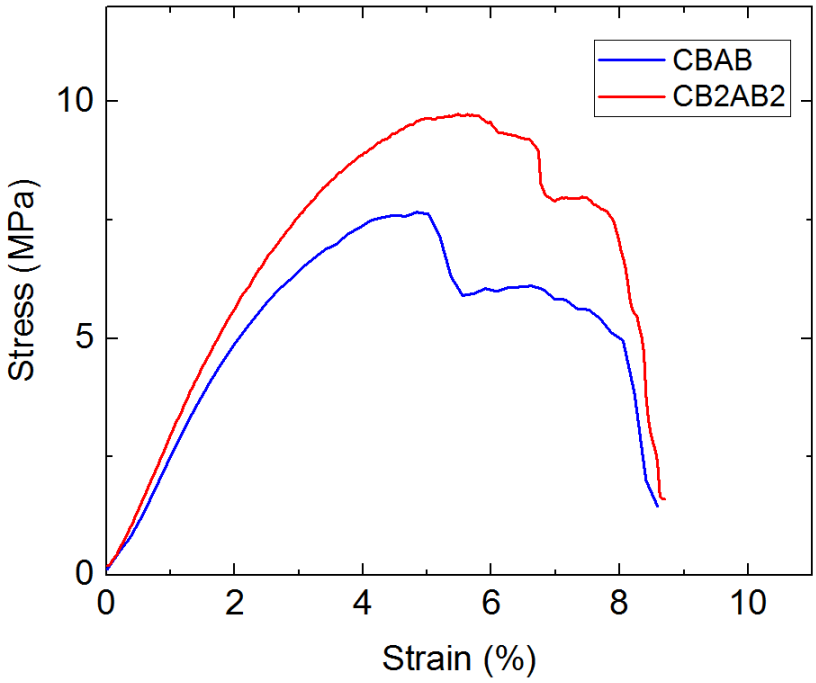

Figure 2.12 Characterization of the compressive mechanical strength of CBAB and CB2AB2 foams.

Table 2.3 Compressive elastic modulus, compressive strength and foam density of CBAB and CB2AB2 foams.

	Modulus (GPa)	**Std. Dev.**	**Strength (MPa)**	**Std. Dev.**	**Density (Mg/m^3)**	**Std. Dev.**	**Relative Density**	**Std. Dev.**
CBAB	0.27	0.04	7.62	0.5	0.54	0.03	0.42	0.03
CB2AB2	0.30	0.04	10.52	2.30	0.63	0.03	0.48	0.03

2.4 Conclusion

This work demonstrated the heat-induced self-foaming capacity and thermo-mechanical properties of the aromatic thermosetting copolyester foams. Instinctively occurring phase transformations during the foaming reaction of the curing polymers were successfully monitored. Cure and post-cure characteristics of the polymers were also studied to design an optimum cure-

cycle for fabrication of the physical products. Then, the foams were characterized by means of thermomechanical properties, high-temperature thermal stability, linear thermal expansion and compressive mechanical strength. The aromatic thermosetting copolyester foams are novel thermoset foams populating a new design space to deliver multifunctional properties for high-end use. The foams are deliberately lightweight, yet quite strong to endure loadings such as carried by the fully dense polymers. Possessing high glass transition and thermal degradation temperatures, ATSP foams can potentially address high-temperature demanding applications that conventional polymers have failed so far.

2.5 References

[1] Georg, M. C.; Gudbrand, T. J., Heat insulation. U.S. Patents 2,023,204: 1935.

[2] Pace, H. A., Preparation of flexible elastomeric cellular polyurethane materials. U.S. Patents 2,888,413: 1959.

[3] Joslyn, W.; Keil, J., Process for making PVC foams. U.S. Patent 3,708,441 1973.

[4] Parrish, R. G., Microcellular foam sheet. U.S. Patent 3,637,458 1972.

[5] General polymeric foams and their applications. in *Polymeric Foams*, CRC Press: 2006; pp 117-130.

[6] Banhart, J., Manufacture, characterisation and application of cellular metals and metal foams. *Progress in Materials Science* **2001,** *46* (6), 559-632.

[7] Studart, A. R.; Gonzenbach, U. T.; Tervoort, E.; Gauckler, L. J., Processing routes to macroporous ceramics: a Review. *Journal of the American Ceramic Society* **2006,** *89* (6), 1771-1789.

[8] Gibson, L. J., Biomechanics of cellular solids. *Journal of Biomechanics* **2005,** *38* (3), 377-399.

[9] Shastri, V. P.; Martin, I.; Langer, R., Macroporous polymer foams by hydrocarbon templating. *Proceedings of the National Academy of Sciences* **2000,** *97* (5), 1970-1975.

[10] Guo, A.; Javni, I.; Petrovic, Z., Rigid polyurethane foams based on soybean oil. *Journal of Applied Polymer Science* **2000,** *77* (2), 467-473.

[11] Krause, B.; Koops, G. H.; van der Vegt, N. F. A.; Wessling, M.; Wübbenhorst, M.; van Turnhout, J., Ultralow-k dielectrics made by supercritical foaming of thin polymer films. *Advanced Materials* **2002,** *14* (15), 1041-1046.

[12] Najib, N. N.; Ariff, Z. M.; Bakar, A. A.; Sipaut, C. S., Correlation between the acoustic and dynamic mechanical properties of natural rubber foam: Effect of foaming temperature. *Materials & Design* **2011,** *32* (2), 505-511.

[13] Rezwan, K.; Chen, Q. Z.; Blaker, J. J.; Boccaccini, A. R., Biodegradable and bioactive porous polymer/inorganic composite scaffolds for bone tissue engineering. *Biomaterials* **2006,** *27* (18), 3413-3431.

[14] Willett, J. L.; Shogren, R. L., Processing and properties of extruded starch/polymer foams. *Polymer* **2002,** *43* (22), 5935-5947.

[15] Gross, R. A.; Kalra, B., Biodegradable polymers for the environment. *Science* **2002,** *297* (5582), 803-807.

[16] Yu, L.; Dean, K.; Li, L., Polymer blends and composites from renewable resources. *Progress in Polymer Science* **2006,** *31* (6), 576-602.

[17] Jain, P.; Pradeep, T., Potential of silver nanoparticle-coated polyurethane foam as an antibacterial water filter. *Biotechnology and Bioengineering* **2005,** *90* (1), 59-63.

[18] Lee, L. J.; Zeng, C.; Cao, X.; Han, X.; Shen, J.; Xu, G., Polymer nanocomposite foams. *Composites Science and Technology* **2005,** *65* (15–16), 2344-2363.

[19] Chen, L.; Rende, D.; Schadler, L. S.; Ozisik, R., Polymer nanocomposite foams. *Journal of Materials Chemistry A* **2013,** *1* (12), 3837-3850.

[20] Li, Q.; Matuana, L. M., Foam extrusion of high density polyethylene/wood-flour composites using chemical foaming agents. *Journal of Applied Polymer Science* **2003,** *88* (14), 3139-3150.

[21] Bledzki, A. K.; Faruk, O., Microcellular injection molded wood fiber-PP composites: part I - effect of chemical foaming agent content on cell morphology and physico-mechanical properties. *Journal of Cellular Plastics* **2006,** *42* (1), 63-76.

[22] Taki, K.; Yanagimoto, T.; Funami, E.; Okamoto, M.; Ohshima, M., Visual observation of CO2 foaming of polypropylene-clay nanocomposites. *Polymer Engineering & Science* **2004,** *44* (6), 1004-1011.

[23] Lee, S. T., Introduction. In *Polymeric Foams*, CRC Press: 2004.

[24] Tomasko, D. L.; Li, H.; Liu, D.; Han, X.; Wingert, M. J.; Lee, L. J.; Koelling, K. W., A Review of CO2 applications in the processing of polymers, *Industrial & Engineering Chemistry Research* **2003,** *42* (25), 6431-6456.

[25] Garcia-Leiner, M.; Lesser, A. J., CO2-assisted polymer processing: a new alternative for intractable polymers. *Journal of Applied Polymer Science* **2004,** *93* (4), 1501-1511.

[26] Sauceau, M.; Fages, J.; Common, A.; Nikitine, C.; Rodier, E., New challenges in polymer foaming: a review of extrusion processes assisted by supercritical carbon dioxide. *Progress in Polymer Science* **2011,** *36* (6), 749-766.

[27] Nofar, M.; Park, C. B., Poly (lactic acid) foaming. *Progress in Polymer Science* **2014,** *39* (10), 1721-1741.

[28] Arora, K. A.; Lesser, A. J.; McCarthy, T. J., Preparation and characterization of microcellular polystyrene foams processed in supercritical carbon dioxide. *Macromolecules* **1998,** *31* (14), 4614-4620.

[29] Nalawade, S. P.; Picchioni, F.; Janssen, L. P. B. M., Supercritical carbon dioxide as a green solvent for processing polymer melts: processing aspects and applications. *Progress in Polymer Science* **2006,** *31* (1), 19-43.

[30] Xu, Z.-M.; Jiang, X.-L.; Liu, T.; Hu, G.-H.; Zhao, L.; Zhu, Z.-N.; Yuan, W.-K., Foaming of polypropylene with supercritical carbon dioxide. *The Journal of Supercritical Fluids* **2007,** *41* (2), 299-310.

[31] Ma, Z.; Zhang, G.; Shi, X.; Yang, Q.; Li, J.; Liu, Y.; Fan, X., Microcellular foaming of poly(phenylene sulfide)/poly(ether sulfones) blends using supercritical carbon dioxide. *Journal of Applied Polymer Science* **2015,** *132* (40).

[32] Zenkert, D.; Burman, M., Tension, compression and shear fatigue of a closed cell polymer foam. *Composites Science and Technology* **2009,** *69* (6), 785-792.

[33] Mills, N. J.; Zhu, H. X., The high strain compression of closed-cell polymer foams. *Journal of the Mechanics and Physics of Solids* **1999,** *47* (3), 669-695.

[34] Lee, P. C.; Wang, J.; Park, C. B., Extruded open-cell foams using two semicrystalline polymers with different crystallization temperatures. *Industrial & Engineering Chemistry Research* **2006,** *45* (1), 175-181.

[35] Jenkins, M. J.; Harrison, K. L.; Silva, M. M. C. G.; Whitaker, M. J.; Shakesheff, K. M.; Howdle, S. M., Characterisation of microcellular foams produced from semi-crystalline PCL using supercritical carbon dioxide. *European Polymer Journal* **2006,** *42* (11), 3145-3151.

[36] Yi, F.; Xu, F.; Gao, Y.; Li, H.; Chen, D., Macrocellular polymer foams from water in oil high internal phase emulsion stabilized solely by polymer Janus nanoparticles: preparation and their application as support for Pd catalyst. *RSC Advances* **2015,** *5* (50), 40227-40235.

[37] Menner, A.; Haibach, K.; Powell, R.; Bismarck, A., Tough reinforced open porous polymer foams via concentrated emulsion templating. *Polymer* **2006,** *47* (22), 7628-7635.

[38] Otsuka, T.; Taki, K.; Ohshima, M., Nanocellular foams of PS/PMMA polymer blends. *Macromolecular Materials and Engineering* **2008,** *293* (1), 78-82.

[39] Siripurapu, S.; Coughlan, J. A.; Spontak, R. J.; Khan, S. A., Surface-constrained foaming of polymer thin films with supercritical carbon dioxide. *Macromolecules* **2004,** *37* (26), 9872-9879.

[40] Jackson, W. J.; Kuhfuss, H. F., Liquid crystal polymers. I. Preparation and properties of p-hydroxybenzoic acid copolyesters. *Journal of Polymer Science Part A: Polymer Chemistry* **1996,** *34* (15), 3031-3046.

[41] Shi, F. F.; Economy, J., Moisture transport studies on newly developed aromatic and aromatic/aliphatic copolyester thin films. *Journal of Polymer Science Part B: Polymer Physics* **1998,** *36* (6), 1025-1035.

[42] Frich, D.; Goranov, K.; Schneggenburger, L.; Economy, J., Novel high-temperature aromatic copolyester thermosets: synthesis, characterization, and physical properties. *Macromolecules* **1996,** *29* (24), 7734-7739.

[43] Vaezian, B.; Meyer, J. L.; Economy, J., Processing of aromatic thermosetting copolyesters into foams and bulk parts: characterization and mechanical properties. *Polymers for Advanced Technologies* **2016**.

CHAPTER 3: AROMATIC THERMOSETTING COPOLYESTER FOAM CORE AND ALUMINUM FOAM FACE THREE-LAYER SANDWICH COMPOSITE FOR IMPACT ENERGY ABSORPTION

3.1 Introduction

Porous morphology allows enhanced energy absorption and impact resistance for materials [1]. In that regard, aluminum foams possess a high strength-to-weight ratio and sustain high strain rate large plastic deformations under compressive loading through a plateau-stress yield region [2, 3]. Hence, the aluminum foams can effectively transform kinetic impact energy into plastic deformation energy, which enables them to absorb substantially more impact energy than most bulk metals [4]. Likewise, polymer foams have high energy absorption capacity so that they can effectively minimize transmitted impact load [5]. However, the polymer foams suffer from poor resistance to localized impact due to insufficient mechanical properties of their host polymers [6]. As core materials in sandwich structures, both material systems are joined to face layers via polymer adhesives. Yet, such adhesives constitute a weak interfacial bonding between the sandwich layers, which ultimately results in delamination.

This work was previously published: Bakir, M., Bahceci, E., Meyer, J.L., Economy, J., and Jasiuk, I., Aromatic thermosetting copolyester foam core and aluminum foam face three-layer sandwich composite for impact energy absorption, Materials Letters, 196, 288-291 (2017)

Special thanks to Dr. Ersin Bahceci (Iskenderun Technical University, Turkey) for providing invaluable guidance on the project.

Special thanks to Dr. David Farrow (Mechanical Testing Instructional Laboratory, University of Illinois) for helping with the lap shear and low-velocity impact tests.

We thereby present an ATSP foam core and aluminum foam face three-layer sandwich composite structure as candidates for impact energy absorption applications. Constituent ATSP oligomers were demonstrated to develop adhesive bonding with aluminum upon thermal curing [7]. Nature of the bonding mechanism was attributed to the attraction of surface hydroxyls on the aluminum to polar ester bonds of the oligomers [8]. Also, we recently introduced a high-performance ATSP foam fabricated via a heat-induced polycondensation reaction releasing self-generated blowing agent [9, 10]. The proposed composite foam design builds on these earlier studies.

3.2 Materials and Methods

Experimental details regarding fabrication of the ATSP foam were explained elsewhere [9, 10]. A356 alloy melt-route fabricated aluminum foam pieces were purchased (Duocel®, McMaster-Carr Co., USA) in 10x10x2.5 cm3 and 10x10x1.25 cm3 (length x width x thickness) sizes.

Lap shear experiments were performed using a tensile load frame (4483 Load Frame, Instron Testing Systems, USA) with a 1 mm/min constant crosshead speed. Three samples were tested. The test specimens had half lap-shear joint configurations where two 10x2.5x1.25 cm3 size aluminum foam pieces lapped over 2.5x2.5x0.5 cm3 size mating edges. About 0.25 cm thick ATSP foam was synthesized between 2.5x2.5 cm2 size joint faces to adhere the two aluminum foam pieces together. Tests were done in accordance with an ASTM D3163 standard.

Low-velocity impact tests were performed using an impact machine (Dynatup 8250, Instron Testing Systems, USA). The sandwich specimens were 10x10x3.1 cm3 in size while the ATSP foam thickness was about 0.6 cm. The specimens weighed about 240 g where ATSP foam weight was about 50 g. A hardened steel impactor with a 1.9 cm diameter and a 0.95 cm radius

of curvature was used. The impactor was measured to have a Rockwell C55 hardness. Static loads of 11.3 kg and 34.0 kg were applied to generate impact energies of 90 J and 200 J, respectively. Drop heights were about 70 cm, and impact velocities were about 4 m/s.

3.3 Results and Discussion

The fabrication process of the sandwich composite structure is shown in Figure 3.1. A powder mixture of acetoxy (red color) and carboxylic acid (blue color) functional group constituent oligomers was sandwiched between two aluminum foam layers, and all were enclosed by a metal frame. The metal frame was covered with a PTFE fabric peel-ply to prevent undesired bonding to the oligomer mixture upon curing. Then, the assembly was placed into a hot press where it was held intact with a steel plate rested on it. Next, a pre-designed thermal cure cycle was applied in which the esterification reaction initiated at elevated temperatures (~200 °C) between the functional groups of the oligomers releasing acetic acid as a reaction by-product. As the process carried on, the oligomers crosslinked to form the ester backbone of the ATSP foam while the acetic acid generated a porous morphology. In the meantime, the molten oligomers wetted aluminum foam surfaces developing intimate contact interlayers. Upon curing, a three-layer sandwich structure was obtained wherein the ATSP foam core solid-state bonded onto the aluminum foam face layers.

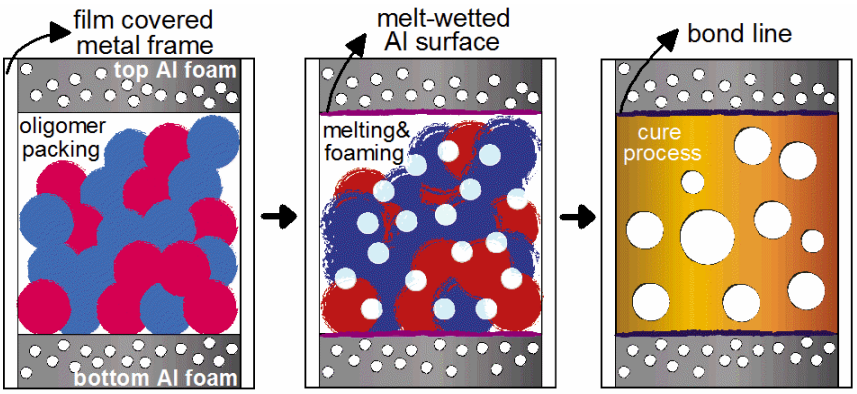

Figure 3.1 Schematic description of the fabrication process of the sandwich composites.

In Figure 3.2 we demonstrate fabricated sandwich composite structures. ATSP foam successfully formed between the two aluminum foam layers having a closed-cell morphology. As seen in the cross-section, ATSP foam established a smooth continuous bond line with both aluminum foam layers wherein neither bonding layer nor flush were formed (Figure 3.2.a). Also, we did not observe any significant outflowed polymer from the aluminum layers. The foaming process tended to evolve inside the enclosed space between the aluminum foam layers and the metal frame (Figures 3.2.b and 3.2.c). Additionally, the ATSP foam did not expand up through pore cavities of the aluminum foams. Overall, the samples were in neat shapes, nor requiring further machining.

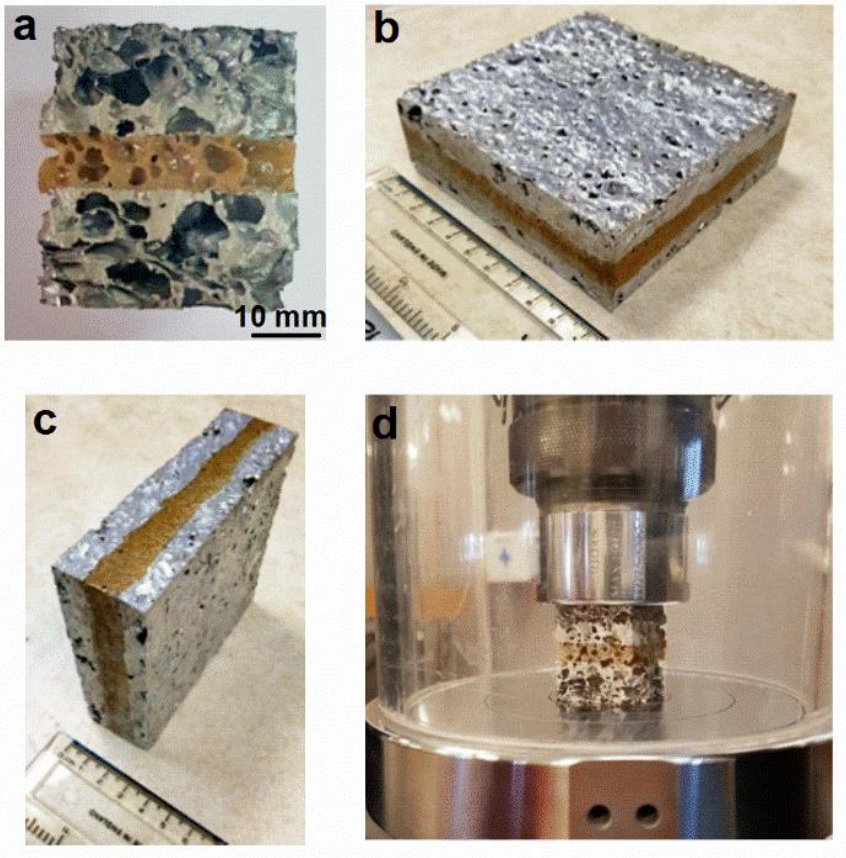

Figure 3.2 Images of the sandwich composite structure.

Lap shear experiments were done to determine adhesion characteristics between the ATSP foam and the aluminum foam layers of the sandwich composites, as shown in Figure 3.3. As specimens were pulled under a controlled deformation rate (1 mm/min), they all yielded over the thinner parts of the aluminum foams with a thickness of about 0.5 cm (Figures 3.3.a and 3.3.b). During this process, the ATSP foam and bonding region remained intact. Lap shear strength results were between 0.6 to 1.0 MPa, which represented mere tensile strengths of the bare aluminum foam parts (~1.2 MPa) (Figure 3.3.c). Such slightly lower values are attributed to uneven pore distributions caused by specimen machining process.

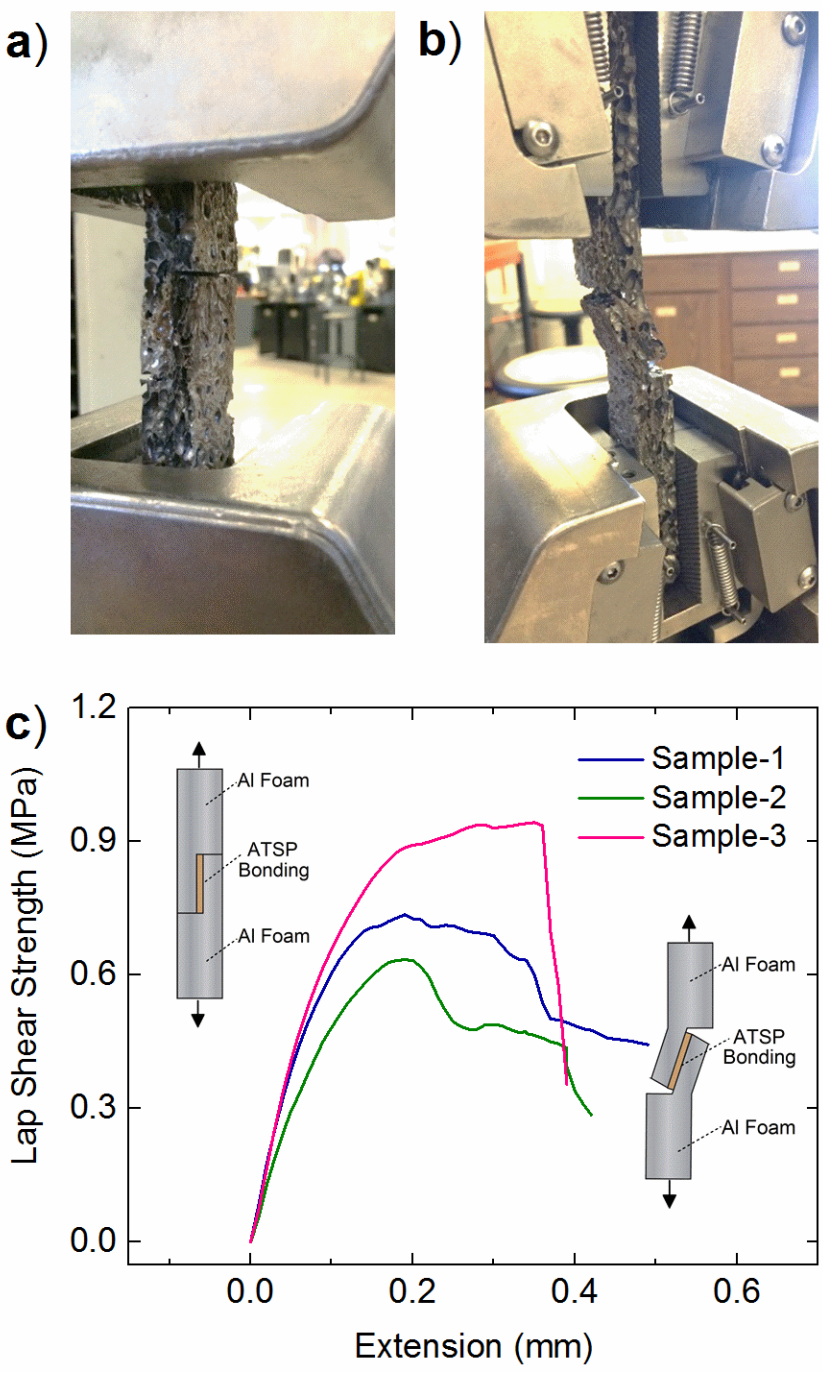

Figure 3.3 Images of a lap shear sample before (a) and after (b) testing. Results of lap shear strength measurements (c).

Figure 3.4 shows drop-weight impact test results of the bare aluminum foams and the sandwich composite structures. The 1.25 cm and 2.5 cm thick aluminum foams were able to withstand up to ~3 kN maximum load, which translates into absorption energies of 26 J and 42 J, respectively, while total applied impact energies were 90 J (Figures 3.4.a and 3.4.b). Consequently, the impactor passed through both aluminum foam specimens (Figures 3.4.c and 3.4.d). However, the sandwich composite structure was able to completely absorb the total of 90 J impact energy, which corresponded to an 8 kN maximum load (Figures 3.4.a and 3.4.b). Furthermore, as we increased the applied impact energy up to 200 J, the sandwich composite structure was able to absorb about 150 J energy.

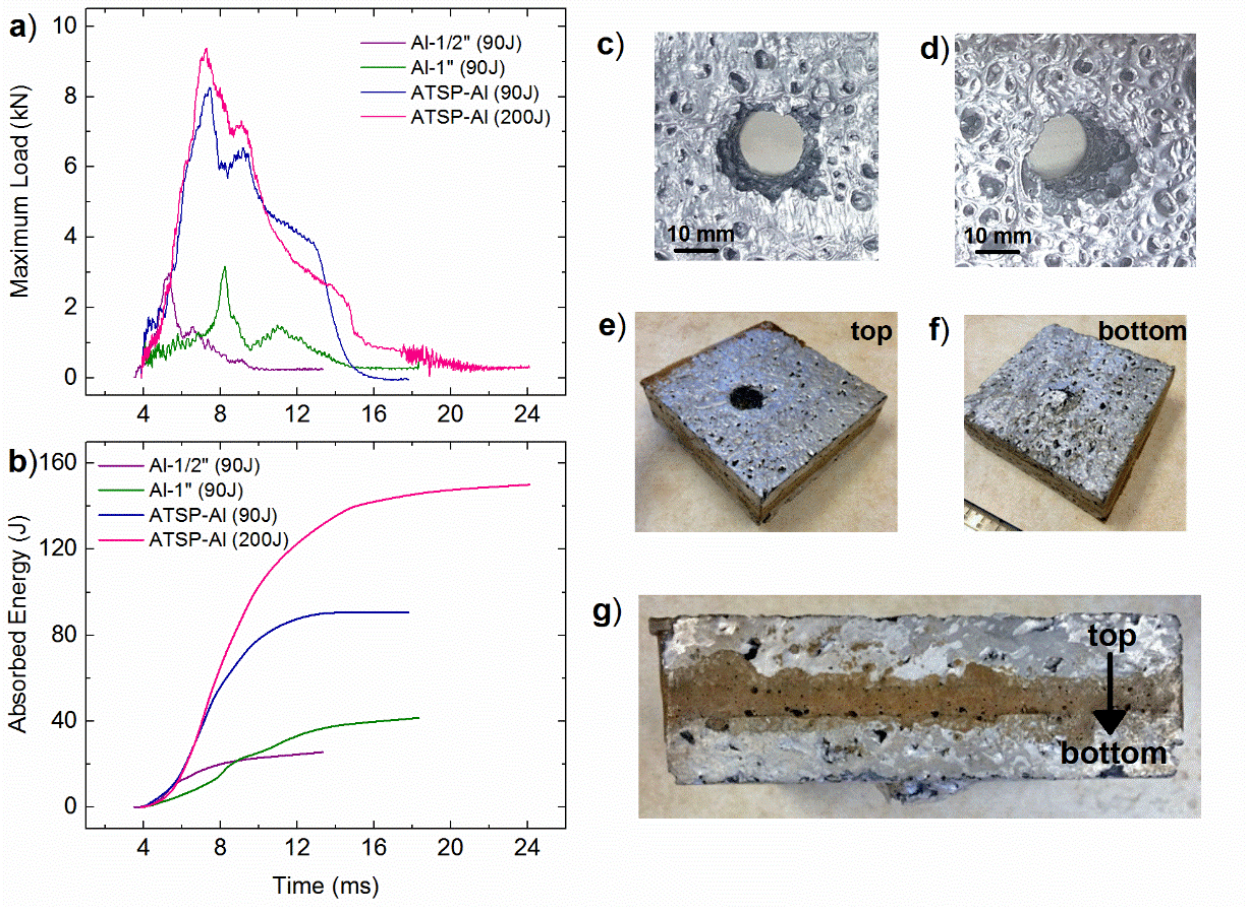

Figure 3.4 Drop-weight impact test results representing maximum load (a) and impact energy absorption (b). Images of impacted bare aluminum foams of 2.5 cm (c) and 1.25 cm (d) thicknesses, and a sandwich composite structure (e-g).

We additionally observed that the bare aluminum foams were deformed through broken cell walls. Although the layer thickness was doubled, the amount of the absorbed impact energy by the bare aluminum foams did not reflect such thickness effect. On the other hand, the three-layer sandwich composite structure was able to absorb up to four-fold higher impact energy, as compared to the bare aluminum foam of the same layer thickness. Its energy absorption density was calculated to be about 200 J-cm3/g. The sandwich structure successfully stopped the impactor inside the ATSP foam core region such that only a small dent was generated on the bottom aluminum foam layer. We concluded that the interfacial bonding along with strong mechanical properties of the ATSP foam core gave rise to such an enhanced impact energy absorptive sandwich composite structure. The ATSP foam cores produce robust interfacial bonding during cure with high-performance aluminum and titanium alloys, stainless steel, and high-temperature polymer composite laminate face sheets [8]. Thus, ATSP foam core sandwich structures can address structural, ballistic, crash impact energy absorption applications.

3.4 Conclusion

We developed an ATSP foam core and aluminum foam face three-layer sandwich structure bonded via the foaming process. The interlayer adhesion strength outperformed mechanical limits of the bare aluminum foam. The sandwich structure had superior impact energy absorption performance as compared to the bare aluminum foams. This work provides a framework for more detailed studies of these materials and demonstrates their utility as composite core materials.

3.5 References

[1] G.J. Davies, S. Zhen, Metallic foams: their production, properties and applications, Journal of Materials Science 18(7) (1983) 1899-1911.

[2] V. Deshpande, N. Fleck, High strain rate compressive behaviour of aluminium alloy foams, International Journal of Impact Engineering 24(3) (2000) 277-298.

[3] Y. Alvandi-Tabrizi, D.A. Whisler, H. Kim, A. Rabiei, High strain rate behavior of composite metal foams, Materials Science and Engineering: A 631 (2015) 248-257.

[4] A.G. Hanssen, M. Langseth, O.S. Hopperstad, Static and dynamic crushing of circular aluminium extrusions with aluminium foam filler, International Journal of Impact Engineering 24(5) (2000) 475-507.

[5] L. Di Landro, G. Sala, D. Olivieri, Deformation mechanisms and energy absorption of polystyrene foams for protective helmets, Polymer testing 21(2) (2002) 217-228.

[6] M.A. Hazizan, W. Cantwell, The low velocity impact response of foam-based sandwich structures, Composites Part B: Engineering 33(3) (2002) 193-204.

[7] D. Frich, J. Economy, K. Goranov, Aromatic copolyester thermosets: high temperature adhesive properties, Polymer Engineering & Science 37(3) (1997) 541-548.

[8] K. Xu, J.C. Selby, M.A. Shannon, J. Economy, Adhesion mechanisms in the solid-state bonding technique using submicrometer aromatic thermosetting copolyester adhesive, Journal of Applied Polymer Science 92(6) (2004) 3843-3856.

[9] B. Vaezian, J.L. Meyer, J. Economy, Processing of aromatic thermosetting copolyesters into foams and bulk parts: characterization and mechanical properties, Polymers for Advanced Technologies 27(8) (2016) 1006-1013.

[10] M. Bakir, J.L. Meyer, J. Economy, I. Jasiuk, Heat-induced polycondensation reaction with self-generated blowing agent forming aromatic thermosetting copolyester foams, Macromolecules 49(17) (2016) 6489-6496.

CHAPTER 4: AROMATIC THERMOSETTING COPOLYESTER NANOCOMPOSITE FOAMS: HIGH THERMAL AND MECHANICAL PERFORMANCE LIGHTWEIGHT STRUCTURAL MATERIALS

4.1 Introduction

The foremost challenge in the development of structural materials for transportation is weight reduction in major load-bearing metal components to increase fuel efficiency. Three viable solution approaches to address this issue include: (1) accommodate conventional metals with reduced density, (2) employ alternative higher performance metals with cost penalty, and (3) explore polymer matrix composites. First, utilizing conventional lightweight metals can readily ensure cost-effective, rapid and reliable solutions. For example, aluminum alloys have been adopted by the automotive industry to enable significant weight reduction by replacing steel components [1]. Second, applications of higher performance metals can provide further improvements (e.g. magnesium alloys) beyond the conventional solutions, yet come along with increased raw material costs [2]. Third, polymer matrix composites can generate very lightweight structures without compromising strength and structural stability [3]. For instance, fiber reinforced polymer matrix composites have become a primary structural element in the aircraft industry due to a substantially improved fuselage weight performance [4]. Currently, the alloy and polymer composite configurations are essentially suitable for panel skin components in the structural applications.

This work was previously published: Bakir, M., Meyer, J.L., Economy, J., and Jasiuk, I., Aromatic thermosetting copolyester nanocomposite foams: high thermal and mechanical performance lightweight structural materials, Polymer, 123, 311-320 (2017)

Hence, there remains a need for space-filling, strong, and lightweight structural materials. Polymer foams have low-density structures [5] along with acoustic damping properties [6], [7], [8] which make them promising candidates for such an application space. However, current polymer foam configurations are lacking in mechanical strength and thermal stability due to limitations stemming from their base polymers. Alternatively, polymer nanocomposites foams, incorporating nanoparticle fillers developed in the past decade, demonstrated notable improvements in thermophysical properties [9], [10], [11], [12], [13] and [14]. Further details on the polymer nanocomposite foams can be found in comprehensive literature reviews [15], [16] and [17].

Particularly, carbon nanofiller incorporated nanocomposite polymer foams have drawn considerable interest to address certain aspects of the structural applications. For instance, graphene oxide infused cellulose matrix nanocomposite foams exhibited improved fire-retardancy and high-performance thermal insulation [18]. Also, polymer nanocomposite foams with relatively low carbon nanofiller loadings (<1 wt.%) obtained substantially increased electrical conductivity and electromagnetic interference shielding effectiveness (~30 dB) [19], [20], [21], [22] and [23]. Furthermore, the CNT incorporation in polymer nanocomposite foams helped to enhance acoustic absorption capabilities [24]. However, as noted above, the demonstrated nanocomposite configurations were deficient in mechanical strength and thermal stability due to mediocre inherent properties of their host thermoplastic polymer matrices. On the other hand, regarding fabrication methods of the polymer nanocomposite foams, solution-mixing and melt-blending approaches were extensively utilized to combine nanofillers and the polymer media. Consecutively, blowing agents (e.g. supercritical CO_2) were injected into the two-compound systems to initiate foaming processes, and then porous morphologies were generated

[14]. However, these conventional approaches were strictly contingent upon, first, homogenous and intact dispersions of the nanofillers, and, second, the solubility of the blowing agents in polymer solutions. The two issues became critical as processing parameters were subject to change since viscosities of the molten media would vary with different geometry and loading levels of the nanofillers [25], [26] and [27]. As a result, such polymer nanocomposite foam structures do not fully benefit from the use of the carbon nanofillers, as also reflected in their limited structural properties.

All in all, the polymer nanocomposite foams bear a technological potential by exclusively embodying multifunctional material properties within low-density structures to address cutting-edge structural application problems. However, contemporary material configurations could only attain limited structural performances, caused either by modest physical properties of host low-performance commodity polymers, or nanofiller-averse processing techniques. As an alternative strategy, we introduce aromatic thermosetting copolyester nanocomposite foams fabricated via *in situ* hydrodynamic forces induced during the polymer condensation reaction which, in return, yielded significant improvements in the thermophysical properties. This method also allowed easy incorporation of arbitrary forms of carbon nanofillers into a polymer matrix, and facilitated homogenous and intact dispersion of the nanoparticles. The high physical property enhancements indicated strong compatibility between the carbon nanofillers and ATSP matrix. Thus, the novel ATSP nanocomposite foams possess superior structural properties as fabricated through a simple and easily adaptable method to potential structural applications.

4.2 Materials and Methods

The carboxylic acid and acetoxy functional group constituent oligomers were synthesized using biphenol diacetate (BPDA), 4-acetoxybenzoic acid (ABA), isophthalic acid (IPA), and

trimesic acid (TMA) (Sigma-Aldrich Co., USA) at particular molar feed ratios of 1:2:3:2 and 1:0:3:3 of TMA:IPA:ABA:BPDA for the matching carboxylic acid-capped and acetoxy-capped oligomers, respectively. Further details regarding synthesis protocols are given in earlier works [28], [29] and [30].

The ATSP nanocomposite foams were obtained via a condensation polymerization reaction between carboxylic acid and acetoxy functional group oligomers, which generated a cross-linked aromatic polyester backbone and emitted acetic acid as a reaction by-product (Figure 4.1.a) [28]. Phase transformations which occur during the thermal cure cycle are illustrated in Figure 4.1.b. The thermal cycle included two dwell stages at 202 °C for 90 minutes and 270 °C for 150 minutes, which corresponded to relaxation/melting of the constituent oligomers and nucleation/bubble growth through the release of the acetic acid, respectively. Additionally, the thermal cycle had a final cure stage at 330°C for 90 minutes. The carboxylic acid and acetoxy-capped oligomers (at 1:1 weight ratio) were mixed in the solid state as dry powders with carbon nanofillers of 3 wt.% at room temperature. The carbon nanofillers were Carbon Black (CB) (Vulcan XC72, Cabot Corp., USA) (bulk density: 264 kg/m^3), Carbon Nanotube (CNT) (Industrial-Grade Multi-Walled Carbon Nanotubes, US Research Nanomaterials, Inc., USA) (outside diameter (OD): 10-30 nm, inside diameter (ID): 5-10nm, length: 10-30 μm, bulk density: 2100 kg/m^3), and Graphene Nanoplatelet (GNP) (Grade M-5, XG Sciences, Inc., USA) (flake diameter: ~5 μm, thickness: 6-8 nm, density: 2200 kg/m^3). We named the neat foam and nanocomposite foam as neat ATSP and ATSP-Nanofiller Type, respectively.

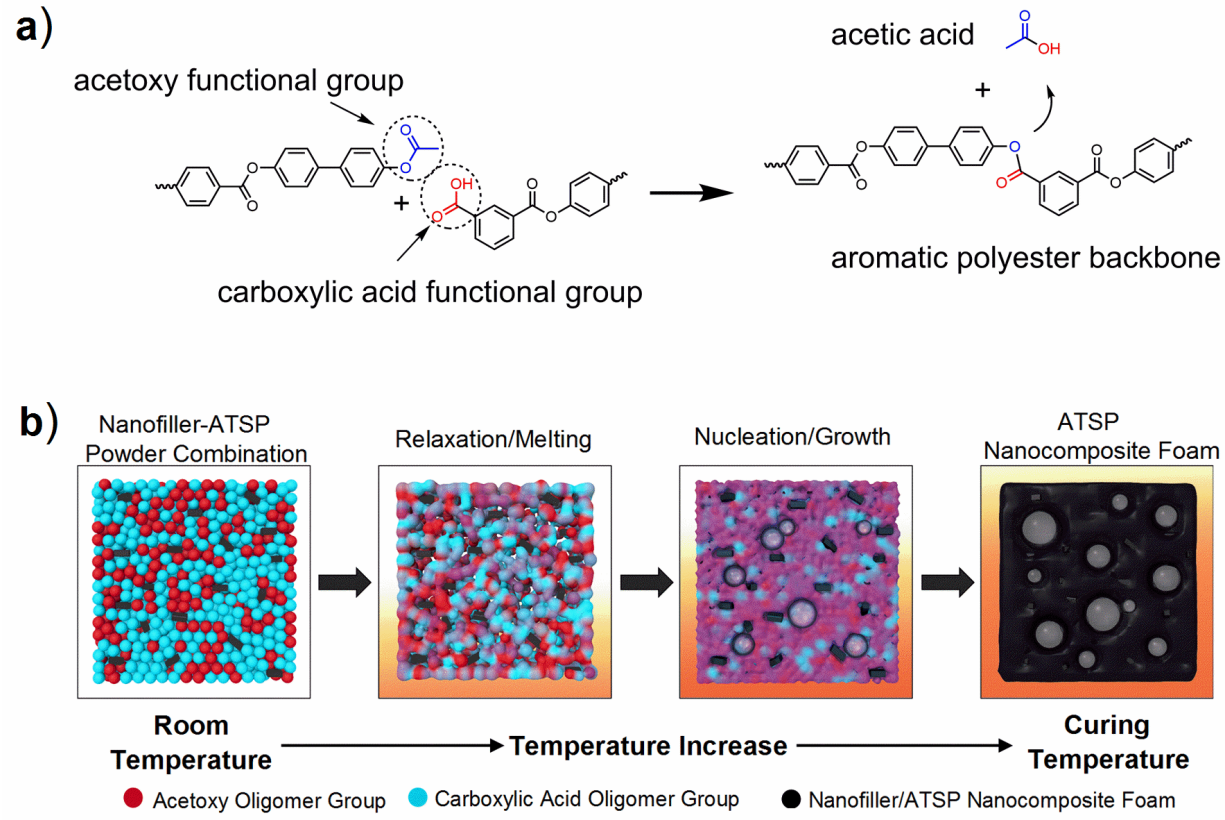

Figure 4.1 Schematic representations of the interchain transesterification polymerization reaction mechanism between the acetoxy and carboxylic acid functional groups generating aromatic polyester backbone and discharging acetic acid (a). Phase transformation stages developed during the thermal cure cycle of the nanocomposites (b).

Regarding the visual analysis of the polymerization reaction, and, particularly, the bubble nucleation/growth image, the powder-form mixed combinations were sandwiched between two glass coverslips, and then the sandwiched piece was placed onto a heating stage (TMS 91 Linkam Scientific Instruments Ltd., UK). The heating stage was then separately set into an upright bright-field optical microscope, and a temperature-ramp heat cycle with constant 40 °C/min heating rate was applied. Ultraviolet (UV) light images were obtained using a handheld lamp at 365 nm wavelength.

The cure characteristics of the nanocomposite foams were analyzed using a Differential Scanning Calorimetry (DSC) (DSC 2910, TA Instruments, USA) and Thermogravimetric

Analysis (TGA) (TGA 2950, TA Instruments, USA). The tests were performed under dry nitrogen. In the DSC measurements, the first cycle denoted curing cycles of the mixed combinations (~15-20 mg) where they were heated up to 400 °C with a 10 °C/min heating rate, in about 40 minutes. Following this, the samples were kept under nitrogen, to minimize exposure to the oxidative environment and thermal degradation effects, until the temperature of the DSC heating cell returned to room temperature, in about 2 hours. Afterward, post-curing cycles were applied on the samples heating them back to 400 °C with a 10 °C/min heating rate. Similarly, in the TGA measurements, the first cycle denoted curing cycles of the mixed combinations in which the combinations were heated up to 330 °C with a 10 °C/min heating rate in about 30 minutes, and then the temperature was held constant at 330 °C for about 90 minutes. As the mixed combinations were cured following the temperature-hold step, the samples were kept under nitrogen, to minimize exposure to the oxidative environment and thermal degradation effects, until the temperature of the TGA heating chamber returned to room temperature, in about 2 hours. Then, post-curing cycles were applied to the cured combinations, heating them again up to 330 °C with 10 °C/min heating rate, and holding the temperature constant at 330 °C for about 90 min.

Scanning Electron Microscopy (SEM) (S-4800, Hitachi, Japan) was used in the high-resolution mode to image microstructures of uncured powder combinations and fracture surfaces of the nanocomposite foams to analyze distributions of the carbon nanofillers in the matrix. The SEM was operated in high-resolution upper detector mode at 10 kV voltage and 5 μA current. The samples were sputter coated with Pd-Au to minimize charging effects.

Morphologies of the nanocomposite foams were characterized using X-ray diffractometer (XRD) (PANalytical/Philips X'pert, Netherlands) with Cu K-alpha source operated at 45 kV and

40 mA, and 0.15148 nm wavelength with 0.01 °/s scanning rate, scanned between diffraction angles of $2\theta=10°$ and $2\theta=60°$.

Linear thermal expansion characteristics of the nanocomposite foams were measured using a horizontal digital dilatometer (Model 2010 B, Edward Orton Jr Ceramic Foundation, USA). The tests were performed under air. A temperature-ramp heating cycle was applied with a constant 3 °C/min heating rate until 200 °C. The samples had cylindrical shapes with a diameter of 1.27 cm and a height of 2.54 cm.

Thermal degradation stability temperatures of the nanocomposite foams were characterized using the TGA. A temperature-ramp heating cycle was applied with a constant 10 °C/min heating rate until 600 °C. Specimens weighed about 10-15 mg.

Compressive mechanical properties of the nanocomposite foams were measured using a compressive load frame (4483 Load Frame, Instron Testing Systems, USA) with a constant crosshead speed of 6 mm/min. The specimens were cylindrical in shape with a diameter of 1.27 cm and a height of 2.54 cm. Structural density calculations were performed using the Buoyancy Method. Relative density was calculated as the ratio of the measured structural density of the nanocomposite foam to the density of neat fully dense ATSP (1.27 Mg/m^3). The compressive mechanical properties were averaged over five test samples, and standard deviations were given by error bars, accordingly.

4.3 Results and Discussion

We first explain the oligomer and nanofiller powder solid state mixing approach utilized for the fabrication of the ATSP nanocomposite foams. In this method, as-purchased chemically pristine (non-functionalized) carbon nanofiller powder (3 wt.% of CNT, GNP and CB, separately) was mixed with uncured ATSP powder (composed of acetoxy and carboxylic acid-

functional group oligomers mixed at 1:1 weight ratio), which formed a carbon nanofiller-ATSP powder combination in solid state. As shown in Figure 4.2.a, the black carbon nanofiller powder turned white ATSP powder to pitch dark, which indicated a sufficiently uniform distribution of the carbon nanofillers with the ATSP precursor oligomers. Additionally, UV light images clearly displayed distribution quality of the carbon nanofillers at macroscale in the powder combination form (Figure 4.2.b). More importantly, the method inherently provided a "soft-bed" (the ATSP being in powder form) for the carbon nanofillers during the mixing step, which helped to retain their as-produced pristine geometries (Figure 4.3. a). This approach is in contrast to conventional liquid-phase shear-mixing based methods, which are known to be "nanofiller-averse," as they typically cause polymer nanocomposites to have broken nanofillers and aggregated nanofiller regions [31] and [32]. Therefore, the polymer nanocomposite configurations demonstrated so far only moderate structural property enhancements through the addition of nanofillers [33]. Herein, as a result of our "nanofiller-friendly" processing method, the ATSP nanocomposite foams yielded significant structural property improvements, as further discussed later in the text. Also, the mixing process established a geometrical conformity between ATSP oligomer particles of ~100 μm in diameter and the carbon nanoparticles having micron-scale surface features, wherein the nanofillers formed additional short-range attractive interactions with the ATSP oligomer particles. Hence, the van der Waals forces between individual nanofiller particles were mitigated through the polymer-nanofiller interactions, which facilitated separation of the individual nanofillers in solid state prior to the polymerization process (Figure 4.3. b-d) [34]. Hence, homogenous distribution of the carbon nanofillers at the micron scale was successfully achieved via the powder mixing technique.

Next, we report observations obtained during the polymerization reaction using a heating-stage assisted optical microscope. Since the nature of the polymerization process between the constituent oligomer groups was discussed in greater details elsewhere [28], only key issues are highlighted here. Briefly, when a temperature-ramp heating cycle was applied, oligomer particles melted at around 170ºC. Then, the polycondensation reaction was observed to start at around 200 ºC, which was indicated by bubble formation in the melt. The acetic acid by-product was evolved as a gas as it was well above its boiling point of 118 ºC. When the temperature was further increased through the polymerization reaction, the gaseous acetic acid formed a porous morphology within the oligomer melt medium. From prior studies, at elevated temperatures (~290 ºC), temperature-driven hydrodynamic motion within the melt apparently caused relocation of the blowing agent bubbles, which in this study enabled redistribution and then rearrangement of the nanofiller particles in the molten domain prior to the curing [28, 35]. This will be systematically studied at microscale via temperature-controlled *in-situ* electron microscopy in the future.

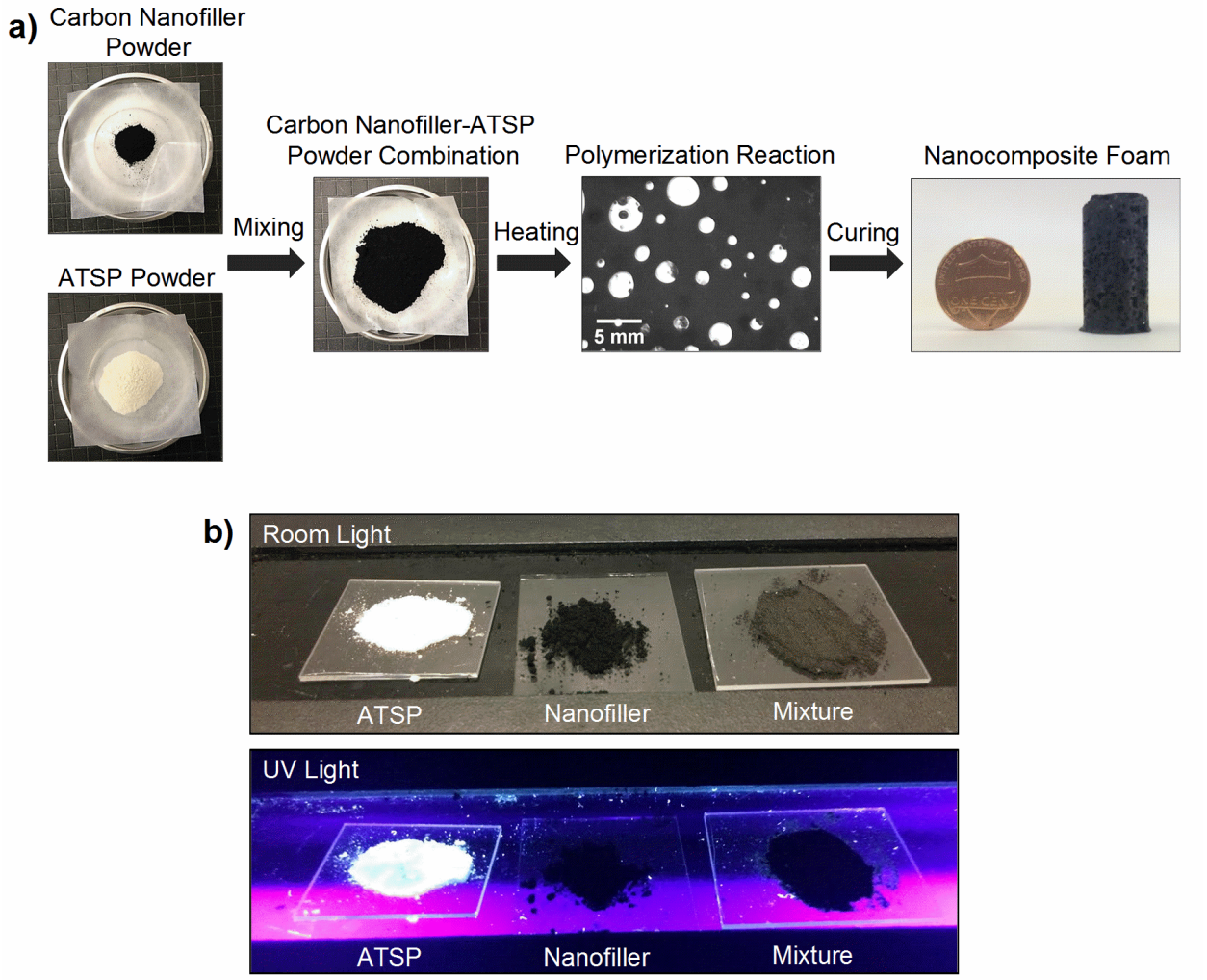

Figure 4.2 Images of the carbon nanofiller powder, uncured ATSP powder, carbon nanofiller-ATSP powder combination, the ATSP-3 wt.% GNP combination during the polymerization reaction at 290 ° C, and a fabricated ATSP nanocomposite foam (a). Room light and UV light images of the uncured ATSP powder, pristine carbon nanofiller, and carbon nanofiller-ATSP powder mixture (b).

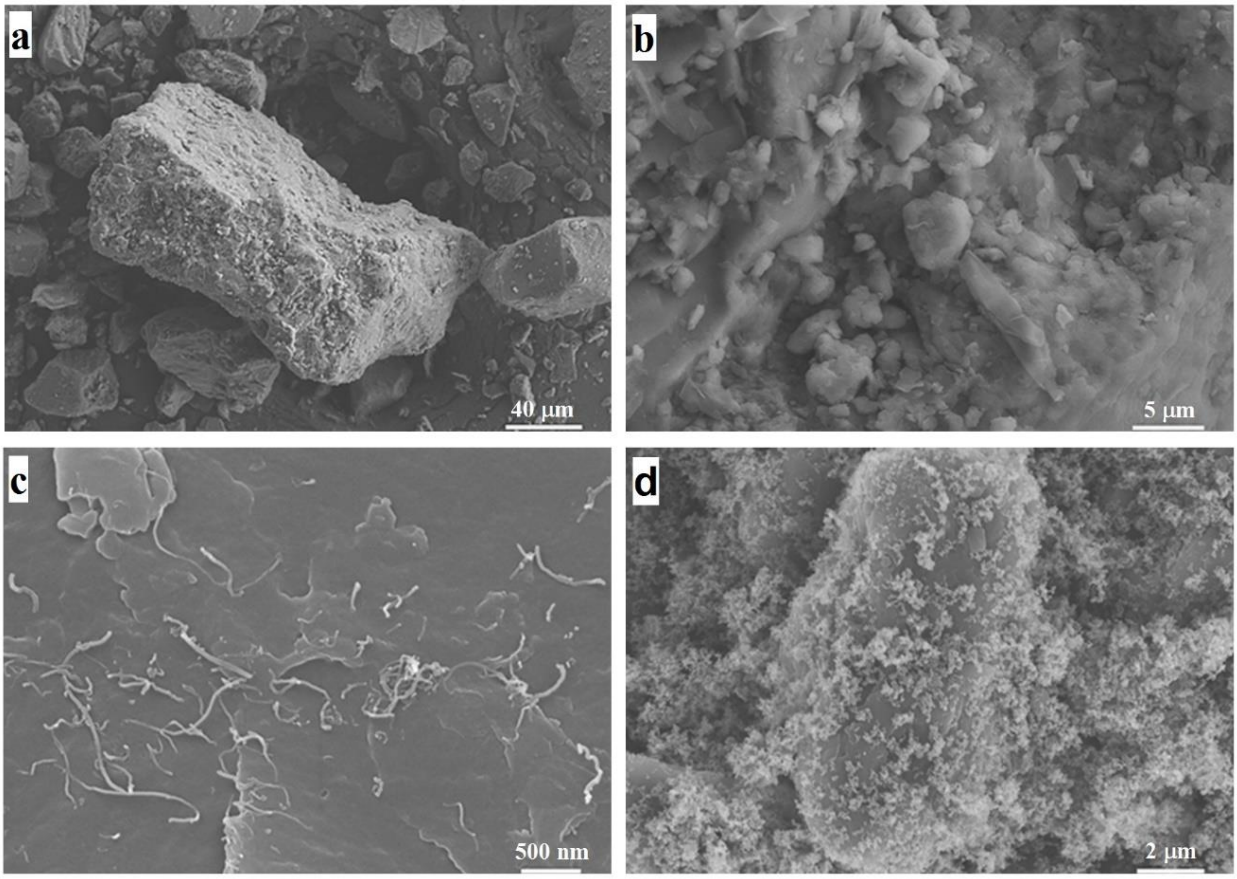

Figure 4.3 SEM images of the powder combinations. An isolated individual oligomer particle decorated with nanofiller particles (a), and distributed GNP (b), CNT (c) and CB (d) nanoparticles on the oligomer particle surfaces.

We analyzed thermal characteristics of the polymerization reaction for each powder combination applying a temperature-ramp heating cycle in the DSC. Figure 4.4 shows cure and post-cure behaviors of the three combinations (ATSP-CNT, ATSP-GNP, and ATSP-CB) in comparison to a parent ATSP powder. We observed that all the powder combinations, as well as the neat ATSP powder, exhibited endothermic profiles during the heating cycle due to the condensation polymerization reaction carried on between the oligomer groups. In the heat flux curves, the combinations initially formed a dimple at around 75-80°C indicating softening of the oligomer groups. Following this, melting of the oligomers started which displayed isothermal-

plateau regions extending until about 200 °C where the polycondensation reaction started. Then, the GNP and CNT combinations showed sharp downward trends corresponding to sudden heat uptakes into their melt systems. We attributed such abrupt behaviors to acetic acid discharge-driven bubble growth during the polycondensation reaction through the presence of the carbon fillers. This behavior can be detailed with the homogenous bubble nucleation model (classical nucleation theory) [36]. The model defines Gibbs free energy (ΔG) as the driving factor for bubble nucleation and growth being functions of volume free energy (ΔG_v) (energy difference between the gas and polymer phases) and gas-liquid (bubble-polymer) interface surface energy (γ). Hence, as the carbon nanofillers increased the viscosity of the molten domains [37], the blowing agent (acetic acid) would require much more heat energy (ΔG_V) to overcome present viscous forces (γ) while working towards maintaining bubble growth, which yielded those endothermic features in the heat curves. After that, the powder combinations revealed distinct cure regions between 270 °C and 330 °C temperature range. The cure regions of the combinations had slightly broader temperature window as well as stronger endothermic nature than the parent material. Moreover, especially in the GNP and CNT combinations, the peak cure temperature slightly shifted to a lower value (~ 300 °C), which could have two underlying reasons. First, the increased melt viscosities for thermosets could cause early initiation of gelation and cross-linking at relatively lower temperatures [38]. Second, the reactive functional groups of the oligomers could graft onto carbon nanofillers that would alter viscous characteristics of the molten domain prompting a lower temperature curing [39]. Following the cure cycles, we subsequently performed post-cure analyses of the corresponding combinations. Nearly-flat isothermal characteristic curves, without any features of the prior curing processes, were obtained for all of the combinations, which clearly indicated their sufficiently cured

conditions. Overall, we observed that the GNP and CNT could marginally change cure characteristics of the powder combinations, yet conclusive remarks would require further systematic rheological and spectroscopical analyses.

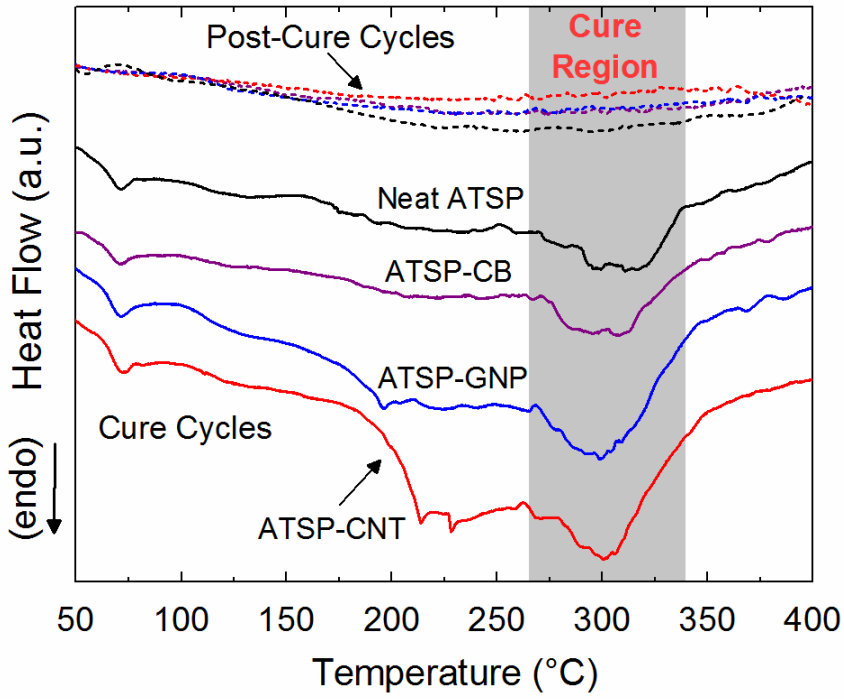

Figure 4.4 DSC analyses of cure and post-cure characteristics of the nanofiller-ATSP powder combinations. Tests were performed under nitrogen. The heating rate was 10 °C/min.

Additionally, thermogravimetric characteristics of the polymerization reaction for the powder combinations were measured using the TGA. Heating cycle included two stages: temperature-ramp until 330°C (the final cure temperature used in the heating cycle), and isothermal temperature-hold at 330°C for 90 minutes. Figure 4.5 shows cure and post-cure behaviors of the three powder combinations in comparison to a parent ATSP powder. The main characteristic of the thermogravimetric curves was the substantial weight loss occurred between 15-40 min. time-window, corresponding to 200-330 ºC temperature-range. Such a steep decrease (~15 wt.% of the initial combination) took place as a result of the acetic acid emission being the

by-product of the polycondensation reaction. The results did not reveal any notable differences among the powder combinations as well as the parent ATSP powder. It indicated that the polymerization reaction ordinarily progressed successfully forming the ATSP backbone of the nanocomposite foams. The subsequent gradual decline in the thermogravimetric curves within the temperature-hold region (40-120 min.) corresponded to cross-linking formation wherein only small weight loss occurred. The slight mass losses happened due to thermal degradation of reactive functional groups in the course of curing at high temperature. Afterward, post-cure cycles of the corresponding combinations demonstrated nearly-flat thermogravimetric curves indicating effectively cured conditions of the combinations during the first cycles.

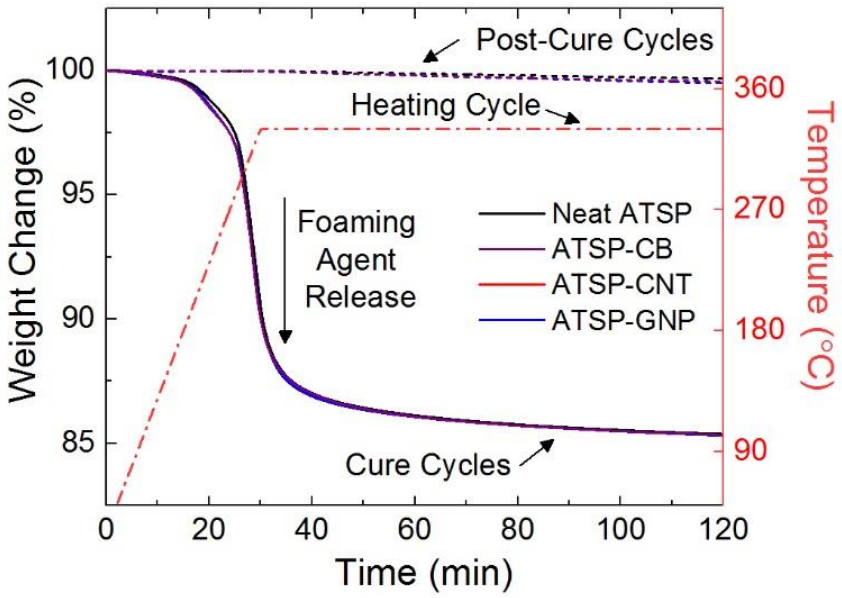

Figure 4.5 TGA analyses of cure and post-cure characteristics of the nanofiller-ATSP powder combinations. Tests were performed under nitrogen. The heating rate was 10 °C/min.

Having the cure characteristics analyzed on the powder combinations, we applied the previously demonstrated thermal cycle [28] to enable sufficient curing for the nanocomposite foams (see experimental section 4.2 for details). Microstructural analyses on the nanocomposite

foams were conducted using SEM, as shown in Figure 4.6. Low-magnification images clearly displayed porous morphologies of the nanocomposite foams (Figures 4.6.a-b) which evinced that the polymerization reaction successfully developed during the fabrication cycle. Furthermore, high-magnification images showed the carbon nanofiller particles dispersed in the ATSP matrix. Although such microscale images were not conclusive about overall macroscale distributions of the nanofillers, we did not observe any significant agglomeration regions formed in the matrix. In particular, the GNP nanofillers were very well distributed in the ATSP matrix (Figure 4.6.c) while preserving their pristine geometries (as-fabricated GNP flake size was ~5 μm) (Figure 4.6.d). Also, CNT nanofillers (Figure 4.6.e) displayed small aggregation sites, about 5 μm in diameter, while CNTs easily bundled up. Micron-size oligomer particles did not necessarily penetrate through very small distances (on the order of nanometers) between individual CNTs. However, those aggregation sites were very well infiltrated and enclosed by the ATSP matrix upon polymerization which enabled CNT to behave like micron size fibers. Interestingly, CNTs preferentially self-aligned along pore surfaces, which could be one of the factors that yielded significant improvements in the mechanical properties, as explained later. Additionally, CB particles (Figure 4.6.f) demonstrated micron-scale segregation groups in the matrix, which in fact was an overall good dispersion condition for the individually nanosized particles. In summary, based on the SEM images, the nature of the mixing process allowed effective dispersion of the GNPs due to the aforementioned geometrical conformity. However, further studies using tranmission electron microscopy would help to understand the dispersion of the nanoparticles at finer scales.

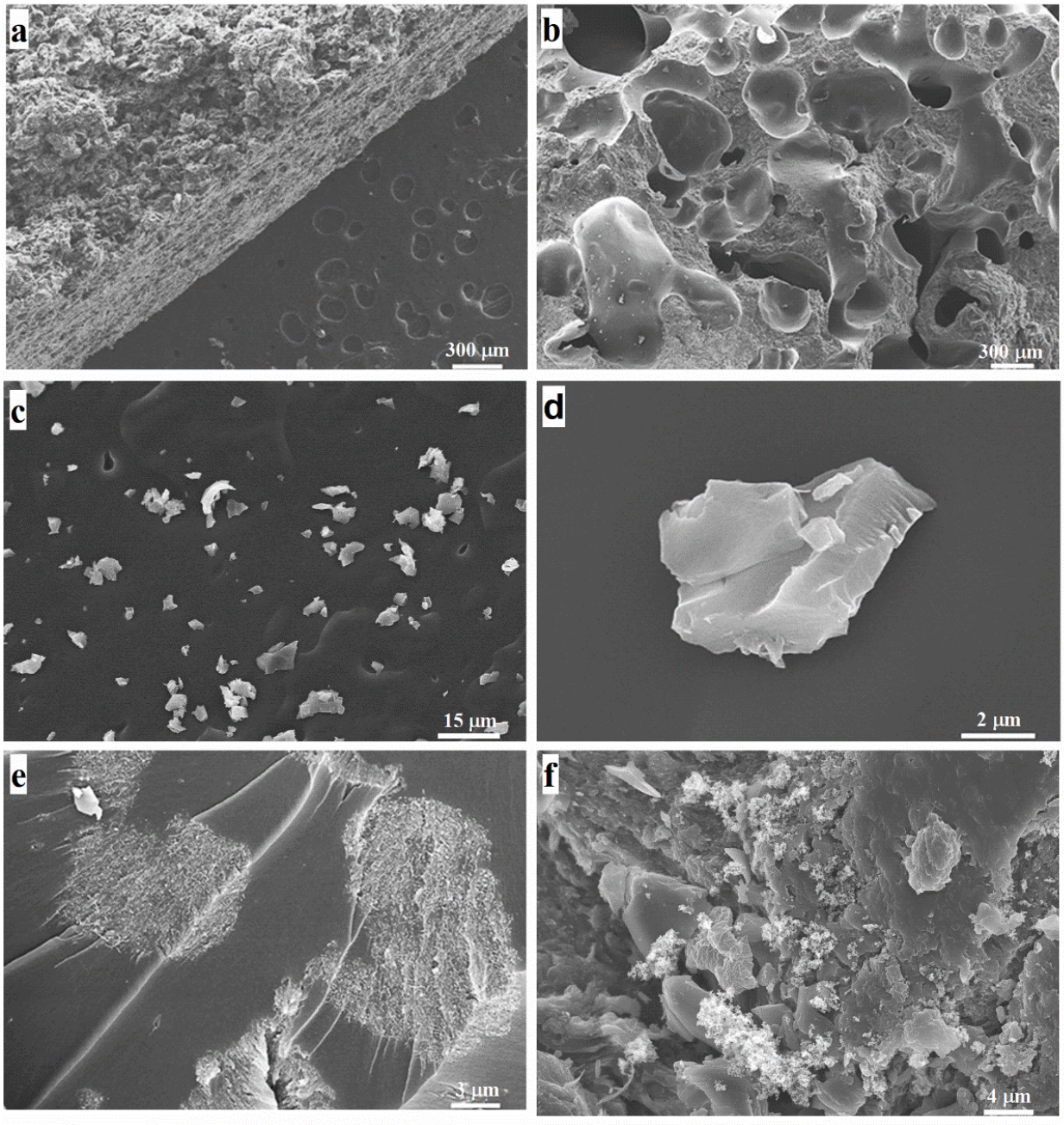

Figure 4.6 SEM images of nanocomposite foams. ATSP-GNP specimen on cross-section (a), surface topology (b), nanofiller distribution on pore surface (c), and an isolated GNP flake (d). ATSP-CNT sample nanofiller distribution (f). ATSP-CB sample nanofiller distribution (e).

In addition to the microstructural analysis, phase morphologies of the ATSP nanocomposite foams were characterized using XRD, as shown in Figure 4.7. The neat ATSP foam demonstrated a very broad primary peak centered around $2\theta=20°$, which was expected due

to amorphous polymer morphology. The nanocomposite foams displayed similarly broad primary peaks, which indicated that amorphous nature of the host ATSP matrix likewise was preserved. We also observed several characteristic effects arising from the carbon nanofillers. We note that hexagonal lattice structure of graphitic carbon displays a (002) diffraction peak, which gives rise to a broad peak in CB [40] and sharp peaks in CNT and GNP [41]. In that regard, the CB nanofiller generated a shoulder on the primary amorphous ATSP peak. These features suggest that highly disordered (amorphous) form of the pristine CB in the matrix caused peak broadening while being well incorporated into the matrix. On the other hand, having highly crystalline *sp2* hybridized networks, the CNT and GNP nanofiller incorporated foams revealed sharp characteristic peaks of the carbon morphology, which also indicated that relatively pristine geometries of the nanofillers remained intact during the fabrication process. Such low intensities of the carbon peaks (as compared to that of the primary peak) indicated effective interactions with the host matrix. Also, quite low carbon nanofiller loadings (3 wt.%) could cause the low intensity for the characteristic carbon peaks.

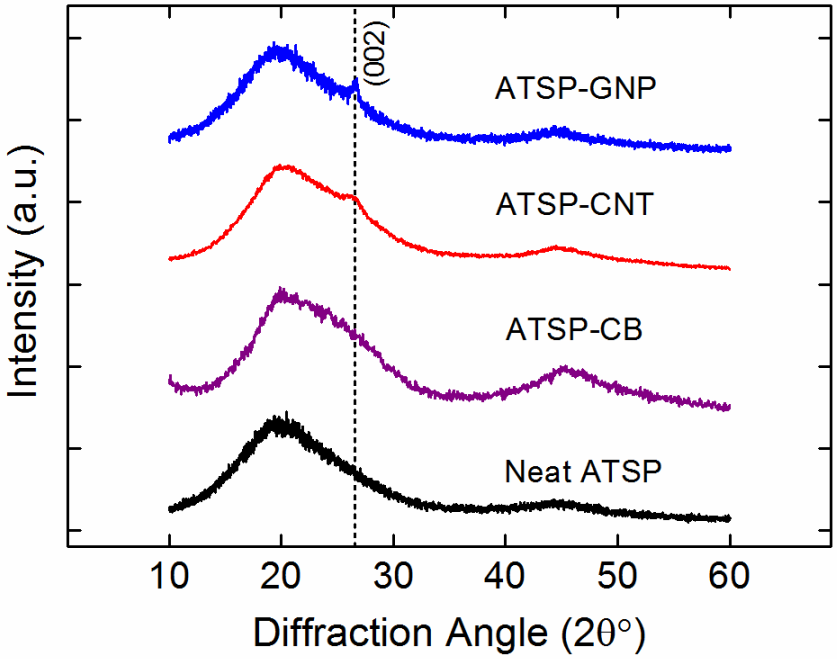

Figure 4.7 XRD spectra of the neat foam and the nanocomposite foams.

The negative CTE of graphene was demonstrated to reduce thermal expansion of polymer nanocomposites [42]. This finding indicates a strong compatibility between carbon nanoparticles and the host matrix. Hence, we analyzed linear thermal expansion characteristics of the nanocomposite foam structures using a dilatometer, as shown in Figure 4.8. We observed that linear expansion ratios tended to decrease for the nanocomposite morphologies. In particular, CNT and GNP nanocomposite foams displayed about 1.1% linear expansions, in the longitudinal direction, as CTEs were calculated to be 75 x 10^{-6} °C^{-1}. The neat ATSP foam had about 1.5% linear expansion with CTE of 100 x 10^{-6} °C^{-1}. Such substantial decreases (~25%) in the CTE for the nanocomposite foams were indicative of favorable interfacial interactions between the GNP and CNT nanofillers with the ATSP matrix, which could result in altered chain relaxation

behaviors [42]. Note that ATSP-CB nanocomposite foams did not show a significant difference from the neat foam.

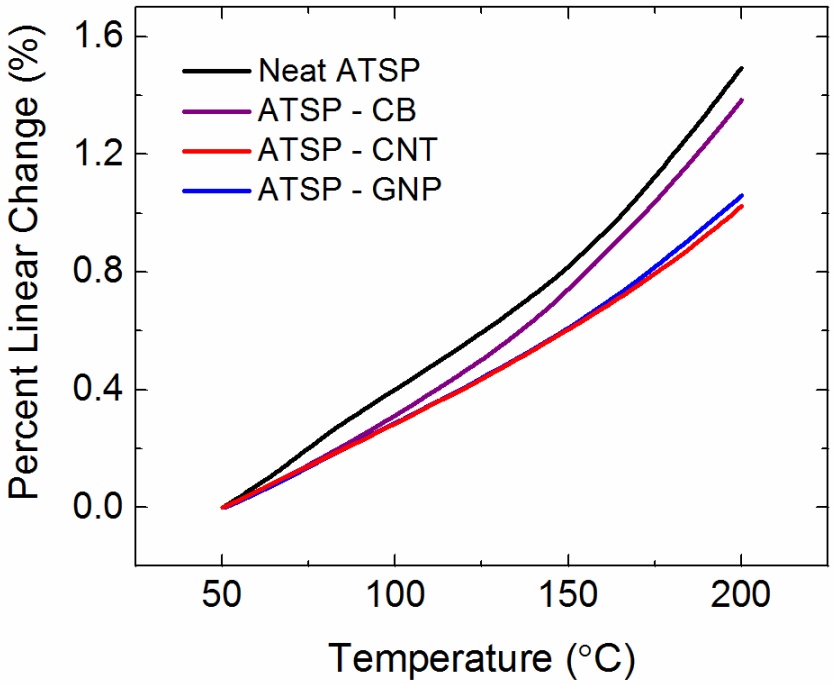

Figure 4.8 Dilatometer analyses of linear thermal expansions on the neat foam and the nanocomposite foams. Tests were performed in air. The heating rate was 3 °C/min.

Figure 4.9 shows thermal degradation stability characteristics of the nanocomposite foams measured using TGA. We evaluated thermal performances of the nanocomposites based on two reference temperature metrics: 5% weight loss and the peak position of the mass derivative. In that regard, we observed that the 5% weight loss temperatures increased by around 20-30 °C for the nanocomposite foams. Similarly, the peak temperatures positively shifted by about 4-8 °C. As well, the nanocomposite foams had the mass derivative rates (which is the thermal degradation rate) marginally suppressed in comparison to the neat foam. The formations of chemical bonds or modifications in chemical structures could cause either positive or negative temperature shifts in thermal decomposition behaviors of polymers. Hence, the non-

functionalized carbon nanofillers could graft onto the ATSP chains that would yield the improved thermal degradation responses. The enhancements in thermal performances of the ATSP nanocomposite foams are noteworthy due to the already exceptionally high thermal performance of the neat ATSP foam [28]. Lacking further evidence on this point, we also understand that the carbon nanofillers constituted thermal barriers that could protect the ATSP backbone from further thermal effects, thereby bond scissions were slowed down during the courses of thermal degradation processes [43].

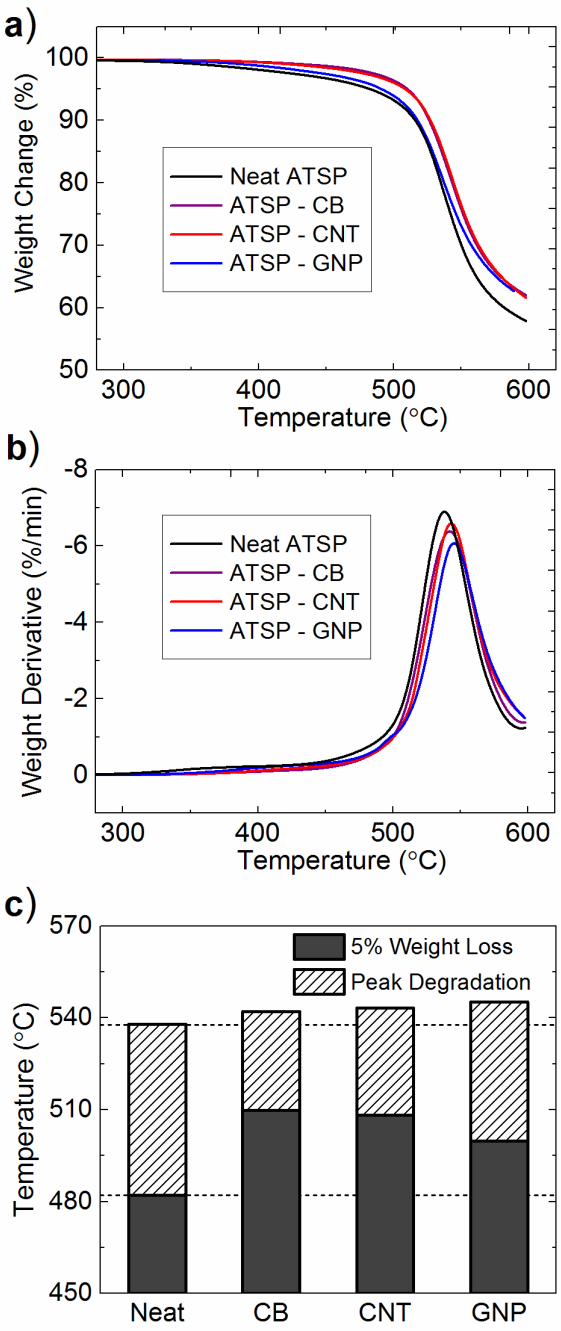

Figure 4.9 TGA measurements of thermal degradation stability of the nanocomposite foams. Thermogravimetric analyses (TG) (a), derivative thermogravimetric analyses (DTG) (b) and comparative results (c). Tests were performed under nitrogen. The heating rate was 10 °C/min.

Lastly, we discuss compressive behaviors and mechanical characteristics of the ATSP nanocomposite foams. Representative compressive stress-strain curves of the nanocomposite foams revealed two distinct features: increased compressive strength and extended compressive

strain ratio at fracture as demonstrated in Figure 4.10. In other words, the nanocomposite foams possessed remarkably stronger, though not necessarily stiffer, and more damage-tolerant morphologies as compared to the neat ATSP foams. Regarding the mechanical strength, earlier studies on polymer nanocomposites (bulk forms) demonstrated that the carbon nanofillers improved mechanical properties [44], yet such significant jumps (up to two-times) observed in this study are quite substantial for the given low-density porous morphologies. More importantly, improved mechanical properties in the polymer nanocomposites came generally along with deformation penalty in which the nanocomposites obtained more brittle characteristics. However, the ATSP nanocomposite foams uniquely enabled simultaneous increases in the strength and the maximum strain, meaning improved material toughness. Hence, the ATSP nanocomposite foams bear exclusive mechanical characteristics that could potentially address conflicts of strength versus toughness in lightweight structural material designs [45].

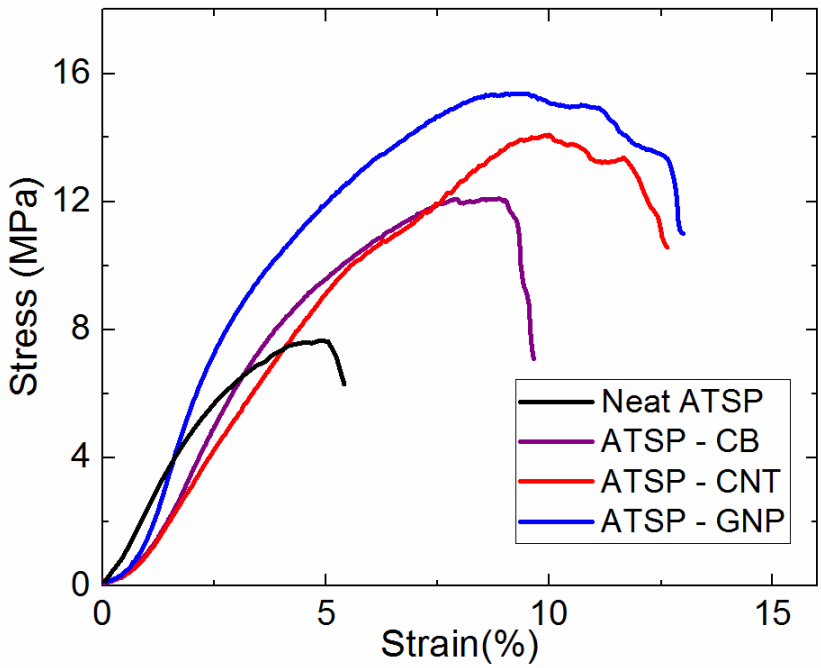

Figure 4.10 Representative compressive stress-strain curves of the nanocomposite foams.

Comprehensive mechanical properties of the nanocomposite foams are presented in Figure 4.11. The compressive mechanical strengths of the nanocomposite foams enhanced by 38.1% (10.5±2.2 MPa) with CB, 109.2% (15.9±2.8 MPa) with CNT and 101.3% (15.3±1.6 MPa) as compared to the neat ATSP foam (7.6±0.5 MPa) (Figure 4.11.a). Also, while the neat foam could maintain 5.3±1.1 % strain ratio at the maximum compressive stress, that property was extended by 31.1% (7±1.5 %) with CB, 78.1% (9.5±1.2 %) with CNT and 46.6% (7.8±1.2 %) with GNP (Figure 4.11.b). In addition, Young's Modulus improved by 3.7% (0.28±0.04 GPa) with CB, 25.9% (0.34±0.15 GPa) with CNT and 74% (0.47±0.04 GPa) with GNP (Figure 4.11.c) compared to parent foam (0.27±0.04 GPa). Similarly, structural densities of the nanocomposite foams increased by 9.2% (0.59±0.03 Mg/m^3) with CB, 33.3% (0.72±0.01 Mg/m^3) with CNT and 38.9% (0.75±0.04 Mg/m^3) with GNP in comparison to neat the ATSP foam (0.54±0.03 Mg/m^3) (Figure 4.11.d). Thus, the nanocomposite foams had higher relative densities of 0.46±0.03 with CB, 0.56±0.01 with CNT and 0.59±0.04 with GNP as compared to 0.42±0.03 of the neat ATSP foam.

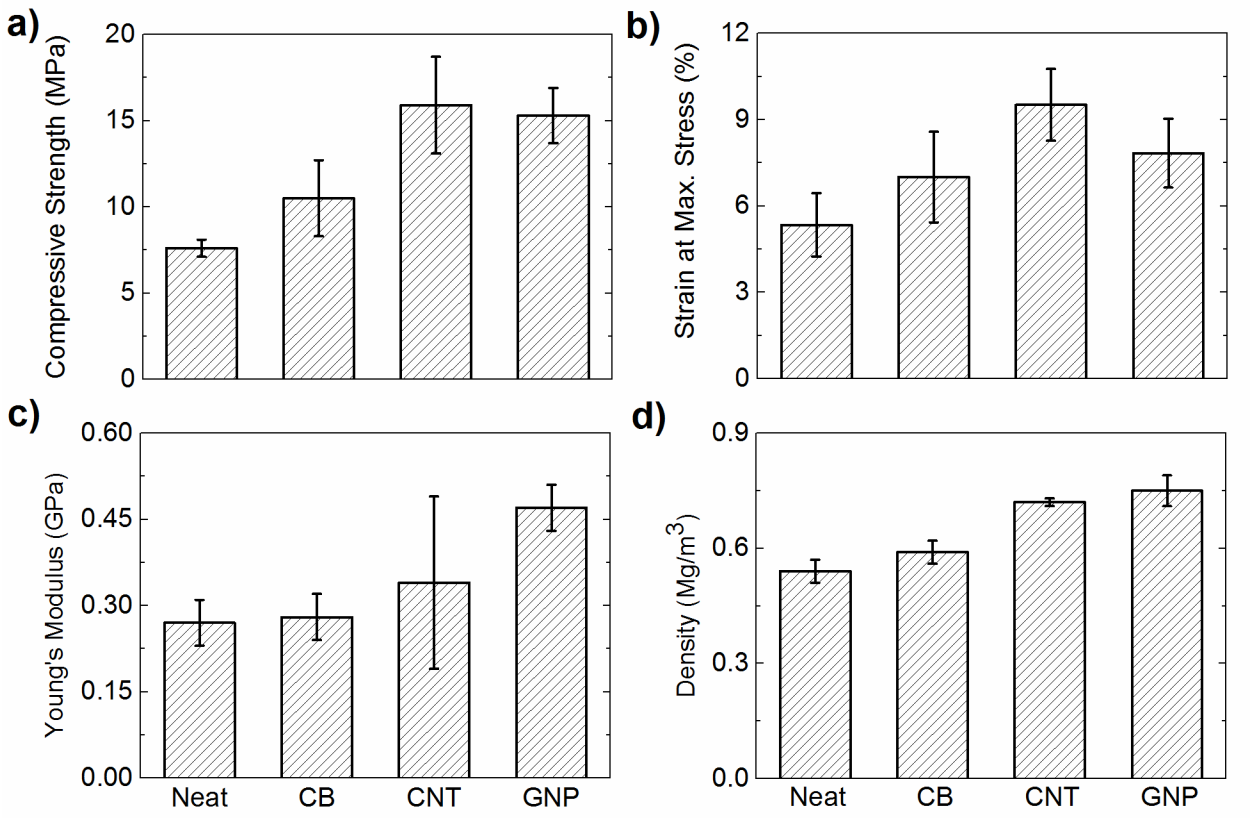

Figure 4.11 Compressive mechanical properties of the nanocomposite foams. Compressive strength (a), strain measured at maximum stress (b), Young's modulus (c) and structural density (d).

Based on these results, the nanocomposite foams possessed higher structural densities than the neat foam by around 9-39%, which appeared to prompt enhancements of the compressive strength and Young's Modulus, as also predicted by analytical models [46] and [47]. As discussed above, preferential self-alignment of the CNTs generated excellent load transfer networks within the nanocomposite foams demonstrating exceptional improvement [48]. Also note that chemical grafting mechanisms between the carbon nanofillers and the ATSP matrix could potentially cause dramatic property improvements, but the ATSP nanocomposites would require further analyses to understand effects of interfacial coupling [49] and [50]. Also, increased maximum load strains indicated more deformation tolerant structures, which

developed excellent load transfer rates coming along with unique morphologies of the nanofillers.

4.4 Conclusion

We introduced the novel high-performance ATSP nanocomposite foams fabricated via a facile powder based mixing method. The nanocomposite foams demonstrated quite homogenous distributions of the nanofillers within the matrix as enabled through the fabrication process. Thermal expansion reduced with the use of the carbon nanofillers that underlined good structural unity in the structures. Also, thermal degradation performance improved with the addition of carbon nanofillers. More importantly, both compressive strength and strain increased substantially giving increased material toughness. Thus, the aromatic thermosetting copolyester nanocomposite foams are lightweight, mechanically strong, and thermally durable multifunctional structures utilizing strong interactions with the carbon nanofillers which can potentially be used for variety of technological structural applications.

4.5 References

[1] J. Hirsch, Aluminium in innovative light-weight car design, Materials Transactions 52(5) (2011) 818-824.

[2] T.M. Pollock, Weight loss with magnesium alloys, Science 328(5981) (2010) 986-987.

[3] L.J. Gibson, M.F. Ashby, The Mechanics of three-dimensional cellular materials, Proceedings of the Royal Society of London. A. Mathematical and Physical Sciences 382(1782) (1982) 43-59.

[4] C. Soutis, Fibre reinforced composites in aircraft construction, Progress in Aerospace Sciences 41(2) (2005) 143-151.

[5] V.P. Shastri, I. Martin, R. Langer, Macroporous polymer foams by hydrocarbon templating, Proceedings of the National Academy of Sciences 97(5) (2000) 1970-1975.

[6] L. Jaouen, A. Renault, M. Deverge, Elastic and damping characterizations of acoustical porous materials: available experimental methods and applications to a melamine foam, Applied Acoustics 69(12) (2008) 1129-1140.

[7] N.N. Najib, Z.M. Ariff, A.A. Bakar, C.S. Sipaut, Correlation between the acoustic and dynamic mechanical properties of natural rubber foam: effect of foaming temperature, Materials & Design 32(2) (2011) 505-511.

[8] C. Zhang, J. Li, Z. Hu, F. Zhu, Y. Huang, Correlation between the acoustic and porous cell morphology of polyurethane foam: effect of interconnected porosity, Materials & Design 41 (2012) 319-325.

[9] H.-B. Zhang, Q. Yan, W.-G. Zheng, Z. He, Z.-Z. Yu, Tough graphene−polymer microcellular foams for electromagnetic interference shielding, ACS Applied Materials & Interfaces 3(3) (2011) 918-924.

[10] R. Verdejo, F. Barroso-Bujans, M.A. Rodriguez-Perez, J. Antonio de Saja, M.A. Lopez-Manchado, Functionalized graphene sheet filled silicone foam nanocomposites, Journal of Materials Chemistry 18(19) (2008) 2221-2226.

[11] R. Verdejo, C. Saiz-Arroyo, J. Carretero-Gonzalez, F. Barroso-Bujans, M.A. Rodriguez-Perez, M.A. Lopez-Manchado, Physical properties of silicone foams filled with carbon nanotubes and functionalized graphene sheets, European Polymer Journal 44(9) (2008) 2790-2797.

[12] M. Martin-Gallego, M.M. Bernal, M. Hernandez, R. Verdejo, M.A. Lopez-Manchado, Comparison of filler percolation and mechanical properties in graphene and carbon nanotubes filled epoxy nanocomposites, European Polymer Journal 49(6) (2013) 1347-1353.

[13] D. Yan, L. Xu, C. Chen, J. Tang, X. Ji, Z. Li, Enhanced mechanical and thermal properties of rigid polyurethane foam composites containing graphene nanosheets and carbon nanotubes, Polymer International 61(7) (2012) 1107-1114.

[14] G. Gedler, M. Antunes, J.I. Velasco, Low density polycarbonate–graphene nanocomposite foams produced by supercritical carbon dioxide two-step foaming. Thermal stability, Composites Part B: Engineering 92 (2016) 299-306.

[15] L.J. Lee, C. Zeng, X. Cao, X. Han, J. Shen, G. Xu, Polymer nanocomposite foams, Composites Science and Technology 65(15–16) (2005) 2344-2363.

[16] L. Chen, D. Rende, L.S. Schadler, R. Ozisik, Polymer nanocomposite foams, Journal of Materials Chemistry A 1(12) (2013) 3837-3850.

[17] J. Lobos, S. Velankar, How much do nanoparticle fillers improve the modulus and strength of polymer foams?, Journal of Cellular Plastics 52(1) (2016) 57-88.

[18] B. Wicklein, A. Kocjan, G. Salazar-Alvarez, F. Carosio, G. Camino, M. Antonietti, L. Bergström, Thermally insulating and fire-retardant lightweight anisotropic foams based on nanocellulose and graphene oxide, Nat Nano 10(3) (2015) 277-283.

[19] Z. Chen, C. Xu, C. Ma, W. Ren, H.-M. Cheng, Lightweight and flexible graphene foam composites for high-performance electromagnetic interference shielding, Advanced Materials 25(9) (2013) 1296-1300.

[20] V. Eswaraiah, V. Sankaranarayanan, S. Ramaprabhu, Functionalized graphene–PVDF foam composites for EMI shielding, Macromolecular Materials and Engineering 296(10) (2011) 894-898.

[21] W.-L. Song, M.-S. Cao, M.-M. Lu, S. Bi, C.-Y. Wang, J. Liu, J. Yuan, L.-Z. Fan, Flexible graphene/polymer composite films in sandwich structures for effective electromagnetic interference shielding, Carbon 66 (2014) 67-76.

[22] S. Maiti, N.K. Shrivastava, S. Suin, B.B. Khatua, Polystyrene/MWCNT/graphite nanoplate nanocomposites: efficient electromagnetic interference shielding material through graphite nanoplate–MWCNT–graphite nanoplate networking, ACS Applied Materials & Interfaces 5(11) (2013) 4712-4724.

[23] K.-Y. Park, S.-E. Lee, C.-G. Kim, J.-H. Han, Fabrication and electromagnetic characteristics of electromagnetic wave absorbing sandwich structures, Composites Science and Technology 66(3–4) (2006) 576-584.

[24] R. Verdejo, R. Stämpfli, M. Alvarez-Lainez, S. Mourad, M.A. Rodriguez-Perez, P.A. Brühwiler, M. Shaffer, Enhanced acoustic damping in flexible polyurethane foams filled with carbon nanotubes, Composites Science and Technology 69(10) (2009) 1564-1569.

[25] L. Chen, R. Ozisik, L.S. Schadler, The influence of carbon nanotube aspect ratio on the foam morphology of MWNT/PMMA nanocomposite foams, Polymer 51(11) (2010) 2368-2375.

[26] H. Kim, A.A. Abdala, C.W. Macosko, Graphene/polymer nanocomposites, Macromolecules 43(16) (2010) 6515-6530.

[27] J.R. Potts, D.R. Dreyer, C.W. Bielawski, R.S. Ruoff, Graphene-based polymer nanocomposites, Polymer 52(1) (2011) 5-25.

[28] M. Bakir, J.L. Meyer, J. Economy, I. Jasiuk, Heat-induced polycondensation reaction with self-generated blowing agent forming aromatic thermosetting copolyester foams, Macromolecules (2016).

[29] D. Frich, K. Goranov, L. Schneggenburger, J. Economy, Novel high-temperature aromatic copolyester thermosets: synthesis, characterization, and physical properties, Macromolecules 29(24) (1996) 7734-7739.

[30] B. Vaezian, J.L. Meyer, J. Economy, Processing of aromatic thermosetting copolyesters into foams and bulk parts: characterization and mechanical properties, Polymers for Advanced Technologies 27(8) (2016) 1006-1013.

[31] R. Andrews, D. Jacques, M. Minot, T. Rantell, Fabrication of carbon multiwall nanotube/polymer composites by shear mixing, Macromolecular Materials and Engineering 287(6) (2002) 395-403.

[32] A. Yasmin, J.-J. Luo, I.M. Daniel, Processing of expanded graphite reinforced polymer nanocomposites, Composites Science and Technology 66(9) (2006) 1182-1189.

[33] P. Podsiadlo, A.K. Kaushik, E.M. Arruda, A.M. Waas, B.S. Shim, J. Xu, H. Nandivada, B.G. Pumplin, J. Lahann, A. Ramamoorthy, N.A. Kotov, Ultrastrong and stiff layered polymer nanocomposites, Science 318(5847) (2007) 80-83.

[34] A.I. Zhbanov, E.G. Pogorelov, Y.-C. Chang, Van der Waals interaction between two crossed carbon nanotubes, ACS Nano 4(10) (2010) 5937-5945.

[35] N. Yousefi, X. Sun, X. Lin, X. Shen, J. Jia, B. Zhang, B. Tang, M. Chan, J.-K. Kim, Highly aligned graphene/polymer nanocomposites with excellent dielectric properties for high-performance electromagnetic interference shielding, Advanced Materials 26(31) (2014) 5480-5487.

[36] J.S. Colton, N.P. Suh, The nucleation of microcellular thermoplastic foam with additives: Part I: Theoretical considerations, Polymer Engineering & Science 27(7) (1987) 485-492.

[37] P. Pötschke, T.D. Fornes, D.R. Paul, Rheological behavior of multiwalled carbon nanotube/polycarbonate composites, Polymer 43(11) (2002) 3247-3255.

[38] C.-Y.M. Tung, P.J. Dynes, Relationship between viscoelastic properties and gelation in thermosetting systems, Journal of Applied Polymer Science 27(2) (1982) 569-574.

[39] S. Li, M. Xiao, D. Wei, H. Xiao, F. Hu, A. Zheng, The melt grafting preparation and rheological characterization of long chain branching polypropylene, Polymer 50(25) (2009) 6121-6128.

[40] T. Ungár, J. Gubicza, G. Ribárik, C. Pantea, T.W. Zerda, The microstructure of carbon blacks determined by X-ray diffraction profile analysis, Carbon 40(6) (2002) 929-937.

[41] S.V. Polschikov, P.M. Nedorezova, A.N. Klyamkina, A.A. Kovalchuk, A.M. Aladyshev, A.N. Shchegolikhin, V.G. Shevchenko, V.E. Muradyan, Composite materials of graphene nanoplatelets and polypropylene, prepared by in situ polymerization, Journal of Applied Polymer Science 127(2) (2013) 904-911.

[42] S. Wang, M. Tambraparni, J. Qiu, J. Tipton, D. Dean, Thermal expansion of graphene composites, Macromolecules 42(14) (2009) 5251-5255.

[43] C. Bao, L. Song, W. Xing, B. Yuan, C.A. Wilkie, J. Huang, Y. Guo, Y. Hu, Preparation of graphene by pressurized oxidation and multiplex reduction and its polymer nanocomposites by masterbatch-based melt blending, Journal of Materials Chemistry 22(13) (2012) 6088-6096.

[44] M. Fang, K. Wang, H. Lu, Y. Yang, S. Nutt, Covalent polymer functionalization of graphene nanosheets and mechanical properties of composites, Journal of Materials Chemistry 19(38) (2009) 7098-7105.

[45] R.O. Ritchie, The conflicts between strength and toughness, Nat Mater 10(11) (2011) 817-822.

[46] L.J. Gibson, M.F. Ashby, Cellular solids: structure and properties, Cambridge university press1999.

[47] P. Alvarez, A. Mendizabal, M.M. Petite, M.A. Rodríguez-Pérez, A. Echeverria, Finite element modelling of compressive mechanical behaviour of high and low density polymeric foams finite element modellierung des druckverhaltens von polymer-schäumen hoher und geringer dichte, Materialwissenschaft und Werkstofftechnik 40(3) (2009) 126-132.

[48] Y.Y. Zhang, C.M. Wang, Y. Cheng, Y. Xiang, Mechanical properties of bilayer graphene sheets coupled by sp3 bonding, Carbon 49(13) (2011) 4511-4517.

[49] Z. Xu, C. Gao, In situ polymerization approach to graphene-reinforced nylon-6 composites, Macromolecules 43(16) (2010) 6716-6723.

[50] C. Bao, Y. Guo, L. Song, Y. Kan, X. Qian, Y. Hu, In situ preparation of functionalized graphene oxide/epoxy nanocomposites with effective reinforcements, Journal of Materials Chemistry 21(35) (2011) 13290-13298.

CHAPTER 5: PERIODIC FUNCTIONALIZATION OF GRAPHENE-LAYERED ALUMINA NANOFIBERS WITH AROMATIC THERMOSETTING COPOLYESTER VIA EPITAXIAL STEP-GROWTH POLYMERIZATION

5.1 Introduction

Fabrication of unidirectionally aligned carbon nanotube (CNT) reinforced polymer matrix nanocomposites has been a long-standing challenge in the structural materials technology [1]. Additionally, realizing a robust interfacial attachment mechanism between nanofillers and host polymer matrix holds great promise to enhance overall macro-scale properties of nanocomposites [2,3]. In this regard, forming periodically functionalized and crystalline texture shish-kebab architectures on matrix-embedded nanostrands through utilizing intrinsic characteristics of semicrystalline polymer systems represents a facile interfacial coupling scheme [4]. Within that framework, the carbon nanostructures essentially pose nucleation sites at the interface with the surrounding polymer medium during a polymer crystallization process. Two factors could be highlighted here that control the development of the crystalline structures. Initially, a concentration gradient develops on the polymer side over the contact boundary region that generates such periodically located nucleation sites. Afterward, the high in-plane thermal conductivity of the carbon surface causes a temperature gradient to develop at the nucleation sites [5].

This work was previously published: Bakir, M., Meyer, J.L., Hussainova, I., Sutrisno, A., Economy, J., and Jasiuk, I., Periodic functionalization of graphene-layered alumina nanofibers with aromatic thermosetting copolyester via epitaxial step-growth polymerization, Macromolecular Chemistry and Physics, 218, 1700338 (2017).

Special thanks to Dr. Irina Hussainova (Tallinn University of Technology, Estonia) for providing invaluable guidance on the project.

Building on this, there are two mechanisms that consecutively modulate the structural forms of the lamellae [6]. The first is that the polymer chains can adopt an epitaxial growth mechanism through a rigorous lattice match with the nanofillers [7]. Alternatively, preferential self-alignment of the chains around such nanofibrils can be enabled via size compatibility wherein the nanofillers merely constitute geometrical confinements; the mechanism is coined as size-dependent soft epitaxy.[4] More importantly, through such an *in situ* functionalization mechanisms, structural integrity and physicochemical properties of the nano-reinforcements can be effectively preserved within the polymer matrix [6].

Recently, successful protocols for the development of periodically assembled shish-kebab structures have been demonstrated on CNTs employing numerous semicrystalline polymers, as tabulated in the comprehensive reviews [5,6]. For example, Li *et al.* showed CNT-driven crystallization in polyethylene and nylon wherein the polymer chains assembled through size-dependent soft-epitaxy [4]. Similarly, Reasco *et al.* demonstrated that single-walled CNT reinforced polypropylene formed an *in situ* crystallinity [8]. Jandt *et al.* investigated poly(ε-caprolacetone) with multi-walled CNTs and they observed the development of hierarchical shish-kebab structures [9] Kumar *et al.* studied the CNT-based fibers in polyethylene and showed the formations of transcrystalline lamella regions upon successive melting and recrystallization processes [10]. Shah *et al.* investigated poly(3-hexylthiophene) with CNTs and demonstrated that the crystallinity formed through an epitaxial growth mechanism [11]. Additionally, isotactic polypropylene was shown to develop ordered-carbon induced transcrystalline domains on graphene oxide fibers [12]. Leibler *et al.* showed the development of crystallinity in polyamide-6 on CNT surface [13]. Lastly, Vilatela *et al.* analyzed macro-scale fibers in polyvinylidene fluoride, isotactic polypropylene, and poly(lactic) acid in which

heterogeneous nucleation initiated non-epitaxial growth of crystalline sites on the fiber surface [14].

Despite these extensive efforts, there remains two major challenges to realize the unidirectionally oriented nanofiber reinforced polymer matrix composites. First, such periodically functionalized nano-hybrid shish-kebab configurations are established via intrinsically semicrystalline thermoplastic resin systems which genuinely constitute inferior physical properties for high-performance demanding structural applications. Second, CNTs are conventionally obtained in relatively smaller lengths, which can only be incorporated into matrix by means of random distribution and mixing. Bulk processing of CNTs into fabrics is still an active area of research which requires development of new manufacturing processes. Hence, further development of the nano-hybrid shish-kebab configurations requires uses of a polymer matrix system which possesses strong physical properties and a nanofiller particle system which can be processed into unidirectionally aligned bulk forms. On top of this, the polymer matrix and nanofiller particles should inherently form robust interfacial coupling. In this paper, we present a solution-driven periodic functionalization and interfacial coupling mechanism of unidirectionally processed chemically pristine ANFC strands with amorphous and highly-crosslinked morphology ATSP matrix. The interfacial attachment of the ATSP resin with ANFCs gives rise to formation of periodically assembled mesomorphic lamellae on the nanofiller surface in which ATSP and ANFCs develop nanohybrid shish kebab structures.

The condensation polymerized thermoset nature of the lamellae also presents a unique synthetic route as compared to previously reported shish-kebab structures. A 3D network of highly-aligned and self-assembled ANFCs provide ultra-high anisotropy ratio to tailor size, orientation and intra-fiber spacing. Yet, conventional mixing process of such nanofillers could

generate inhomogeneous distribution throughout the matrix. The multi-layer graphene coating of the ANFCs introduces electronic functionality to the non-conductive matrix system. The electroconductivity is highly directional via unidirectionally oriented configuration of the ANFC bundles. The ANFCs can simultaneously introduce structural stiffness combined with enhanced toughness and increased electroconductivity for development of anisotropic bioinspired nanocomposites. The ANFC surface is chemically pristine (non-functionalized), yet due to the presence of inherent oxygen-bearing reactive groups interfacial coupling is facilitated with the host ATSP matrix [15,16].

Unidirectionally oriented ANFC bundles were dip-coated with both dilute (0.05 g/mL) and concentrated (0.5 g/mL) ATSP oligomers as dissolved in dimethyl sulfoxide (DMSO) solvent. Following a thermal (condensation) polymerization process, the ATSP resin showed crystalline carbonaceous surface-induced lamella formation on the ANFC surface. Particularly, the low concentration ATSP specimen demonstrated periodically located lamellae resembling a nano-hybrid shish-kebab structure. As well, the high concentration ATSP specimen clearly displayed an epitaxial growth mechanism on the ANFC surface. We hereby discuss a working mechanism based on the Plateau-Rayleigh instability, the Marangoni effect, and epitaxial lamella growth to explain governing factors during this process. XRD analyses clearly demonstrated the development of mesomorphic lamella domains in the ATSP chains. Also, ssNMR and TGA measurements showed an effectual interfacial chemical coupling mechanism between the ATSP matrix and the ANFCs network.

5.2 Materials and Methods

The carboxylic acid (C1) and acetoxy (A1) functional groups oligomers were used to produce crosslinked morphology amorphous aromatic thermosetting copolyester (ATSP) resin. The constituent oligomers were synthesized using trimesic acid (TMA), isophthalic acid (IPA), 4-acetoxybenzoic acid (ABA) and hydroquinone diphthalic anhydride (HQDA) (Sigma-Aldrich Co.) via melt-oligomerization method at molar feed ratios of 2:3:6:4 and 2:2:2:7 of TMA:IPA:ABA:HQDA for C1 and A1, respectively.

The pristine alumina nanofibers with extremely high aspect ratio (10^7) while an individual fiber diameter was 10 ±2 nm were coated with graphene through a chemical vapor deposition (CVD) process. In this process, inherently porous fiber bundles were placed into a quartz tube where gas flow promoted graphemic surface formation through the structures.

The carboxylic acid and acetoxy functional group oligomers were mixed at 1.1:1 weight ratio both in powder forms. Then, the oligomer mixtures (C1A1) were dissolved in dimethyl sulfoxide solutions at 0.05 g/mL (dilute), 0.2 g/mL and 0.5 g/mL (concentrated) concentrations. The 0.2 g/mL concentration sample was not characterized. The solutions were stirred on a temperature-controlled magnetic stirrer at about 80°C until the homogenous dispersion of the oligomer particles was observed. Then, the pristine graphene encapsulated alumina fiber bundles specimens were separately dipped into the prepared solutions and kept in place until effective surface wetting was observed. Afterward, the specimens were applied a thermal cure cycle, wherein the cross-linked aromatic thermosetting copolyester matrix formed via a condensation polymerization reaction between the carboxylic acid and acetoxy functional group oligomers. The cure cycle comprised of two dwell stages at 202 °C for 90 minutes and 270 °C for 150

minutes, and a final cure stage at 330°C for 90 minutes. The specimens were applied a pressure of ~700Pa.

Scanning electron microscopy was operated in high-resolution and upper detector mode (10-20 kV, 10 μA) to analyze microstructures of the specimens (Hitachi S-4800). The specimens were sputter-coated with Pd-Au for 40 seconds to minimize charging effects. Energy dispersive X-ray spectroscopy (EDX) measurements were done using environmental scanning electron microscopy (Philips XL30 ESEM-FEG) with an attached EDAX tool.

Solid-state Nuclear Magnetic Resonance (ssNMR) spectroscopy measurements were carried out using specimens (~40 mg) packed into NMR rotors (on aVarian Unity Inova 300 MHz spectrometer). ^{1}H and ^{13}C NMR spectra were obtained using direct pulse (DP) and cross-polarization (CP) excitations, respectively, under magic-angle spinning (MAS). Specimens were spun at 8 kHz. Data analysis was performed using the MestreNova software.

X-ray diffraction measurements were obtained using an X-ray diffractometer (PANalytical/Philips, X'Pert) with Cu K-alpha source operated at 45 kV and 40 mA, and 0.15148 nm wavelength with 0.01 °/s scanning rate between diffraction angles of $2\theta=5°$ and $2\theta=80°$.

Thermogravimetric analyses of the specimens were obtained using a TGA (TGA 2950 TA Instruments). A temperature-ramp heating cycle was applied with a constant 10 °C/min heating rate until 800 °C. Specimens weighed about 10-20 mg.

5.3 Results and Discussion

Firstly, we discuss characteristic features of the in situ formed ATSP lamellar structures on the ANFC surface observed via scanning electron microscopy (SEM). As shown in Figure 5.1.a, the dilute ATSP solution effectively developed nano-hybrid shish-kebab form lamella

domains while growing off of the graphenic surface, and being periodically located along an ANFC strand. Quantitatively, individual lamellar structures were formed with a periodicity of ~5-10 μm while extending out by ~15-20 μm in length. This form of the ATSP-ANFC structure was similar in form to the nano-hybrid shish-kebab structures with the ANFC strand being "shish" and the ATSP lamellae being "kebab". Yet, the lamellae herein did not surround the entire circumference of the strand, which in fact indicated an epitaxial growth mechanism being effective in the crystallization process. In particular, the perpendicular alignment of the lamella to the ANFC strand surface was to be controlled by the crystalline lattice orientation of the graphene substrate as the ATSP chains were self-aligned to obtain a crystallographic match. Meanwhile, macromolecular ATSP chains interacted with the graphenic surface of the ANFC through a diffusion mechanism wherein intrinsic mesogenicity of the ATSP chains could be modulated by the ordered surface of the ANFC. Furthermore, the diameter of the ANFC strands imposed another important processing factor that the radius of gyration of the ATSP chains was not quite compatible with the micron-scale ANFC fiber strands. The lamellar structure conceptually grew on a flat surface while failed to surround.[4] Also, as can be seen in Figure 5.1.b, the off-grown lamellae between two ANFC strands reorganized their extension directions in the course of crystallization process, which could indicate an effective electrostatic charge formation within the ATSP solution [17]. In Figure 5.1.c, a growing lamellar structure was demonstrated to effectively branch out as far as the extension proceeded likewise evincing the self-reorientation mechanism. It is worth mentioning that the individual ANFC fibers were effectively coated with the ATSP, yet formation of a nano-hybrid shish-kebab structure was not observed at the nanoscale, as shown in Figure 5.1.d. On the other hand, the concentrated ATSP solution did not form morphologies akin to the shish-kebab structures, yet epitaxial growth

induced localized lamellae formation was clearly observed. In Figure 5.1.e, an epitaxially grown ATSP lamella domain on the ANFC fiber surface is shown. Furthermore, similar lamella structure was demonstrated while formed over an ANFC surface in Figure 5.1.f. Note that the off-surface growth mechanism of the mesomorphic lamellae (bright) clearly took place within an amorphous domain (dark). Also, the nano-hybrid shish-kebab structures formed only within the dilute ATSP solution, indicating the role of the polymer concentration in this process.

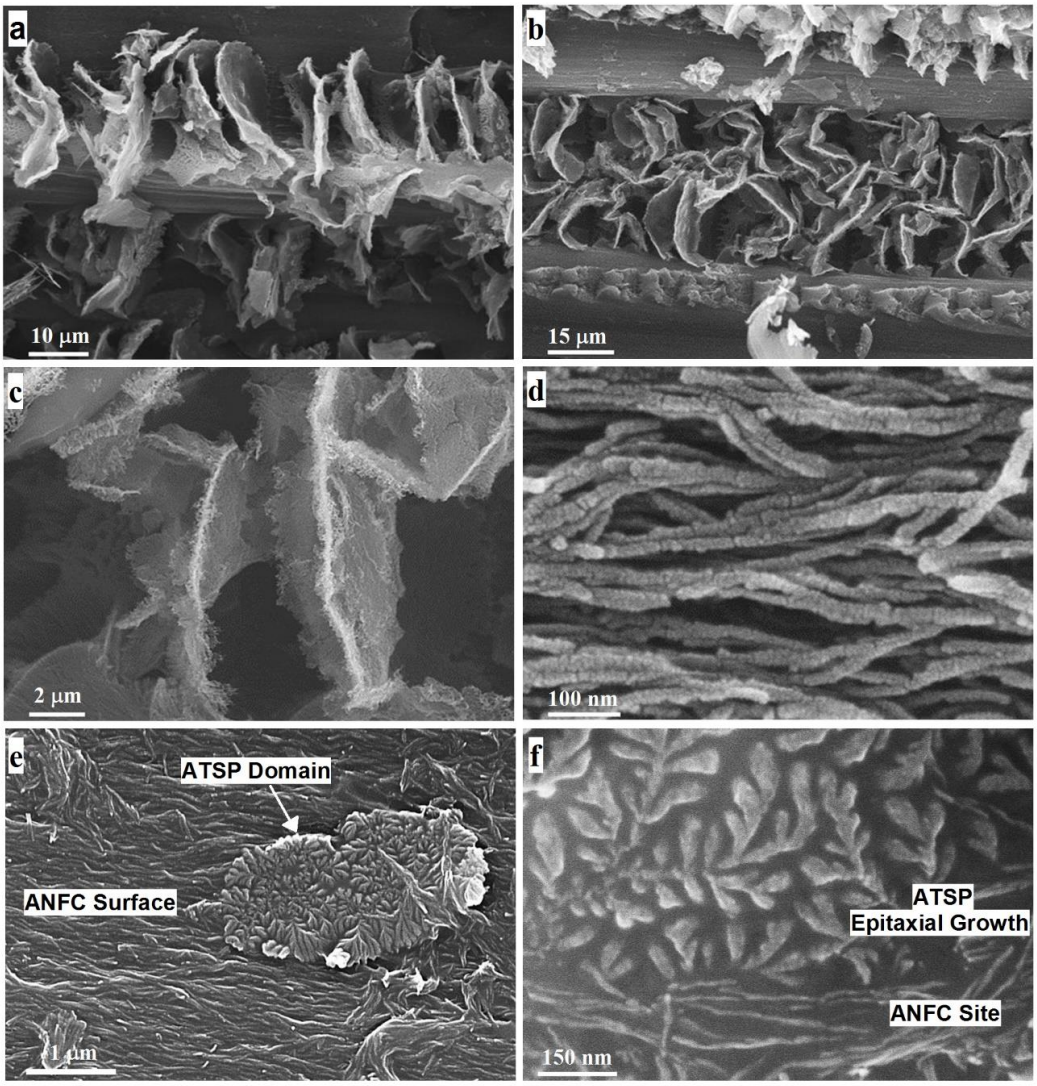

Figure 5.1 Scanning electron microscopy images of the dilute ATSP solution (0.05 g/mL) dip-coated ANFCs; formation of the nano-hybrid shish-kebab structures on the ANFC surface (a,b), close-up images of a lamella domain (c) and individual fibers coated with the ATSP resin (d). The concentrated ATSP solution (0.5 g/mL) dip-coated ANFCs; epitaxially growth from the ANFC surface (e, f).

We then propose a working system which could produce such above demonstrated nano-hybrid shish-kebab structures through interactions between the ATSP matrix and the ANFCs (Figure 5.2). Three major mechanisms were conjectured to stimulate this process in the given order: the Plateau-Rayleigh instability, the Marangoni effect, and the epitaxial crystal growth. PRI is a phenomenon to explain the instability of a falling liquid jet under gravitational force as a liquid column breaks up into smaller droplets due to effective surface tension [18]. Recently, this approach was adopted to study the behavior of a thin polymer coating on a cylindrical fiber surface, wherein the surface tension was controlled by the intimate liquid-solid interface [19]. The polymer coating therein receded, upon heating to above its glass transition temperature, and formed liquid bulges wrapping around the circumference of the fiber strand. In particular, the non-Newtonian viscosity profile of the polymer solution predominantly overcame inertial forces and thereby ultimately altered the form of the liquid layer. Thus, the ATSP-DMSO solution film, especially at the low concentration, initially covered the micron-diameter ANFC strands, and then underwent PRI at elevated temperatures during the thermal cure process. Due to the PRI coming into effect, surface undulations were generated, producing a periodicity regulated by the PRI model, being proportional in size to the diameter of the strands [20]. Following this, the Marangoni effects took place to further drive the process. As the ATSP polymer solution formed such undulations on the ANFC surface, the reduced thickness of the ATSP coating on the ANFC surface acquired an increased surface tension. In the meantime, the obtained bulges lowered surface tension under heating while the DMSO solvent was gradually being evaporated. Hence, in the course of this process, the ATSP oligomer molecules were relocated, driven by the effective capillary forces on site, inside the bulges. The oligomer molecules thereby were adsorbed on the spot forming periodically located concentrated particle sites [21,22].Then,

through the cure reaction of the ATSP, an epitaxial growth mechanism proceeded. Regarding such an epitaxial growth, studies on different polymer similar systems such as Nylon 6, poly(tetrahydrofuran), poly(oxacyclobutane), and poly(ethylene oxide) showed epitaxial growth mechanism on the graphite surface while the polymer chains were conceived to reorient with respect to the crystalline carbon lattice [4]. Additionally, in the ATSP system, acetoxy and carboxylic acid-capped reactive functional groups of the oligomers could react with oxygenated functional sites on the ANFCs which would produce a physicochemical attachment mechanism on the site [23,24]. Additionally, as carbonaceous materials could behave as a nucleation agent, the crystal conformation of the polymer systems aligned with low energy adsorption sites on the surface [5,14,25,26]. Besides, the aromatic structure of the graphitic layers could form a base for π-π predominant interactions with corresponding aromatic rings in the ATSP backbone. Furthermore, due to the structural order of the ANFC surface, ATSP chains re-organized their chain configurations, enabled through polymer intrinsic flexibility at elevated temperatures, and subsequently formed lamellar structures [27]. Also, we highlight that the ANFC strands did not substantially change the genuine cure characteristics of the ATSP resin. DSC cure cycles operated on neat ATSP and dip-coated ATSP-ANFC specimens displayed similar characteristic thermal profiles. Regarding the DSC thermograms of cured specimens, we did not detect a lower/higher thermal characteristic peak (e.g. glass transition) that would strongly indicate that the cure cycles progressed similarly in both systems. Hence, during the thermal cure process, the ATSP chains clung on the ANFC fibers which gave rise to such lamellae formation, yet did not observably alter the cure characteristics.

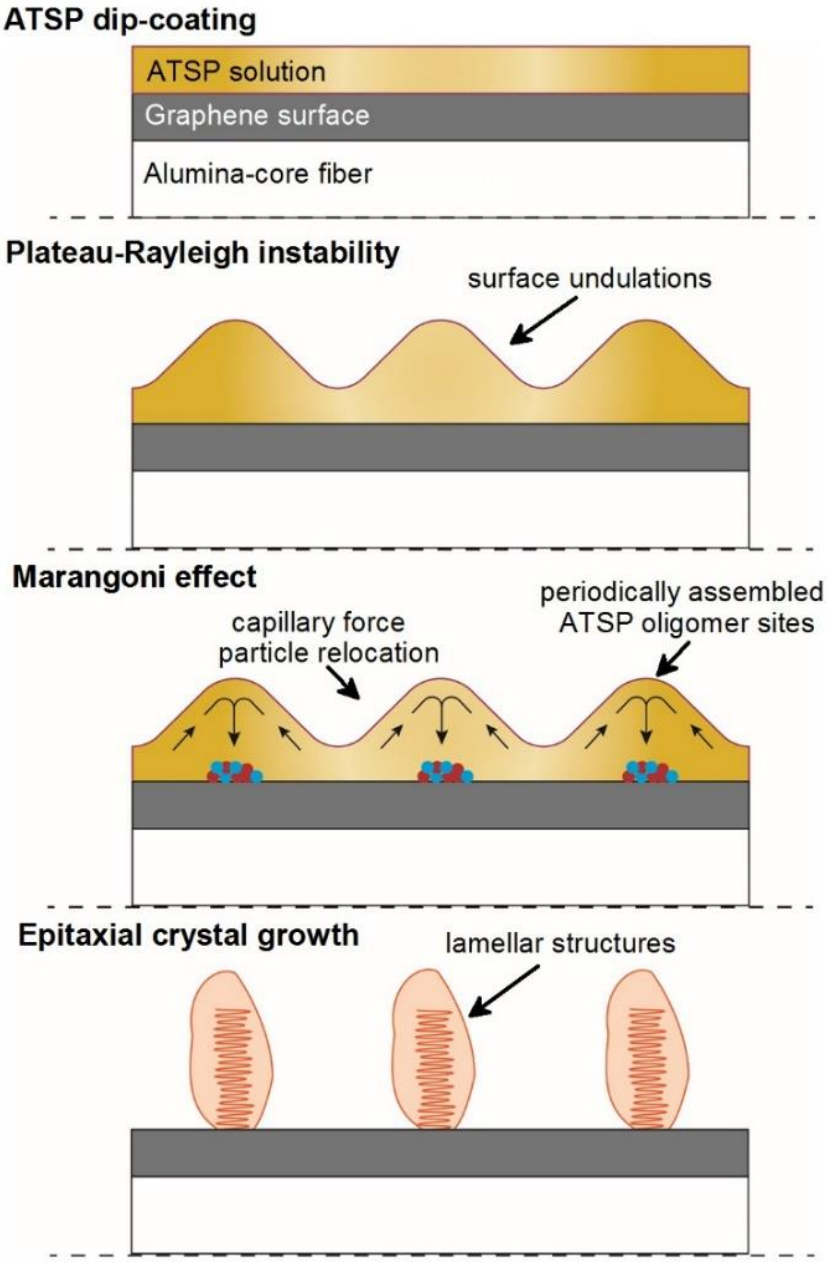

Figure 5.2 Proposed working mechanism for the development of crystalline ATSP domains being periodically assembled on the graphenic layer of alumina fibers to form shish-kebab architecture.

We performed solid-state Nuclear Magnetic Resonance (ssNMR) spectroscopy measurements to characterize corresponding modifications in the backbone chain configuration of the ATSP matrix. Figure 5.3 demonstrates ^{13}C cross-polarization magic-angle spinning

(CPMAS) spectra of the ANFCs coated with the dilute (0.05 g/mL) and concentrated (0.5 g/mL) ATSP solutions, and neat ATSP matrix. The spectrum of the parent material displayed two characteristic peak domains: the aromatic groups (C-C and C-H) and the functional side groups (C-O and C=O). As shown, the ATSP-ANFC interaction caused the aromatic group peaks to convolute into a single broader peak within the same spectral range. Measured line widths were ~379 Hz, ~535 Hz and ~637 Hz for neat ATSP, 0.05g/mL ATSP with ANFC, and 0.5 g/mL ATSP with ANFC, respectively (^{13}C NMR spectra were processed using 25 Hz line broadening). Note that NMR spectra of the pristine ANFCs did not display any characteristic carbon peaks in this spectral range under same operational conditions. On the other hand, the ^{1}H spectra demonstrated a decrease in the measured line width for the ATSP-ANFC samples through sharper peaks (~2344 Hz for neat ATSP and ~1979 Hz for 0.5 g/mL ATSP) (^{1}H NMR spectra were processed using 1 Hz line broadening). We speculate that peak broadening effect could be arising from a strong interfacial J-coupling between the ANFCs and the ATSP. In this regard, several other works demonstrated that intermolecular interactions within polymer systems could cause peak broadening effects [28,29]. In particular, due to the coupling of segmental relaxation times of two different systems (ANFC and ATSP), we observed large mobility difference reflected into the properties of the composite. The spectra showed that chemical shift values were almost constant for the functional group domain. Since the peaks were broad, indicating fast decay or relaxation, which would not be affected by dielectric alumina core, yet the conductive graphene layer governed the fast relaxation. Furthermore, such reduced line widths in the proton spectra indicated that the ATSP chains acquired a mesomorphic profile upon interaction with the fibers. Particularly, in the lamellar mesomorphic region the structure was ordered, and so molecular mobility reduced, which caused to narrow proton peaks.

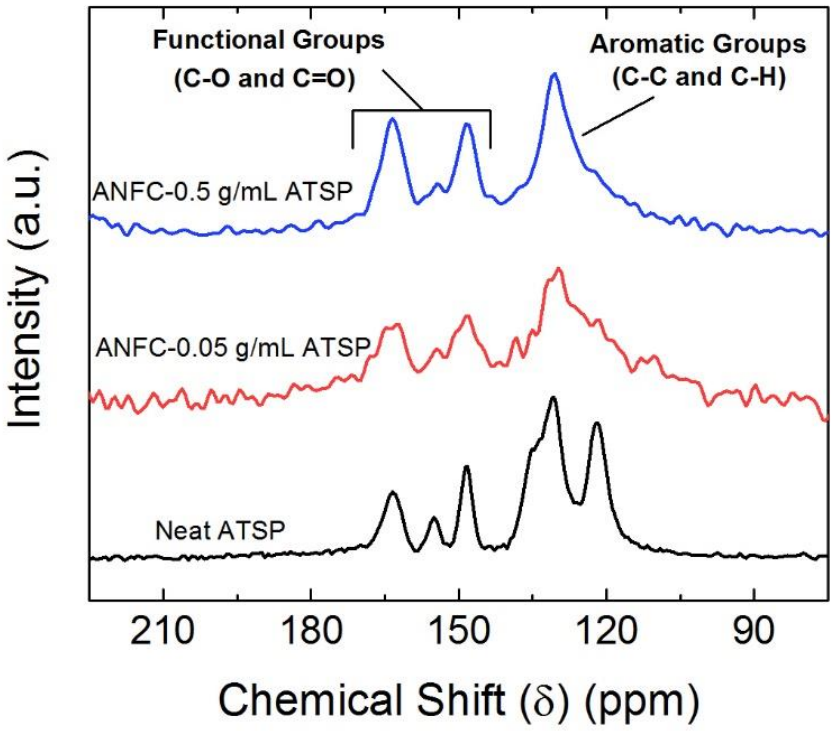

Figure 5.3 ^{13}C Solid-state Nuclear Magnetic Resonance spectra of the neat ATSP, ANFC coated with dilute (0.05 g/mL) ATSP and with concentrated (0.5 g/mL) ATSP.

To validate epitaxial growth induced lamellae formation within the ATSP matrix domain, we carried out X-ray Diffraction (XRD) spectroscopy measurements, as demonstrated in Figure 5.4. In the XRD spectra, the neat ATSP sample displayed highly amorphous nature having a broad characteristic peak centered around $2\theta=20°$, and the pristine fibers exhibited crystalline γ-phase alumina structure. In Figure 5.4, a self-supporting and concentrated ATSP dip-coated ANFC bundle was initially placed perpendicular to the fiber axis direction, wherein the spectra showed the amorphous nature of the polymer matrix. However, when the sample was placed parallel to the fiber axis direction, the mesomorphic phase characteristics was clearly observed. Also, note that roughly $2\theta=18°$ hump arose predominantly from the mesomorphic lamella ATSP domain since other characteristic peaks of the ANFC structure were not distinguishable within the spectral window. Hence, the XRD spectra clearly showed that epitaxial lamellae regions

were preferentially aligned in a perpendicular direction to the ANFCs. To interrogate the presence of the mesomorphic lamellae domains, we additionally performed temperature-ramp differential scanning calorimetry (DSC) thermal analyses. DSC cycles on cured neat ATSP and dip-coated ATSP-ANFC bundle specimens revealed similar thermal characteristics. Due to the highly-crosslinked morphology of the ATSP, and relatively small volumetric content of the lamellae within the nanocomposite structures, we did not observe any distinct peaks that could be associated with thermal response of the lamella structure (e.g. melting). In the mesomorphic morphology, both crystalline and amorphous domains possess fully cured states so DSC thermograms, in fact, represented comparable thermal characteristics.

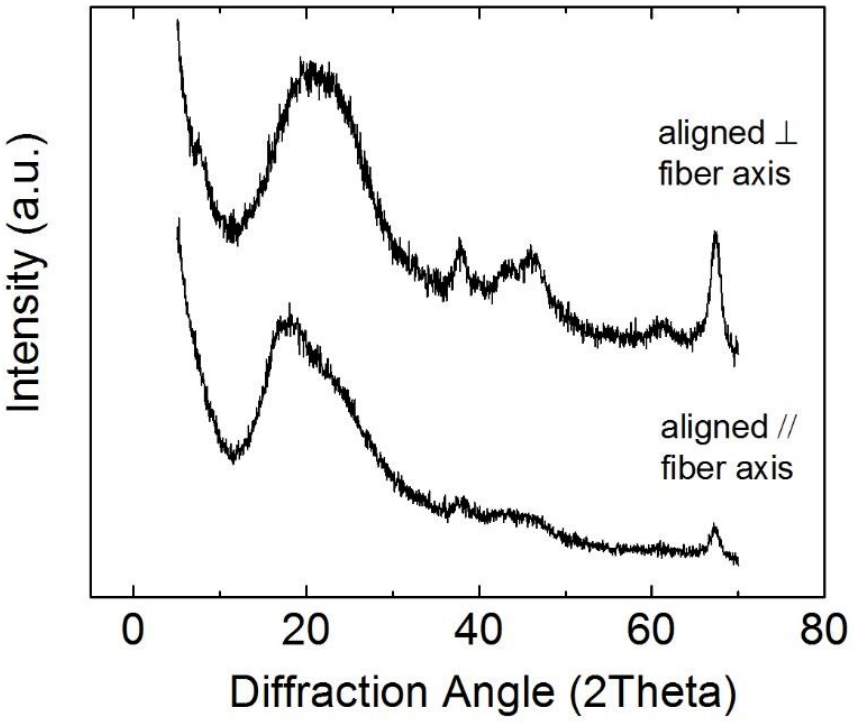

Figure 5.4 X-ray diffraction spectra of the high-concentrated ATSP dip-coated self-supporting ANFC bundle specimen aligned both perpendicular and parallel to the fiber axis direction.

We additionally studied thermo-chemical effects induced through the interfacial entanglement of the ATSP matrix using Thermogravimetric Analysis (TGA), as demonstrated in Figure 5.5. As expected, the thermal profiles of the pristine ANFC were nearly flat within the temperature range of interest and characteristics of the nanocomposites predominantly reflected imprints of the matrix and nanofiller interactions. In Figure 5.5.a, the thermogravimetric outlines of the neat ATSP matrix, as well as both high and low concentration nanocomposites, lined up closely until about 300°C. Then, the nanocomposites acquired sharper downward slopes than the parent material corresponding to side chains scissions, which clearly evinced chemical coupling with the ANFCs. Such *in situ* formed oxygen-functionalized bonds can only remain thermally stable within a limited temperature range. Furthermore, the backbone scission, where the major weight loss occurred, displayed rather positive temperature shifts along with extended ranges with the nanocomposites. In this regard, in Figure 5.5.b, derivative thermogravimetric curves displayed substantially suppressed and similarly upshifted peak temperatures. Hence, the graphenic ANFC surface is conjectured to be effectively incorporated into the cross-linked network of the ATSP matrix, wherein their presence of the ANFCs within the ATSP matrix considerably retarded the decomposition process, which could be attributed to such intrinsic higher thermal stability of the ANFCs forming a heat barrier over the polymer chains. It worth mentioning that the remaining char products following the complete decomposition, beyond 800°C, indeed qualitatively correlated with the amount of the ATSP initially incorporated into the nanocomposite forms.

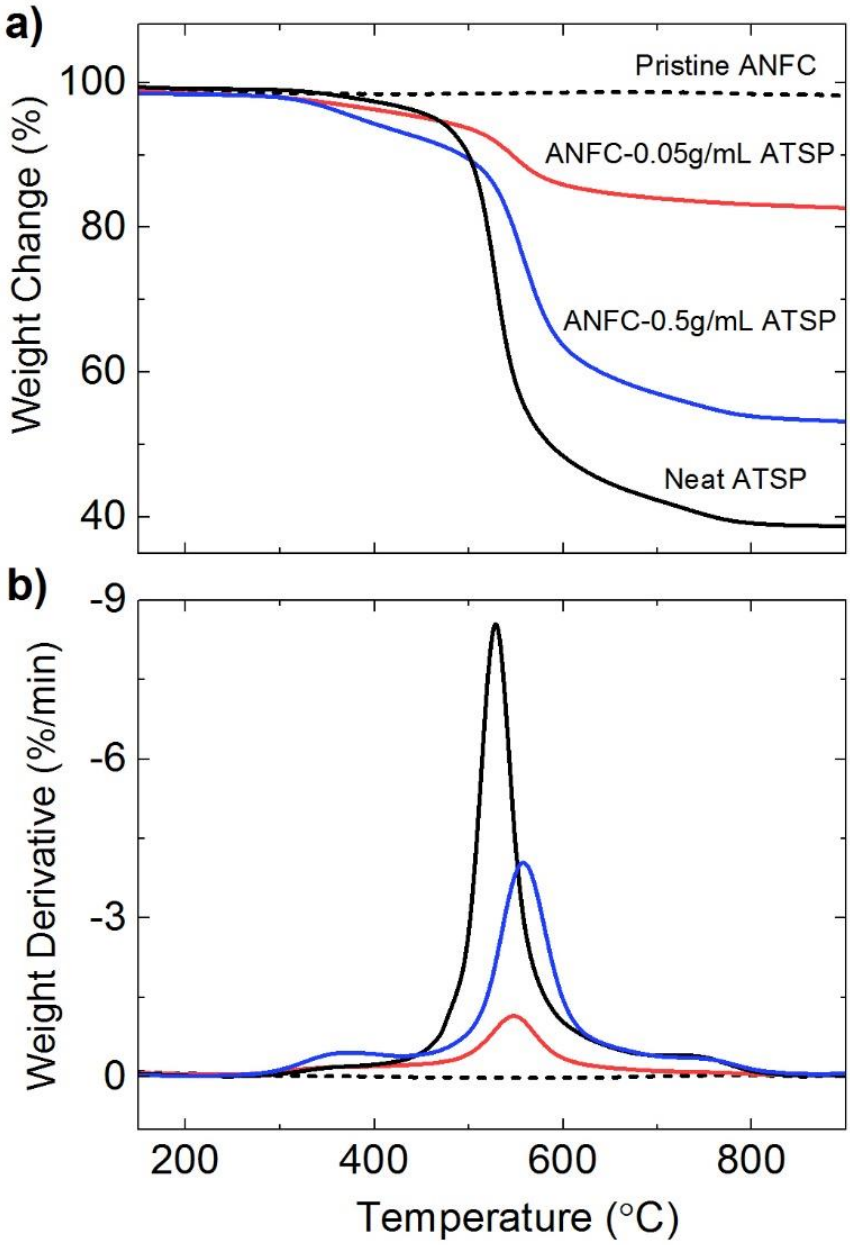

Figure 5.5 Thermogravimetric (a) and derivative thermogravimetric (b) analyses of the pristine ANFC, neat ATSP, dilute (0.05 g/mL) ATSP coated ANFC and concentrated (0.5 g/mL) ATSP coated ANFC specimens. Tests were performed under inert atmosphere of nitrogen at 10°C/min heating rate.

5.4 Conclusion

We demonstrated the development of the i*n situ* mesomorphic lamellar structure formation in the intrinsically amorphous aromatic thermosetting copolyester matrix through interactions with the graphenic surface of the ceramic fibers during the thermal cure process. Particularly, the dilute ATSP solution developed unique nano-hybrid shish-kebab structures along the micron-scale fiber strands. Besides, the concentrated ATSP solution coating clearly revealed epitaxial crystal growth mechanism. Thereafter, we discussed a working mechanism built upon the PRI, the Marangoni effect and the epitaxial crystal growth phenomena to explain this observation. The XRD analyses clearly showed the presence of the mesomorphic lamella domains in the ATSP matrix. The ssNMR and TGA measurements, additionally, indicated the formation of interfacial coupling between the ATSP chains and the ANFCs. This study lays the groundwork to initiate further analyses of the ATSP with various other nanofiller reinforcements on the *in situ* surface functionalization.

5.5 References

[1] V. P. Veedu, A. Cao, X. Li, K. Ma, C. Soldano, S. Kar, P. M. Ajayan, M. N. Ghasemi-Nejhad, Nat. Mater. 2006, 5, 457.

[2] L. S. Schadler, S. C. Giannaris, P. M. Ajayan, Appl. Phys. Lett. 1998, 73, 3842.

[3] H. D. Wagner, O. Lourie, Y. Feldman, R. Tenne, Appl. Phys. Lett. 1998, 72, 188.

[4] L. Li, C. Y. Li, C. Ni, J. Am. Chem. Soc. 2006, 128, 1692.

[5] E. D. Laird, C. Y. Li, Macromolecules 2013, 46, 2877.

[6] L. Li, B. Li, M. A. Hood, C. Y. Li, Polymer 2009, 50, 953.

[7] Y. Takenaka, H. Miyaji, A. Hoshino, A. Tracz, J. K. Jeszka, I. Kucinska, Macromolecules 2004, 37, 9667.

[8] B. P. Grady, F. Pompeo, R. L. Shambaugh, D. E. Resasco, J. Phys. Chem. B 2002, 106, 5852.

[9] M. M. L. Arras, R. Jana, M. Mühlstädt, S. Maenz, J. Andrews, Z. Su, C. Grasl, K. D. Jandt, Macromolecules 2016, 49, 3550.

[10] S. Zhang, W. Lin, C.-P. Wong, D. G. Bucknall, S. Kumar, ACS Appl. Mater. Interfaces 2010, 2, 1642.

[11] R. D. K. Misra, D. Depan, V. S. A. Challa, J. S. Shah, Phys. Chem. Chem. Phys. 2014, 16, 19122.

[12] J. P. Abdou, G. A. Braggin, Y. Luo, A. R. Stevenson, D. Chun, S. Zhang, ACS Appl. Mater. Interfaces 2015, 7, 13620.

[13] A.-C. Brosse, S. Tencé-Girault, P. M. Piccione, L. Leibler, Polymer 2008, 49, 4680.

[14] H. Yue, A. Monreal-Bernal, J. P. Fernández-Blázquez, J. Llorca, J. J. Vilatela, Sci. Rep. 2015, 5, 16729.

[15] R. Ivanov, I. Hussainova, M. Aghayan, M. Drozdova, D. Pérez-Coll, M. A. Rodríguez, F. Rubio-Marcos, J. Eur. Ceram. Soc. 2015, 35, 4017.

[16] I. Hussainova, R. Ivanov, S. N. Stamatin, I. V. Anoshkin, E. M. Skou, A. G. Nasibulin, Carbon 2015, 88, 157.

[17] J. M. Deitzel, J. Kleinmeyer, D. Harris, N. C. Beck Tan, Polymer 2001, 42, 261.

[18] L. Rayleigh, Proc. London Math. Soc. 1878, 1, 4.

[19] S. Haefner, M. Benzaquen, O. Bäumchen, T. Salez, R. Peters, J. D. McGraw, K. Jacobs, E. Raphaël, K. Dalnoki-Veress, Nat. Commun. 2015, 6, 7409.

[20] S. Shabahang, J. J. Kaufman, D. S. Deng, A. F. Abouraddy, Appl. Phys. Lett. 2011, 99, 161909.

[21] C. B. Kim, J. C. Wistrom, H. Ha, S. X. Zhou, R. Katsumata, A. R. Jones, D. W. Janes, K. M. Miller, C. J. Ellison, Macromolecules 2016, 49, 7069.

[22] A. L. Yarin, W. Liu, D. H. Reneker, J. Appl. Phys. 2002, 91, 4751.

[23] D. Frich, J. Economy, K. Goranov, Polym. Eng. Sci. 1997, 37, 541.

[24] K. Xu, J. C. Selby, M. A. Shannon, J. Economy, J. Appl. Polym. Sci. 2004, 92, 3843.

[25] S. Hobbs, Nature 1971, 234, 12.

[26] A. Pawlak, E. Piorkowska, Colloid Polym. Sci. 2001, 279, 939.

[27] A. Espinoza-Martinez, C. Avila-Orta, V. Cruz-Delgado, O. Olvera-Neria, J. Gonzalez-Torres, Medellin-Rodriguez, F., J. Nanomater. 2012, 2012, 10.

[28] H. Feng, Z. Feng, L. Shen, Polymer 1993, 34, 2516.

[29] T. Terao, S. Maeda, A. Saika, Macromolecules 1983, 16, 1535.

CHAPTER 6: EFFECTS OF ENVIRONMENTAL AGING ON PHYSICAL PROPERTIES OF AROMATIC THERMOSETTING COPOLYESTER MATRIX NEAT AND NANOCOMPOSITE FOAMS

6.1 Introduction

High-performance/high-temperature (HP/HT) polymers demonstrate high physicochemical stability against severe environmental conditions while clearly outperforming conventional engineering and commodity polymers [1]. Well-known examples of the HP/HT polymers include poly ether ether ketone (PEEK), poly phenylene sulfide (PPS), and polyimide (PI) [2]. Particularly, due to their outstanding thermal degradation stability [3], high glass transition temperatures [4], and superior mechanical performance [5], the HP/HT polymers have found uses in a plethora of applications spanning coatings, composite matrices, fibers, foams, and membranes [6-8]. With the recent introduction of polymer nanocomposites, base thermophysical properties of polymers have been demonstrated to be considerably improved through the addition of miscellaneous nanofiller particles [9-11].

This work was previously published: Bakir, M., Henderson, C.N., Meyer, J.L., Oh, J., Miljkovic, N., Kumosa, M., Economy, J., and Jasiuk, I., Effects of environmental aging on physical properties of aromatic thermosetting copolyester matrix neat and nanocomposite foams, *Polymer Degradation and Stability*, 147, 49-56 (2018).

Special thanks to Chrissy Henderson (Bureau of Reclamation, Denver) for performing environmental aging tests.

Special thanks to Junho Oh (Department of Mechanical Science and Engineering, University of Illinois) for performing contact angle measurements.

Furthermore, when the polymer morphologies are supplemented with the multifunctional structural properties of nanocomposites, the use of polymers holds a great promise for high-end applications such as energy storage [12], biomaterials [13], recyclable/renewable materials [14], and additive manufacturing [15]. In order to achieve industrial implementation, the polymeric domains need to sustain superb degradation stability through chemical inertness and low moisture absorption in various aqueous solutions.

In a broad sense, polymers have three main degradation mechanisms: (1) physical, (2) chemical, and (3) hydrothermal [16]. First, physical aging involves the combined effects of stress, temperature, and time which result in physical property changes without permanent modifications to chemical chain configurations. Physical aging is also a thermally reversible process so that upon heating above the glass transition temperature, the virgin polymer properties can be recovered [17]. Second, chemical aging takes place at elevated temperatures through exposure to damaging environments which can drastically alter physical properties. In particular, thermal, photochemical, and radiochemical environments can irreversibly decompose chain arrangements at the molecular level [16], [18]. Lastly, hydrothermal aging occurs in the presence of moisture at high temperatures that ultimately triggers a physical aging process. In such conditions, diffusion of water molecules into the matrix degenerate the interaction mechanisms within chain networks (e.g. swelling effect). Hence, increased chain mobility accelerates physical aging which leads to plasticization of the matrix and subsequent formation of microcracks [19]. Considering all these deterioration mechanisms, promising polymer systems to be employed in the industrial applications should demonstrate excellent resistance to aging phenomena when subjected to hostile environments for long durations.

Aromatic thermosetting copolyester (ATSP) was developed in the late 1990s utilizing low cost and easily processable oligomers to design a high-temperature/high-performance polymer system [20-22]. ATSP can be conveniently prepared into various forms including coatings [23], continuous fiber composites [24], thick section/bulk machinable parts [22], adhesives [25], and foams [26]. Compared to other contemporary HP/HT polymers, ATSP demonstrates superior mechanical properties, including unfilled fully dense compressive strengths approaching 300 MPa [22], enhanced thermal degradation performance, and glass transition temperatures up to 310°C [22]. In addition, ATSP can be used as an ablative material with very high limiting oxygen index (LOI) [27], as a tribological wear coating with a low coefficient of friction, excellent wear and abrasion resistance [23], and dielectric strength for microelectronics applications [28]. Earlier work on ATSP studied moisture transport characteristics under various temperatures and humidity conditions for its different chemical structures [29]. The study showed that below 100% relative humidity (RH) at room temperature, the moisture uptake proceeded via diffusion, while increased RH and temperature caused the diffusion to progress through an irreversible relaxation mechanism. In this work, we study the effects of water immersion and salt fog spray aging environments on the physical properties of the neat and nanofiller incorporated forms of ATSP. We utilize foam ASTP morphology to enable increased surface area-to-volume ratio to accelerate the deterioration mechanisms. We analyze moisture sorption behavior of the structures as well as image the microstructural features after exposure to understand the physicochemical response of the ATSP matrix to the aging environments. We also characterize changes in glass transition temperature, thermal degradation performance, and compressive mechanical properties of the neat and nanocomposite foams.

6.2 Materials and Methods

The neat and nanocomposite ATSP foams were fabricated via a condensation polymerization reaction between carboxylic acid and acetoxy functional groups in matched oligomer sets. The oligomer groups were initially mixed in solid state at a 1:1 weight ratio. Upon the polymerization process, the oligomer mixture developed a cross-linked aromatic polyester backbone and released acetic acid as a reaction by-product. The acetic acid behaved as a foaming agent during the polymerization process that eventually promoted a porous morphology [26]. The carboxylic acid and acetoxy-capped oligomers were synthesized using biphenol diacetate (BPDA), 4-acetoxybenzoic acid (ABA), isophthalic acid (IPA), and trimesic acid (TMA) (Sigma-Aldrich Co., USA) as detailed in prior literature [22], [25], [26]. To fabricate nanocomposite foams, the constituent oligomer groups were additionally incorporated with graphene nanoplatelet (GNP) nanofillers of 3 wt.% in solid state at room temperature [30]. The GNP nanofillers (Grade M-5, XG Sciences, Inc., USA) (flake diameter: ~5 μm, thickness: 6-8 nm, density: 2200 kg/m^3) were used as received. The neat and nanocomposite foams were obtained by applying a thermal cure cycle to the mixed oligomer and oligomer-nanofiller combinations [26], [30], [31]. The thermal cure cycle comprised of two temperature-dwell stages at 202 °C for 90 minutes and 270 °C for 150 minutes, which enabled effective structural relaxation/melting of the constituent oligomers while facilitating blending of the GNP nanoparticles, and nucleation/bubble growth through the release of the acetic acid to form the porous morphology, respectively. Additionally, the thermal cycle had a final cure stage at 330°C for 90 minutes. The neat foam and nanocomposite foam refer to neat ATSP and ATSP-GNP loading levels in weight percent, respectively. To characterize the advancing and receding contact angles with water, the ATSP and ATSP-nanofiller powder combinations (2 wt.% and 5

wt.%) were coated on smooth steel plates using an electrostatic powder coating method and then cured via the applied thermal cycle [23], [32].

Accelerated salt spray tests were carried out using a Q-FOG model SSP600 apparatus (Q-Lab Corporation, USA) in accordance with the ASTM D5894 standard during cyclical salt fog conditions. The corrosive electrolyte used during exposure was a dilute Harrison's solution (DHS) including 3.5 wt.% ammonium sulfate ($(NH_4)_2SO_4$) and 0.5 wt.% sodium chloride (NaCl). Water immersion tests were conducted for extended immersion periods in deionized water in accordance with ASTM D870. The specimens were kept immersed at all times and were only removed for weight measurements once a week.

Water immersion and salt spray specimens were patted dry prior to weight measurements. Weight measurements were obtained once a week using a digital scale with a resolution of 0.001 g. Physical characterization measurements were performed on 2-week and 4-week exposed specimens. Scanning Electron Microscopy (SEM) (S-4800, Hitachi, Japan) was operated in high-resolution upper detector mode (10-15 kV voltage, 5-10 μA current) to image microstructures of water immersion and salt fog exposed neat and the nanocomposite foams to analyze local degradation effects. The samples were sputter coated for 20-30 sec with Pd-Au (≈ 10 nm thickness) to minimize charging effects.

The contact angle measurements were carried out by placing ≈100 nL water droplets on the steel coated samples using a microgonimeter (MCA-3, Kyowa Interface Science, Japan). A droplet was deposited on the surface using a piezoelectric injector at a rate of 70 droplets/sec. Both advancing and receding contact angles were characterized on multiple spots of the sample surface. The contact angles were analyzed using a commercial software (FAMAS, interFAce

Measurement & Analysis System) with the half-angle method. The results were averaged over 10 measurements.

Glass transition characterization of the nanocomposites was carried out using a Dynamic Mechanical Analyzer (DMA) with a tensile clamp fixture (Q800, TA Instruments, USA). A temperature-ramp cycle was operated with a 3°/min heating rate. The specimens were in prismatic geometries in dimensions of 5x10x25.4 mm^3 (thickness x width x length). The tests were performed in air. The glass transition characteristic curve of the virgin neat ATSP was obtained from a previous study [26].

Thermal degradation stability of the nanocomposite foams was characterized using a thermogravimetric analyzer (TGA) (TGA2950, TA Instruments, USA). A temperature-ramp heating cycle was applied with a constant 10 °C/min heating rate until 600°C. The tests were performed in a nitrogen environment with approximately 10-20 mg of the specimen. Thermal degradation characteristic curves of the virgin neat ATSP foam were obtained from a previous study [26].

Compressive mechanical properties of the nanocomposite foams were measured using a compressive load frame (4483 Load Frame, Instron Testing Systems, USA) with a constant crosshead speed of 6 mm/min. The cylindrical specimens had diameters of 12.7 mm and length of 25.4 mm. The samples weighed 1.5-1.8 g. Density was calculated as the ratio of the measured weight to the volume of the structures. Highlighted unexposed regions denote virgin properties of the neat foam and nanocomposite foam specimens [26].

6.3 Results and Discussion

First, we show results of mass uptake by the ATSP foam morphologies during the environmental aging tests. Figure 6.1 shows the mass sorption in weight percent mass change

measured on a weekly basis for the neat and nanocomposite foams subjected to the water and salt fog environments. Based on the results, water immersion specimens displayed higher mass gains than the salt fog specimens. For the water immersion tests, both neat and nanocomposite structures reached their mass transfer equilibriums by the end of a 4-week period. In particular, the neat foam demonstrated a moisture uptake of 6.5 ± 0.7 wt.% while the nanocomposite foam showed 9.8 ± 2.9 wt.% uptake. As per our understanding, the GNP particles increased the surface area due to a larger specific surface area exposed to the surrounding media for the nanocomposites while the surface wettability (as characterized by contact angle) did not change accordingly [20]. Note that contact angle measurements and surface wettability characteristics will be discussed later in the text. Hence, the increased surface area of the nanocomposites resulted in increased mass adsorption. For the salt spray tests, the measured mass uptakes were lower than the immersed samples since adsorption of salt particles was the major constituent of the mass gain. Both neat and nanocomposite specimens yielded similar characteristic curves during the first 3 weeks, followed by an increased mass sorption for the nanocomposites indicating collection of more salt particles. Likewise, this result was due to the enhanced surface area which eventually extended the mass equilibrium point. Following the 4-week period, the mass uptake by the neat ATSP was 2.4 ± 1.0 wt.% while that of the nanocomposite sample was 5.8 ± 5.6 wt.%. We highlight that the weekly basis mass sorption measurements were solely performed to observe aging-driven mass changes occurring in the neat and nanocomposite samples which were subsequently to be characterized for physicochemical properties correlated with polymer chain network integrity. A systematic moisture transport study on ATSP that discusses the effective mass absorption/adsorption mechanisms in greater details can be found in an earlier work [29].

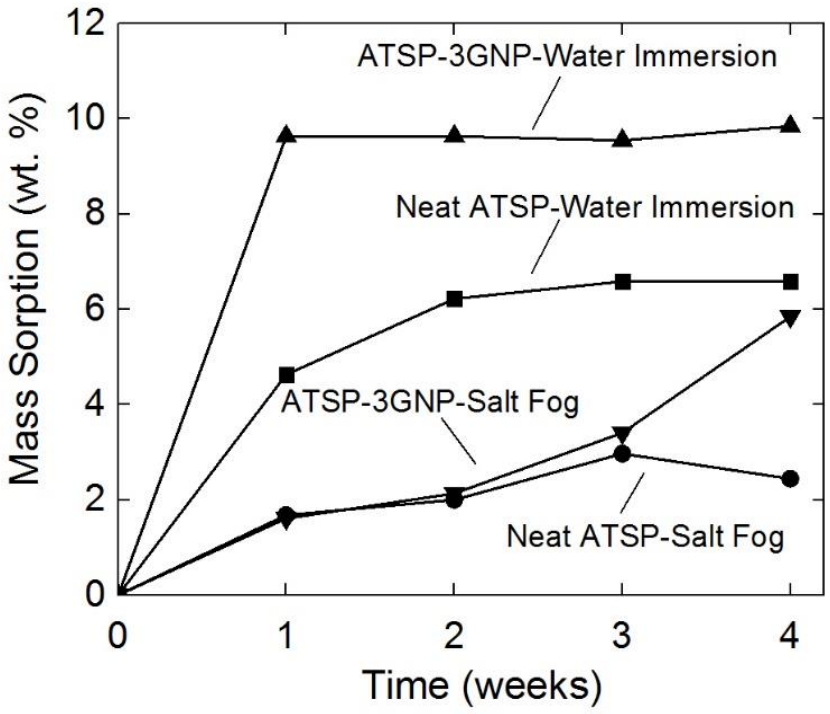

Figure 6.1 Average results of mass sorption by the neat and nanocomposite foams following cyclic water immersion and salt fog exposure tests.

Moisture absorption and transportation in polymers is mainly governed by two factors: (1) the free-volume and (2) polymer-water interactions [33]. The free-volume is defined as the volume within the polymer chain networks that can be occupied by the volume of liquids through mass diffusion [34]. The free-volume (packing density) is also a function of the effective ambient temperature, concentration of exposing solution, and molecular weight of polymer [35]. The packing density, particularly in thermosets, is directly related to the crosslink density of the polymer networks [36], which controls the mass transportation through selectivity over the diffusing species [37]. Besides, increased surface-area-to-volume ratio (e.g. foam morphology having a higher effective surface area through pore surfaces) could result in enhanced mass sorption and aggravated degradation effects reflected in the physical properties. Hence, having a highly-crosslinked morphology, the ATSP matrix delivered a relatively compact chain network

along with restricted chain mobility which in fact enabled early saturations (~1 week) while affording reduced diffusion rates. Second, the polymer-water surface interaction is controlled by the presence of hydrogen-bearing functional sites in the polymer chains. Thus, water molecules, being polar in nature, can establish hydrogen bonds with the hydroxyl groups on polymer surfaces which can alter the polymer chain configuration, and consecutively degenerate the macroscopic physical properties [38], [39]. Initiation of the moisture uptake at isothermal conditions obeys classical diffusion kinetics, which induces swelling within the crosslinked network of thermosets [40]. Considering this fact, we note that the fully cured and crosslinked network of the ATSP morphology minimized the presence of the polar groups, which mitigated water absorption into the matrix. Hence, adsorption prevailed over absorption in the case of the ATSP structures [41].

During salt fog aging, the ATSP foams similarly displayed increased mass uptake characteristics during the exposure periods. The amounts of the mass uptake were lower than the immersed specimens due to inhibited diffusion of relatively larger salt particles through the polymer matrix [37]. The results also showed that the salt fog samples did not necessarily reach an equilibrium state within the given period because of adsorption-driven mass transportation, which did not saturate while additional salt layers were built. We note that the standardized towel-blotting technique may not be an effective method to dry the porous ATSP structures because capillary forces potentially draw water and salt molecules in notable amounts over small pores. Further discussions regarding a detailed understanding of the moisture transport characteristics of ATSP can be found elsewhere [29]. In the following sections, results of the physical characterization measurements on the neat and nanocomposite foams are demonstrated to evaluate the effects of the aging conditions on the macroscopic performance of the structures.

To investigate the effect of GNP incorporation on the wettability of the ATSP matrix as well as to elucidate the mass sorption characteristics, contact angle (CA) measurements were performed using a contact angle microgoniometer. Figure 6.2 shows images of deionized water droplets in the receding state on the virgin neat and nanocomposite specimens. Furthermore, Table 6.1 provides the results of the advancing and receding contact angle measurements. Neat ATSP demonstrates a modestly hydrophobic behavior with an advancing contact angle of 87.2 ± 1.8° and a receding contact angle of 29.1 ± 2.6°, indicating significant hysteresis. As the GNP content was increased in the ATSP matrix, the increase in the advancing CA was insignificant, with ~0.8° and ~4° increases at 2 wt.% and 5 wt.% of GNP, respectively, with negligible change in the receding contact angle. Although the wetting characteristics of graphene is still an active area of research, single- and multi-layer smooth graphene sheets were demonstrated to be intrinsically hydrophilic [42,43]. Hence, the increments in the advancing CA are most likely due to increased surface roughness [44]. If we assume that the graphene is hydrophobic in nature [45], the results point to the GNPs being coated by the ATSP matrix, which would change the CA results [30]. The contact angle hysteresis (the difference between the advancing CA and the receding CA) also demonstrated slight increases with respect to the GNP content which likewise illustrated increased surface roughness, and pinning, through GNP incorporation. Hence, the GNP content did not help to increase the hydrophobicity of the nanocomposites that could mitigate further adsorption. Thus, the increased mass uptake of the nanocomposites could be related to enhanced surface area and surface roughness of the nanocomposite matrix, which could facilitate enhanced mass transportation by means of aggravation agents being adhered on the surface.

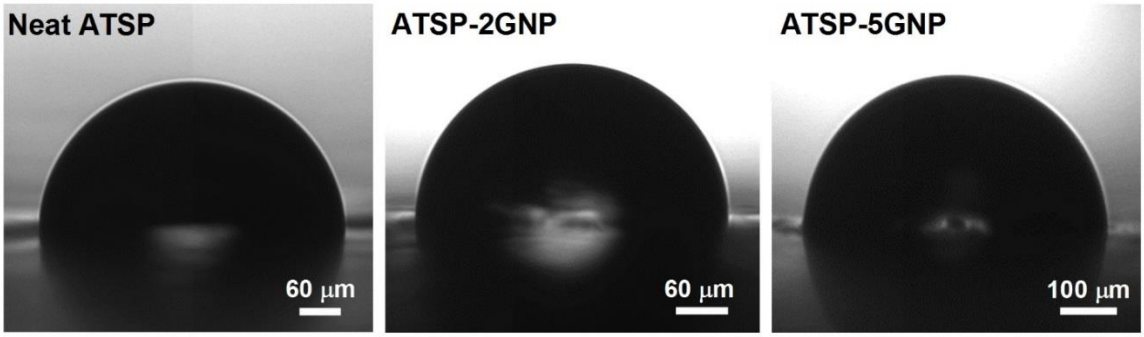

Figure 6.2 Images of water droplets resting on the virgin neat and nanocomposite coating specimens.

Table 6.1 Averaged advancing and receding contact angles (CA) obtained on the virgin neat and nanocomposite coating specimens.

	Advancing CA	**Std. Dev.**	**Receding CA**	**Std. Dev.**
Neat ATSP	87.2	1.8	29.1	2.6
ATSP-2GNP	88.0	3.4	24.0	2.6
ATSP-5GNP	91.2	6.0	28.9	1.2

Figure 6.3 shows the microstructural images of the neat and nanocomposite foams obtained using scanning electron microscopy following the 4-week water immersion and salt fog exposure periods. For the water immersion specimens, no physical deterioration was observed on the specimens. However, the salt spray specimens clearly demonstrated that the ammonium sulfate and salt particles present in the Harrison's solution substantially covered the ATSP surfaces (brighter domains) [46]. The salt accumulation on the specimens also justified the increases in the mass of the specimens, as explained earlier. We did not observe any physical damage or degeneration on the salt fog spray exposed samples. Note that the ATSP matrix exhibited an outstanding performance against the aging effects while the extent of the deterioration remained limited to the surfaces without causing any permanent structural effects (e.g. cracks, voids, pits) [47]. The chemically inert nature of the ATSP resin could be attributed to the highly crosslinked network of the aromatic rings combined with oxygen-bearing chemical

linkages [26]. The absence of surface cracks also indicated that the moisture uptake mechanism took place through the adsorption on the surface rather than the absorption into the matrix [48].

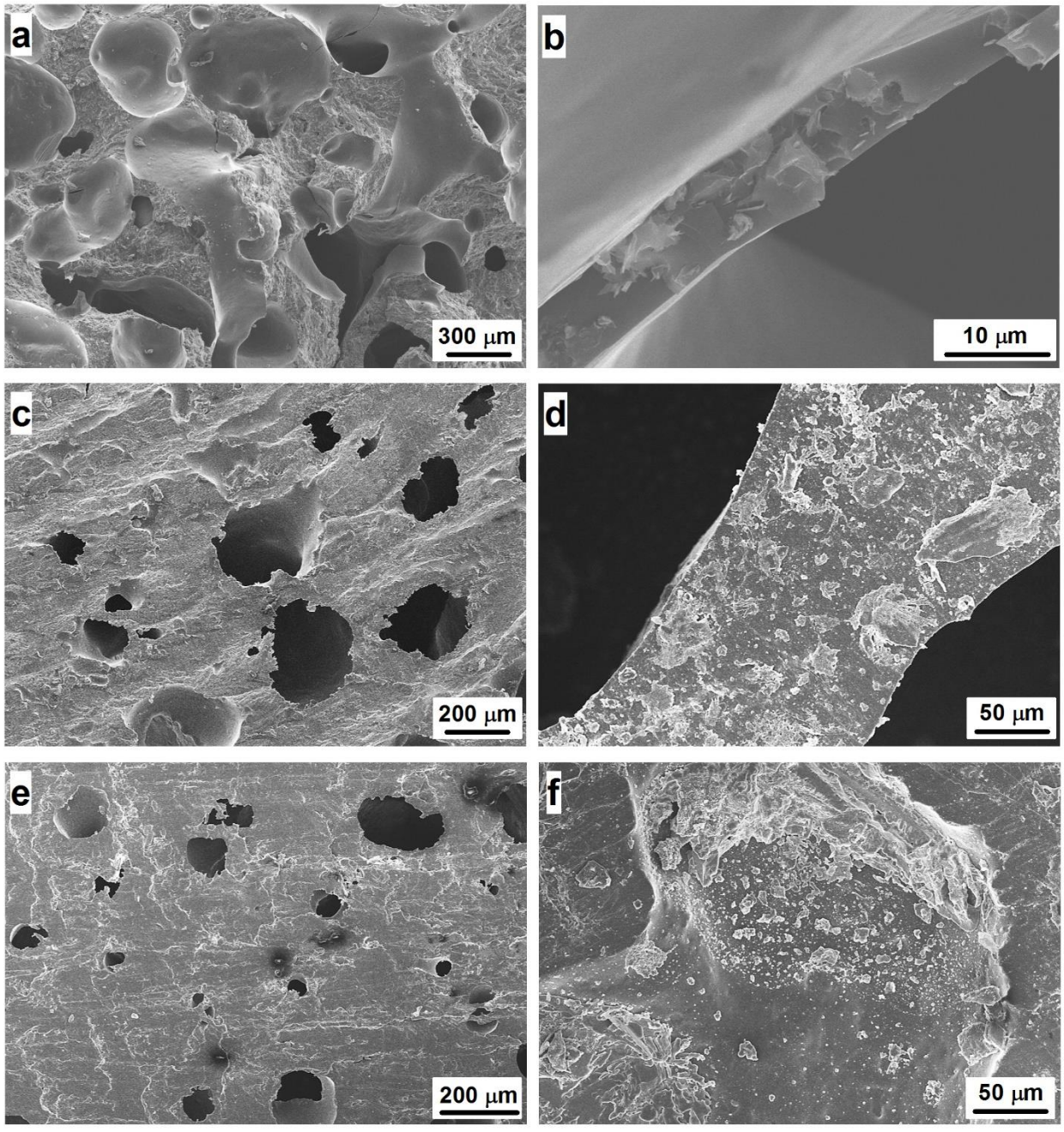

Figure 6.3 Scanning electron microscopy images of fractured virgin nanocomposite foams displaying an intrinsic porous morphology (a), and a cross-section image over a pore surface (b). Neat foams after water immersion (c) and salt fog (d) exposures. The nanocomposite foams after water immersion (e) and salt fog (f) exposures. The images were obtained following 4-week periods of testing. The pores in the matrices were inherent to the porous morphology of the structures.

Glass transition characteristics of polymers can directly reflect modifications in their chemical chain configurations [49]. Hence, we carried out thermomechanical glass transition temperature characterization on the environmentally aged specimens to analyze effects of the aggravative agents on the chemical structure of ATSP. Figure 6.4 shows tangent delta (tan δ) glass transition temperature (T_g) results obtained on the neat and the nanocomposite foams using a dynamic mechanical analyzer. Tan δ is defined as the ratio of the loss modulus to the storage modulus. The glass transition temperature of the neat foam was earlier reported to be 172°C while the nanocomposite foam with 3 wt.% GNP addition displayed a T_g of 186°C [26]. For the neat foams run through the water immersion tests, T_g was measured to be 168°C and 170°C following 2-week and 4-week exposures, respectively. Neat foams after salt fog tests showed T_g = 167°C and 162°C after 2-week and 4-week exposures, respectively. For the nanocomposite foam after water immersion tests, T_g was measured to decrease to 180°C and 168°C for 2-week and 4-week periods, respectively. For the nanocomposite foam subject to salt fog tests, T_g was measured to be 176°C and 170°C following 2-week and 4-week aging. Based on these results, the salt fog condition had a more notable impact on T_g than the water exposure. Also, as highlighted above, the water interaction characteristics of the nanocomposites were similar to those of the neat foams. Thus, the larger glass transition shifts in the nanocomposites occurred due to the increased surface interaction area generated via the GNP nanoparticle incorporation. Regarding the changes in the T_g via moisture absorption, the prior literature on amorphous polymers demonstrated that swelling caused similar decreases in the glass transition temperature [50]. Such observation is explained by the free volume theory, which is also used to explain glass transition behavior of amorphous polymers. The increase in the volume due to absorption of the water causes a steep change in the activation energy of the polymer chains, which subsequently

decreases glass transition temperature [51]. However, due to low moisture absorption nature of the ATSP matrix, as also later demonstrated in thermal degradation characteristics, the decreases in the glass transition temperature could stem from slight deterioration in the chemical morphology that came into effect following the aging conditions. Similarly, upon exposure to the salt environment, due to the fully cured state of the ATSP resin, any changes to the chemical structure are not expected to occur, which is the reason for the small T_g [52]. Furthermore, increase in the free volume due to the presence of the electrolyte solutions caused a decrease in T_g [53]. All in all, due to the free volume occupied by the aqueous media, the ATSP structures demonstrated moderate changes in the glass transition temperatures while preserving their virgin chemical configurations.

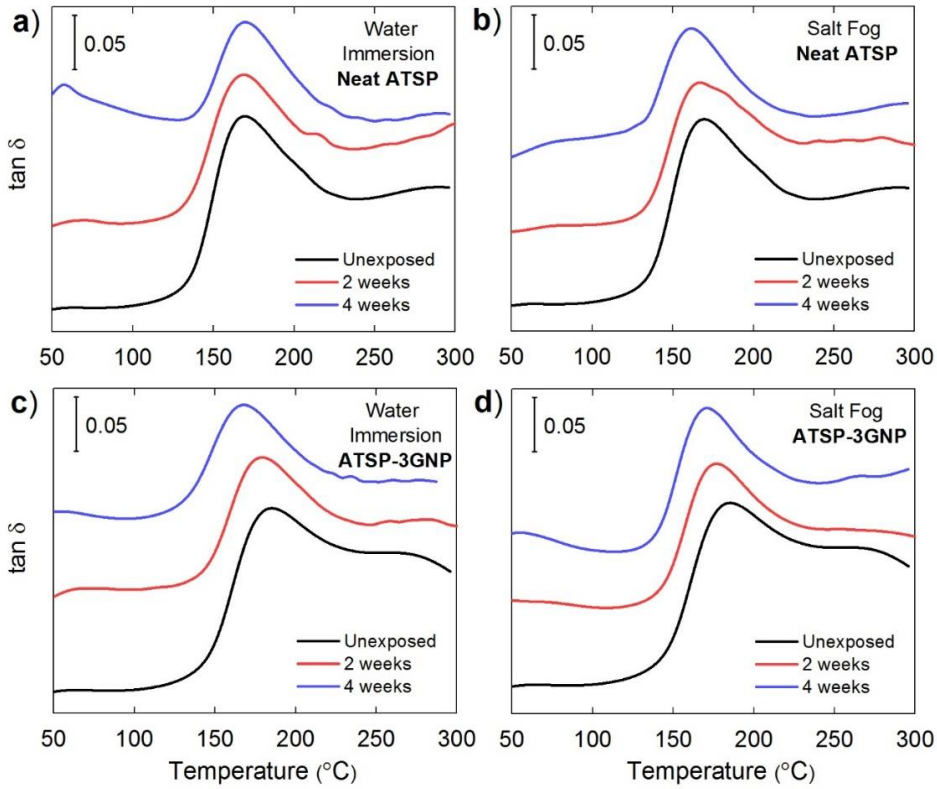

Figure 6.4 Representative dynamic mechanical analysis tangent delta (tan δ) glass transition temperature measurements of the neat foam following water immersion (a) and salt fog (b) exposures, and the nanocomposite foam following water immersion (c) and salt fog (d) exposures. The tan δ curves are stacked by arbitrary offsets to illustrate peak position shifts. The measurements were performed in air.

Correlating with the glass transition behaviors, thermal degradation characteristics of polymers can also provide an understanding of the relationship between matrix chain modulations and environmental aging effects. Figure 6.5 demonstrates the thermogravimetric analyses results of the neat and the nanocomposite structures after being subjected to the water immersion and salt spray tests. The thermal degradation characteristics of both aged specimens showed that the thermal performance of the ATSP was not substantially affected by the environmental conditions. Here, we assessed the degradation behaviors on the basis of two temperature metrics: 5% weight loss and the peak position of the mass derivative. These two reference temperatures were observed to slightly upshift by about 10-20°C for the neat foams following a 2-week water immersion condition. In addition, the nanocomposite structures revealed a similar trend within the same duration, yet the temperature shifts were not as noticeable. We note that these two reference temperatures of the thermal performance of the ATSP matrix can be improved relatively in accordance with the GNP incorporation [30]. The thermal degradation characteristics are a group property of the overall polymer network configuration which hence can precisely display major segmental modifications induced in the backbone arrangement. The ATSP polymer backbone reveals only marginal changes following the aging tests which indicate overall integrity of the crosslinked polymer morphology. Hence, based on these results, aging effects in thermal degradation performance of the neat morphology was more pronounced as compared to the nanocomposite domain. The presence of the nanofillers helped to preserve the nanocomposite morphology forming a robust physicochemical barrier [54]. The temperature shifts could also be due to the slightly plasticized morphology of the neat ATSP matrix upon exposure to the aging conditions [19]. These results highlight two other important conclusions. First, as described earlier in the text, moisture was not absorbed

significantly within the ATSP matrix since there is no corresponding change in mass loss indicating evaporation of water during the thermogravimetric cycles. Hence, adsorption was the major mass uptake mechanism. Second, surface interactions of ATSP with water and salt molecules did not form any chemical bonds (e.g. hydrogen bonds) which are usually stable up to 90-100°C. These bonds did not reveal any characteristics in the thermal curves, so the degradation processes occurred through an adsorption driven mechanism [55].

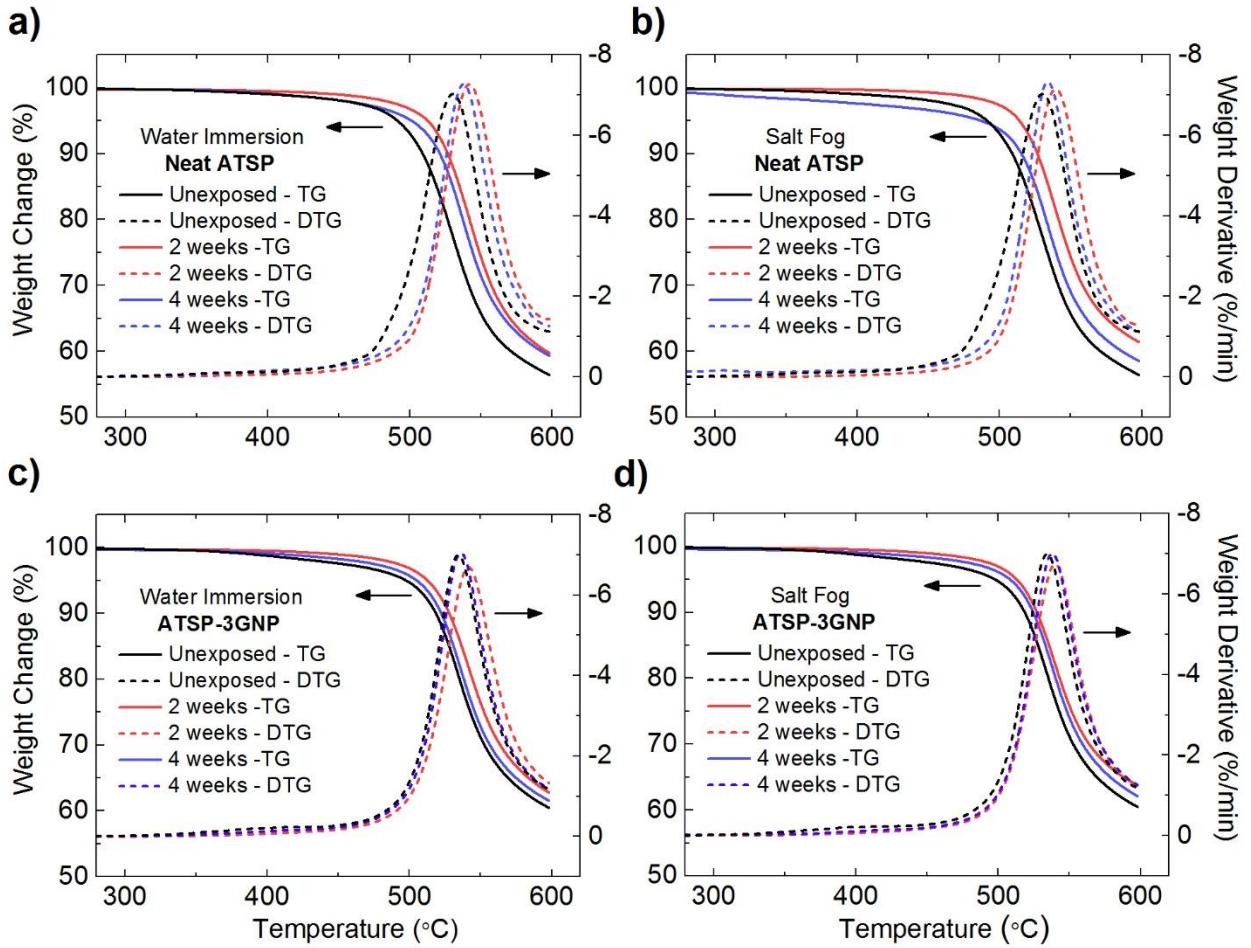

Figure 6.5 Representative thermogravimetric (DT) and derivative thermogravimetric (DTG) analyses of the neat foam following water immersion (a) and salt fog (b) tests, and the nanocomposite foam following water immersion (c) and salt fog (d) tests. The measurements were performed in nitrogen.

Figures 6.6 and 6.7 show results of compressive mechanical strength and density measurements obtained on the neat and nanocomposite foam specimens, respectively. Regarding the compressive mechanical strength results, both the neat and nanocomposite samples of the water immersion and salt spray tests performed within the expected mechanical property space that was obtained for their virgin counterparts. Results for neat specimens were 11.1 MPa after 2-weeks of water immersion, 7.9 MPa after 2-weeks of salt spray, 9.4 MPa after 4-weeks of water immersion, and 6.9 MPa after 4-weeks of salt spray. The virgin neat sample was measured to be 10.5 ± 2.3 MPa [26]. Furthermore, measured strengths for the nanocomposite specimens were 9.3 MPa after 2-weeks of water immersion, 10.9 MPa after 2-weeks of salt fog, 8.9 MPa after 4-weeks of water immersion, and 8.5 MPa after 4-weeks of salt fog. The virgin nanocomposite sample was measured to be 12.2 ± 3 MPa. The obtained compressive strengths following aging were higher than the lower limit of the virgin compressive strength, which indicated that the mechanical performances of the ATSP morphologies were slightly degraded [56]. The measurements were conducted on limited select specimens to see whether the mechanical properties of these aged structures would remain within the standard deviation domains of their virgin counterparts. This assumption was validated by closely agreeing results of both neat and nanocomposite morphologies. Such marginal changes could be due to small amounts of moisture absorbed by the matrix that slightly plasticized the morphology making it relatively softer. Regarding the density results, the measurements were obtained on the mechanical testing specimens prior to the compression tests. The density results fell into the unexposed domain of the virgin materials. It is noteworthy that the density change is a major factor that can directly affect mechanical properties. Hence, for example, although the density results of the neat foam were within the upper limit, the compressive mechanical properties were

over the lower limit. This also validates the presence of the plasticization effects. As well, as correspondence to the earlier demonstrated mass sorption data, given delay between the mass sorption measurements and the compressive mechanical tests, the adsorbed moisture could rapidly evaporate which would not be reflected in the density results.

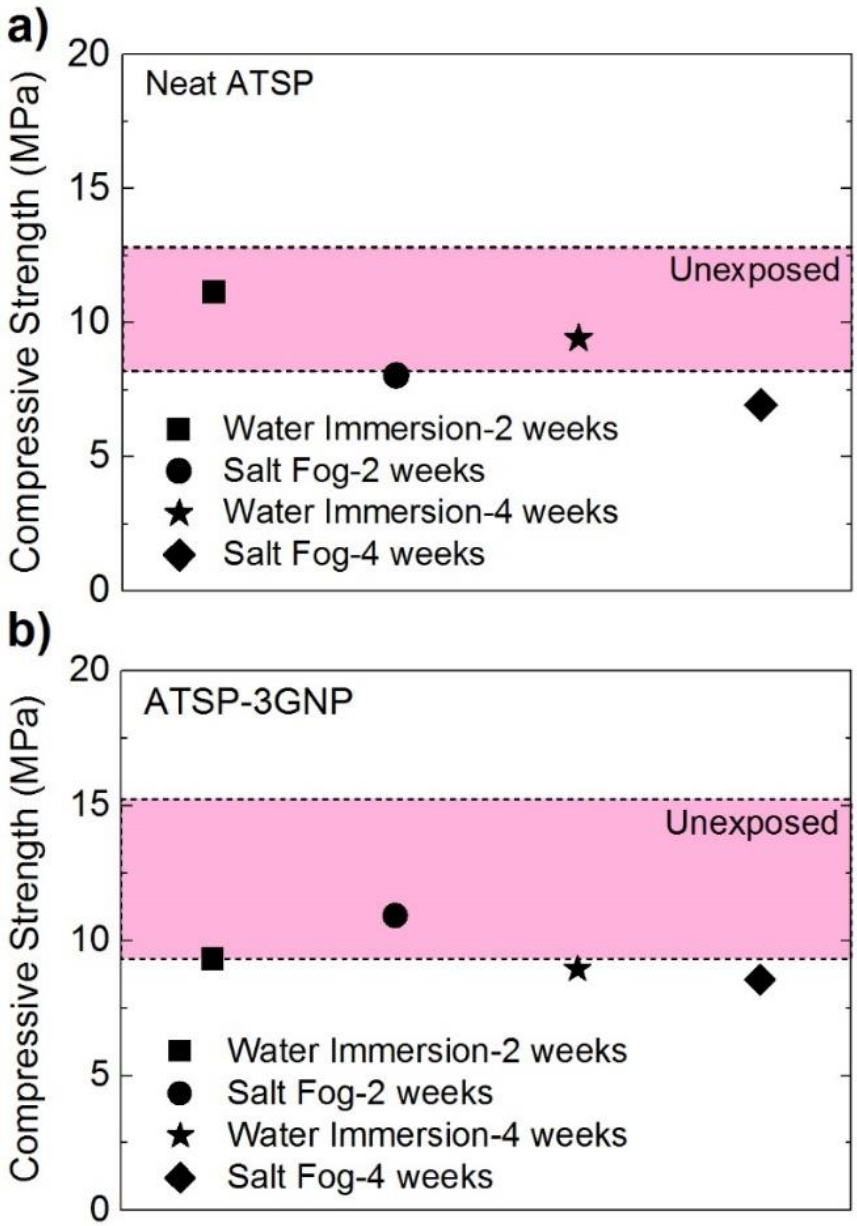

Figure 6.6 Compressive mechanical measurements of the neat (a) and nanocomposite foams (b) following water immersion and salt fog testing.

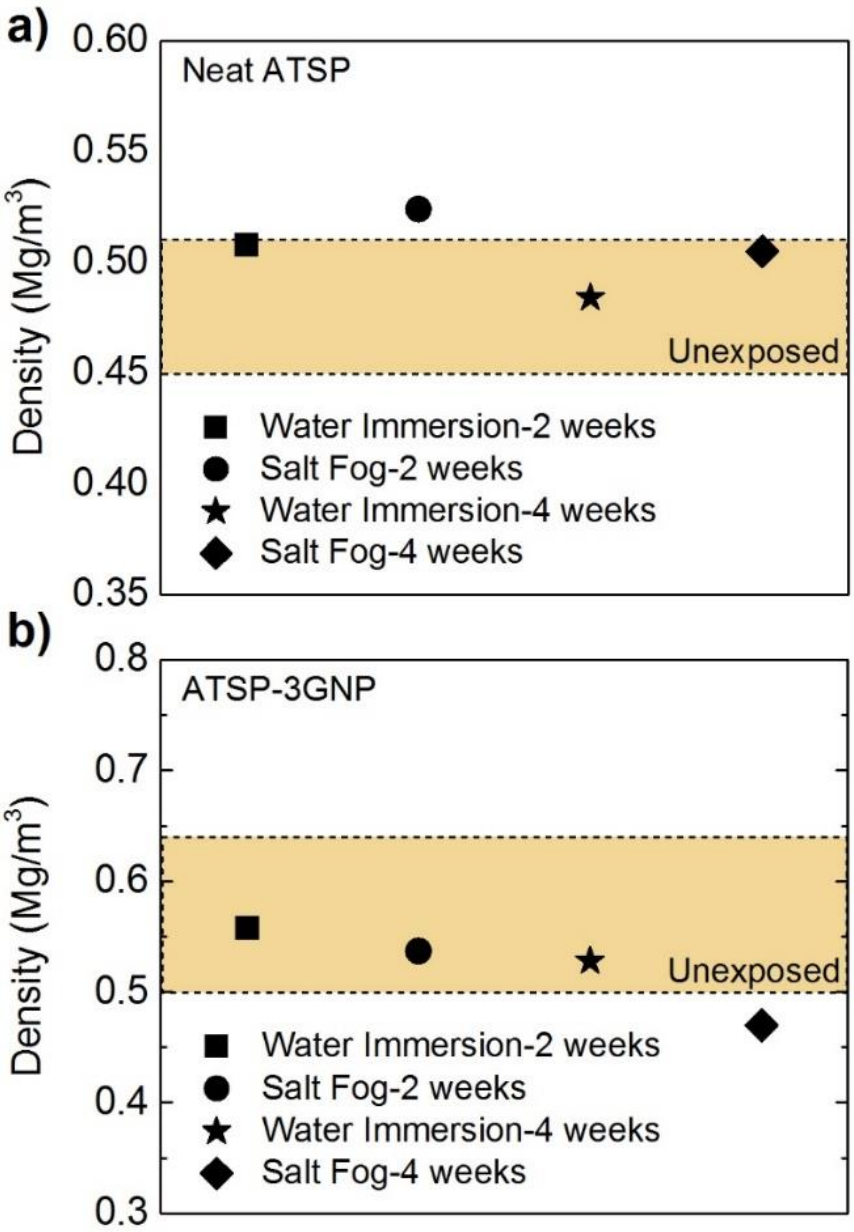

Figure 6.7 Density measurements of the neat (a) and nanocomposite foams (b) following water immersion and salt fog testing.

6.4 Conclusion

We demonstrated physical property performance of the neat and nanocomposite ATSP matrices following extended exposure periods to water immersion and salt spray environmental conditions. ATSP foam structures were utilized in this study due to their increased surface area-to-volume ratio in order to accelerate effects of degradation processes. The ATSP morphology

displayed an adsorption-driven moisture uptake behavior which in fact helped to preserve its chemical structure during the environmental degradation processes. Incorporation of GNP particles in the nanocomposite forms did not alter surface wetting characteristics, yet increased effective surface area subjected the samples to intensified attack of aggravative agents. Electron microscopy revealed that the pristine nature of ATSP morphology was effectively preserved during deterioration. Due to only minute hygroscopic swelling, the glass transition temperatures of both neat and nanocomposite structures displayed only small shifts. Thermal degradation performance of the ATSP matrix was effectively maintained. Compressive mechanical properties slightly degraded due to hygroscopic swelling, yet results were in accordance with the virgin specimens. Having an excellent aging resistance, the ATSP matrix can potentially find use in high performance demanding structural applications requiring sustainable operations in extreme conditions. The findings of this study may also lead to further efforts to investigate aging resistance of the ATSP matrix for particular environments demanded by application requirements. A comparative study with other well-known HP/HT polymers may systematically show relative changes incurred in various polymeric chemical structures.

6.5 References

[1] P.M. Hergenrother, The use, design, synthesis, and properties of high performance/high temperature polymers: an overview, High Performance Polymers 15(1) (2003) 3-45.

[2] M.G. Dhara, S. Banerjee, Fluorinated high-performance polymers: poly (arylene ether) s and aromatic polyimides containing trifluoromethyl groups, Progress in Polymer Science 35(8) (2010) 1022-1077.

[3] R. Torrecillas, A. Baudry, J. Dufay, B. Mortaigne, Thermal degradation of high performance polymers—influence of structure on polyimide thermostability, Polymer Degradation and Stability 54(2) (1996) 267-274.

[4] R. Yokota, S. Yamamoto, S. Yano, T. Sawaguchi, M. Hasegawa, H. Yamaguchi, H. Ozawa, R. Sato, Molecular design of heat resistant polyimides having excellent processability and high glass transition temperature, High Performance Polymers 13(2) (2001) S61-S72.

[5] J.C. Seferis, Polyetheretherketone (PEEK): Processing-structure and properties studies for a matrix in high performance composites, Polymer Composites 7(3) (1986) 158-169.

[6] R.L. Fusaro, Effect of atmosphere and temperature on wear, friction, and transfer of polyimide films, Asle Transactions 21(2) (1978) 125-133.

[7] E.S. Weiser, T.F. Johnson, T.L. St Clair, Y. Echigo, H. Kaneshiro, B.W. Grimsley, Polyimide foams for aerospace vehicles, High Performance Polymers 12(1) (2000) 1-12.

[8] L.M. Robeson, W.F. Burgoyne, M. Langsam, A.C. Savoca, C.F. Tien, High performance polymers for membrane separation, Polymer 35(23) (1994) 4970-4978.

[9] P. Podsiadlo, A.K. Kaushik, E.M. Arruda, A.M. Waas, B.S. Shim, J. Xu, H. Nandivada, B.G. Pumplin, J. Lahann, A. Ramamoorthy, N.A. Kotov, Ultrastrong and stiff layered polymer nanocomposites, Science 318(5847) (2007) 80-83.

[10] H. Kim, A.A. Abdala, C.W. Macosko, Graphene/polymer nanocomposites, Macromolecules 43(16) (2010) 6515-6530.

[11] J. Jordan, K.I. Jacob, R. Tannenbaum, M.A. Sharaf, I. Jasiuk, Experimental trends in polymer nanocomposites—a review, Materials Science and Engineering: A 393(1) (2005) 1-11.

[12] J. Zhang, X. Zhao, Conducting polymers directly coated on reduced graphene oxide sheets as high-performance supercapacitor electrodes, The Journal of Physical Chemistry C 116(9) (2012) 5420-5426.

[13] M. Navarro, A. Michiardi, O. Castaño, J.A. Planell, Biomaterials in orthopaedics, Journal of the Royal Society Interface 5(27) (2008) 1137-1158.

[14] L. Yu, K. Dean, L. Li, Polymer blends and composites from renewable resources, Progress in polymer science 31(6) (2006) 576-602.

[15] A.C. de Leon, Q. Chen, N.B. Palaganas, J.O. Palaganas, J. Manapat, R.C. Advincula, High performance polymer nanocomposites for additive manufacturing applications, Reactive and Functional Polymers 103 (2016) 141-155.

[16] G.M. Odegard, A. Bandyopadhyay, Physical aging of epoxy polymers and their composites, Journal of Polymer Science Part B: Polymer Physics 49(24) (2011) 1695-1716.

[17] J.M. Hutchinson, Physical aging of polymers, Progress in Polymer Science 20(4) (1995) 703-760.

[18] J. Verdu, Aspects common to all oxidation processes, Oxidative ageing of polymers, John Wiley & Sons, Inc.2012, pp. 17-43.

[19] C. Bockenheimer, D. Fata, W. Possart, New aspects of aging in epoxy networks. II. Hydrothermal aging, Journal of Applied Polymer Science 91(1) (2004) 369-377.

[20] D. Frich, K. Goranov, L. Schneggenburger, J. Economy, Novel high-temperature aromatic copolyester thermosets: synthesis, characterization, and physical properties, Macromolecules 29(24) (1996) 7734-7739.

[21] D. Frich, J. Economy, Thermally stable liquid crystalline thermosets based on aromatic copolyesters: Preparation and properties, Journal of Polymer Science Part A: Polymer Chemistry 35(6) (1997) 1061-1067.

[22] B. Vaezian, J.L. Meyer, J. Economy, Processing of aromatic thermosetting copolyesters into foams and bulk parts: characterization and mechanical properties, Polymers for Advanced Technologies 27(8) (2016) 1006-1013.

[23] P. Lan, J.L. Meyer, J. Economy, A.A. Polycarpou, Unlubricated tribological performance of aromatic thermosetting polyester (ATSP) coatings under different temperature conditions, Tribology Letters 61(1) (2016) 10.

[24] J.L. Meyer, Development of aromatic polyesters for high performance applications and use of interchain transesterification reactions as a solid-state fabrication tool, M.S. thesis. University of Illinois at Urbana-Champaign, 2015.

[25] D. Frich, J. Economy, K. Goranov, Aromatic copolyester thermosets: high temperature adhesive properties, Polymer Engineering & Science 37(3) (1997) 541-548.

[26] M. Bakir, J.L. Meyer, J. Economy, I. Jasiuk, Heat-induced polycondensation reaction with self-generated blowing agent forming aromatic thermosetting copolyester foams, Macromolecules 49(17) (2016) 6489-6496.

[27] Z. Parkar, Design of unique composites based on aromatic thermosetting copolyesters, Ph.D. dissertation. University of Illinois at Urbana-Champaign, 2011.

[28] F.F. Shi, L.A. Schneggenburger, J. Economy, New photoimageable dielectric insulating copolyester thin films: Synthesis and characterization, Journal of Applied Polymer Science 63(9) (1997) 1199-1211.

[29] F.F. Shi, J. Economy, Moisture transport studies on newly developed aromatic and aromatic/aliphatic copolyester thin films, Journal of Polymer Science Part B: Polymer Physics 36(6) (1998) 1025-1035.

[30] M. Bakir, J.L. Meyer, J. Economy, I. Jasiuk, Aromatic thermosetting copolyester nanocomposite foams: High thermal and mechanical performance lightweight structural materials, Polymer 123 (2017) 311-320.

[31] W. Wang, J. Meyer, Q. Zeng, M. Li, B. Vaezian, J. Economy, Adhesion characteristics of aromatic thermosetting copolyester and glass fiber laminates with copper foils for improved circuit boards, Polymers for Advanced Technologies 27(12) (2016) 1577-1585.

[32] P. Lan, J.L. Meyer, B. Vaezian, A.A. Polycarpou, Advanced polymeric coatings for tilting pad bearings with application in the oil and gas industry, Wear 354 (2016) 10-20.

[33] A.F. Abdelkader, J.R. White, Water absorption in epoxy resins: The effects of the crosslinking agent and curing temperature, Journal of Applied Polymer Science 98(6) (2005) 2544-2549.

[34] J.S. Vrentas, J.L. Duda, Diffusion in polymer—solvent systems. I. Reexamination of the free-volume theory, Journal of Polymer Science: Polymer Physics Edition 15(3) (1977) 403-416.

[35] J.S. Vrentas, J.L. Duda, Diffusion in polymer–solvent systems. II. A predictive theory for the dependence of diffusion coefficients on temperature, concentration, and molecular weight, Journal of Polymer Science: Polymer Physics Edition 15(3) (1977) 417-439.

[36] L.C.E. Struik, Physical aging in plastics and other glassy materials, Polymer Engineering & Science 17(3) (1977) 165-173.

[37] J. Vrentas, J. Duda, Diffusion of small molecules in amorphous polymers, Macromolecules 9(5) (1976) 785-790.

[38] T.K. Kwei, Strength of epoxy polymers. I. Effect of chemical structure and environmental conditions, Journal of Applied Polymer Science 10(11) (1966) 1647-1655.

[39] M.J. Adamson, Thermal expansion and swelling of cured epoxy resin used in graphite/epoxy composite materials, Journal of Materials Science 15(7) (1980) 1736-1745.

[40] C.-H. Shen, G.S. Springer, Moisture absorption and desorption of composite materials, Journal of Composite Materials 10(1) (1976) 2-20.

[41] S. Li, R. Vatanparast, H. Lemmetyinen, Cross-linking kinetics and swelling behaviour of aliphatic polyurethane, Polymer 41(15) (2000) 5571-5576.

[42] G. Hong, Y. Han, T.M. Schutzius, Y. Wang, Y. Pan, M. Hu, J. Jie, C.S. Sharma, U. Müller, D. Poulikakos, On the mechanism of hydrophilicity of graphene, Nano Letters 16(7) (2016) 4447-4453.

[43] M. Munz, C.E. Giusca, R.L. Myers-Ward, D.K. Gaskill, O. Kazakova, Thickness-dependent hydrophobicity of epitaxial graphene, ACS Nano 9(8) (2015) 8401-8411.

[44] M. Parvinzadeh, S. Moradian, A. Rashidi, M.-E. Yazdanshenas, Surface characterization of polyethylene terephthalate/silica nanocomposites, Applied Surface Science 256(9) (2010) 2792-2802.

[45] S. Wang, Y. Zhang, N. Abidi, L. Cabrales, Wettability and surface free energy of graphene films, Langmuir 25(18) (2009) 11078-11081.

[46] R. Christy, W. Harte, Electrical conductivity of X-irradiated NaCl, Physical Review 109(3) (1958) 710-715.

[47] B. Marungsri, H. Shinokubo, R. Matsuoka, S. Kumagai, Effect of specimen configuration on deterioration of silicone rubber for polymer insulators in salt fog ageing test, IEEE Transactions on Dielectrics and Electrical Insulation 13(1) (2006) 129-138.

[48] H.N. Dhakal, Z.Y. Zhang, M.O.W. Richardson, Effect of water absorption on the mechanical properties of hemp fibre reinforced unsaturated polyester composites, Composites Science and Technology 67(7) (2007) 1674-1683.

[49] H. Oh, P.F. Green, Polymer chain dynamics and glass transition in athermal polymer/nanoparticle mixtures, Nat Mater 8(2) (2009) 139-143.

[50] E.L. McKague, J.D. Reynolds, J.E. Halkias, Swelling and glass transition relations for epoxy matrix material in humid environments, Journal of Applied Polymer Science 22(6) (1978) 1643-1654.

[51] J.S. Vrentas, J.L. Duda, A free-volume interpretation of the influence of the glass transition on diffusion in amorphous polymers, Journal of Applied Polymer Science 22(8) (1978) 2325-2339.

[52] J.W. Chin, W. Hughes, A. Signor, Elevated temperature aging of glass fiber reinforced vinyl ester and isophthalic polyester composites in water, salt water, and concrete pore solution, American Society for Composites, 16th technical conference. Proceedings (2001) 1-12.

[53] A. Chakraverty, U. Mohanty, S. Mishra, A. Satapathy, Sea water ageing of GFRP composites and the dissolved salts, IOP Conference Series: Materials Science and Engineering, IOP Publishing 75 (2015) 012029.

[54] C. Bao, L. Song, W. Xing, B. Yuan, C.A. Wilkie, J. Huang, Y. Guo, Y. Hu, Preparation of graphene by pressurized oxidation and multiplex reduction and its polymer nanocomposites by masterbatch-based melt blending, Journal of Materials Chemistry 22(13) (2012) 6088-6096.

[55] K.-H. Liao, S. Aoyama, A.A. Abdala, C. Macosko, Does graphene change Tg of nanocomposites? Macromolecules 47(23) (2014) 8311-8319.

[56] J.M. Augl, R. Trabocco, Environmental studies on carbon fiber reinforced epoxies, Battelle's Colombus Laboratories, AFOSR Workshop on Durability Characteristics of Resin Matrix Composites (1975).

CHAPTER 7: NANOFILLER-CONJUGATED PERCOLATING CONDUCTIVE NETWORK MODIFIED POLYMERIZATION REACTION CHARACTERISTICS OF AROMATIC THERMOSETTING COPOLYESTER RESIN

7.1 Introduction

Technological advancements of structural materials currently count on the development of alternative lightweight materials possessing physical properties commensurate with contemporary systems while enabling cost-effective and industrially scalable high-throughput production solutions [1-4]. Polymer nanocomposites are combinations of nanofiller reinforcement particles and host polymer matrix, which uniquely embody multifunctional properties within low-density morphologies [5-7]. Physical properties of the polymer nanocomposites can be adjusted by controlling the nanofiller loading at large. Yet, optimization of such properties involves many factors coming into effect including but not limited to processing conditions of the nanocomposites as well as morphology, dispersion quality, and chemical functionalization of the nanofillers [8-11]. In this regard, recent efforts have sought to realize robust interfacial attachment schemes between edge-or-surface-functionalized nanofillers and backbone chains of various polymers [12]. Yet, current nanocomposite configurations are limited in the ultimate physical properties due to the presence of only weak intermolecular coupling mechanisms [13].

This work was previously published: Bakir, M., Meyer, J.L., Sutrisno, A., Economy, J., and Jasiuk, I., Nanofiller-conjugated percolation conductive network modified polymerization reaction characteristics of aromatic thermosetting copolyester resin, RSC Advances, 8, 4946-4954 (2018).

Special thanks to Dr. Andre Sutrisno (NMR/ERP Laboratory, University of Illinois) for providing invaluable guidance on NMR analysis.

In particular, electrically conductive polymer nanocomposites have been a subject of extensive studies in the interest of immense potential for broad spectrum of applications spanning batteries, membranes, and electromagnetic shielding [14-16]. Within this framework, the formation of conductive networks of interconnected nanofillers - past the electrical percolation transition threshold - within intrinsically insulating polymer domains is imperative as far as the performances of the electrically conductive nanocomposites are concerned [17]. The percolation threshold is recognized to vary with respect to morphology, size, and distribution of nanofillers as well as rheological characteristics of resins [18] Besides, it is well acknowledged that the increased nanofiller loading fractions near or above the percolation transition substantially deteriorate the structural integrity of the nanocomposites [19]. Hence, a primary research thrust has been centered on efforts to realize minimal loading levels for percolation thresholds utilizing various types of nanofillers and polymer combinations prepared via different processing methods [20, 21]. Although, there are comprehensive studies reporting on the rheological properties of the nanocomposites as a result of incremented nanofiller contents, not much is still known about the physicochemical effects of the nanofillers on characteristics of in situ polymerization processes [22].

Aromatic thermosetting copolyester (ATSP) utilizes low cost, easily processable and crosslinkable oligomers to develop a high-performance polymer morphology (Figure 7.1) [23]. Tailorable chemical structure of the backbone chain as well as convenient reconfigurability of the matrix into various form factors enable effectively controllable physical properties [24]. Recently, ATSP nanocomposites have been introduced that facilitate improved distributions of nanofillers via a solid-state mixing route, which then result in substantially increased thermal and mechanical properties [5]. In this work, we report on the physicochemical changes observed

during in situ polycondensation reaction through formation of electrically conductive percolating GNP networks within the ATSP resin. ATSP nanocomposite foams are obtained through a polycondensation reaction between carboxylic acid- and acetoxy-capped constituent oligomers, which releases acetic acid as a reaction by-product to generate porous morphology. In the course of in situ polymerization reaction, the GNPs covalently conjugate with the functionalized oligomers while the resin is advancing in molecular weight to develop foam structure. The varied GNP size controls the electrical percolation transition thresholds and measured ultimate electrical conductivities. As well, microstructural analysis displays the morphological effects caused by the percolating networks of the GNPs. Cure characteristics reveal the influence of the nanofillers on the polymerization reaction. Chemical characterization of the nanocomposite backbone displays strong interfacial entanglement of the GNPs and ATSP matrix.

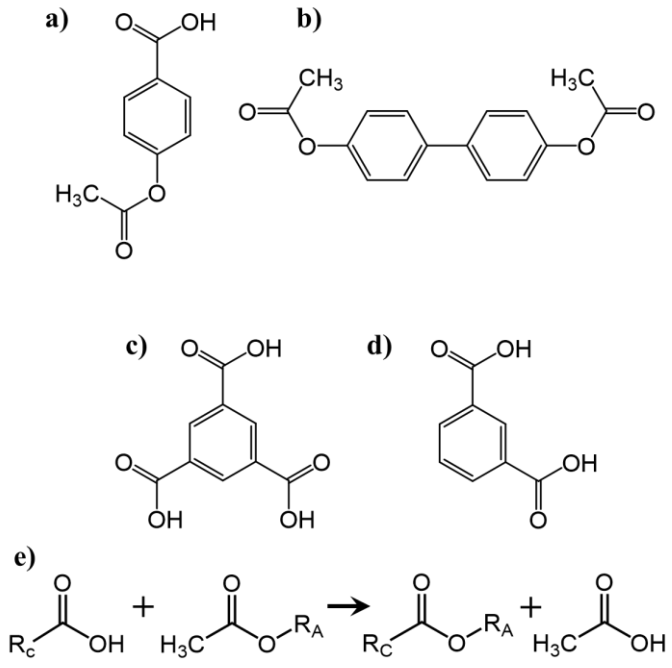

Figure 7.1 Chemical structures of the monomers a) 4-acetoxybenzoic acid (ABA), b) biphenol diacetate (BDPA), c) trimesic acid (TMA) and d) isophthalic acid (IPA). (e) Chemical representation of the polycondensation reaction carried out between the acetoxy functionalized oligomer (R_A) and carboxylic acid functionalized oligomer (R_C) yielding a crosslinked polymer backbone and releasing acetic acid as a reaction by-product.

7.2 Materials and Methods

The constituent carboxylic acid and acetoxy functional group matching oligomers of the aromatic thermosetting copolyester are synthesized using biphenol diacetate (BPDA), 4-acetoxybenzoic acid (ABA), isophthalic acid (IPA), and trimesic acid (TMA) monomers (Sigma-Aldrich Co., USA) at particular molar feed ratios as further explained in earlier studies [23-25]. The carboxylic acid (~1201 g/mol) and acetoxy-capped (~1203 g/mol) oligomers (premixed at 1:1 weight ratio) are individually mixed in solid state with chemically pristine (non-functionalized) graphene nanoplatelet (GNP) particles of 1 μm (thickness: 8-15 nm) (Cheap Tubes, Inc., USA), 5 μm (thickness: 6-8 nm) (XG Sciences, Inc., USA), and 25 μm (thickness: 6-8 nm) (XG Sciences, Inc., USA) average flake diameters at 1, 3, 4, 5, 6, 7, 8, and 10 wt % loading levels [5]. The GNPs and ATSP precursor oligomers mixtures form powder combinations in solid state. The mixing process is performed via rigorous shaking until white oligomers powder turns to pitch dark, as also investigated under UV light. Such a color change indicates effective distribution of the nanofillers at macroscale in the oligomer powder bed [25]. The ATSP nanocomposites are obtained via condensation polymerization (polycondensation) reaction between the constituent oligomers, which generates a crosslinked aromatic polyester backbone polymer network [25]. The thermal polymerization process includes two dwell stages at 202 °C for 90 minutes and 270 °C for 150 minutes, respectively. The cycle has a final cure stage at 330°C for 90 minutes [5]. The nanocomposite foams are labeled as ATSP-GNP Type as their naming convention.

Solid-state Nuclear Magnetic Resonance spectroscopy measurements are performed using ground nanocomposite specimens (~50 mg) packed into NMR rotors with Unity Inova 300 MHz NMR spectrometer (Varian Inc., USA). ^{1}H and ^{13}C spectra are acquired using direct pulse

(DP) (pulse width (pw) =2.5 μs, recycle time (d1) = 2 s) and cross-polarized (CP) (pulse width (pwH) =2 μs, recycle time (d1) = 2 s, and contact time (tHX) = 4 ms) excitations, respectively. Specimens are spun at 10 kHz. Data analysis is performed using the MestreNova software. ^{1}H and ^{13}C NMR spectra are processed using 1 Hz and 25 Hz line broadenings, respectively.

Scanning Electron Microscopy (SEM) (S-4800, Hitachi, Japan) is operated in the high-resolution mode (10 kV voltage and 5 μA current) to image microstructural features and distributions of the GNPs in the ATSP matrix.

Transmission electron microscopy is employed in bright-field mode (200 kV, 102 μA) to analyze the interfacial interactions of the GNPs with the ATSP chains (2010LaB_6, JEOL, Japan). Fabricated nanocomposite specimens are ground using a laboratory grinder and the powder is settled in methanol solution for 10-15 min. Floating particles in the solution are collected using a pipette and passed through a copper grid, which is then dried at 80°C for 1 hour.

Raman spectroscopy (Raman 11, Nanophoton, Japan) measurements are carried out using an excitation source of 633 nm, a 20x objective lens, and a total acquisition time of 5 min.

Direct current (DC) electrical conductivity measurements are performed on foam morphology specimens using 4 point-probe method (6517 B, Keithley Instruments, USA). The specimens are in 5 x 5 x 12 mm^3 (width x thickness x length). The DC electrical conductivity results are averaged over four samples per loading fraction, and standard deviations are given by error bars, accordingly. For the loading levels corresponding to percolation transitions, the nanocomposite specimens are labeled, in addition to the GNP size, with $<\varphi_c$, $\sim\varphi_c$, $>\varphi_c$ denoting below percolation, around percolation, and above percolation GNP contents, respectively.

Volumetric microstructural images are obtained on foam morphology specimens using a high-resolution X-ray micro-computed tomography (Micro-CT) (Xradia MicroXCT-400). The

3D objects are reconstructed utilizing total 1441 images taken at every 0.25° corresponding to sample rotation during the imaging process. The samples are in 10 mm x 20 mm cross-section with 4 mm thickness.

Density is calculated as the ratio of measured weight to volume of the specimens. The density of neat fully dense ATSP is 1.27 Mg/m^3.

The cure characteristics of the nanocomposite foams are investigated using a Differential Scanning Calorimetry (DSC) (DSC 2910, TA Instruments, USA). The tests are performed under an inert atmosphere of nitrogen. The cure cycle involves a temperature-ramped heating process with a 10 °C/min heating rate.

7.3 Results and Discussion

First, we highlight the chemical principles of the polycondensation reaction carried out between the matching oligomer groups that form the crosslinked network of the ATSP matrix. The polymerization process involves the acetoxy and carboxylic acid-capped constituent oligomers conducting an esterification condensation reaction at sufficiently high temperatures exceeding 200 °C. In the course of this reaction, ether oxygen groups of the acetoxy-capped oligomer exchange with the hydroxyl groups of the carboxylic acid-capped oligomer that produces the crosslinked aromatic backbone morphology while releasing acetic acid as a by-product, which deliberately generates a porous morphology [25]. Figure 7.2 demonstrates solid-state Nuclear Magnetic Resonance (ssNMR) spectra of the individual carboxylic acid (C-group)- and acetoxy (A-group)-capped oligomer groups, uncured combination of the oligomers (C+A mixed), and cured ATSP matrix (ATSP). In Figure 7.2.a, ^{13}C cross-polarization magic-angle spinning (CPMAS) spectra of the individual oligomers exhibit two main peak domains corresponding to aromatic main chains (C-C/C-H bonds) and functional side chains (C-O/C=O

bonds). Measured chemical shift positions of the A-group are δ=168.7 162.8, 154.8, 150.5, 136.2, 131.2, 127.3, 122.1, and 20.6 ppm and the C-group are δ=171.7, 162.9, 154.8, 150.5, 134.9, 129.9, 122.1 ppm. The solid-state uncured combination of the oligomers (C+A mixed) displays similar characteristic peaks detected at δ= 172.9, 168.9, 162.9, 154.8, 150.5, 135.2, 129.9, 122.1, and 20.6 ppm. Following the polymerization reaction (performed outside of the NMR station), the cured ATSP morphology exhibits peaks at δ=160.5, 152.6, 148.2, 132.9, 128.4, 125.2, 118.8 ppm. Hence, the two identified peak domains, emerging from the constituent oligomer groups, are effectively preserved within the ATSP morphology whereby a crosslinked aromatic backbone linked via oxygen bonds is formed [25]. Regarding the chemical imprints of the reactive caps, the peaks observed at δ=171.7 ppm in C-group and δ=168.7 and 20.6 ppm in A-group (as indicated with asterisks in the figure) likewise transmits to the spectrum of the uncured mixture, yet disappears upon polymerization, and are absent from the ^{13}C spectrum of the cured ATSP matrix. It highlights that these peaks are associated with the reactive caps that participate in the reaction. In particular, the ether oxygen of the acetoxy cap (with the methyl (-CH_3) group displays at δ=20.6 ppm and the oxygen-bearing groups (C-O/C=O) display at δ=168.7 ppm as observables) interacts with the hydroxyl group of the carboxylic acid cap (with the oxygen-bearing groups (C-O/C=O) show a peak at δ=171.7 ppm) in the course of the polycondensation reaction which then release acetic acid foaming as the by-product while the crosslinked morphology is formed [26]. Besides, in Figure 7.2.b, ^{1}H direct pulse magic-angle spinning (DPMAS) spectra show chemical shifts of the C-group at δ=7.4 ppm, A-group at δ=7.4, 1.7 ppm, C+A mixed at δ=7.4, 2.1 ppm, and ATSP at δ=5.0 ppm (The shifts are referenced to zero in the figure for clarity). Particularly, the spectrum of the A-group displays a shoulder formation (at δ=1.7 ppm) over the main peak, which represents the acetoxy based reactive cap of

the oligomer [27]. Note that although the acetoxy cap is detected in the ^{1}H spectrum of the uncured mixture, it is no longer observable after the esterification process. Hence, based on both ^{1}H and ^{13}C spectra, the formation of the crosslinked aromatic backbone is mainly controlled by the functional groups of the constituent oligomers reacting at elevated temperatures during the polymerization reaction.

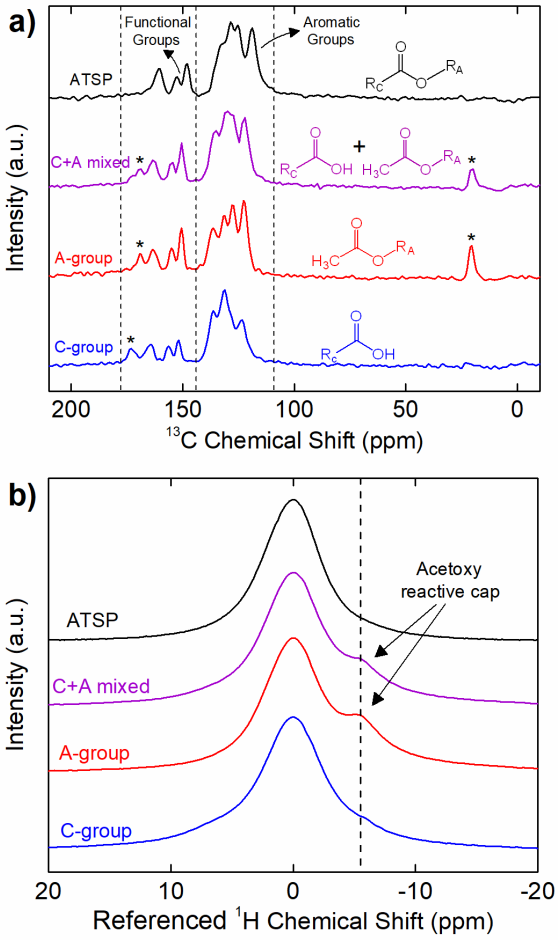

Figure 7.2 Solid-state Nuclear Magnetic Resonance (ssNMR) ^{13}C cross-polarization magic-angle spinning (CPMAS) (a) and ^{1}H direct pulse magic-angle spinning (DPMAS) (b) spectra of the carboxylic acid (C-group) and acetoxy (A-group) capped individual oligomers, uncured combination of the C-and A-groups (C+A mixed), and cured matrix (ATSP). Aromatic groups and functional groups represent C-C/C-H and C-O/C=O bonds participated in the oligomer sets as well as the cured matrix. R_C and R_A indicate aromatic chain configurations of the carboxylic acid and acetoxy group oligomers, respectively. Asterisks highlight the peaks associated with the reactive caps involving in the polymerization reaction. ^{1}H spectra referenced to zero to display the additional peak formations, corresponding chemical shift values are given in the text.

Next, we highlight the in situ intermolecular attraction and interfacial coupling mechanism effective between the GNP nanoparticles and ATSP backbone chains, as shown in Figure 7.3. During the thermal polymerization reaction between the constituent oligomers, the GNP particles interact with the reactive functional groups of the oligomers, and, consecutively, integrate with the crosslinked network upon curing. The underlying in situ interaction mechanism stems from intermolecular attraction forces between highly polar acetoxy and carboxylic acid caps of the oligomers and inherently oxygen-containing polar sites on the GNP particles [28]. Within this scheme, molten oligomers at high temperatures blend together, and wet the GNP particles through effective hydrodynamic forces emerging during the acetic acid by-product release [5]. It then facilitates the polar force induced interfacial interaction between the GNPs and ATSP. Subsequently, the oligomers – containing acetoxy and carboxylic acid reactive groups - crosslink with the oxygen-bearing polar sites on the GNP particles upon the cure process which effectively tethers the GNPs to the crosslinked domain of the ATSP. Since the interfacial coupling occurs through oxygen bonds, it enables high physicochemical stability which effectively enhances the thermomechanical properties of the ATSP nanocomposites [25]. Scanning electron microscopy (SEM) analysis reveals that the GNP particles are thickly coated by the matrix indicating effective surface wettability enabled through the in situ attraction mechanism (Figure 7.3.a). Hence, the GNP particles are not phobic to the molten oligomer groups during the polymerization process. More importantly, such an in-situ present interaction scheme indicates that the GNPs can also modify the polymerization reactions characteristics, which will be discussed later in the text. To highlight the interfacial coupling effect, transmission electron microscopy (TEM) image displays a GNP flake having ATSP chain fragments (darker domains) tethered on the surface that clearly indicates the molecular level extent of the coupling formation

(Figure 7.3.b). In addition, Raman spectroscopy measurements, as shown in Figure 7.3.c, display the pristine GNP spectrum as compared to that of the GNP interacted with the ATSP matrix. The pristine GNP produces a conventional spectrum with two characteristic peaks at 1360 cm^{-1} and 1590 cm^{-1} which correspond to D (disordered hybridized structure with impurities) and G (ordered graphitic structure) bands, respectively [29]. Upon the GNP particles interacting with the ATSP backbone chains, additional peak formations are observed, as denoted with asterisks. The peaks arise from the polymer domain for which the polymer chains are excited while strongly attached to the GNP structure for Raman spectrum of the neat ATSP). Also note that the presence of the additional peaks disturbs the D band region, which indicates that the grafting takes place through a disordered area of the GNP flakes where the oxygen-containing sites are present. Hence, it is clearly evident that the GNP and ATSP matrix constitute a strong interfacial attachment. We note that the GNP particles remained intact in the ATSP matrix upon the polymerization reaction which apparently did not exfoliate, based on X-ray diffraction (XRD) spectroscopy demonstrated in an earlier work [5]. Besides, temperature-driven hydrodynamic motion within molten oligomer domain caused relocation of the acetic acid blowing agent bubbles enabling redistribution and rearrangement of the GNP particles prior to the curing that minimized nanoparticle aggregation in the nanocomposite matrix [5].

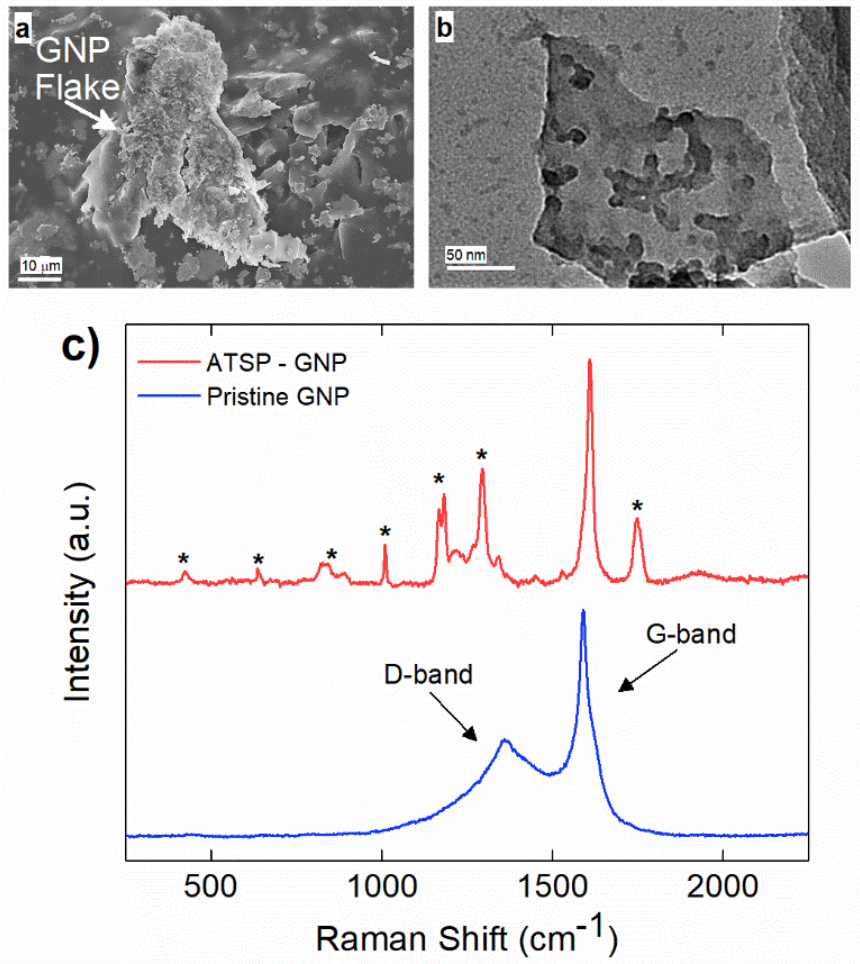

Figure 7.3 A scanning electron microscopy image obtained on a single GNP flake (GNP 25 μm) thickly coated by ATSP matrix (a). A bright-field transmission electron microscopy image of a GNP flake (GNP 5 μm) decorated with interfacially tethered ATSP chain fragments (b). Raman spectra of pristine GNP flakes (GNP 5 μm) and GNPs within the ATSP matrix (c). Asterisks denote additional peaks formed upon interactions with the ATSP backbone chains.

Afterwards, we investigate the electrical percolation characteristics of the ATSP nanocomposites incorporated with the GNP particles of 1 μm, 5 μm, and 25 μm sizes. Direct Current (DC) electrical conductivity results of the ATSP nanocomposites obtained employing a four-point probe method are shown in Figure 7.4. The neat ATSP (without addition of the GNPs) displays a characeristic non-conductive behavior with a DC conductivity of $4.04 \times 10^{-13} \pm 7.73 \times 10^{-14}$ S/m being in agreement with similar polymer systems [30]. Upon selectively incremented

nanofiller content, the electrical conductivity remains almost constant until the percolation threshold transitions of each GNP sizes. The percolation thresholds are observed to vary with respect to the GNP particle sizes. In particular, GNP 1 μm forms the conductive percolating network around 5 wt % while GNP 5μm and GNP 25 μm reach obtain the interconnected domains near 4 wt % and 3 wt %, respectively. The percolation thresholds are visually determined with respect to the S-shape characteristic curve of the percolation transition. The observed percolation thresholds concur with the findings in the literature [31-33]. The downshifts in the percolation thresholds with the larger GNPs occur due to the prompt development of the percolating networks which increases the probability of the formation of nanoparticle conductive paths in the matrix [34]. The generalized connectedness percolation theory describes that the percolation threshold is independent of the aspect ratio for monodisperse disc-shaped platelet nanofillers [17,35]. Yet, from an experimental point of view, difference in the average diameters of the GNPs (polydispersity) is expected at each nanocomposite, although they are formed through a single GNP size, considering the bulk manufacturing processes of the pristine GNPs as well as the processing conditions of the nanocomposites. Hence, shifts in the percolation thresholds with respect to different GNP sizes are conceivable. In this regard, as polydispersity ratio (the variation of the GNP size for a certain given diameter) is increased, in this case through the presence of the larger GNP particles (assuming same thicknesses for all sizes), the percolation threshold decreases [17]. Above the percolation transitions, the nanocomposites acquire highly conductive states. As a matter of fact, we observe that the 10 wt % of GNP loading level displays electrical conductivities of $4.08 \times 10^{-3} \pm 1.81 \times 10^{-3}$ S/m for GNP 1 μm, 21.2 ± 9.08 S/m for GNP 5 μm, and $1.6 \times 10^{3} \pm 4.78\ 10^{2}$ S/m for GNP 25 μm. A possible reason which gives rise to lower electrical conductivities with the

smaller aspect ratio of the GNPs is the increased interfacial contact resistance through larger contact area [36]. Another reason may be the different intrinsic electrical conductivities for each different GNP size induced through the presence of inherent functional groups or defect sites, yet conclusive remarks require further analysis. Based on the electrical conductivity results, we determine 3 percolation-based GNP contents for further physical analysis: below percolation ($<\varphi_c$), around percolation ($\sim\varphi_c$), and above percolation ($>\varphi_c$). For GNP 1 μm, $<\varphi_c$, $\sim\varphi_c$, $>\varphi_c$ correspond to 1 wt %, 5 wt %, and 10 wt %, respectively. For GNP 5 μm, $<\varphi_c$, $\sim\varphi_c$, $>\varphi_c$ correspond to 1 wt %, 4 wt %, and 10 wt %, respectively. For GNP 25 μm, $<\varphi_c$, $\sim\varphi_c$, $>\varphi_c$ correspond to 1 wt %, 3 wt %, and 10 wt %, respectively.

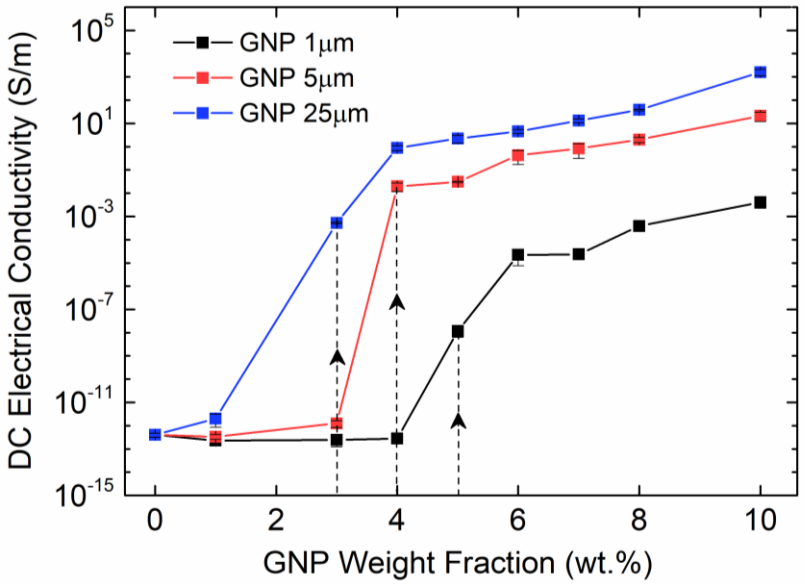

Figure 7.4 Results of DC electrical conductivity measurements on the ATSP-GNP nanocomposites with GNPs of 1 μm, 5 μm, and 25 μm. Standard deviations were represented with error bars. Dashed lines indicate assigned percolation thresholds for each GNP size.

To further interrogate the percolation characteristics, we perform microstructural analysis via a Scanning Electron Microscope (SEM) on a set of specimens with GNP contents of below percolation ($<\varphi_c$), around percolation ($\sim\varphi_c$), and above percolation ($>\varphi_c$). As shown in Figure 7.5.a-c, GNP 1 μm exhibits very random and wide distributions until the percolation threshold

after which the GNP flakes are observed to effectively cover the surface of the matrix. In addition, in Figure 7.5.d-f, GNP 5 μm specimens are observed to form some small clusters below the percolation point owing to the larger particle size. Upon increases in the content, the GNPs are embedded in the matrix. As well, above the percolation transition, the GNP particles are thickly coated with ATSP while dispersed over the matrix. In Figure 7.5.g-i, GNP 25 μm specimens display similar characteristics as GNP 5 μm, yet due to the larger particle size, formations of cluster islands are clearly marked. The findings here indicate that the GNPs of the larger sizes (5 μm and 25 μm) form cluster through percolation formation, significantly interact with the matrix, and effectively alter the topological features of the nanocomposite morphologies. Also, based on modeling perspective, the establishment of the percolating networks through the fomation of clusters (defined as connectedness) for the larger GNPs significantly affect the percolation transition characteristics as well as the ultimate electrical conductivities. As such, the larger size of the clusters gives rise to the lower percolation transition in the non-conductive matrices, which is completely analogous to the polydispersity effect [37]. We subsequently carry out a supplementary visual characterization on the nanocomposites having the corresponding GNP loading fractions to observe modifications in the volumetric morphologies. In micro computed tomography (micro-CT) 3D reconstructed scanning images of the ATSP-GNP foam morphology nanocomposites, the intrinsic porous morphology of GNP 1 μm does not change with respect to the formation of the percolating network. On the other hand, GNPs of 5 μm and 25 μm demonstrate notable changes in their morphologies obtaining nearly densified structural forms above the percolation transitions (Table 7.1) (Figure 7.6).

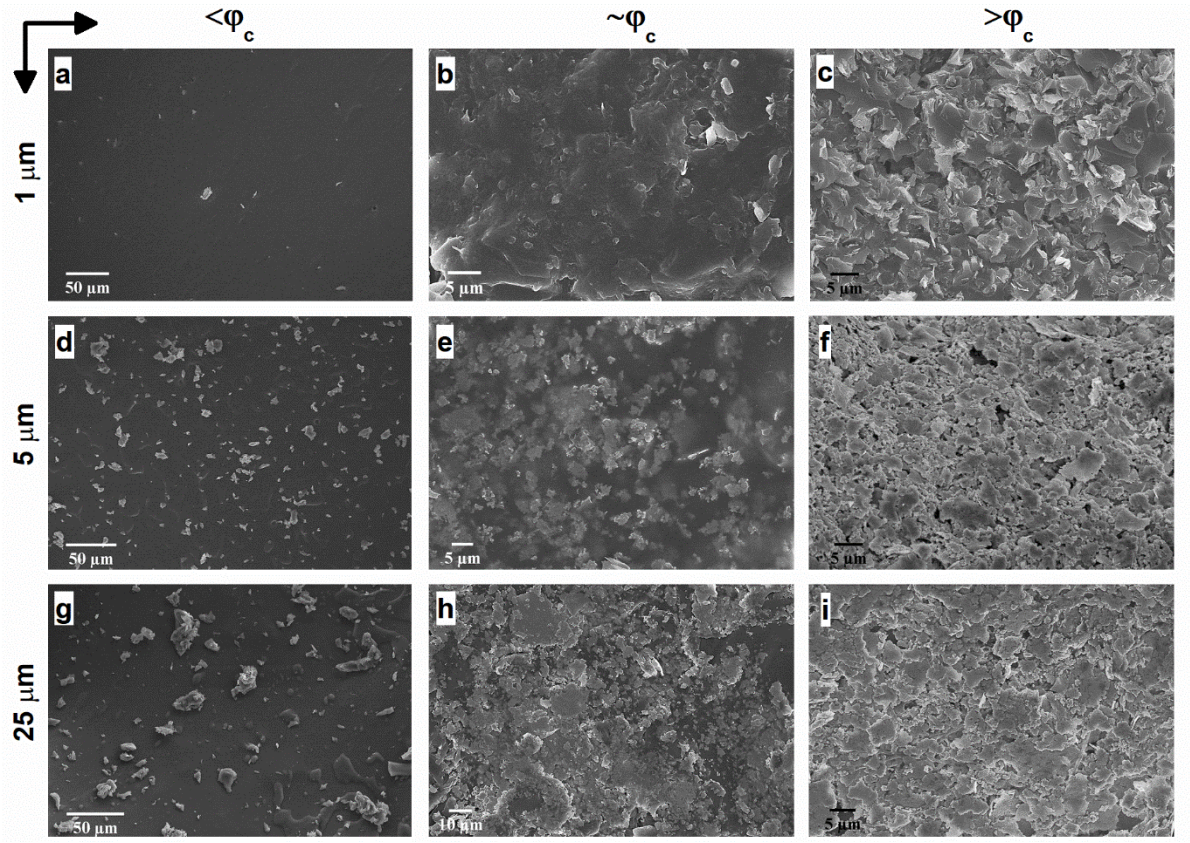

Figure 7.5 Scanning electron microscopy (SEM) images of the ATSP-GNP nanocomposites highlighting differences in surface morphologies and nanoparticle distributions for the GNPs of 1 μm (a, b, c), 5 μm (d, e, f) and 25 μm (g, h, i) below percolation ($<\varphi_c$), around percolation ($\sim\varphi_c$), and above percolation ($>\varphi_c$) thresholds. For GNP 1 μm, $<\varphi_c$, $\sim\varphi_c$, $>\varphi_c$ correspond to 1 wt %, 5 wt %, and 10 wt %, respectively. For GNP 5 μm, $<\varphi_c$, $\sim\varphi_c$, $>\varphi_c$ correspond to 1 wt %, 4 wt %, and 10 wt %, respectively. For GNP 25 μm, $<\varphi_c$, $\sim\varphi_c$, $>\varphi_c$ correspond to 1 wt %, 3 wt %, and 10 wt %, respectively.

Table 7.1 Density of ATSP-GNP foam morphology nanocomposites with respect to the size and content of the nanofiller particles. The density is given in Mg/m^3. The neat ATSP foam has a density of 0.54 Mg/m^3. The density of fully dense ATSP is 1.27 Mg/m^3. Corresponding loading fractions are given in the text.

	1 μm	**5 μm**	**25 μm**
$<\varphi_c$	0.51±0.05	0.45±0.09	0.46±0.04
$\sim\varphi_c$	0.46±0.07	0.58±0.03	0.56±0.15
$>\varphi_c$	0.52±0.01	0.70±0.04	0.65±0.02

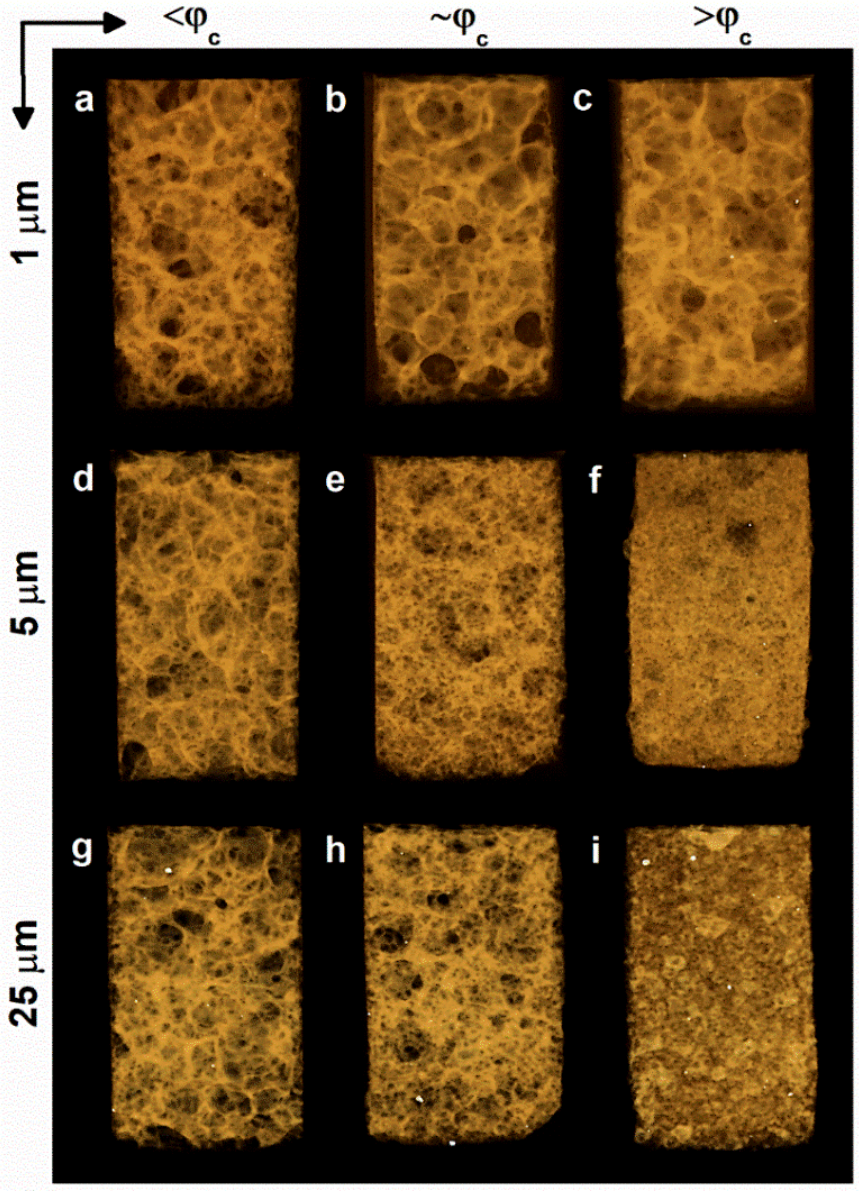

Figure 7.6 Micro-Computed Tomography (Micro-CT) images of the ATSP nanocomposites demonstrating variations in the porous morphology with respect to the size of 1 μm (a), 5 μm (b), and 25 μm (c) and content ($<\varphi_c$, $\sim\varphi_c$, $>\varphi_c$) of the nanofiller particles. Corresponding loading fractions are given in the above text.

To investigate the chemical basis that causes the structural modifications with the increased GNP contents, we analyzed the thermal characteristics of the in situ endothermic condensation polymerization reaction at the percolation-determined loading levels. The combined mixtures of the precursor oligomers with the GNPs are subjected to a temperature-ramp differential scanning calorimetry (DSC) cycle at a 10 °C/min constant heating rate. The obtained thermal profiles of the GNP combined mixtures are then compared to that of the neat mixture of the constituent oligomers [25]. In Figure 7.7, we compare only the above-percolation GNP content to the parent material to highlight the thermochemical changes that are effective for other GNP sizes. As shown in Figure 7.7, at the beginning of the heating processes, the heat flux curve of the GNP combined mixture likewise reveals a dimple around 70 °C denoting structural softening of the constituent oligomers, which is similarly observed in the base formulation [25]. Afterwards, especially for GNP 1μm, the thermal profile maintains similarly endothermic patterns akin to the neat mixture during which melting and polycondensation reaction stages accordingly take place. However, both GNP 5μm and GNP 25μm reveal significant heat uptakes into the molten oligomer domain, which are particularly observed for the above-percolation loading levels ($>\varphi_c$). Such abrupt behaviors are related to acetic acid discharge-driven bubble growth during the condensation reaction that is greatly affected by the presence of the carbon fillers [38]. Following this stage, the cure process initiates (denoted as cure onset) around at 260 °C for the parent form in which the thermal curve displays a genuine endothermic cure region [25]. For GNP 1μm, only the $>\varphi_c$ loading level exhibits a distinctly broader cure region than the neat oligomers for which the completion of the cure process extends beyond 350 °C. In addition, upon completion of the cure process, a thermal relaxation peak, a small hump (denoted as cure end, indicated with an arrow) is observed. Likewise, for both GNP 5μm and GNP 25μm, similar

broadening of the cure domains as well as the peak formations are observed at above-percolation loading levels. The broadening of the cure region is likely to occur due to increased melt viscosity of the oligomers caused by the presence of the nanofillers that required more energy input to carry out the crosslinking process, which could subsequently stimulate an early gelation of the crosslinked matrix [39]. Also, the reactive functional groups of the oligomers graft onto carbon nanofillers that can alter viscous characteristics of the molten domain during curing [40]. The thermal relaxation peaks form due to devitrification of the matrix in the thermal process during which the glass transition temperature increased above the cure temperature [41].

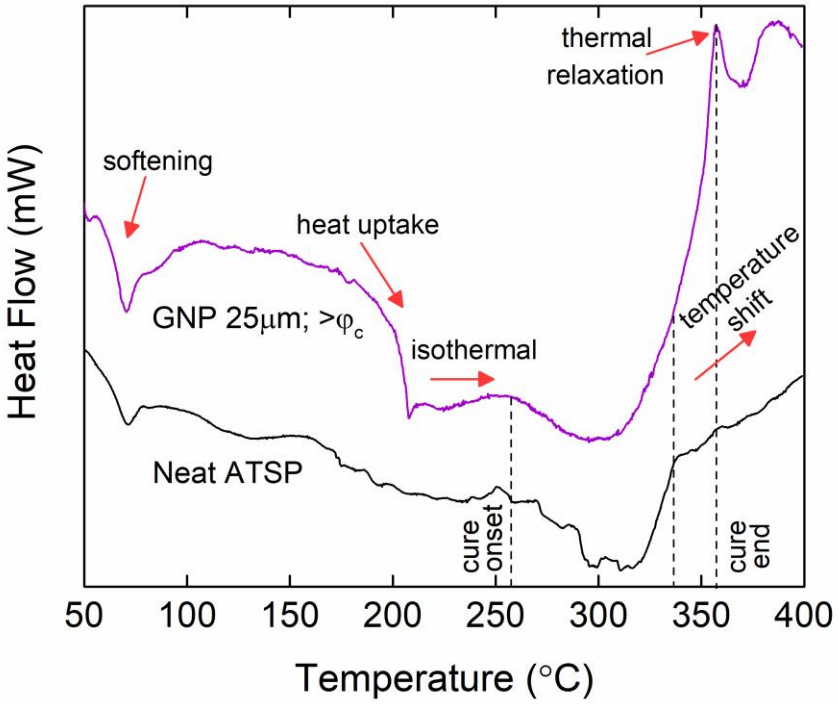

Figure 7.7 Differential scanning calorimetry (DSC) thermal characteristics of the condensation polymerization reaction for the neat mixture of the precursor oligomers and combined mixture of the oligomers with GNP 25 μm having $>\varphi_c$ loading level (10 wt %). DSC curves are arbitrarily shifted to highlight differences. Tests are performed under an inert atmosphere of nitrogen. The heating rate is 10 °C/min.

In addition, in Figure 7.8, we demonstrate solid-state Nuclear Magnetic Resonance (ssNMR) spectroscopy measurements performed on above-percolation GNP content in comparison to the

parent material to identify chemical modifications in the backbone chain configuration as well as manifesting the interfacial attachment scheme in the nanofiller incorporated matrix. ^{13}C cross-polarization magic-angle spinning (CPMAS) spectrum of the parent material (neat ATSP) display the two characteristic peak domains: the aromatic groups (C-C and C-H) and the functional side groups (C-O and C=O), with a line width of ~860 Hz over the highest intensity peak (~130 ppm) (^{13}C NMR spectra are processed using 25 Hz line broadening). ^{1}H direct pulse magic-angle spinning (DPMAS) NMR spectrum of the neat ATSP shows a single characteristic having a line width of ~1640 Hz (^{1}H NMR spectra are processed using 1 Hz line broadening). Based on these NMR analyses, we observe that both ^{1}H and ^{13}C spectra of the nanocomposites with GNPs 5 μm and 25 μm (Figure 7.8) reveal clearly broadened characteristic peaks with respect to the neat parent matrix. Whereas GNP 1 μm display characteristic peaks similar to the base ATSP, yet decreased line widths with respect to increased GNP content may indicate only moderate interactions with the matrix. For GNPs 5 μm and 25 μm, such peak broadening is formed due to strong interfacial coupling between the GNP particles and ATSP backbone chain, which then modifies the structural relaxation behavior of the nanocomposite matrix [42, 43]. In particular, the attachment scheme incurs an electron mobility difference due to individually dissimilar relaxation times of highly conductive GNP particles and highly dielectric ATSP matrix. More importantly, we do not observe any characteristic peaks in ^{13}C spectra coming from the matrix of GNP 5 μm at above-percolation loading level. As well, ^{13}C spectrum of the GNP 25 μm for $>\varphi_c$ form a single slightly broader peak associated with only the aromatic group of the backbone configuration (Figure 7.8). Hence, the presence of larger GNP particles alter polymerization process at a significant extent, as also justified with the above-mentioned results.

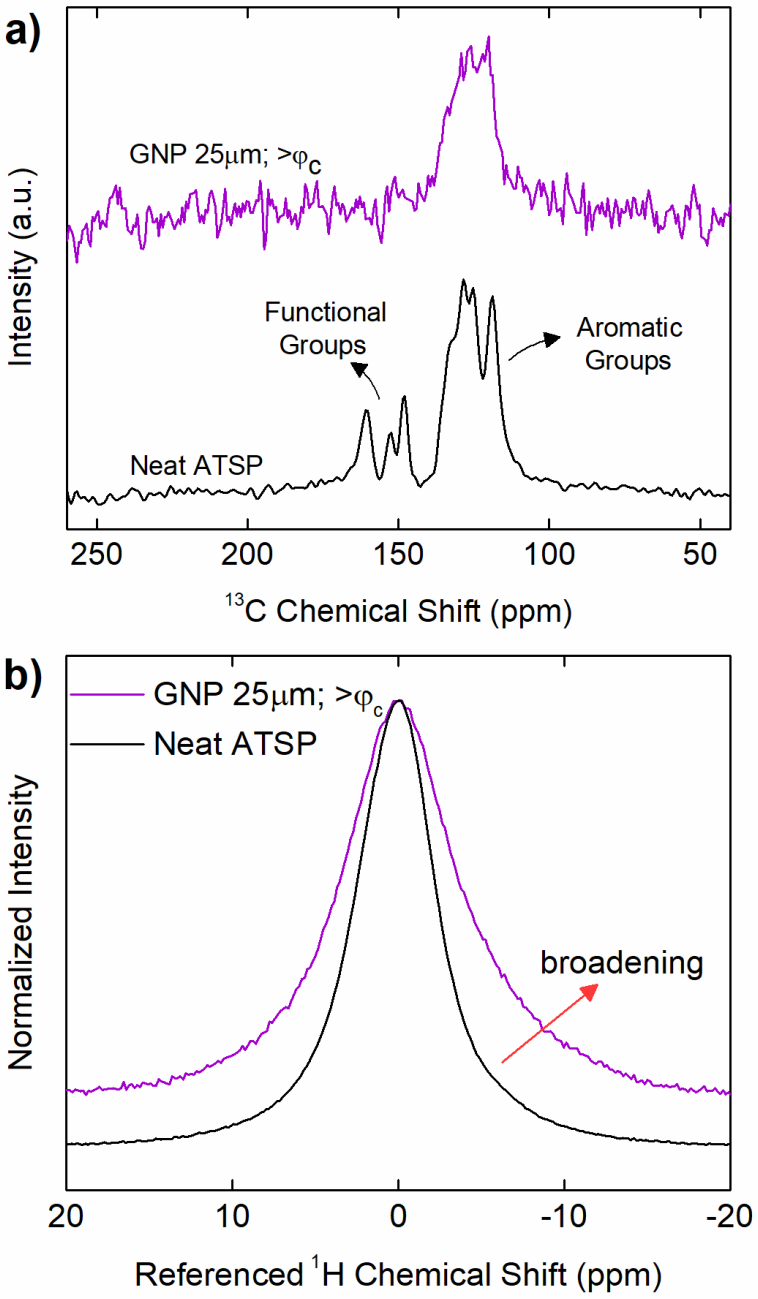

Figure 7.8 Solid-state Nuclear Magnetic Resonance (ssNMR) ^{13}C cross-polarization magic-angle spinning (CPMAS) (a) and ^{1}H direct pulse magic-angle spinning (DPMAS) (b) spectra of the neat ATSP morphology with respect to ATSP nanocomposites with GNP 25 μm having $>\varphi_c$ loading level (10 wt %). ^{1}H and ^{13}C NMR spectra are processed using 1 Hz and 25 Hz line broadenings, respectively. The figures were given in normalized intensity axes.

Based on the characterization results presented here, we understand that due to the interfacial attachment mechanism coming into effect during the polymerization reaction, a fraction of the functional groups of the oligomer structures are reacted with the GNP particles (especially 5 μm and 25 μm), which consequently reduces the fraction of the functional groups that participate in the ordinary crosslinking polymerization process. Indeed, the GNP-coupled configurations of the oligomers prompt an early gelation point during the polymerization reaction without necessitating completion of the crosslinking process. As a consequence of the gelation, the DSC profiles of 5 μm and 25 μm with loadings near and above their percolation thresholds display nearly flat regions following the sudden heat uptakes until cure onset. Under such a circumstance, the modified polymerization process does not solely perform the esterification reaction, which conjugates the two oligomer groups releasing acetic acid by product. This reduces the foaming agent released during the cure process, rendering higher density morphologies as observed in GNP 5 μm and 25 μm above percolation transitions. In this context, the temperature-wise broadening characteristic observed in the cure regions indicates that the advancing crosslinking resin requires more heat input to activate unreacted bonds to complete the cure process. Due to the effect of such an interfacial entanglement mechanism, glass transition characteristics of similar polymer nanocomposites are demonstrated to be modified displaying significant temperature shifts[13]. Hence, in this case, the glass transition temperature (~191 °C) may positively shift to a higher temperature in the cure region such that the polymer chains display the glass transition relaxation while the isothermal cure process is still in progress [25]. Therefore, the peak formation at cure end point takes places due to devitrification (phase transformation from glassy state to rubbery state upon the glass transition) of the polymer network. Note that the vitrification induces slower cure rates wherein the cure reaction becomes

more diffusion controlled rather than kinetic controlled, which also correlates to the cure region temperature broadening [44]. Characterization of rheological properties of the nanofiller incorporated ATSP resin during the in situ polymerization reaction will be the subject of a follow-up study.

7.4 Conclusion

We present the physicochemical characteristic effects influenced by the GNPs of different sizes on the polycondensation reaction of the ATSP resin via the formation of electrically conductive percolating network. During the polymerization process, carboxylic acid and acetoxy-capped precursor oligomers, combined with the GNPs, form the crosslinked aromatic backbone of the ATSP matrix while the nanofillers interact with the reactive caps of the oligomers, and combine with the crosslinked polymer network. The varied GNP size causes different electrical percolation thresholds and ultimate electrical conductivities. Microstructural characterization display the GNP distributions in the matrix as well as morphological modifications formed through the conductive percolating networks. Cure characteristics reveal the thermochemical changes occurred on the polymerization processes. ssNMR spectroscopies on the ATSP nanocomposite morphology exhibit the formation of a robust interfacial coupling mechanism between the GNPs and ATSP backbone.

7.5 References

[1] J. C. Williams and E. A. Starke, Acta Materialia, 2003, 51, 5775-5799.

[2] T. M. Pollock, Science, 2010, 328, 986-987.

[3] J. Hirsch, Materials Transactions, 2011, 52, 818-824.

[4] M. Telford, Materials Today, 2004, 7, 36-43.

[5] M. Bakir, J. L. Meyer, J. Economy and I. Jasiuk, Polymer, 2017, 123, 311-320.

[6] P. Podsiadlo, A. K. Kaushik, E. M. Arruda, A. M. Waas, B. S. Shim, J. Xu, H. Nandivada, B. G. Pumplin, J. Lahann, A. Ramamoorthy and N. A. Kotov, Science, 2007, 318, 80-83.

[7] J. Jordan, K. I. Jacob, R. Tannenbaum, M. A. Sharaf and I. Jasiuk, Materials Science and Engineering: A, 2005, 393, 1-11.

[8] M. Moniruzzaman and K. I. Winey, Macromolecules, 2006, 39, 5194-5205.

[9] V. Yudin, J. U. Otaigbe, V. Svetlichnyi, E. Korytkova, O. Almjasheva and V. Gusarov, XPRESS Polymer Letters, 2008, 2, 485-493.

[10] J. Liang, Y. Huang, L. Zhang, Y. Wang, Y. Ma, T. Guo and Y. Chen, Advanced Functional Materials, 2009, 19, 2297-2302.

[11] H. Kim, A. A. Abdala and C. W. Macosko, Macromolecules, 2010, 43, 6515.

[12] J. R. Potts, S. H. Lee, T. M. Alam, J. An, M. D. Stoller, R. D. Piner and R. S. Ruoff, Carbon, 2011, 49, 2615-2623.

[13] K.-H. Liao, S. Aoyama, A. A. Abdala and C. Macosko, Macromolecules, 2014, 47, 8311-8319.

[14] H. Wu, G. Yu, L. Pan, N. Liu, M. T. McDowell, Z. Bao and Y. Cui, Nature communications, 2013, 4, 1943.

[15] G. Shi, M. Rouabhia, Z. Wang, L. H. Dao and Z. Zhang, Biomaterials, 2004, 25, 2477-2488.

[16] P. Karimi, M. Ostoja-Starzewski and I. Jasiuk, Journal of Applied Physics, 2016, 120, 145103.

[17] S. Kale, F. A. Sabet, I. Jasiuk and M. Ostoja-Starzewski, Journal of Applied Physics, 2015, 118, 154306.

[18] W. Zheng, S.-C. Wong and H.-J. Sue, Polymer, 2002, 43, 6767-6773.

[19] A. Shalwan and B. Yousif, Materials & Design, 2014, 59, 264-273.

[20] W. Bauhofer and J. Z. Kovacs, Composites Science and Technology, 2009, 69, 1486-1498.

[21] Z. Spitalsky, D. Tasis, K. Papagelis and C. Galiotis, Progress in Polymer Science, 2010, 35, 357-401.

[22] P. Pötschke, T. Fornes and D. Paul, Polymer, 2002, 43, 3247-3255.

[23] D. Frich, K. Goranov, L. Schneggenburger and J. Economy, Macromolecules, 1996, 29, 7734-7739.

[24] B. Vaezian, J. L. Meyer and J. Economy, Polymers for Advanced Technologies, 2016, 27, 1006-1013.

[25] M. Bakir, J. L. Meyer, J. Economy and I. Jasiuk, Macromolecules, 2016, 49, 6489-6496.

[26] P. A. Couperus, A. D. H. Clague and J. P. C. M. van Dongen, Organic Magnetic Resonance, 1978, 11, 590-597.

[27] W. Bubb, C. Fallick and S. Sternhell, Magnetic Resonance in Chemistry, 1977, 9, 167-174.

[28] F. Wang, L. T. Drzal, Y. Qin and Z. Huang, Journal of Materials Science, 2015, 50, 1082-1093.

[29] J. Xiang and L. T. Drzal, Polymer, 2012, 53, 4202-4210.

[30] J. A. King, F. A. Morrison, J. M. Keith, M. G. Miller, R. C. Smith, M. Cruz, A. M. Neuhalfen and R. L. Barton, Journal of Applied Polymer Science, 2006, 101, 2680-2688.

[31] J. B. Bai and A. Allaoui, Composites Part A: Applied Science and Manufacturing, 2003, 34, 689-694.

[32] J. T. Choi, D. H. Kim, K. S. Ryu, H.-i. Lee, H. M. Jeong, C. M. Shin, J. H. Kim and B. K. Kim, Macromolecular Research, 2011, 19, 809-814.

[33] S. Kale, F. A. Sabet, I. Jasiuk and M. Ostoja-Starzewski, Journal of Applied Physics, 2016, 120, 045105.

[34] A. Aharony and D. Stauffer, Introduction to percolation theory, Taylor & Francis, 2003.

[35] R. H. J. Otten and P. v. d. Schoot, The Journal of Chemical Physics, 2011, 134, 094902.

[36] K. Nagata, H. Iwabuki and H. Nigo, Composite Interfaces, 1998, 6, 483-495.

[37] A. V. Kyrylyuk and P. van der Schoot, Proceedings of the National Academy of Sciences, 2008, 105, 8221-8226.

[38] P. Pötschke, T. D. Fornes and D. R. Paul, Polymer, 2002, 43, 3247-3255.

[39] C.-Y. M. Tung and P. J. Dynes, Journal of Applied Polymer Science, 1982, 27, 569-574.

[40] S. Li, M. Xiao, D. Wei, H. Xiao, F. Hu and A. Zheng, Polymer, 2009, 50, 6121-6128.

[41] I. Fraga, S. Montserrat and J. M. Hutchinson, Macromolecular Chemistry and Physics, 2008, 209, 2003-2011.

[42] J. Chen, H. Liu, W. A. Weimer, M. D. Halls, D. H. Waldeck and G. C. Walker, Journal of the American Chemical Society, 2002, 124, 9034-9035.

[43] A. D. Bain, D. R. Eaton, A. E. Hamielec, M. Mlekuz and B. G. Sayer, Macromolecules, 1989, 22, 3561-3564.

[44] M. Kamal and S. Sourour, Polymer Engineering & Science, 1973, 13, 59-64.

CHAPTER 8: INTERFACIAL LIQUID CRYSTALLINE MESOPHASE DOMAIN ON CARBON NANOFILLERS IN AROMATIC THERMOSETTING COPOLYESTER MATRIX

8.1 Introduction

Liquid crystallinity is a state of condensed matter displaying characteristics associated with both solids and liquids; liquid crystals possess mesomorphic structures with ordered arrangement and fluidity [1]. Achieving formation of such mesophase domains is contingent on the presence of rigid anisotropic mesogenic moieties which are usually composed of phenyl and biphenyl groups [2-4] Polymer chains can accommodate the mesogen units via two main mechanisms: being either incorporated into backbone chains or conjugated with dangling side chains [3,4] Flexible and conformable moieties of the mesogens essentially modulate molecular level orientation of chains – mesogenicity – which develops the LC morphology [5,6].

This work was previously published: Bakir, M., Elhebeary, M., Meyer, J.L., Sutrisno, A., Economy, J., and Jasiuk, I., Interfacial liquid crystalline mesophase domain on carbon nanofillers in aromatic thermosetting copolyester matrix, Journal of Applied Polymer Science, 135, 46584 (2018).

Special thanks to Mohamed Elhebeary (Department of Mechanical Science and Engineering, University of Illinois) for performing SEM imaging.

Particularly, thermotropic liquid crystal phases contain homogenous rod-like calamitic mesogens for which the LC morphology can only appear within a particular temperature range: between the melting temperature of the crystalline matrix and the clearing temperature of the isotropic amorphous liquid. Hence, thermotropic LC morphology is uniquely distinguishable by scattering of polarized light by the ordered arrangement of the mesogens, while the isotropic form exhibits absolute opacity in cross-polarized light microscopy [1,3,7].

Motivated by structural applications for the development of high-performance polymer matrix composites, the liquid crystalline polymers (LCPs) have drawn considerable attention due to their unique interfacial compatibility with conventionally used carbonaceous reinforcements. For instance, p-acetoxybenzoic acid/diacetoxy hydroquinone based thermotropic LCP developed covalently bonded and self-oriented LC mesophase domain around carbon fibers [8,9]. Also, phenyl ester containing inherently amorphous ATSP formed surface-induced LC mesophase on carbon fiber surface [2,10]. Note that these two resin systems could effectively maintain the LC morphologies in the cured state at room temperature. Regarding the studies with nanofillers, azobenzene containing LCP promoted preferentially ordered LC domain around carbon nanotubes [11] Another work reported phenylene group incorporated LCP with the GNPs showing that Young's modulus and DC electrical conductivity of nanocomposites significantly improved with fairly low nanofiller content [12] Also, LC epoxy with graphene oxide (GO) nanoparticles demonstrated improved thermal degradation stability and mechanical toughness along with an upshifted glass transition temperature [13] Likewise, GOs exhibited a strong interaction with azido functionalized thermotropic LCP which enhanced bulk thermophysical properties in nanocomposite structures [14] These efforts mainly employed inherently liquid crystalline morphology polymer systems that accordingly demonstrated macroscopic physical

property improvements with the incorporation of nanofiller particles. However, no prior study has investigated an amorphous polymer configuration that develops a surface functionality with nanofiller particles via the formation of an interfacial liquid crystalline domain. Therefore, through such a unique physicochemical condition, thermally induced phase transition characteristics of liquid crystalline mesophase structure, as well as nanoparticle-polymer chain interfacial bonding mechanism and polymer chain relaxation characteristics of nanocomposite structures, can be systematically studied.

In this paper, we demonstrate the formation and characterization of the LC mesophase interlayer domain which developed conformal to GNP nanoparticles within a highly crosslinked and inherently amorphous ATSP matrix [15-18]. Employing an environmental scanning electron microscope (ESEM) equipped with a temperature-controlled heating stage, a precursor oligomers-GNP base mixture was initially thermally cured on-site under a nitrogen atmosphere. Upon cooling down to room temperature, an LC interlayer contour formed, encapsulating a matrix-embedded GNP particle aggregation site while exclusively replicating edge pattern of the carbonaceous nanostructure. Application of a temperature-ramp heating cycle caused the LC domain to gradually vanish at elevated temperatures above the glass transition temperature of the surrounding matrix. Upon a successive cooling cycle, the LC phase domain restored its initial ordered morphology in which the LC mesogenicity demonstrated a reversible thermophysical phase transition characteristic. Cross-polarized light illuminations also supported the presence of the LC morphology over the GNP-ATSP interface. ssNMR spectroscopy results exhibited a strong interfacial bonding mechanism between the GNPs and ATSP backbone chains. Glass transition of the nanocomposites marginally increased, induced by the LC interlayer and interfacial attachment mechanisms.

8.2 Materials and Methods

Carboxylic acid-capped (C1) and acetoxy-capped (A1) oligomers were used to produce highly crosslinked and amorphous aromatic thermosetting copolyester resin. The constituent oligomers were synthesized using trimesic acid (TMA), isophthalic acid (IPA), 4-acetoxybenzoic acid (ABA) and hydroquinone diphthalic anhydride (HQDA) (Sigma-Aldrich Co.) via melt-oligomerization method at molar feed ratios of 2:3:6:4 and 2:2:2:7 of TMA:IPA:ABA:HQDA for C1 and A1, respectively. The base solution mixture for the hot-stage assisted environmental scanning electron microscopy (ESEM) experiments was prepared via mixing the carboxylic acid and acetoxy functional group oligomers at a 1.1:1 weight ratio. The oligomer mixture (C1A1) was initially dissolved in N-Methyl-2-pyrrolidone (NMP) solution at a 0.25 g/mL concentration. Then, GNP particles (Grade M-5, XG Sciences, Inc.) (diameter: ~5 μm, thickness: 6-8 nm, density: 2200 kg/m^3) were incorporated into the C1A1-NMP solution. The highly viscous C1A1-GNP solution was rested on aluminum foil placed in a magnesium oxide heating crucible of the ESEM hot stage, wherein *in situ* chemical reaction and thermal curing was performed under nitrogen environment. For the NMR and the DMA analyses, foam morphology ATSP nanocomposites were obtained via a condensation polymerization reaction between carboxylic acid and acetoxy functional group oligomers, which generated a crosslinked aromatic polyester backbone and emitted acetic acid as a reaction by-product. The carboxylic acid (C1) and acetoxy-capped (A1) oligomers (at 1.1:1 weight ratio) were solid-state mixed with the GNP nanofillers of 1 wt.% and 5 wt.% at room temperature. The specimen without the addition of the GNP was named neat ATSP. The C1A1-GNP mixtures were subjected to a thermal cure cycle, which comprised of two dwell stages at 202 °C for 90 minutes and 270 °C for 150 minutes, which corresponded to relaxation/melting of the constituent oligomers and nucleation/bubble

growth through the release of the acetic acid, respectively. Additionally, the thermal cycle had a final cure stage at 330°C for 90 minutes.[1] The base solution mixture used in the cross-polarized optical microscope imaging experiment was cured on glass slides by applying the cure cycle.

In-situ thermal characterization inside the environmental scanning electron microscopy (Quanta 450 ESEM FEG) chamber was performed using a heating stage setup placed in a nitrogen gas environment at 1.45 Torr. The heating/cooling cycles were operated at a 5°C/min heating rate. The images were obtained at 30 kV operation voltage in the high-resolution upper detector.

Optical microscopy images were obtained using a bright-field inverted optical microscope in transmission mode having cross-polarizers set to 0° (without cross-polarizer) and 90° (with cross-polarizers) polarization angles at different magnifications (Zeiss Jenavart).

Solid-state Nuclear Magnetic Resonance (ssNMR) spectroscopy measurements were carried out using ground nanocomposite specimens (~45-50 mg) packed into NMR rotors (on a Varian Unity Inova 300 MHz spectrometer). ^{1}H and ^{13}C spectra were obtained using direct pulse (DP) and cross-polarized (CP) excitations, respectively. Specimens were spun at 10 kHz. Data analysis was performed using the MestreNova software.

Glass transition characterization of the nanocomposites was carried out using Dynamic Mechanical Analysis with a dual-cantilever beam (DCB) bending clamp fixture (Q800 TA Instruments). A temperature-ramp cycle was operated with a 3°C/min heating rate. Specimens were in 35 x 10 x 5 mm^3 (length x width x thickness). The tests were performed in the air.

8.3 Results and Discussion

First, we discuss the formation process of the LC mesophase domain at the GNP particle and ATSP matrix interface. Following thermal polymerization and successive cooling cycles

applied to the base mixture, an interlayer domain emerged entirely enclosing a matrix-embedded GNP particle aggregate site over the basal plane of the GNP structure (Figure 8.1.a). The domain lay within a few microns outside of the GNP agglomeration site while being discerned through a sharp contrast to the brighter surrounding matrix with different electronic properties. Uniquely, the LC phase contour precisely mimicked the tortuous outline of the GNP aggregate region, which emphasizes the presence of a local surface induced orientation mechanism [19]. Additionally, cross-polarized optical microscopy images revealed birefringence patterns emanating from the GNP site over the interface region (Figure 8.1.b). Hence, the ATSP resin effectively produced preferentially oriented LC mesophase domain around the GNP particles upon curing. This observation concurs with the prior findings on the carbon fiber reinforced ATSP matrix composites which exhibited similar refractive anisotropy on the fiber surface arising from the presence of the LC mesophase [2]. As well, several other LC melts developed intrinsic orientational configurations likewise through interactions with the carbon fibers [9,20] The presence of structural defect sites or reactive functional groups presented on the carbon fiber surface were conceived to stimulate such alignment mechanism within the LC network [8,21,22]. Hence, the development of the LC network within the ATSP matrix occurred not only through the physical presence of the GNPs but also through interfacial interactions with reactive oxygen-containing functional groups on the GNPs. X-ray photoelectron spectroscopy (XPS) results on the GNPs illustrate that the inherently present oxygen-containing functional groups are approximately 3 at %. Thus, the *in situ* polymerization reaction enabled the reactive carboxylic acid and acetoxy functional groups of the constituent oligomers to interact with the oxygenated polar sites on the GNPs. Therefore, the nanoparticles subsequently attached to the advancing crosslinked network of the ATSP backbone chains during the curing process. Also, we highlight

that the LC phase domain was only viable around the surrounding edge boundary of the GNP particle site within an amorphous morphology which indicated the presence of surface stabilized nematic mesogenicity.

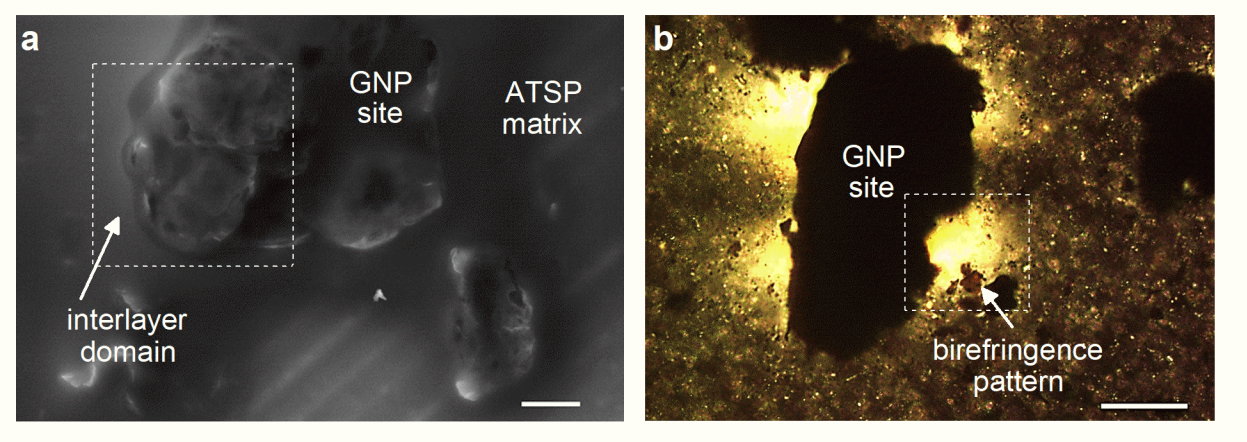

Figure 8.1 Scanning electron microscopy image of the interlayer LC mesophase domain (darker) around a GNP particle aggregation site in the amorphous ATSP matrix (brighter) (a). Cross-polarized optical microscopy image of the birefringence patterns (brighter) radiating from an individual GNP particle site (darker) (b). The scanning electron microscope image was obtained under an inert atmosphere of nitrogen. Both images were obtained at room temperature. The scale bars are 20 μm.

The aromatic polyesters are among well-known thermotropic LCPs [23]. Referring to the previous argument on the thermotropic liquid crystals having a temperature-dependent transient mesomorphic state, we performed subsequent heating/cooling cycles on the cured mixture to investigate thermophysical features of the LC domain. Figure 8.2 and 8.3 demonstrate scanning electron microscopy images obtained at distinct temperatures during a heating process. The LC contour remained intact and was likewise observable below the glass transition temperature of the matrix (~214°C). Beyond the glass transition temperature, the mesophase domain obtained an isotropic form which displayed a visual uniformity with the surrounding matrix. Particularly, the primary highly-ordered nematic LC domain acquired an amorphous structure with respect to the increased temperature, which eventually suppressed orientational effects within the mesogenic compounds. The crosslinked morphology of the ATSP matrix stimulated the phase transition in

such a way that significantly differs from the melting induced structural decomposition of the mesogenicity observed in the conventional LC thermoplastics. Essentially, the heating process promoted structural relaxation on the ATSP chains to a rubbery state through the glass transition mechanism. Thus, the orientational order of the mesogenic segments was disrupted mainly via the structural relaxation of the polymer chains. As also displayed in the corresponding figures, the LC region completely disappeared at the temperatures well above the glass transition. Hence, the LC mesophase domain around the carbonaceous site can modulate temperature-dependent chain relaxation dynamics of the host ATSP matrix within a wide temperature window until the glass transition point, as discussed later in the text.

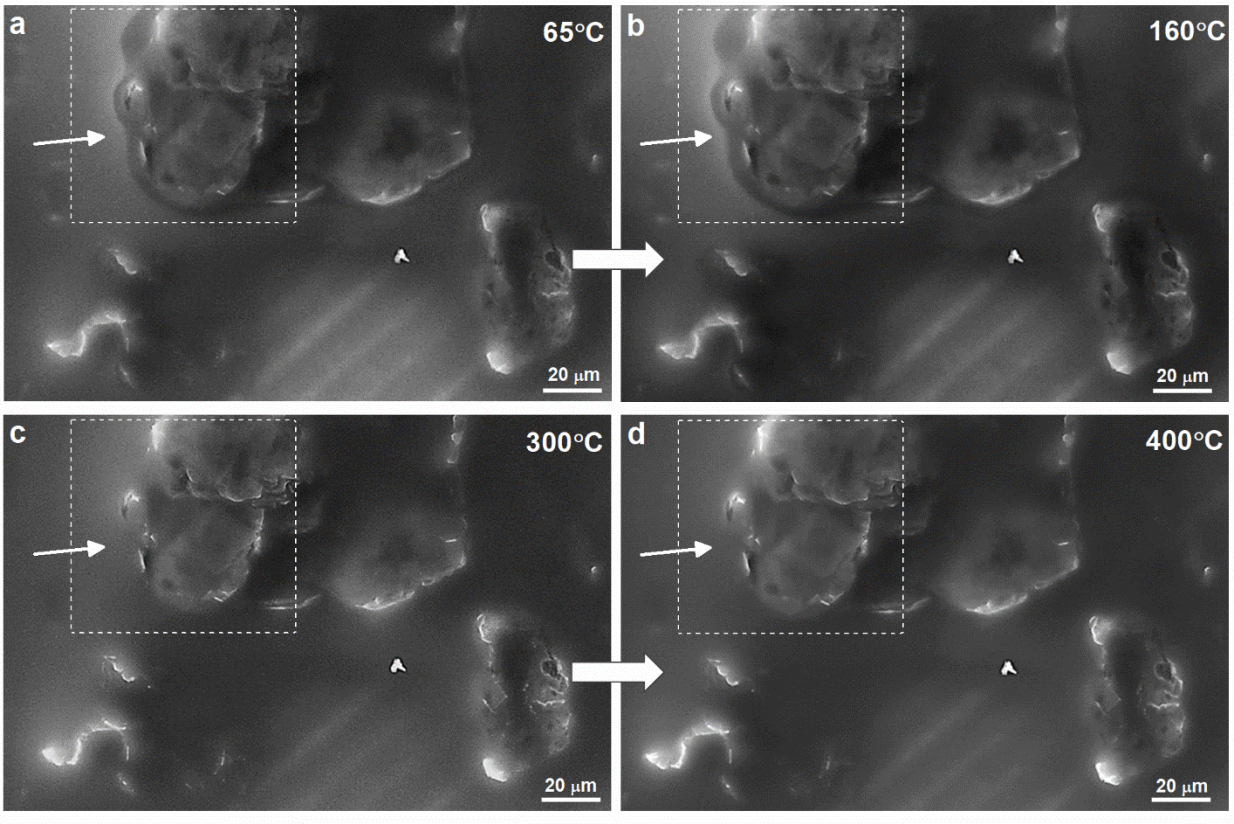

Figure 8.2 Scanning electron microscopy images of the LC mesophase around a GNP particle aggregation site showing the thermally induced transformation of the LC domain from a nematic mesophase (a, b) to an amorphous isotropic (c, d) morphology during a temperature-ramped heating process. The images were obtained under an inert atmosphere of nitrogen. The heating rate was 5°C/min.

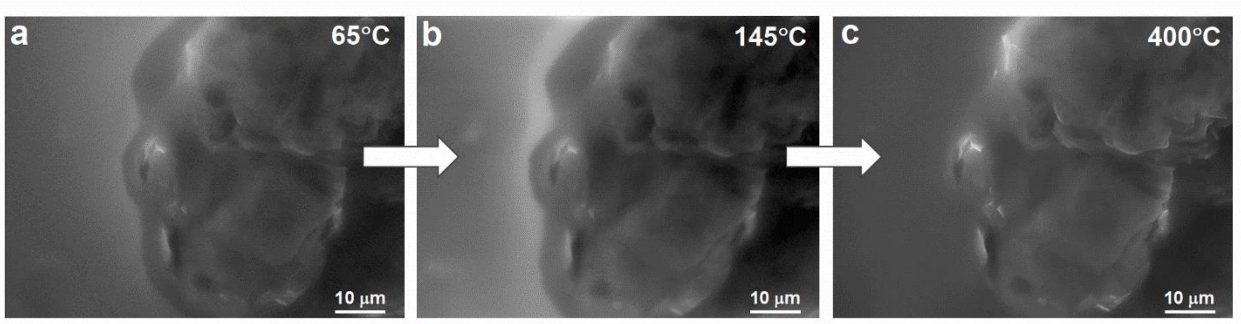

Figure 8.3 Scanning electron microscopy close-up images of the nematic to isotropic phase transformation of the LC domain. The images were obtained under an inert atmosphere of nitrogen (a-c).

The initial configuration of the mesogens within the LC interphase domain is restorable upon application of a cooling cycle [3]. As demonstrated in Figure 8.4, following a successive cooling process back to room temperature, the LC contour, which initially developed around the GNPs, completely recovered its original form, likewise mirroring the geometrical outline of the GNP site. Essentially, the reduced temperature enabled the backbone chains to reorient along with the mesogen molecules facilitated through conformity and flexibility of the aromatic chains. In fact, this observation illustrates another important factor coming into effect in this process: the ATSP backbone chains covalently conjugated to the GNPs. The thermophysical recovery of the original pattern indicated that the *in situ* formed oxygen bonds remained thermally stable and physically intact at such elevated temperatures. Hence, the combination of these two major mechanisms successfully enabled thermophysical reversibility of the mesogenic network. As well, the structural recovery gradually progressed during this process, as inferred by partial recovery of the LC zone at the intermediary temperature step, as given in the corresponding figure. In the following section, we investigate the influence of the interfacial coupling mechanism on the physicochemical properties of the ATSP-GNP nanocomposites.

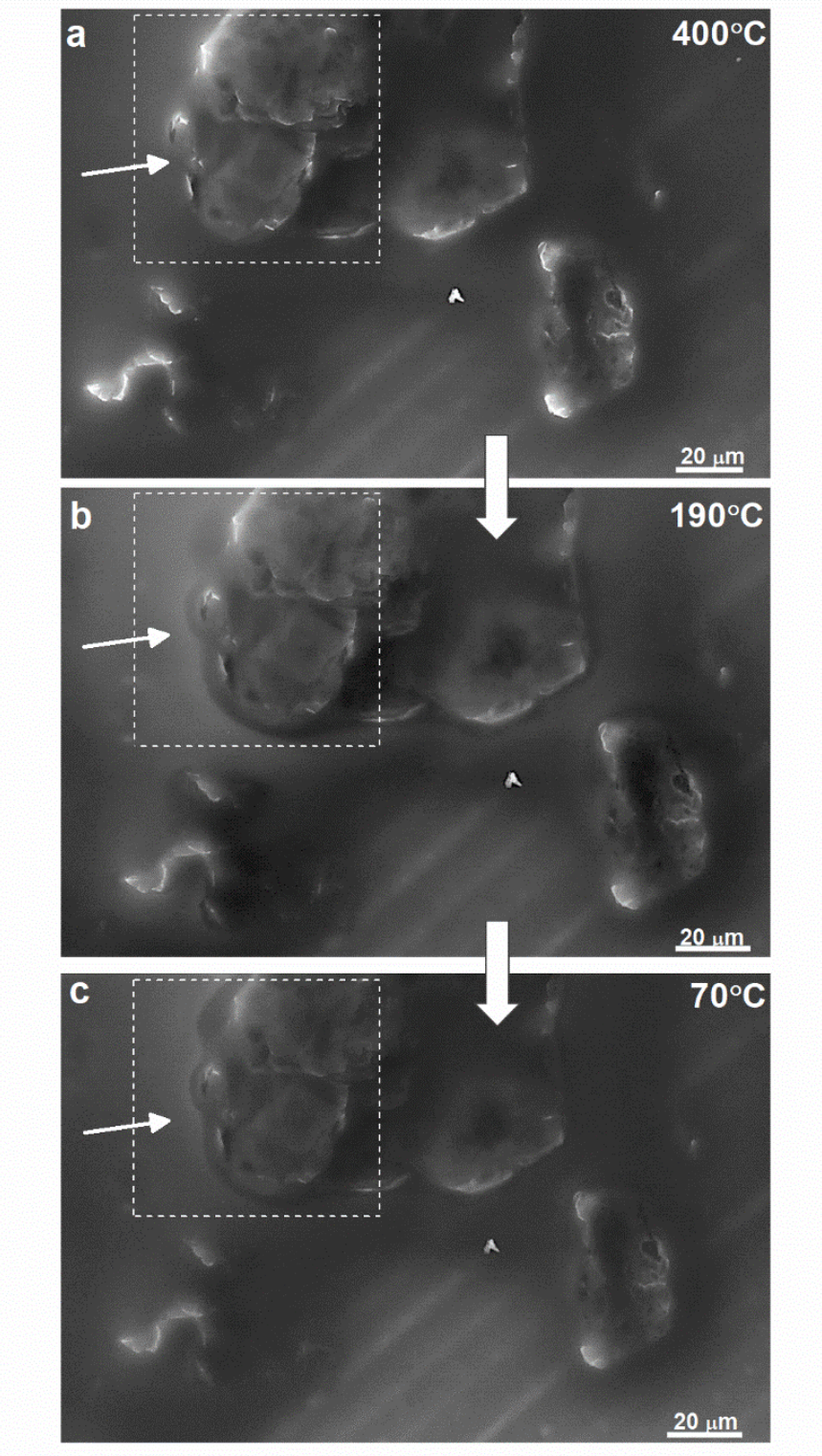

Figure 8.4 Scanning electron microscopy images of the interfacial LC mesophase around the GNP particle aggregate site showing complete structural recovery of the LC domain following a cooling process (a-c). The images were obtained under an inert atmosphere of nitrogen.

We carried out ssNMR spectroscopy measurements to interrogate the interfacial interaction mechanism between the GNPs and the ATSP backbone chains. Figure 8.5 demonstrates ^{1}H and ^{13}C ssNMR spectra of the 1 wt % (ATSP-1GNP) and 5 wt % GNP (ATSP-5GNP) incorporated nanocomposites in comparison to the neat ATSP matrix. In Figure 8.5.a, ^{1}H direct pulse magic-angle spinning (DPMAS) spectra revealed distinctly broadened characteristic peaks for the nanocomposites. The measured linewidths were ~1700 Hz, ~1865 Hz and ~2515 Hz for the neat ATSP, ATSP-1GNP, and ATSP-5GNP, respectively (^{1}H NMR spectra were processed using 1 Hz line broadening). We note that ^{1}H chemical shift peak meanwhile remained nearly constant concerning incremented GNP content. Also, ^{13}C cross-polarization magic-angle spinning (CPMAS) spectra, shown in Figure 8.5.b, illustrate that the neat ATSP displayed two characteristic peak domains which were assigned to be aromatic groups (C-C and C-H) and functional groups (C-O and C=O). ^{13}C spectra likewise exhibited increased linewidths for the nanocomposites concerning the parent material. The linewidths were measured to be ~618 Hz for the neat ATSP, ~650 Hz for ATSP-1GNP and ~806 Hz for ATSP-5GNP over the highest intensity peaks (~130 ppm) (^{13}C NMR spectra were processed using 25 Hz line broadening). The peak broadening effect in both the ^{1}H and the ^{13}C spectra was due to the strong interfacial attachment between the GNPs and the ATSP backbone chain [24]. Such a physicochemical attachment scheme through the LC interphase domain significantly altered the chain relaxation behavior of the backbone chains. In a similar context, intermolecular interactions within polymer systems were elsewhere reported to cause similar broadening effects [25]. Besides, neither the pristine GNPs exhibited characteristic peaks in the ^{13}C and ^{1}H spectra nor the nanocomposites displayed any additional peaks different than the reference spectra, which indicates an immediate interaction mechanism between the chains and the GNPs. Thus, the interfacial tethering of the

GNPs and the ATSP backbone through their particularly different relaxation times caused significant mobility difference within the chains which then resulted in broadening in the NMR characteristics of the nanocomposites [25].

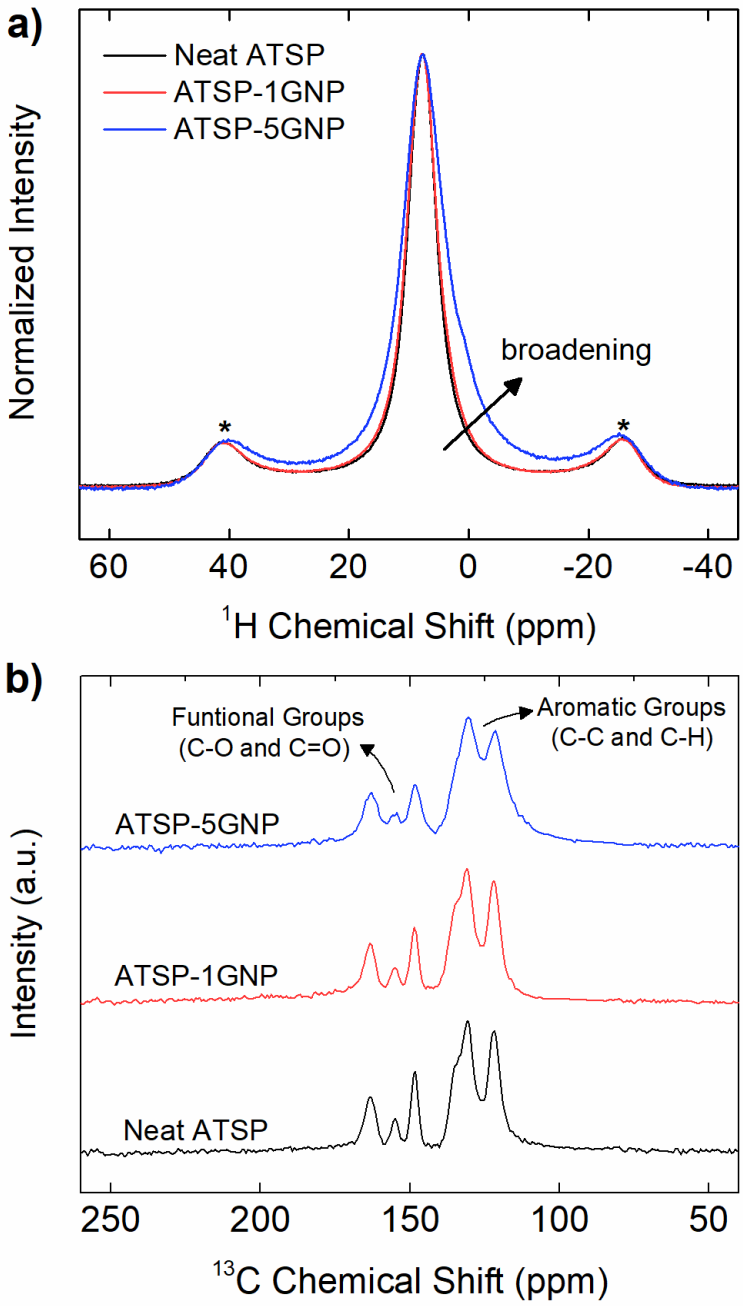

Figure 8.5 Solid-state Nuclear Magnetic Resonance ^{1}H direct pulse (DP) (a), and ^{13}C cross polarization (CP) spectra (b) of the ATSP-GNP nanocomposites and neat ATSP matrix. Asterisks denote spinning sidebands of the ^{1}H spectra.

Also, we studied glass transition characteristics of the ATSP-GNP nanocomposites. The glass transition temperature can reflect modifications in the backbone chain relaxation dynamics induced through interfacial attachment mechanisms. Figure 8.6 shows glass transition tangent delta (tan δ) peaks of the ATSP-GNP nanocomposites and neat ATSP obtained using dynamic mechanical analyzer (DMA). The parent material displayed a characteristic tan delta peak at ~214 °C, which corresponded to the glass transition (α-transition) temperature of the neat matrix. On the other hand, the nanocomposites showed glass transition temperatures of ~220 °C and ~227 °C for ATSP-1GNP and ATSP-5GNP, respectively. The corresponding increases in the glass transition temperature occurred due to the LC network being robustly attached to the GNPs. The present rigid-core mesogen units introduced an additional intermolecular stiffening while the backbone chains underwent structural relaxation during the phase transition. Hence, the LC interphase invoked restricted chain mobility within the cross-linked network of the ATSP matrix which resulted in upshifted glass transition temperatures [26]. Similarly, thermoplastic LC polymers were demonstrated to obtain increased melting temperatures likewise through LC mesogenicity induced chain modifications [3]. We highlight that the acetoxy and carboxylic acid-capped oligomers of ATSP and oxygen-containing functional groups of the GNPs develop an *in situ* molecular level attraction mechanism (the GNPs are not phobic to the oligomer melt). Such a scheme promotes initial interaction and interfacial tethering of the GNPs to the ATSP chains prior to the formation of the LC structure upon thermal curing.

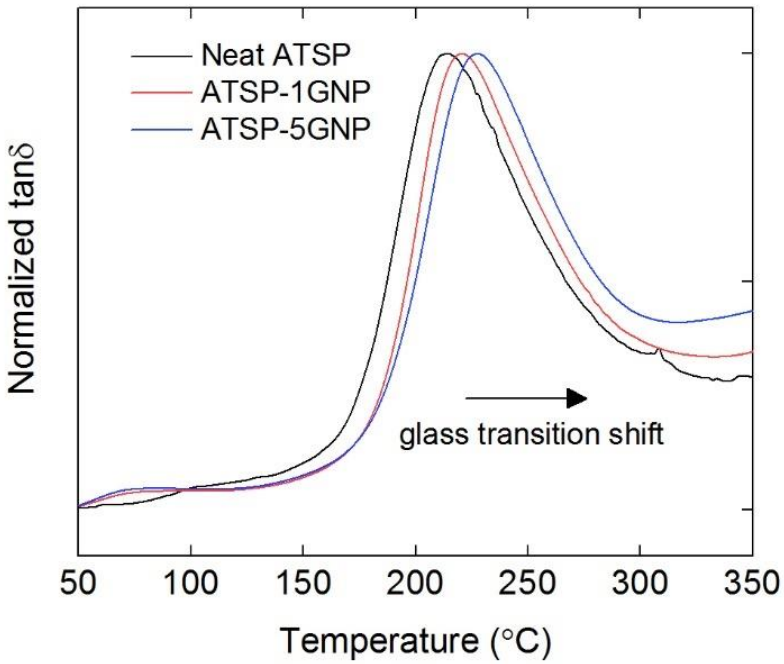

Figure 8.6 Dynamic mechanical analysis tangent delta (tan δ) profiles of the glass transition characteristics of the ATSP-GNP nanocomposites and neat ATSP matrix.

8.4 Conclusion

In conclusion, we demonstrated the *in situ* formed and cure-stable LC mesophase domain conformably surrounding ATSP matrix-embedded GNP nanoparticles. Micron-scale LC interlayer displayed a local preferential orientation closely mimicking the encapsulated geometry of the GNPs. The physical presence of the LC zone was thermally reversible; the mesophase can conveniently phase transform between the nematic and the isotropic states through successive heating and cooling processes. ssNMR spectroscopy analyses revealed conformal chain modifications induced by the *in situ* formed interfacial coupling of the LC domain with the GNPs, which also upshifted the glass transition temperature of the ATSP matrix. Having such a unique LC interlayer formed around the carbon nanofillers along with strong interfacial coupling could improve the thermomechanical performance of polymer nanocomposites through robust physicochemical properties of the nanofillers.

8.5 References

[1] Lagerwall, J. P.; Scalia, G., Current Applied Physics 12, 1387 2012.

[2] Parkar, Z., Design of unique composites based on aromatic thermosetting copolyesters; University of Illinois at Urbana-Champaign, 2011.

[3] Donald, A. M.; Windle, A. H.; Hanna, S., Liquid crystalline polymers; Cambridge University Press, 2006.

[4] Frich, D. J., The effect of interchain transesterification reactions on the development of aromatic copolyesters; University of Illinois at Urbana-Champaign, 1996.

[5] Jin, J. I.; Antoun, S.; Ober, C.; Lenz, R. W., British Polymer Journal 12, 132 1980.

[6] Cheng, X.; Liu, F.; Zeng, X.; Ungar, G.; Kain, J.; Diele, S.; Prehm, M.; Tschierske, C., Journal of the American Chemical Society 133, 7872 2011.

[7] Vertogen, G.; de Jeu, W. H., Thermotropic liquid crystals, fundamentals; Springer Science & Business Media, 2012.

[8] Bhama, S.; Stupp, S. I., Polymer Engineering & Science 30, 603 1990.

[9] Bhama, S.; Stupp, S. I., Polymer Engineering & Science 30, 228 1990.

[10] Economy, J.; Parkar, Z. In 100+ Years of Plastics. Leo Baekeland and Beyond; ACS Publications, 2011.

[11] Wang, W.; Sun, X.; Wu, W.; Peng, H.; Yu, Y., Angewandte Chemie International Edition 51, 4644 2012.

[12] Biswas, S.; Fukushima, H.; Drzal, L. T., Composites Part A: Applied Science and Manufacturing 42, 371 2011.

[13] Lu, S.; Li, S.; Yu, J.; Yuan, Z.; Qi, B., RSC Advances 3, 8915 2013.

[14] Jing, Y.; Tang, H.; Yu, G.; Wu, P., Polymer Chemistry 4, 2598 2013.

[15] Bakir, M.; Meyer, J. L.; Economy, J.; Jasiuk, I., Macromolecules 49, 6489 2016.

[16] Bakir, M.; Meyer, J. L.; Economy, J.; Jasiuk, I., Polymer 123, 311 2017.

[17] Frich, D.; Goranov, K.; Schneggenburger, L.; Economy, J., Macromolecules 29, 7734 1996.

[18] Vaezian, B.; Meyer, J. L.; Economy, J., Polymers for Advanced Technologies 27, 1006 2016.

[19] Bakir, M.; Meyer, J. L.; Hussainova, I.; Sutrisno, A.; Economy, J.; Jasiuk, I., Macromolecular Chemistry and Physics 218, 1700338 2017.

[20] Chung, T.; Gurion, Z.; Stamatoff, J., Polymer composites 6, 181 1985.

[21] Lee, J. Y.; Jang, J., Polymer Bulletin 59, 261 2007.

[22] Adams, P.; Mallon, J., Molecular Crystals and Liquid Crystals 208, 65 1991.

[23] Krigbaum, W. R.; Asrar, J.; Toriumi, H.; Ciferri, A.; Preston, J., Journal of Polymer Science: Polymer Letters Edition 20, 109 1982.

[24] Bakir, M.; Meyer, J. L.; Sutrisno, A.; Economy, J.; Jasiuk, I., RSC Advances 8, 4946 2018.

[25] Terao, T.; Maeda, S.; Saika, A., Macromolecules 16, 1535 1983.

[26] Velasco-Santos, C.; Martínez-Hernández, A. L.; Fisher, F. T.; Ruoff, R.; Castaño, V. M., Chemistry of Materials 15, 4470 2003.

CHAPTER 9: IMPARTING OPTICAL FUNCTIONALITY TO AROMATIC THERMOSETTING COPOLYESTER BY LUMINESCENT SILICON NANOPARTICLES CROSSLINKED VIA IN SITU THERMAL POLYMERIZATION REACTION

9.1 Introduction

The last two decades have witnessed the development of ATSP which utilizes low-cost, easily processable and highly crosslinkable oligomers to produce a new family of aromatic polyesters [1–3]. The ATSP morphology is formed of a crosslinked network of ester backbone chains interconnected via covalent oxygen bonds. Owing to such unique macromolecular configuration, ATSP demonstrates outstanding thermal and mechanical properties, excellent environmental aging stability, and robust adhesive bonding with prominent metals [4–6]. Specifically, the backbone network enables the isolation of delocalized electrons through conjugated saturated spacers, namely C-C and C-O bonds, which forms a highly dielectric matrix [7,8]. Besides, controllable porosity (void to solid ratio) through a foam morphology can be used to tailor the dielectric properties of ATSP morphology [9,10]. Hence, ATSP can potentially find applications in high-performance silicon-based microelectronics, such as complementary metal-oxide-semiconductors (CMOS) [11] and microelectromechanical systems (MEMS) [12].

This work was previously published: Kocyigit, A., Bakir, M., Cifci, O.S., Enders, B., Jasiuk, I., and Nayfeh, M.H., Imparting optical functionality to aromatic thermosetting copolyester by luminescent silicon nanoparticles crosslinked via in situ thermal polymerization reaction, European Polymer Journal, 103, 351-361 (2018).

Special thanks to Dr. Adem Kocyigit (Igdir University, Turkey) for his invaluable contributions.

The electro-optical properties of ATSP (e.g., oxidation potential, fluorescence, and band gaps) are local and mediated by isolated individual aromatic rings which are the low-molecular-weight building blocks [13,14]. Hence, the ATSP matrix exhibits a weak luminescence in the blue/green range, displaying the characteristic feature of the individual aromatic rings. Therefore, doping the ATSP matrix with luminescent nanomaterials can potentially enable high optical activity. The enrichment of the matrix with photoluminescence, in addition to the superior thermomechanical properties, may expedite the implementation of the ATSP nanocomposites in photonics applications, such as solar energy harvesters, filters, concentrators, down conversion thin film coatings [15–18]. Hence, to efficiently control the global optical and thermomechanical properties of the nanocomposite structures [19,20], it is pivotal to investigate the fundamental basis of intermolecular interaction mechanisms between ATSP and luminescent materials, such as Sinps, to understand physicochemical changes that may be imposed during the polymerization process.

In this work, we examined the prospect of doping ATSP with ultra-small Sinps to impart optical properties in a nanocomposite morphology. Carboxylic acid- and acetoxy-terminated matched oligomers carry out a polycondensation reaction wherein ether oxygen of the acetoxy-group oligomer is exchanged with hydroxyl groups of the carboxylic acid-group oligomer, forming the crosslinked ATSP backbone chain [21]. On the other hand, the Sinps are attractive owing to their strong luminescence feature and being amenable to the formation of reactive Si-H termination [22]. The Si–H bond can be easily softened or cleaved to form a charged state under relatively mild reaction conditions, which facilitate thermal activity around 100–150 °C or photo-activation with UV/white light [23]. Thus, the reactive Si-H sites can conveniently interact with the unsaturated reactive functional groups (the acetoxy and carboxylic acid terminals) of the

precursor oligomers, which introduces hydroxyl-group advanced intermolecular coupling mechanism [24–26]. We investigated the polymerization process in solution with the presence of the luminescent Sinps under both UV exposure and thermal treatment. The unique formation of luminescent ATSP–Sinps complexes in 2-D thin film forms was observed. Ultraviolet-visible and photoluminescence spectroscopies along with electron microscopy were employed to examine the topological features, interfacial attachment mechanism, and in situ polymerization processes of these complexes. This work for the first time demonstrates imparting strong and novel optical characteristics to the otherwise weakly blue/green luminescent ATSP nanocomposites. We particularly studied the effects of the in situ polymerization reaction and nanofiller interfacial coupling mechanism on the global photoluminescent features of the nanocomposites. This semiconductor-polymer nanocomposite may potentially open up concepts of advanced device applications such as UV shielding to mitigate photo-degradation, and enhanced operational efficiency for photonics applications.

9.2 Materials and Methods

We incorporated pristine Sinps into a matched set of constituent oligomers of ATSP in tetrahydrofuran (THF) solution to prepare ATSP–Sinps combinations for the pre-polymerization process. The precursor oligomers were functionalized with carboxylic acid (C-group) and acetoxy (A-group) end groups. The oligomers were synthesized using trimesic acid (TMA), isophthalic acid (IPA), 4-acetoxybenzoic acid (ABA) and hydroquinone diphthalic anhydride (HQDA) (Sigma-Aldrich Co.) as further detailed in the prior literature [1,4,9]. The calculated molecular weights of A- and C-group oligomers are 1750 g/mol and 1900 g/mol, respectively [27]. Figure 9.1.a displays the chemical structures of the C-group and A-group oligomers, respectively [8]. The C- and A-group oligomer contained four terminal sites of carboxylic acid (-

COOH) and acetoxy (-CH_3COO), respectively. The oligomer networks consisted unsaturated oxygen atoms available to interact with free radicals. Reactive hydroxyl group (-OH) was abundant in the C-group oligomer which hence formed aggregates in the THF solvent by hydrogen bonding to itself [1]. Whereas the A-group oligomer lacked the hydroxyl group, so it instead dissolved in the solvent with minimum aggregation [27]. On the other hand, the Sinps, 2.9±0.1nm in diameter, were prepared from Si wafers by chemical etching in HF/H_2O_2 using an hexachloroplatinic acid catalyst, as details were further discussed in the literature [28–30]. Figure 9.1.b shows bright field transmission electron microscopy (TEM) image of the pristine Sinps. The nanoparticles were H-terminated (Si-H) [31–33]. The Si–H groups were confirmed using solution ^1H Nuclear Magnetic Resonance (NMR) [22]. The nanoparticle suspensions were separately prepared in the THF solvent to enable stable dispersions prior to mixing with the oligomers.

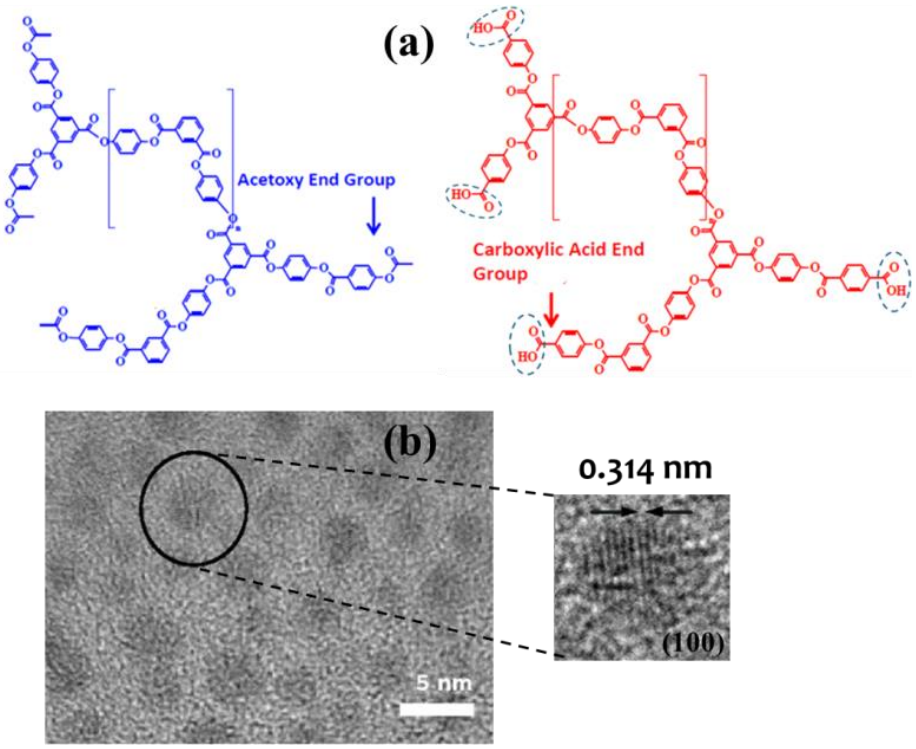

Figure 9.1 a) The chemical structures of the acetoxy- (A-group) (blue) and carboxylic acid-capped (C-group) (red) oligomers [8]. b) Bright-field transmission electron microscope images of the silicon nanoparticles [34]. The enlarged image resolves atomic planes within a single nanoparticle. The observed atomic plane spacing of 0.314 nm in (100) plane is the characteristic of silicon crystals.

The control solutions of the C-group and A-group oligomers were prepared in THF solvent to examine the interaction mechanism of the Sinps with each of the individual oligomers and oligomer mixture. The pristine Sinps solution had a molarity of 10 μM, and the oligomer solutions were in 1.65 mM. For the preparation of the solutions, 0.5 ml of the individual oligomer solutions were added to Sinps solutions in separate glass vials. Then, these two Sinps-oligomer solutions were combined to obtain an oligomer mixture and Sinps solution [4,35].

We mixed the three components: C-group oligomer, A-group oligomer, and Sinps at given concentrations above. A specific volume (1 ml) of the mixture was spread on a preheated glass plate at 50 °C in a glovebox, and then the specimen was subjected to a thermal treatment. The temperature of the film was incremented up to 300 °C and held for 30 minutes to complete the curing process. The sample was then optically tested.

We prepared free-standing films of both neat ATSP and ATSP–Sinps nanocomposites. We initially centrifuged the ATSP precursor oligomer solution at 2000 rpm for 20 minutes to remove both excess undissolved and large clusters of the oligomer particles from the solution, which results in clear and transparent solutions. Residual undissolved clusters would create defects in the film that would compromise the uniformity and mechanical properties. Neat ATSP and ATSP–Sinps solutions were cast on aluminum foils wrapped around glass substrates by doctor-blade technique. An equal volume of the Sinps (10 μM) and ATSP (1.65 mM) solutions were mixed to obtain the nanocomposite specimens. Upon thermal curing, the substrates were dipped into HCl solution (%37) to etch aluminum foils, which produced the free-standing polymer films without inducing any physicochemical effect to the specimen [36]. The Sinps were preserved within the ATSP matrix against the corrosive environment of HCl, owing to chemically inert nature of the crosslinked ATSP backbone and saturated H-termination of Sinps [32]. Generally, silicon does not *react* with HCl as it needs to form tetravalent covalent bonds. The reaction, however in the presence of a catalyst, such as copper, takes place at high temperatures near 350°C, *forming Si* tetrachloride accompanied with release hydrogen. For Si-H terminated silicon such as the nanoparticles, HCl lowers the *ph* of the solution (by providing hydrogen ions) that improves the hydrogen termination of the nanoparticles, hence improves the photoluminescence efficiency [37].

The temperature measurements on the vials were carried out using a remote source of He-Ne laser sensor. The photoluminescence spectroscopy measurements were obtained under 365 nm ultraviolet excitation source (Hg lamp source) (UVP LLC) via a fiber-optic spectrometer (Ocean Optics HR2000). The morphological analysis was performed using scanning electron microscopy (SEM) (S-4800, Hitachi) in upper detector mode at 10-15 kV voltage and 5-10 μA

current. The thickness measurements of the ATSP–Sinps nanocomposite thin films were carried out via Dektak surface profilometer. The glass transition temperature characterization of the neat ATSP and ATSP–Sinps nanocomposite free-standing films was performed using a dynamic mechanical analyzer (DMA) (TA Instruments Q800 DMA). The DMA was operated in a tensile mode in room atmosphere. A temperature-ramp cycle was performed at a constant heating rate of 3 °C/min. The film specimens were 5 μm x 5 mm x 10 mm (thickness x width x length). Varian Cary 5G ultraviolet-visible (UV-Vis) spectrometer was employed to perform absorption measurements on ATSP-Sinps thin films.

9.3 Results and Discussion

We monitored the in situ interactions between the Sinps and individual C- and A-group constituent oligomers of ATSP as well as the oligomers mixture during the pre-polymerization process. Figure 9.2.a shows the luminescence spectra of the neat C- and A-group oligomer mixture, pristine Sinps, and Sinps combined with the oligomer mixture (C- and A- groups combined) all in THF solution. Also, Figure 9.2.b exhibits the corresponding luminescent images of the vials. The spectra and images were obtained under UV excitation at a constant wavelength of 365 nm. The oligomers manifested a weak blue-green luminescence at 498 nm, which is characteristic of the polymer whereas the pristine Sinps displayed a red/orange luminescence at 644 nm. The Sinps and oligomers combination showed a pink color due to the color mixing of the red and blue-green components. The overall emission band is dominated by the red luminescence with a slightly shifted maximum to a wavelength of about 655 nm. The results highlighted that the Sinps did not comprise the luminescence when mixed with the oligomers; rather preserved the intrinsic strong photoluminescence. The small red shift of 11 nm corresponds to a lower energy state in the Sinps structure due to coupling/attachment to the

backbone of the polymer via Si-O bond, which effectively lowers the quantum confinement for radiative recombination of UV-excited excitons. Note that all solutions were transparent in room light.

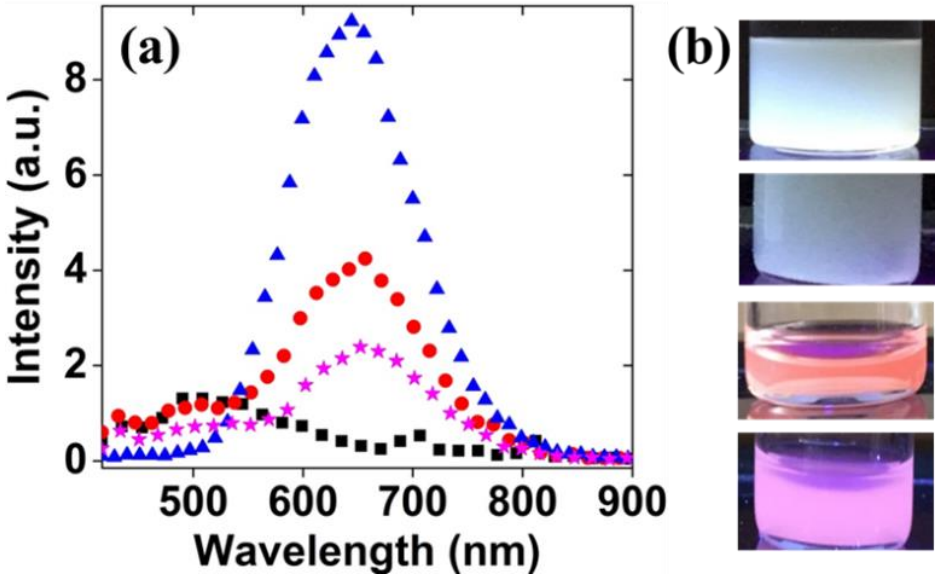

Figure 9.2 a) The luminescence spectra of the C-group- and A-group oligomer mixture (■), pristine Sinps (▲), Sinps combined with oligomers mixture (●), and Sinps and oligomer mixture combination after 1-hour settlement in room condition (★), all in THF solution. The spectra were obtained under UV radiation excitation at a wavelength of 365 nm. b) The luminescent images of the C-group oligomer, A-group oligomer, pristine Sinps, and Sinps with oligomer mixture combination under same excitation conditions, given from top to bottom, respectively.

With time, following the preparation of the Sinps and oligomers mixture, small clusters were observed to form in the solution, which progressively increased in size. Multiple clusters were then collected forming a larger distinct structure which accumulated near the center bottom of the vial, as shown in Figure 9.3.a. The aggregate was initially weakly bound and broken up easily upon a moderate shaking. However, during the continuous bombardment by individual clusters, it became relatively stable as more clusters were captured within the structure. Eventually, nearly all clusters, which were visible to naked eye, were gathered at the center in a relatively loosely bound structure, being as large as 3 mm. We note that the aggregation occurred within a few minutes through a heat source of a hot plate or a strong UV light under the given

conditions. Whereas, a similar clustering behavior took place at a much slower rate, in several days, at room temperature in the absence of direct UV exposure (data not shown) [38].

The photoluminescence spectrum of the aggregates, while resting on the bottom of the vial, was acquired under UV irradiation at a wavelength of 365 nm using a fiber-optic spectrometer. Figure 9.3.b demonstrates the red luminescent imprint of the nanoparticles and the blue-green luminescent imprint of the oligomers, which confirmed the presence of the Sinps as well as the aromatic structure of the oligomers in the collection. The structures were then scooped and dried on a silicon wafer substrate. Figure 9.3.c shows a photoluminescent image of the Sinps-oligomer mixture combinations obtained using a fluorescence microscope operated at a 365 nm wavelength. The photoluminescence spectra of the dry sample under a 365 nm excitation is shown in Figure 9.3.d.

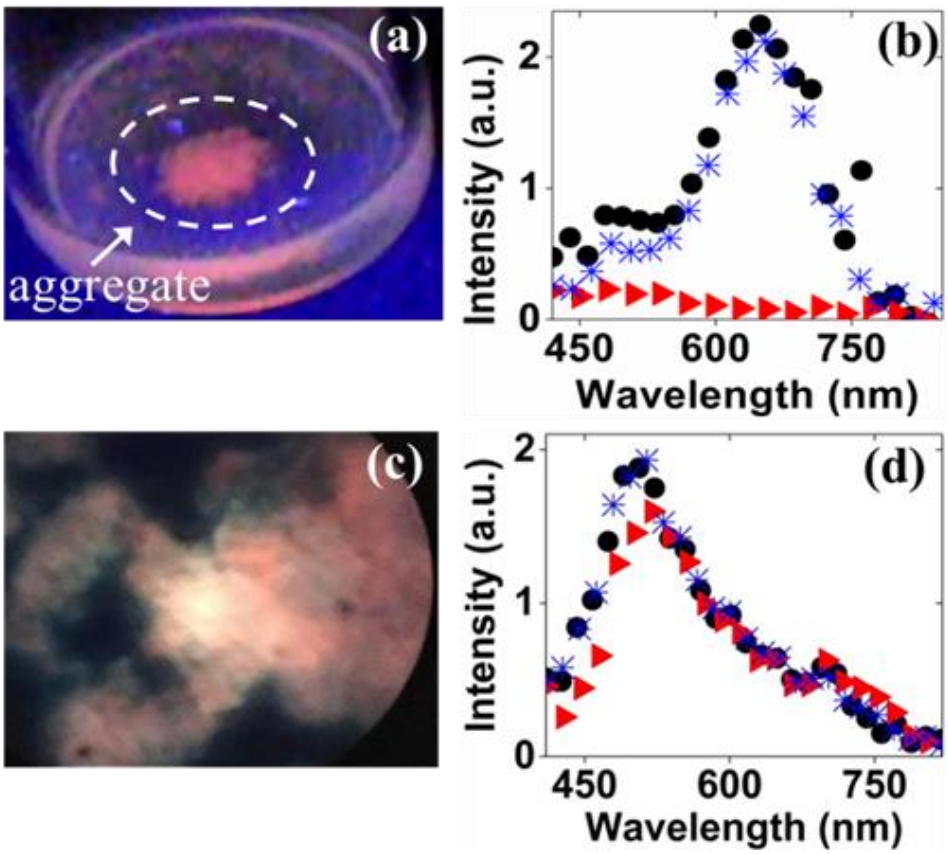

Figure 9.3 a) A top view snapshot of the accumulated aggregate of the Sinps and oligomers mixture (C- and A-groups together) obtained under UV light. b) The photoluminescence spectrum of the accumulation on the bottom of the vial acquired using a fiber-optic spectrometer operated at 365 nm UV irradiation (●); (★) represents the combination subtracted from the substrate spectrum (►). c) A fluorescence microscope image of the dried accumulation on a silicon substrate obtained under 365 nm source excitation. The bright red domains represent the Sinps and ATSP composite structures in the dark background of scattering of the incident UV radiation. d) The photoluminescence spectra of (c) collected on clusters in the dark (●), under UV (★), and under UV following a shaking (►) using the fiber-optic spectrometer.

We studied the interactions of the Si nanoparticles with the individual oligomers. At first, the aggregation of C-group and Sinps were decanted and dried on a silicon wafer substrate. It was loosely bound, so easily broken into individual clusters during this process. We obtained images of the aggregated structure using SEM. In Figure 9.4.a, we observed the formation of 2-D nanosheet composites, as small as 50 to 100 nm. Some clusters piled upon decanting and drying. Thus, accumulation layers, as wide as several micrometers, were observed wherein relatively larger layers were even readily observable by the naked eye or a moderately magnified optical

camera. Figure 9.4.b shows that the nanosheets were decorated with smaller clusters of 10-13 nm across; in some cases, one can observe 4-6 substructures in the domain.

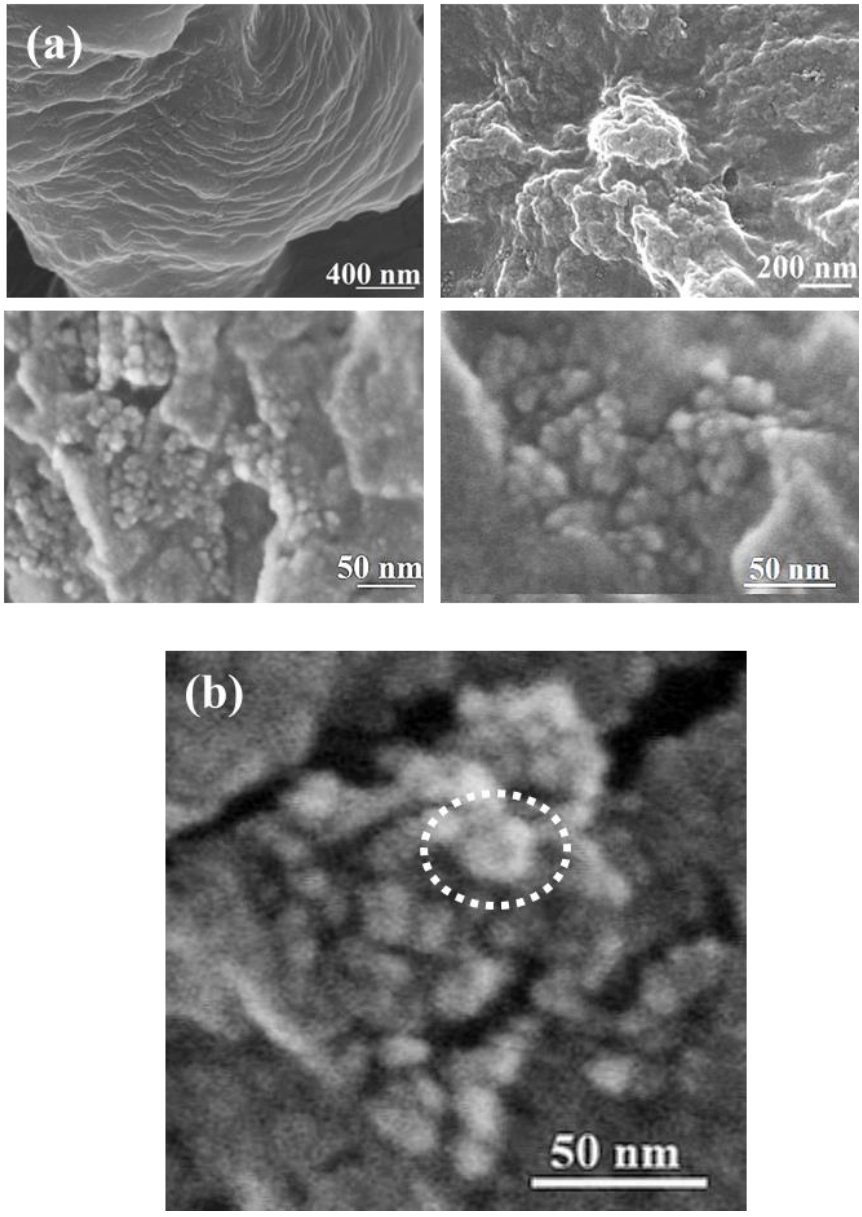

Figure 9.4 a) Scanning electron microscope images obtained on the dry aggregate of Sinps and C-group oligomer. 2-D nanosheet composites, with dimensions as small as 50-100 nm, were observed. b) A close-up image showing that the nanosheets were decorated with smaller clusters that are 10-13 nm across for which the formation of 4-6 substructures was observed.

Following that, for the A-group, we observed several other distinct features as compared to the C-group. Note that the A-group was the cross-linker in the polymerization process of

ATSP, which had only double-bonded active sites. Hence, for the A-group oligomer and Sinps solution mixture, large enough clusters formed, which were discernible to the naked eye, while similar accumulation behavior took place at the center bottom of the vial, as shown in a luminescent image in Figure 9.5.a. SEM images, in Figure 9.5.b-d, show the formation of 13 nm large composite clusters at different magnifications, but unlike the C-group oligomer, the A-group oligomer developed larger accumulation layers. It is likely that the oligomer particles were too large as compared to 13 nm Sinps complexes to perform such a collective motion. It might also indicate the shortage of hydrogen bonding to form aggregates [27].

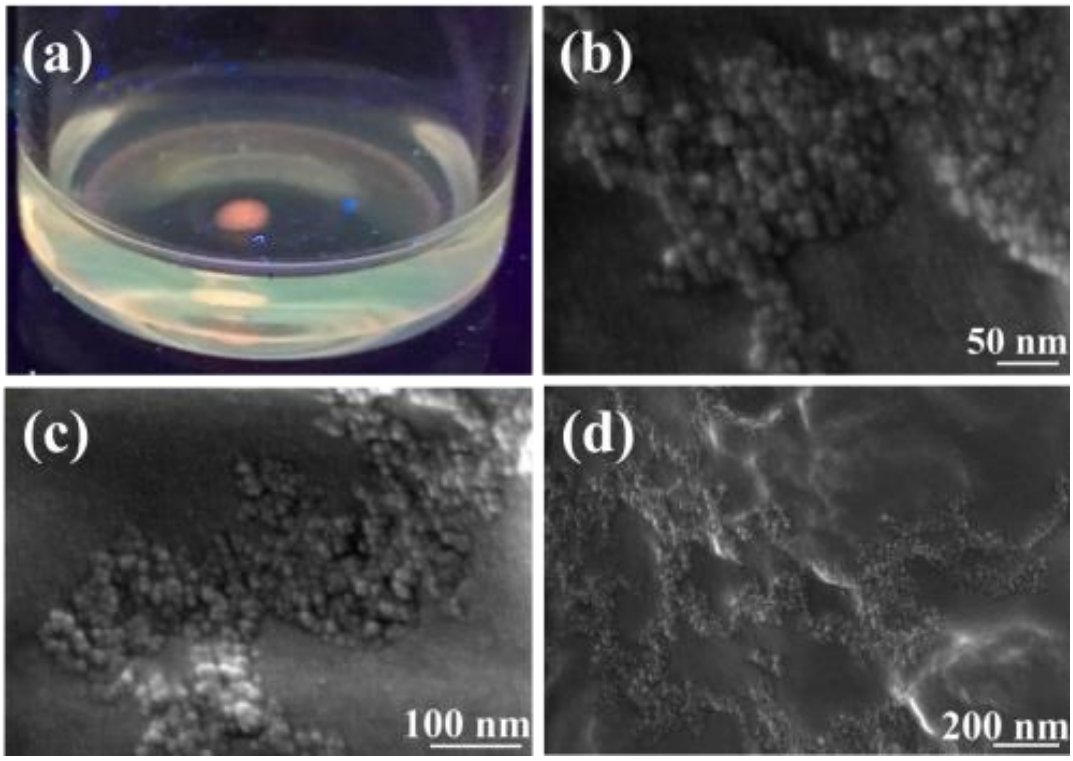

Figure 9.5 a) A luminescent image of the A-group oligomer interacted with the Sinps showing accumulation at the center bottom of a vial. b-d) Scanning electron microscope images obtained on the A-group oligomers and Sinps combination at different magnifications highlighting the presence of 13 nm large composite clusters along with the formation of larger layers than the C-group oligomer-Sinps mixture.

Figure 9.6.a sketches the attachment scheme of the Sinps to C-group oligomer. Under UV irradiation, the hydrogen bond on the Sinps was cleaved, which turned the particles into reactive charged free radical structures. In fact, the activation of homolytic cleavage of a Si–H bond can be achieved under relatively mild reaction conditions including thermal activation at 100–150°C, or photo-activation with white light [23]. In this case, the process was enhanced for the ultra-small particles due to spatial quantum confinement and strong surface re-construction. Hence, the Sinps considerably reduced electron affinity, and Si-H bonds became highly polarized [22]. On the other hand, C-group oligomer was a weak Lewis acid, which could potentially interact with both neutral and charged particles. Hence, the interfacial interaction with a neutral particle could occur via the carboxylic acid terminals which would form a Si–O–C bond while releasing hydrogen (H_2). Alternatively, a charged particle could interact with the double-bond oxygen sites in the C-group oligomer. These two processes could result in the formation of a charged complex wherein the oligomer would act as a bi-linker. Due to the presence of multiple functional groups and double oxygen bonds, as well as the Si-H bonds, the two processes formed a complex of 4-6 nanoparticles interconnected by the C-oligomer structure. In fact, ab initio studies, using first-principles density-functional calculations in a supercell approach of the chemisorption reactions for carboxylic acids on hydrogenated silicon surfaces, demonstrated that such an attachment to a double oxygen bonded configuration is favored, and the Si−O−C bridge, in this case, does not block charge transfer from surface to molecule [39]. Figure 9.6.b represents the corresponding composite structure of the C-group oligomer with 4 silicon nanoparticles (each ~ 3nm across) attached to the four reactive sites of the oligomer. Thus, when the C-group oligomer was stretched, the composite cluster could extend to ~ 13 nm across. Figure 9.6.c outlines the attachment scheme of the Sinps to the A-group oligomer; the A-group oligomer

could only attach to a charged free radical via double bond sites, which hence resulted in neutral two-nanoparticle complexes. Figure 9.6.d demonstrates the composite structure of the A-group oligomer with 4 Sinps (each ~ 3nm across) which were bonded to the reactive caps of the oligomer. When the A-group oligomer was likewise stretched, the composite cluster could reach to ~ 13 nm extent.

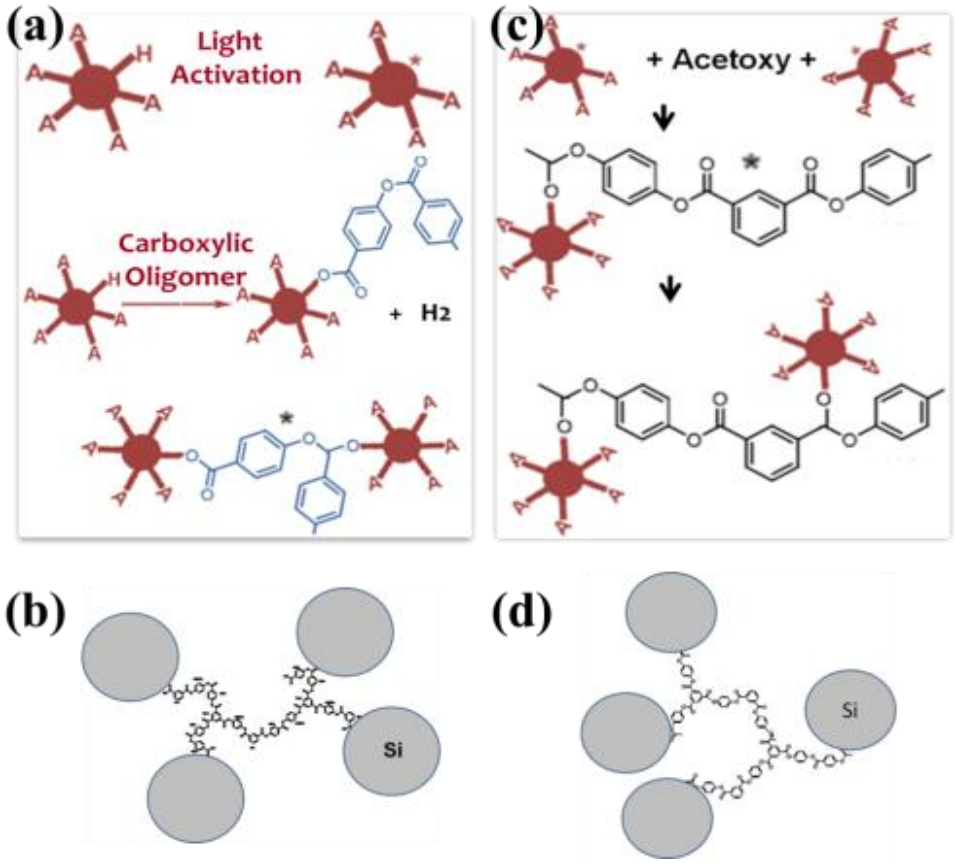

Figure 9.6 a) The sketch of the attachment scheme of the Sinps to the C-group oligomer. The oligomer interacted with a neutral particle via one of four terminals by releasing hydrogen (H_2) via the formation of Si–O–C bonds. b) The composite configuration of the C-group oligomer with 4 nanoparticles (each ~ 3nm across) attached to the four branches of the carboxyl cap. c) The sketch of the attachment scheme of the Sinps to the A-group oligomer. d) The composite configuration of the A-group oligomer with 4 nanoparticles (each ~ 3nm across) attached to the four branches at the acetoxy caps.

We note that during the particle collection process of the Sinps and the precursor oligomers, a convective motion was observed as long as a temperature gradient existed across the liquid medium. In this case, upon UV exposure, the temperature at the bottom of the vial was

measured to be higher than the top surface of the liquid. The temperature at the bottom rose from ~25°C (room temperature) to ~33°C while the liquid surface was at ~28°C after half an hour, which established a temperature gradient of 5°C across the liquid medium. The temperature increase occurred due in part to the heating and UV absorption by the Sinps. Then, the clusters began to execute a continuous convection-like motion between the center bottom and the center top parts of the solution. Consecutively taken representative snapshots from a top perspective during this process are given in Figure 9.7.a. The images displayed that the clusters increased in size forming aggregation as well as executing a circulatory motion between the wall and the center of the vial. With time, multiple clusters were collected developing a larger structure and then accumulated near the center. The aggregates were weakly bound and broke up momentarily due to bombarding individual clusters. Visually, it became stable while further bombarding clusters were captured in the aggregated body. Eventually, nearly all clusters were trapped at the center of a relatively loosely bound structure of as large as 3 mm. At this point, the convection-like motion halted.

To understand the convection like motion, we focused on the cluster formation collected and trapped at the bottom of the vial. Recent studies showed that convection forces generated by spatially confined heat sources of micro-scale electric thermal heaters could trap micrometer-sized dielectric particles, such as polystyrene spheres and E. coli [40,41]. The heat-induced trapping phenomenon was confirmed using a steady-state heat equation along with the Navier-Stokes equation [42]. The temperature gradient was found to lead to a steady-state particle concentration gradient, c, according to $dc/dz = -c\ ST\ dT/dz$, where ST is the ratio of the thermal diffusion coefficient to mass diffusion coefficient (under negligible viscous drag condition). For a negative ST, particles were driven to the hotter region while with a positive ST, they were

forced to the colder region [43]. The results, in Figure 9.7.b, show that the magnitude and the sign of the diffusion coefficient depended on both the temperature regime and particle size wherein smaller particles, generally having negative coefficients, were driven to the hotter regions. We note that, for which dT/dz = 8K and T = 297-305K, two trapped-cluster domains were observed in the center and at the side, as demonstrated in Figure 9.7.a. We understand that the trapped structure at the center (the hottest region) was the smaller clusters, while the trapped structure at the side (the coldest region) was the larger clusters.

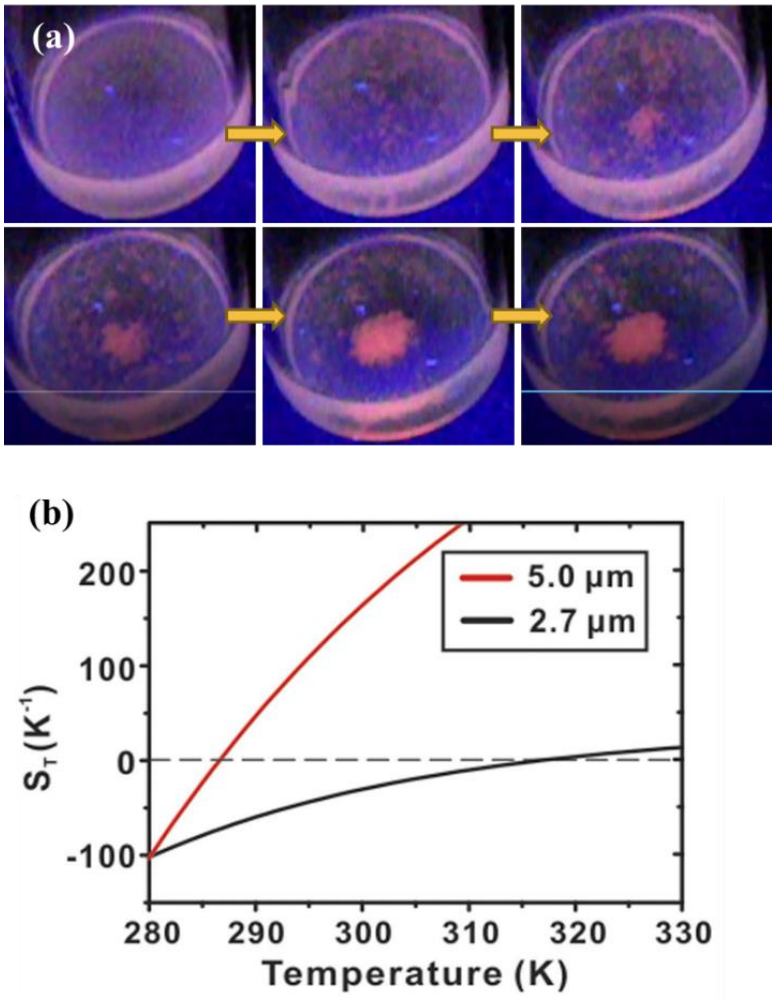

Figure 9.7 a) Top view representative consecutive snapshots (from left to right) obtained during interactions between the Sinps-oligomer mixtures in the liquid medium upon UV exposure. b) The calculated magnitude and sign correlation of the S_T (Soret coefficient) as a function of temperature and particle size [42].

To provide more details on the thermal motion, we also observed the solution of Sinps and oligomer mixture (C- and A- groups together) from a side view of the vial under white light exposure. Figure 9.8.a displays top view snapshots of the Sinps-ATSP oligomers solution (obtained on a different vial). Figure 9.8.b depicts a sketch of the convective motion of the clusters. On the liquid surface, the clusters were relocated from the center to the wall, while, the clusters were relocated from the wall to the center in the liquid. Figure 9.8.c shows several consecutive snapshots of the motion of a pair of clusters displaying the convective motion. The clusters were transported relatively slower in the liquid as compared to their motion on the surface, which could be due to viscous resistance to the motion.

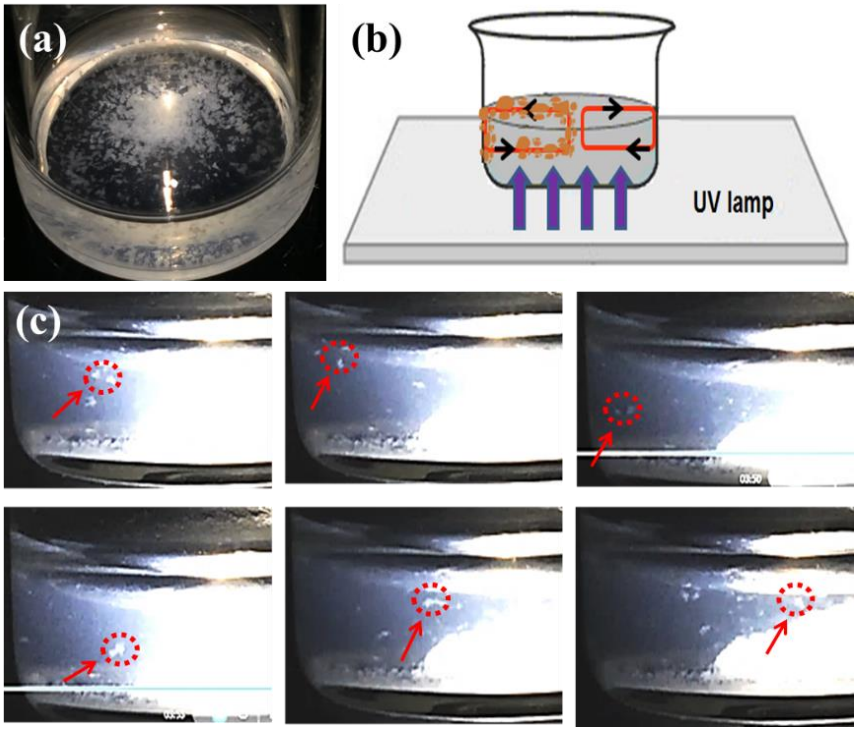

Figure 9.8 a) A top view snapshot of the Sinps-oligomer mixture combination under white light exposure. b) A sketch of the convection motion of the clusters to indicate circulatory thermal motion directions. Top three images display the motion circulating from center to edge. Bottom three images show the motion from edge to center. c) Several consecutive side view snapshots of the convection motion of a pair of clusters.

The convection motion also indicated the presence of distinct size regimes. In other words, a typical mixture might comprise several components: pristine Sinps (not reacted), unreacted oligomers, and oligomers conjugated with Sinps. Hence, we investigated the flow patterns of the mixtures of the individual oligomers with Sinps as well as the unreacted individual oligomers upon drop-drying on a glass surface. Figure 9.9 shows a series of images which were obtained under UV light after individual drops of neat C-group (a), Sinps – C-group mixture (b) and neat A-group (c), and Sinps – A-group mixture (d) were dried on glass substrates. Due to gravitational impact, the Sinps-oligomer mixture droplets initially produced luminescent donut shapes upon landing but quickly filled the donut. In the second phase, the liquid first spread and then contact lines were pinned to the underlying substrate, and eventually dried forming rings. The rings appeared to be a red luminescent material. The initial pinning of the contact line might be mainly caused by the surface wettability, as well as the surface roughness, being another contributing factor, but it was strengthened by arriving nanocomponents while effectively constituting a self-pinning mechanism. The drying caused a strong radially outward capillary-like flow inside the drop with velocity on the order of 10μm/s, which carried the nanocomponents into the domain [44]. The complete dried forms allowed observing the imprint of the flow at the instant of impact. The image also displayed the flow behavior of components of different sizes. The smallest nanoparticles were the fastest, while oligomer components with larger sizes lagged. This conclusion was consistent with the dependence of the amount of liquid resistance on the shape and the diameter of the component; the larger the cross-section of the objects, the larger the dragging they experienced. In addition to the size-dependent dragging, the interaction-driven attachment with the surface played an important role in the formation of the shapes. Unlike the acetoxy caps, the carboxyl caps might

attach to glass by interacting with partially charged states of silicon on the surface as resulted from oxygen defects. The reactive sites included dimerized (Si^{+1}) interface, and an oxygen bridge (Si^{+2}) interface as compared to the neutral charge state in the case of a full oxide (Si0). Therefore, we expected the pristine Sinps to be the fastest, as followed by the Sinps-oligomer complexes, and the unreacted oligomers which may spread over a disk.

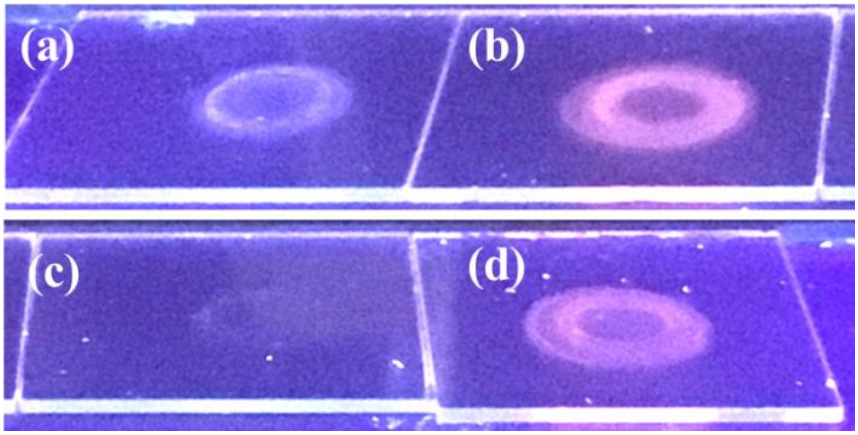

Figure 9.9 Dried droplet images of a) C-group oligomer, b) Sinps – C- group oligomer mixture, c) A-group oligomer and d) Sinps – A-group oligomer on glass substrates. The images were obtained under UV light.

Building on these findings, we examined the thermal polymerization process of ATSP in the presence of the Sinps. In room light, the cured films cast on glass substrates were transparent, as shown in Figure 9.10.a; but under UV, it displayed a "red luminescence," as shown in Figure 9.10.b. We also presented SEM images which were obtained from the films displaying microstructural features formed by the Sinps. In Figure 9.10.c-d, we observed a smooth surface interrupted by the clusters that varied in size from nearly 50-100 nm to several micrometers with an average interspacing distance of several micrometers. In other regions, in Figure 9.10.e, we noticed smooth surfaces interrupted by voids due to the acetic acid by-product release in the course of the condensation polymerization reaction [9]. Some of these voids were as small as several nanometers, while others were as wide as several micrometers. Additionally, the

thickness of the films was measured roughly 50 nm using a surface profilometer (data not shown). Figure 9.10.f shows a close-up image of the smallest structures observed in the composite films. The structures were 10-13 nm across; in some cases, we observed 4-6 substructures. The results confirmed the presence of the ATSP–Sinps complexes. To minimize the clustering formation in the cured films, the incubation period from the initial mixing to the preparation of the films might be shortened.

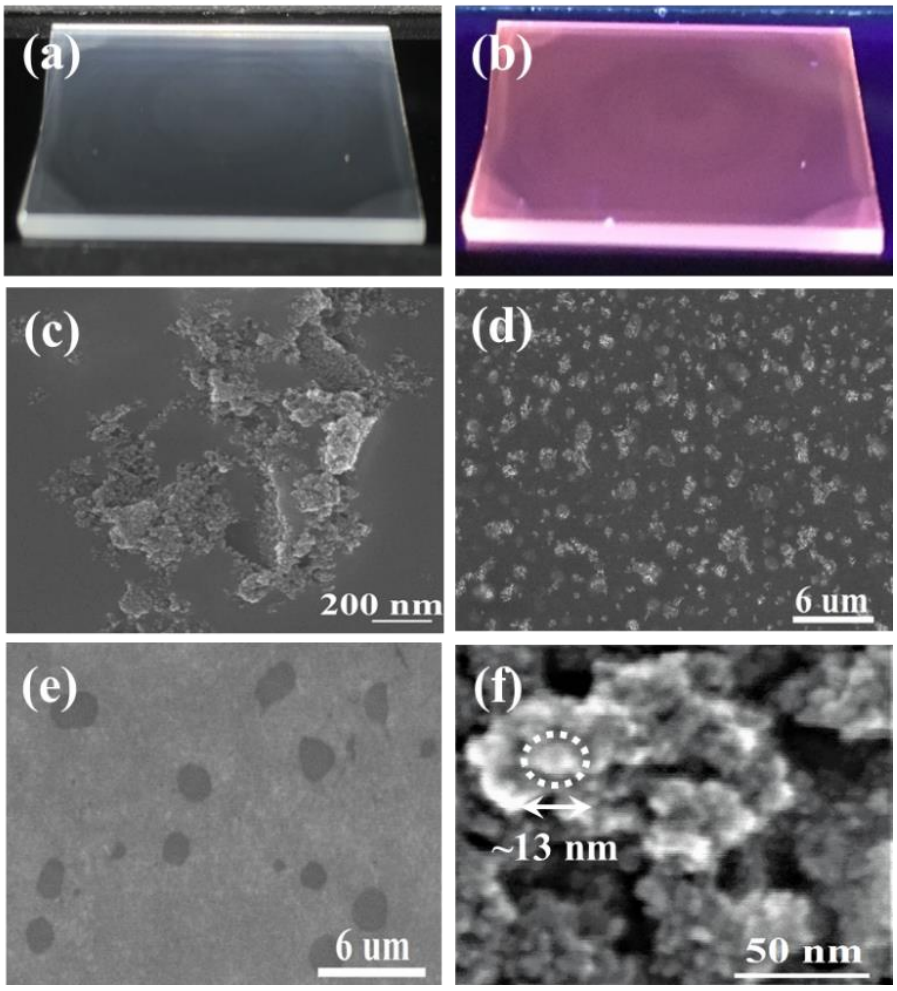

Figure 9.10 The thermal polymerization process of ATSP with the Sinps to obtain a thin film sample on glass slides a) A room light image of the thin films showing optical transparency. b) A luminescent image under UV irradiation displaying "red luminescence" in the samples. c,d) SEM images of the films showing smooth surface interrupted by clusters that varied in size from nearly 50-100 nm to several micrometers with an average interspacing of several micrometers. e) Smooth surfaces regions interrupted by voids due to the acetic acid by-product release. f) Close-up images of the smallest structures. The structures were 10-13 nm across forming 4-6 substructures.

Figure 9.11.a-b show images a free-standing film and a cross-sectional view of the ATSP–Sinps nanocomposite films, respectively. The thickness of the films was measured ~5 μm via SEM. We note that glass transition temperature (Tg) reveals the feature of thermomechanical chain relaxation behaviors of polymers. Thus, Tg would identify chemical modifications in polymer networks by Sinps incorporation. Figure 9.11.c shows tangent delta (tanδ) peaks of the neat ATSP and ATSP–Sinps nanocomposite films obtained using a DMA. The neat ATSP film displayed a glass transition temperature (α-transition) at ~258 °C. The neat ATSP possessed highly crosslinked and amorphous morphology. In comparison, the Sinps–ATSP nanocomposite film yielded a Tg at 259±2.84 °C (averaged over independent measurements on three different specimens). The similar glass transition temperatures and characteristics of neat ATSP and ATSP–Sinps nanocomposite films indicated that Sinps were well incorporated into the ATSP matrix. As such, the Sinps conjugated with the crosslinked network of ATSP while they did not change the network configuration or molecular chain length distribution. Sinps bore unique structural compatibility with the ATSP backbone chains exhibiting harmonized thermomechanical response [45].

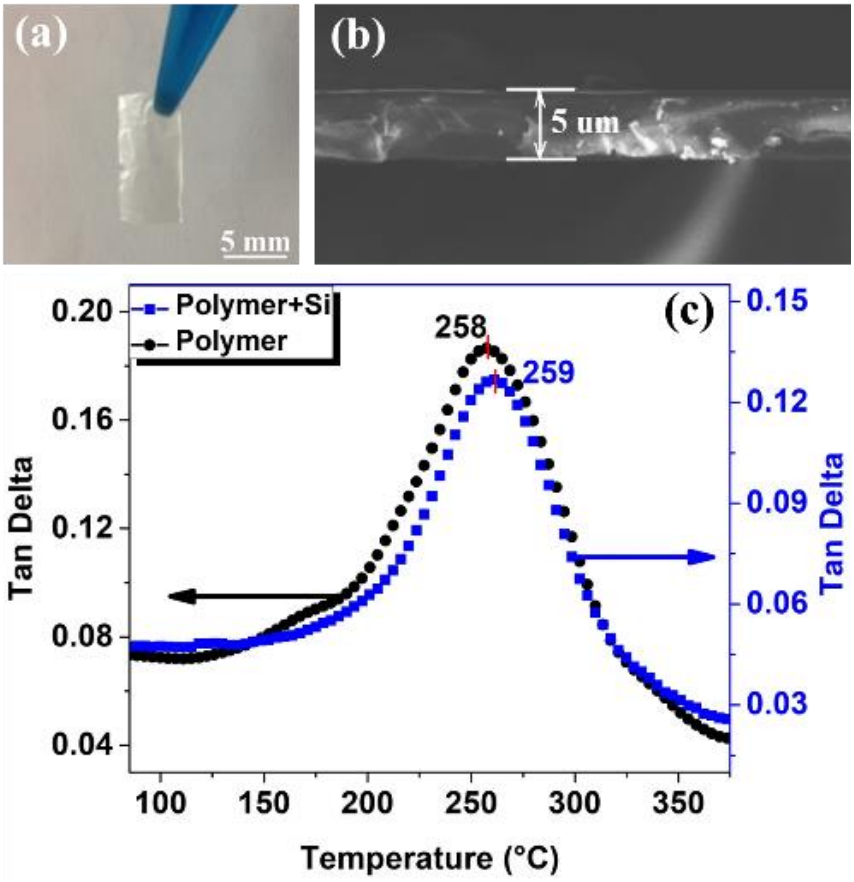

Figure 9.11 a) An image of optically transparent and free-standing ATSP–Sinps nanocomposite thin films. (b) A scanning electron microscopy image of a cross-section of the film. (c) Dynamic mechanical analysis of tangent delta glass transition temperatures of neat ATSP and ATSP–Sinps nanocomposite films obtained using DMA.

We performed absorption measurements on the cured nanocomposite films using a UV-Vis spectrometer. Figure 9.12.a gives the absorption spectrum in which we employed light with variable photon energy in the range of 1.5-6 eV, above the indirect bandgap of silicon. The figure and the inset showed absorption edges near 1.5-3 eV. To obtain more accurate absorption edges, we plotted, in Figure 9.12.b, the square of the absorption as a function of photon energy. We observed the feature around 2 eV pertained to the confinement band gap of silicon nanoparticles, while at ~ 3 eV pertained to the direct bandgap of silicon and that near 4 eV was related to the direct bandgap of ATSP. Since near direct bandgaps of no phonons were involved, we fitted the response to multiple expressions of the form $\alpha 2 = Kd\ (Ep - Eg)$. This expression

was appropriate since for edges are near direct band gaps [46,47]. Each expression involved only one proportional constant because direct bandgap materials did not involve phonons (lattice vibrations) in electron band-to-band transitions.

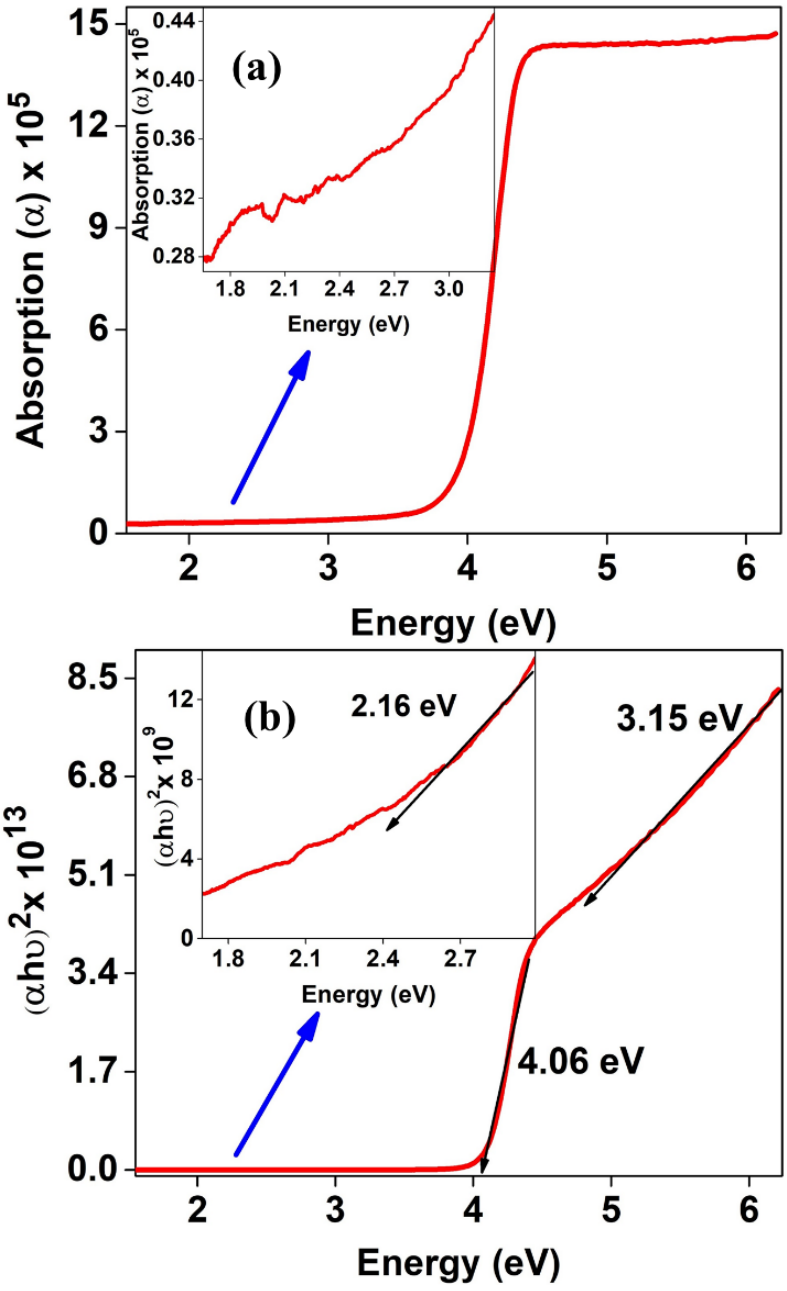

Figure 9.12 a) Absorption spectrum of ATSP–Sinps nanocomposite thin film versus photon energy b) The square of the absorption as a function of photon energy of ATSP–Sinps nanocomposite films.

9.4 Conclusion

In conclusion, we investigated the interactions of ATSP polymer-Si nanoparticles composite nanostructures under UV excitation. UV-Vis and photoluminescence spectroscopies and electron microscopy analyses were employed to observe the development of the topography, material, and *in situ* motion of the complexes. We observed the convection-like motion of the composite nanostructures under UV irradiation. The results were explained via UV induced silylation/charging of the nanoparticles which acted as an auxiliary free-radical crosslinker to form charged nanocomplexes. Glass transition characteristics indicated successful incorporation of silicon nanoparticles into highly crosslinked ATSP backbone chains. Through promising thermomechanical properties enriched with luminescence, the ATSP–Sinps nanocomposites may find applications in photonics.

9.5 References

[1] D. Frich, K. Goranov, L.A. Schneggenburger, J. Economy, Novel high temperature aromatic copolyester thermosets: synthesis, characterization, and physical properties, Macromolecules 29 (1996) 7734–7739.

[2] N. V. Handa, S. Li, J.A. Gerbec, N. Sumitani, C.J. Hawker, D. Klinger, Fully aromatic high performance thermoset via sydnone–alkyne cycloaddition, J. Am. Chem. Soc. 138 (2016) 6400–6403.

[3] M. Iqbal, B. Norder, E. Mendes, T.J. Dingemans, All-aromatic liquid crystalline thermosets with high glass transition temperatures, J. Polym. Sci. Part A Polym. Chem. 47 (2009) 1368–1380.

[4] B. Vaezian, J.L. Meyer, J. Economy, Processing of aromatic thermosetting copolyesters into foams and bulk parts: characterization and mechanical properties, Polym. Adv. Technol. 27 (2016) 1006–1013.

[5] F.F. Shi, J. Economy, Moisture transport studies on newly developed aromatic and aromatic/aliphatic copolyester thin films, J. Polym. Sci. Part B Polym. Phys. 36 (1998) 1025–1035. [6] K. Xu, J.C. Selby, M.A. Shannon, J. Economy, Adhesion mechanisms in the solid-state bonding technique using submicrometer aromatic thermosetting copolyester adhesive, J. Appl. Polym. Sci. 92 (2004) 3843–3856.

[7] X. Kun, J. Economy, Hyperbranched thermosetting poly(imide−ester): synthesis and properties, Macromolecules 37 (2004) 4146–4155.

[8] W. Wang, J. Meyer, Q. Zeng, M. Li, B. Vaezian, J. Economy, Adhesion characteristics of aromatic thermosetting copolyester and glass fiber laminates with copper foils for improved circuit boards, Polym. Adv. Technol. 27 (2016) 1577–1585.

[9] M. Bakir, J.L. Meyer, J. Economy, I. Jasiuk, Heat-induced polycondensation reaction with self-generated blowing agent forming aromatic thermosetting copolyester foams, Macromolecules 49 (2016) 6489–6496.

[10] J. Liu, D. Gan, C. Hu, M. Kiene, P.S. Ho, W. Volksen, R.D. Miller, Porosity effect on the dielectric constant and thermomechanical properties of organosilicate films, Appl. Phys. Lett. 81 (2002) 4180–4182.

[11] F. Shoucair, Design consideration in high temperature analog CMOS integrated circuits, IEEE Trans. Components, Hybrids, Manuf. Technol. 9 (1986) 242–251.

[12] W.-H. Chuang, T. Luger, R.K. Fettig, R. Ghodssi, Mechanical property characterization of LPCVD silicon nitride thin films at cryogenic temperatures, J. Microelectromechanical Syst. 13 (2004) 870–879.

[13] D. Frich, A. Hall, J. Economy, Nature of adhesive bonding via interchain transesterification reactions (ITR), Macromol. Chem. Phys. 199 (1998) 913–921.

[14] J.A. Fernandes, Y. Morisaki, Y. Chujo, Aromatic-ring-layered polymers composed of fluorene and xanthene, Polym. J. 43 (2011) 733–737.

[15] C.-H.M. Chuang, P.R. Brown, V. Bulović, M.G. Bawendi, Improved performance and stability in quantum dot solar cells through band alignment engineering, Nat. Mater. 13 (2014) 796-801.

[16] J. Bao, M.G. Bawendi, A colloidal quantum dot spectrometer, Nature. 523 (2015) 67–70.

[17] N.D. Bronstein, Y. Yao, L. Xu, E. O'Brien, A.S. Powers, V.E. Ferry, A.P. Alivisatos, R.G. Nuzzo, Quantum dot luminescent concentrator cavity exhibiting 30-fold concentration, ACS Photonics 2 (2015) 1576–1583.

[18] O.E. Semonin, J.M. Luther, M.C. Beard, Quantum dots for next-generation photovoltaics, Mater. Today. 15 (2012) 508–515.

[19] M.A. Mumin, W.Z. Xu, P.A. Charpentier, Quantum dots/silica/polymer nanocomposite films with high visible light transmission and UV shielding properties, Nanotechnology. 26 (2015) 315702.

[20] G. Carotenuto, A. Longo, C.L. Hison, Tuned linear optical properties of gold-polymer nanocomposites, J. Mater. Chem. 19 (2009) 5744-5750.

[21] D. Frich, J. Economy, K. Goranov, Aromatic copolyester thermosets: High temperature adhesive properties, Polym. Eng. Sci. 37 (1997) 541–548.

[22] M.H. Nayfeh, L. Mitas, Silicon nanoparticles. new photonic and electronic material at the transition between solid and molecule, in: V. Kumar (Ed.), Nanosilicon, First Edition, Elsevier, Oxford UK, 2008: pp. 1–78.

[23] E. V. Rogozhina, D.A. Eckhoff, E. Gratton, P. V. Braun, Carboxyl functionalization of ultrasmall luminescent silicon nanoparticles through thermal hydrosilylation, J. Mater. Chem. 16 (2006) 1421-1430.

[24] G. Wang, S.-T. Yau, K. Mantey, M.H. Nayfeh, Fluorescent Si nanoparticle-based electrode for sensing biomedical substances, Opt. Commun. 281 (2008) 1765–1770.

[25] O. Akcakir, J. Therrien, G. Belomoin, N. Barry, J.D. Muller, E. Gratton, M. Nayfeh, Detection of luminescent single ultrasmall silicon nanoparticles using fluctuation correlation spectroscopy, Appl. Phys. Lett. 76 (2000) 1857-1859.

[26] G. Belomoin, E. Rogozhina, J. Therrien, P. V. Braun, L. Abuhassan, M.H. Nayfeh, L. Wagner, L. Mitas, Effects of surface termination on the band gap of ultrabright Si 29 nanoparticles: experiments and computational models, Phys. Rev. B. 65 (2002) 193406.

[27] S.-H. Kim, Y.-H. Kim, H.-N. Cho, S.-K. Kwon, H.-K. Kim, S.-K. Choi, Unusual optical absorption behavior, polymer structure, and air stability of poly(1,6-heptadiyne)s with substituents at the 4-Position, Macromolecules 29 (1996) 5422–5426.

[28] T. Hoang, N. Elhalawany, B. Enders, E. Bahceci, L. Abuhassan, M.H. Nayfeh, Strong 1.54 μ m cathodoluminescence from core-shell structures of silicon nanoparticles and erbium, Appl. Phys. Lett. 109 (2016) 261103.

[29] M.H. Nayfeh, S. Rao, N. Barry, J. Therrien, G. Belomoin, A. Smith, S. Chaieb, Observation of laser oscillation in aggregates of ultrasmall silicon nanoparticles, Appl. Phys. Lett. 80 (2002) 121–123.

[30] F.I. Chowdhury, A. Alnuaimi, N. El-Atab, M. Nayfeh, A. Nayfeh, Enhanced performance of thin-film amorphous silicon solar cells with a top film of 2.85nm silicon nanoparticles, Sol. Energy. 125 (2016) 332–338.

[31] S. Rao, K. Mantey, J. Therrien, A. Smith, M. Nayfeh, Molecular behavior in the vibronic and excitonic properties of hydrogenated silicon nanoparticles, Phys. Rev. B. 76 (2007) 155316.

[32] K. Mantey, A. Zhu, J. Boparai, M. Nayfeh, C. Marsh, G. Al Chaar, Observation of linear solid-solid phase transformation in silicon nanoparticles, Phys. Rev. B. 85 (2012) 85417.

[33] N. El-Atab, B.B. Turgut, A.K. Okyay, M. Nayfeh, A. Nayfeh, Enhanced non-volatile memory characteristics with quattro-layer graphene nanoplatelets vs. 2.85-nm Si nanoparticles with asymmetric Al2O3/HfO2 tunnel oxide, Nanoscale Res. Lett. 10 (2015) 248.

[34] G. Belomoin, J. Therrien, A. Smith, S. Rao, R. Twesten, S. Chaieb, M.H. Nayfeh, L. Wagner, L. Mitas, Observation of a magic discrete family of ultrabright Si nanoparticles, Appl. Phys. Lett. 80 (2002) 841–843.

[35] M. Bakir, J.L. Meyer, I. Hussainova, A. Sutrisno, J. Economy, I. Jasiuk, Periodic functionalization of graphene-layered alumina nanofibers with aromatic thermosetting copolyester via epitaxial step-growth polymerization, Macromol. Chem. Phys. (2017) 1700338.

[36] M. Bakir, C.N. Henderson, J.L. Meyer, J. Oh, N. Miljkovic, M. Kumosa, J. Economy, I. Jasiuk, Effects of environmental aging on physical properties of aromatic thermosetting copolyester matrix neat and nanocomposite foams, Polym. Degrad. Stab. 147 (2018) 49–56.

[37] N. Elhalawany, Y. Maximenko, Z. Yamani, S.T. Yau, M.H. Nayfeh, Soluble silicon nanoparticles-polyaniline capsules for biosensing and imaging, J. Mater. Res. 28 (2013) 210–215.

[38] J. Vandenbergh, B. Schweitzer-Chaput, M. Klussmann, T. Junkers, Acid-induced room temperature RAFT polymerization: synthesis and mechanistic insights, Macromolecules 49 (2016) 4124–4135.

[39] C.S. Cucinotta, A. Ruini, M.J. Caldas, E. Molinari, Ab initio study of chemisorption reactions for carboxylic acids on hydrogenated silicon surfaces, J. Phys. Chem. B 108 (2004) 17278-17280.

[40] A. Lehmuskero, P. Johansson, H. Rubinsztein-Dunlop, L. Tong, M. Käll, Laser trapping of colloidal metal nanoparticles, ACS Nano 9 (2015) 3453–3469.

[41] J. Chen, H. Cong, F.-C. Loo, Z. Kang, M. Tang, H. Zhang, S.-Y. Wu, S.-K. Kong, H.-P. Ho, Thermal gradient induced tweezers for the manipulation of particles and cells, Sci. Rep. 6 (2016) 35814.

[42] S. Schneiderbauer, M. Krieger, What do the Navier–Stokes equations mean?, Eur. J. Phys. 35 (2014) 15020.

[43] P. Blanco, H. Kriegs, B. Arlt, S. Wiegand, Thermal diffusion of oligosaccharide solutions: The role of chain length and structure, J. Phys. Chem. B. 114 (2010) 10740–10747.

[44] R.D. Deegan, O. Bakajin, T.F. Dupont, G. Huber, S.R. Nagel, T.A. Witten, Capillary flow as the cause of ring stains from dried liquid drops, Nature. 389 (1997) 827–829.

[45] A. Bansal, H. Yang, C. Li, K. Cho, B.C. Benicewicz, S.K. Kumar, L.S. Schadler, Quantitative equivalence between polymer nanocomposites and thin polymer films, Nat. Mater. 4 (2005) 693–698.

[46] S.O. Kasap, Principles of Electronic Materials and Devices, 4th ed., Mc Graw Hill Education, New Delhi, 2005.

[47] B.G. Streetman, S. Banerjee, Solid state electronic devices, 6th ed., Prentice Hall, New Delhi, 2005.

CHAPTER 10: AROMATIC THERMOSETTING COPOLYESTER BIONANOCOMPOSITES AS RECONFIGURABLE BONE SUBSTITUTE MATERIALS: INTERFACIAL INTERACTIONS BETWEEN REINFORCEMENT PARTICLES AND POLYMER NETWORK

10.1 Introduction

Synthetic bone substitution is the second most frequent transplantation procedure, following blood transfusion, with over two-million surgical operations worldwide per year while incurring an estimated cost of $2.5 billion [1-3]. In a broad sense, the replacement process is sought to repair bone defects in orthopaedic, neurosurgical, and dental practices in which the bone substitutes induce healing through reconstruction of the bone defects or serve as implants [4-6]. Particularly, several types of bone substitutes have been adopted so far including bone grafts and synthetic scaffolds for bone reconstruction [3]. Autologous bone grafting - utilizing a bone obtained from a donor site - is still considered the gold standard, while biomaterials or synthetic scaffolds hold promises as alternative materials [7,8]. At present, the state-of-art bone substitutes are rather customized, being more than mere replacement materials, to individually generated composite biomaterials that can host bone-forming cells to allow expedited defect rehabilitations[9].

This work was previously published: Bakir, M., Meyer, J.L., Sutrisno, A., Economy, J., and Jasiuk, I., Aromatic thermosetting copolyester bionanocomposites as reconfigurable bone substitute materials: interfacial interactions between reinforcement particles and polymer network, Scientific Reports, 8, 14869 (2018).

More recently, polymer bionanocomposites have drawn attention in the development of synthetic bone substitutes [10]. Polymer bionanocomposites are combinations of an inorganic phase (bioactive reinforcements) and a polymer phase (host matrix), which can serve two main purposes: improved biomechanical properties and enhanced biological activity for the polymeric domains [11]. Calcium phosphate (CaP) and hydroxyapatite (HA) are the most well-adopted inorganic cements utilized in bone replacement applications, as they are biocompatible, have genuine morphologies akin to mineral phase of bone, and enable protein adhesion to stimulate cell proliferation [12]. Regarding the polymeric matrix of the nanocomposite replacements, prominent polymers are poly(lactic acid), poly(glycolic acid), and poly(ε-caprolactone), which undergo a diffusion-driven hydrolytic decomposition process in *in vivo* conditions [13]. These polymers, as well as their derivatives, are subjected to bulk erosion which allows for new bone to form and replace them. Regarding the enhancement of interfacial interactions between the nanofiller reinforcements and polymers matrices, the most viable approach is to utilize selectively surface functionalized nanofiller particles through an *in situ* polymerization process [14,15]. Via this approach, the nanofiller particles conjugate with polymer chains and are immobilized within the matrix. This method also enables a near-homogenous dispersion of nanofiller particles within polymer matrix [16,17] Hence, artificial bone scaffold nanocomposites demonstrate improved mechanical strength and enriched biocompatibility. Along this line, permanent implant applications require alternative polymer systems that ensure mechanochemical reliability in *in vivo* as well as forming a strong interfacial adhesion mechanism with the bioactive particles for ultimately improved structural properties.

Aromatic thermosetting copolyester (ATSP), introduced in the late 1990s, utilizes low cost, easily processable and highly cross-linkable oligomers to form a high-performance polymer

system [18-20]. The crosslinked network of the ATSP morphology is composed of an aromatic polyester backbone interconnected via covalent single/double oxygen bonds which enables superior physical properties and provides outstanding chemical inertness [21,22]. Besides, ATSP is conveniently reconfigurable into miscellaneous physical forms including foam, fully-densified bulk part, coating, and adhesive, which therefore can address various synthetic bone applications [16,17,19,20] More recently, ATSP nanocomposites have been developed adopting a facile production route via solid-state mixing of precursor oligomers with nanofiller particles. As well, the ATSP nanocomposites uniquely enable the near-homogenous distribution and good incorporation of nanofillers which then constitute significantly enhanced physical properties [23]. Earlier work on ATSP shows direct-contact cytotoxicity test results that fibroblasts remain healthy and still adhered to the ATSP specimen following an incubation period [24]. Hence, ATSP matrix enriched with bioactive reinforcements can be a promising bionanocomposite candidate as an insoluble artificial bone substitute material due in part to water and salt aging resistance [25]. For example, owing to the strong adhesive bonding formed with most metals including titanium, significant specific impact energy absorption capacity, and promising tribological properties of low coefficient of friction, superior wear, and abrasion resistances, ATSP bionanocomposites are strong candidates for orthopaedic implant applications [19,20,24-26]

In this study, we demonstrate the hydroxyapatite bioceramic particles reinforced aromatic thermosetting copolyester matrix bionanocomposite. The scope of this paper is reserved to give an insight into interfacial interaction and adhesion mechanisms between the HAs and ATSP matrix, which may lead to systematical biocompatibility analysis of the ATSP bionanocomposites in a follow-up study. Herein, we initially investigate the physicochemical

effects of the HAs on the thermal polymerization reaction. To understand the structural state of the HAs in the matrix, morphological analysis is performed on the nanocomposite. Mechanical characterization reveals a crack-arresting mechanism induced by the HAs that considerably enhances material deformation tolerance. Besides, glass transition characteristics are altered by segmental confinement of the polymer network instigated by the HAs. Chemical spectroscopy of the backbone chain configuration shows the formation of a covalent interfacial coupling between the HAs and ATSP matrix.

10.2 Materials and Methods

The ATSP-HA bionanocomposite is obtained via condensation polymerization reaction between carboxylic acid and acetoxy functional group constituent oligomers, which generate a cross-linked aromatic polyester backbone and emit acetic acid as a reaction by-product [21]. The matching oligomers are obtained using biphenol diacetate (BPDA), 4-acetoxybenzoic acid (ABA), isophthalic acid (IPA), and trimesic acid (TMA) (Sigma-Aldrich Co., USA) at particular molar feed ratios of 1:2:3:2 and 1:0:3:3 of TMA:IPA:ABA:BPDA for the carboxylic acid-capped and acetoxy-capped oligomers, respectively. Further details of the oligomer synthesis protocols are explained in earlier works [18,20]. For the preparation of the nanocomposite, the carboxylic acid and acetoxy-capped oligomer powders (pre-mixed at 1:1 weight ratio) are combined in solid state with 10 wt% of HA particle powder (particle size: 5μm±1μm, surface area ≥ 100m^2/g) (Sigma-Aldrich Co., USA) [23]. The nanocomposite specimens are produced using a thermal cure cycle applied to the powder mixture, which includes two dwell stages at 202 °C for 90 minutes and 270 °C for 150 minutes, and a final cure stage at 330°C for 90 minutes [21].

The cure characteristics of the ATSP-HA nanocomposite are analyzed using a Differential Scanning Calorimeter (DSC) (DSC 2910, TA Instruments, USA) and a

Thermogravimetric Analyzer (TGA) (TGA 2950, TA Instruments, USA). The cure characteristics of the neat mixture of the matching oligomers shown in the text are taken from reference [21]. The measurements are carried out under an inert atmosphere of nitrogen. The DSC and TGA samples weigh about 20 mg. A constant 10 °C/min of heating rate is applied during both cure and post-cure cycles in the DSC and TGA analyses. The DSC thermal cycle includes only a temperature-ramp process while the TGA thermal cycle comprises a temperature-ramp stage and a temperature-hold stage for 90 min at 330°C. As the HA-oligomer mixture is cured following the thermal cycle, it is kept under nitrogen atmosphere, to minimize exposure to the oxidative environment and thermal degradation effects, until the temperatures of the heating chambers of the DSC and TGA return to room temperature [23].

A Scanning Electron Microscope (SEM) (S-4700, Hitachi, Japan) is employed to image microstructures of uncured powder combinations, assisted with Energy Dispersive Spectroscopy (EDS) (Oxford Instruments, UK) to perform an elemental analysis. An SEM (S-4800, Hitachi, Japan) is utilized to image fracture surfaces of the nanocomposites. SEM images are obtained in high-resolution upper detector mode at 10-15 kV voltage and 5-10 μA current.

Morphologies of the ATSP nanocomposite and pristine HA particles are characterized using a powder X-ray diffractometer (XRD) (Siemens/Bruker D-5000) with Cu K-alpha source operated at 45 kV and 30 mA, and 0.15148 nm wavelength with 0.5°/s nominal scanning rate between diffraction angles of $2\theta=5°$ and $2\theta=60°$. The XRD spectrum of the neat ATSP shown in the text is taken from reference [23].

Compressive mechanical properties of foam morphology nanocomposite are determined using a compressive load frame (4483 Load Frame, Instron Testing Systems, USA) with a constant crosshead speed of 5 mm/min. The specimens are cylindrical with a diameter of 1.27

cm and a height of 2.54 cm. Density is calculated as the ratio of measured weight to volume of the specimens. Relative density is calculated as the ratio of the measured density of the nanocomposite foam morphology to the density of neat fully dense ATSP (1.27 Mg/m^3). The compressive mechanical properties are averaged over four test samples, and standard deviations are given by error bars, accordingly. The mechanical property results of the neat ATSP foams shown in the text are taken from reference [21].

Glass transition characterization of foam morphology nanocomposite is performed using a Dynamic Mechanical Analyzer (DMA) (Q800 TA Instruments) operated with a dual-cantilever beam (DCB) bending fixture. Three samples are tested and all exhibit overlapping thermal profiles. A temperature-ramp cycle is operated with a 3°C/min heating rate. The specimens are in dimensions of 35 x 10 x 5 mm^3 (length x width x thickness), and the tests are carried out in the air. The glass transition characteristic curve of the neat ATSP shown in the text is taken from reference [21].

Solid-state nuclear magnetic resonance (ssNMR) spectroscopy measurements are carried out using ground specimens (~50 mg) packed into NMR rotors with Varian Unity Inova 300 MHz NMR spectrometer. ^{1}H spectrum is obtained using direct pulse (DP) (pulse width (pw) = 2.5μs, recycle time (d1) = 2s) excitation. ^{13}C and ^{31}P spectra are obtained using cross-polarized (CP) (^{13}C; pulse width (pwH) = 2μs, recycle time (d1) = 2s, and contact time (tHX) = 4ms) (^{31}P; pulse width (pwH) = 2μs, recycle time (d1) = 2s, and contact time (tHX) = 3ms) excitations. The specimens are spun at 10 kHz. Data processing is performed using the MestreNova software.

X-ray photoelectron spectroscopy (XPS) (Kratos Axis ULTRA, Kratos Analytical) analyses are performed under a monochromatic Al source operated at 210 W with 1000 meV

step size, 100 ms dwell time, and 220 s total acquisition time. Data processing is carried out using the CasaXPS software.

10.3 Results

First, we discuss the effects of the solid-state mixing process on HA particle distribution of the HA particles within the oligomer powder domain. A 10 wt% of the HA particles is incorporated with the precursor carboxylic acid and acetoxy oligomer groups (premixed at 1:1 wt ratio) which forms the precuring ATSP-HA combination, which is then subjected to a thermal polymerization process. Hence, the ATSP-HA nanocomposite is obtained through an *in situ* polycondensation reaction between the functionalized constituent oligomers while the HA particles are also present [17,19] (refer to Materials and Methods section for details). The polymerization process generates a crosslinked polymer network while releasing acetic acid as a reaction by-product. The acetic acid evolves in the gas form at ~200 °C during the reaction, which acts as a blowing agent to develop porous matrix morphology. In Figure 10.1, a scanning electron microscope (SEM) image demonstrates HA particles (white spheres) effectively dispersed over an oligomer particle. We highlight that, due to the presence of the interparticle forces, the HAs are pinned down on the surface of the oligomer particles. The representative chemical configurations given in the same figure show that the constituent oligomer chains, as well as the ATSP backbone chain, comprise H, C, and O while the HA contains H, O, P, and Ca. Through a correlative analysis using an energy-dispersive spectrometer (EDS), elemental mapping of the very same region reveals the presence of the corresponding elements. The content of C dominates over other elements due to the abundance of C in the precursors. More importantly, P and Ca element maps clearly unveil the HA particles in the domain.

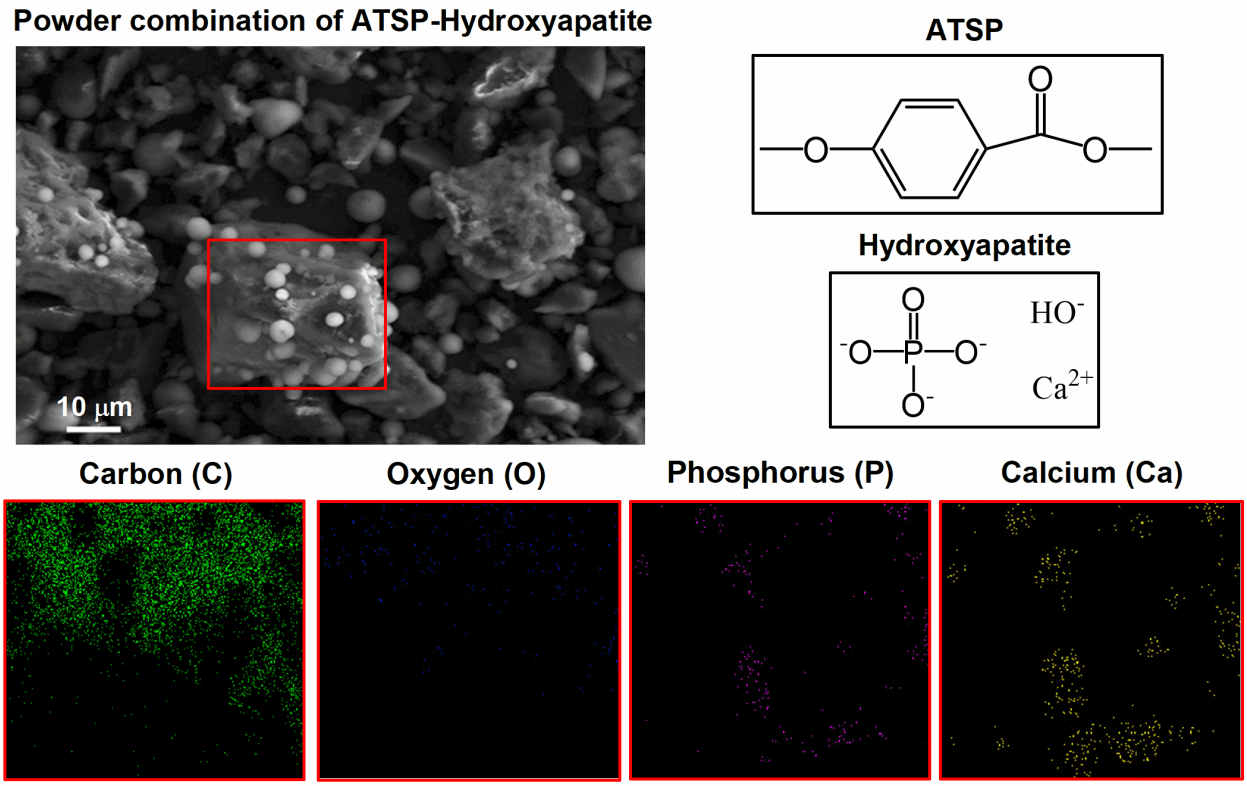

Figure 10.1 Microstructural analysis of solid-state mixed precursor oligomers and hydroxyapatite particles. Scanning electron microscopy (SEM) image of uncured powder combination of an precursor oligomer particle (appears darker) decorated with hydroxyapatite (HA) particles (appears brighter). Energy dispersive X-ray spectroscopy (EDS) surface maps of elemental composition (C, O, P, and Ca) of the combination highlighted in the red frame. Chemical representations of the ATSP backbone chain and hydroxyapatite structures.

Next, we explain the influence of the HA particles on the *in situ* endothermic condensation polymerization reaction carried out between the matching precursors. In this regard, a temperature-ramp differential scanning calorimetry (DSC) cycle is initially applied to the combined mixture of the precursor oligomers and HAs (ATSP-HA), as illustrated in Figure 10.2.a. In the beginning, the thermal profile reveals a dimple around 70 °C which corresponds to structural softening of the oligomers [21]. Afterward, the heat flux curve maintains an endothermic behavior during which melting and polycondensation reaction stages progress ordinarily. The corresponding portions of the thermal curve do not differentiate from the neat mixture of the precursor oligomers (neat ATSP) [21,23]. Following this, the curing process

initiates (denoted as cure onset) around at 260 °C, similar to that of the parent form, where the thermal curve displays a genuine endothermic cure region. The combined mixture of the ATSP-HA exhibits a distinctly broader cure region than the neat precursors for which the completion of the curing process extends beyond 360 °C. In addition, upon completion of the curing process, a thermal relaxation peak, a small hump (denoted as cure end) is observed. Following the cure cycle, subsequent post-cure analysis exhibits an isothermal characteristic curve, without any features arising from the curing process, indicating sufficient curing for the nanocomposite system.

To supplement the DSC characterization, we carry out thermogravimetric analysis of the polycondensation reaction on the precuring ATSP-HA combination using a thermogravimetric analyzer (TGA). As noted above, the polymerization process releases acetic acid as a reaction by-product, so the TGA characterization is sought to resolve temperature and mass changes for the acetic acid release step during the reaction. Hence, a two-stage thermal cycle is applied in which a temperature-ramp is initially performed until 330°C, and then a temperature-hold at 330°C is applied for 90 min [23]. Figure 10.2.b demonstrates cure and post-cure cycles obtained from the combined mixture of the precursor oligomers and HAs (ATSP-HA). The TGA curve displays a substantial mass loss of ~15 wt% that is associated with the release of acetic acid. More importantly, the TGA analysis reveals a delayed higher temperature release of the acetic acid for the ATSP-HA combination in comparison to the neat mixture of the precursor oligomers. The subsequent gradual decline in the thermogravimetric curve within the temperature-hold region (40-120 min) corresponds to crosslinking network formation during which only small weight loss occurs, which takes place due to thermal degradation of reactive functional groups at elevated temperatures. Afterward, post-cure cycles demonstrate nearly-flat

thermogravimetric curves indicating fully cured conditions during the first cycles for the given period.

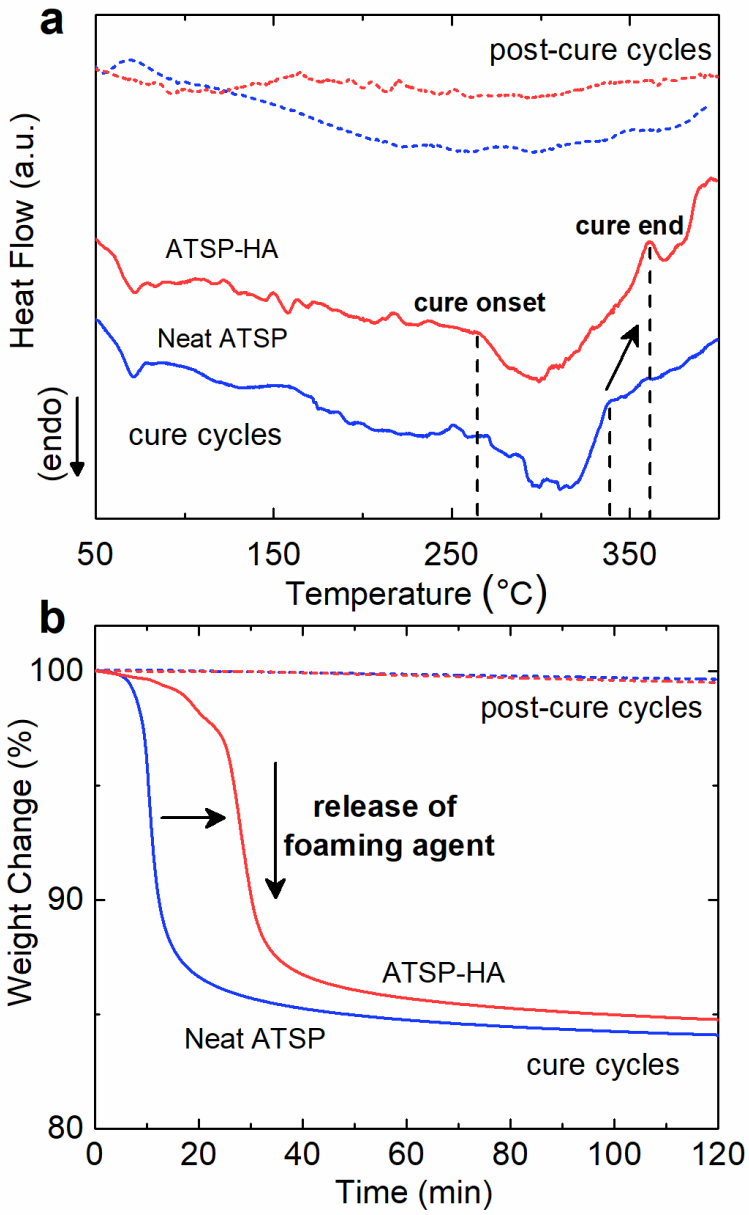

Figure 10.2 Thermal characteristics of polymerization reaction. (a) Differential scanning calorimetry (DSC) analyses of cure and post-cure characteristics of the neat mixture of the precursor oligomers (neat ATSP) and combined mixture of the precursor oligomers with hydroxyapatite (HA) particles (ATSP-HA). The DSC curves are stacked by arbitrary offsets to illustrate chemical features. (b) Thermogravimetric analysis (TGA) characterization of cure and post-cure profiles of the neat mixture of the constituent oligomers (neat ATSP) and combined mixture of the oligomers with hydroxyapatite (HA) particles (ATSP-HA). The tests are performed under an inert atmosphere of nitrogen with a heating rate of 10°C/min.

To evaluate the structural state of the HAs within the ATSP matrix as well as the overall morphology of the nanocomposite structure, we perform X-ray diffraction (XRD) analysis. Figure 10.3 shows XRD spectra of the neat ATSP, pristine HA particles, and ATSP-HA nanocomposite. The neat ATSP matrix displays a very broad primary peak centered around $2\theta=20°$ meaning an extensively amorphous morphology [23]. Also, the pristine HAs reveal a characteristic crystalline domain for which the detected main peaks are marked in the figure. The peaks are located at $2\theta=25.8°$ corresponding to lattice planes of (002), $2\theta = 31.8^{\circ}$ of (211), $2\theta = 32.8^{\circ}$ of (112), $2\theta = 34^{\circ}$ of (300), $2\theta = 39.7^{\circ}$ of (130), $2\theta = 46.7^{\circ}$ of (222), $2\theta = 49.4^{\circ}$ of (213), $2\theta = 53.1^{\circ}$ of (004) [26,27]. In this regard, the ATSP-HA nanocomposite displays a similarly broad primary peak at a similar diffraction angle as the neat ATSP, which indicates that the amorphous nature of the host ATSP matrix likewise is preserved. We also observe that the characteristic peaks arising from the HAs are effectively transmitted into the spectra highlighting that the HA particles are well incorporated into the nanocomposite morphology.

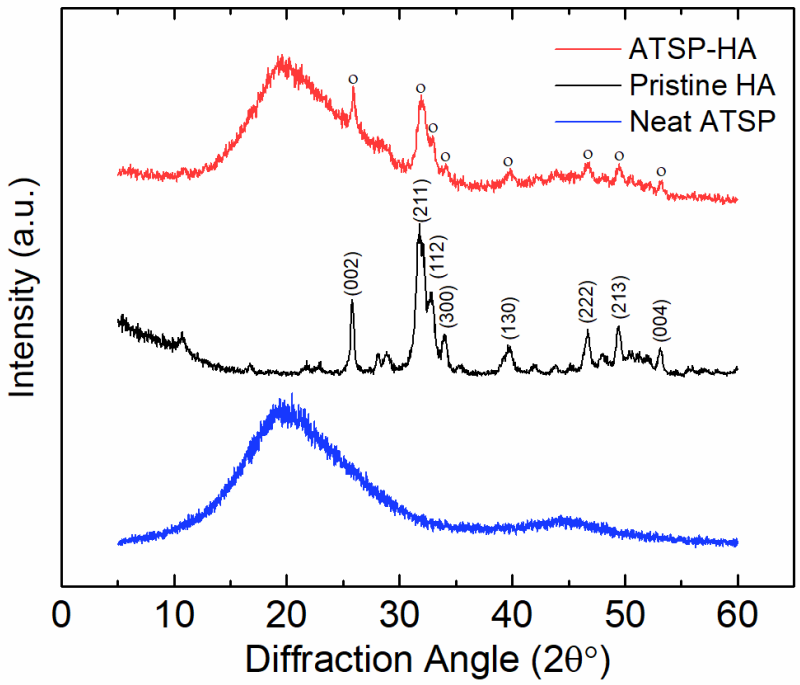

Figure 10.3 Morphological characterization of nanocomposite. X-ray diffraction (XRD) characterization of neat ATSP foam (neat ATSP), pristine hydroxyapatite particles (pristine HA), and hydroxyapatite particles incorporated ATSP nanocomposite foam (ATSP-HA). The XRD curves are stacked by arbitrary offsets to illustrate morphological features.

Microstructural analysis of fracture surfaces via scanning electron microscopy (SEM) shows several visual characteristic features of such interfacial interactions coming into effect between the HAs and ATSP matrix, as demonstrated in Figure 10.4. First, the HAs are well dispersed into the matrix with minimal aggregation sites (Figure 10.4.a). As noticed, fracture propagates through HA particle sites. In some cases, fracture propagation results in such HA particles that crack in place, which is also a strong indication of the intrinsic physical response of the HAs being effectively transmitted to the overall physical response of the nanocomposite structure (Figure 10.4.b). Also, as fracture progresses and damages the HA particles, some HAs are broken and remain embedded in the matrix, which indicates the presence of an interfacial coupling between the HAs and ATSP matrix chains (Figure 10.4.c). We also observe that some HAs slip off the surface, so the partially reduced interfacial bonding strength is a downside of

this attachment mechanism (Figure 10.4.d). Note that the HAs are not coated with the ATSP resin such that the particles and the precursor oligomers may not effectively form *in situ* interactions during the polymerization process [23]. We also highlight that the homogenous dispersion state, as promoted in the prepolymerization solid-state mixing stage, is effectively preserved during the polymerization reaction. Hence, to further interrogate the bonding mechanism between the HAs and ATSP backbone chains, we employ mechanical, thermomechanical and chemical analyses, as presented in the remaining text.

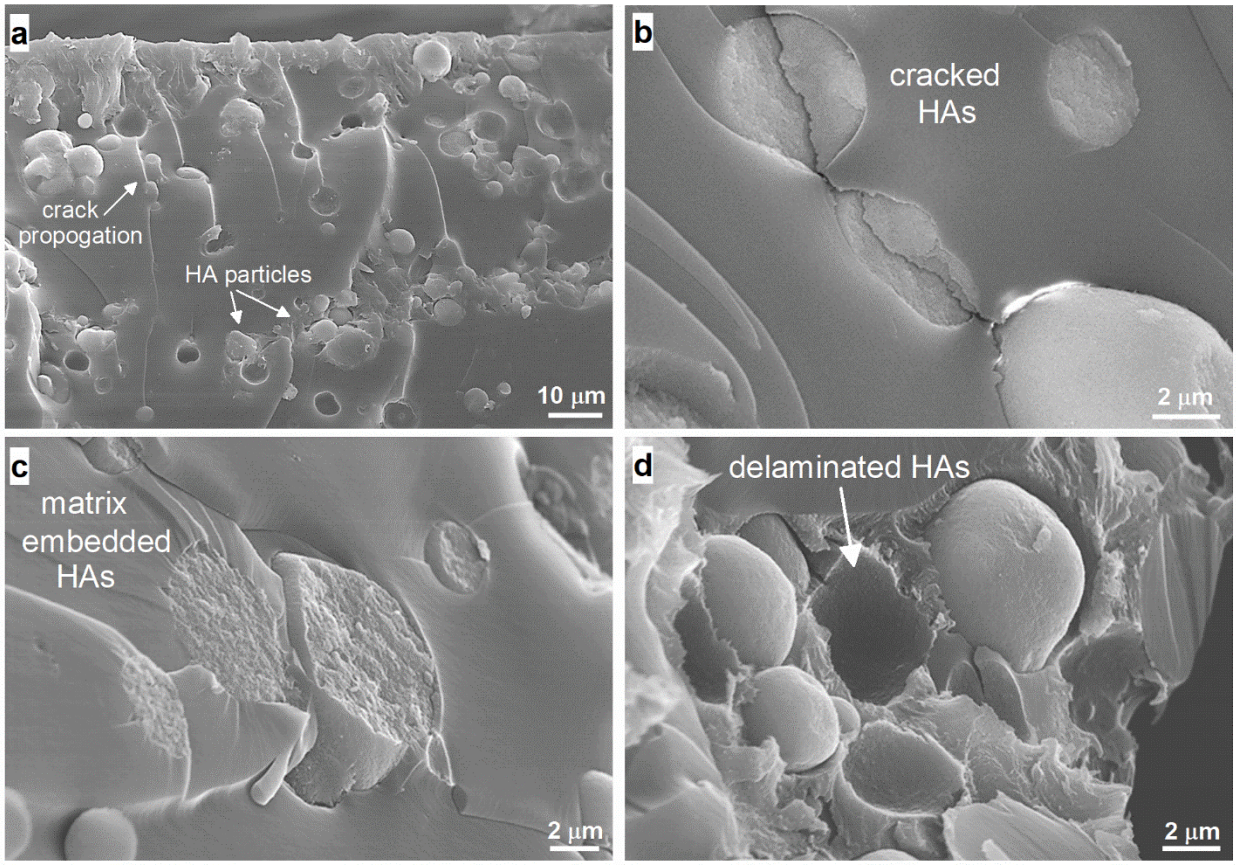

Figure 10.4 Microstructural characterization of the ATSP-HA nanocomposite. Scanning electron microscopy (SEM) images obtained on fracture surfaces of the nanocomposites. Well-dispersed HAs behave as crack-arresters within the matrix (a), fracture propagates through the HA particles (b), HAs remain broken and embedded in the matrix upon fracture (c), and some HAs slip due to limited strength of interfacial coupling (d).

To observe the extent of the crack-arresting mechanism as well as the interfacial coupling scheme on the deformation response, we perform compressive mechanical tests on the nanocomposite structure. Figure 10.5 shows representative stress-strain curves obtained on the neat ATSP and ATSP-HA porous nanocomposite structures. The HA nanocomposite displays the two unique features of improved stress and strain at fracture. The compressive mechanical strength is increased by about 10% compared to the parent ATSP form. Also, the strain at maximum stress is enhanced by approximately 18% in comparison to the neat structure. Besides, the ATSP-HA nanocomposites become relatively softer structures where Young's modulus decreases by approximately 15%. The densities of the two forms are almost same. Note that theoretical density of hydroxyapatite is 3.16 Mg/m^3, which is subject to change for different sintering temperatures employed during the manufacturing process (the neat porous ATSP morphology possesses a density of 0.54±0.03 Mg/m^3) [28].

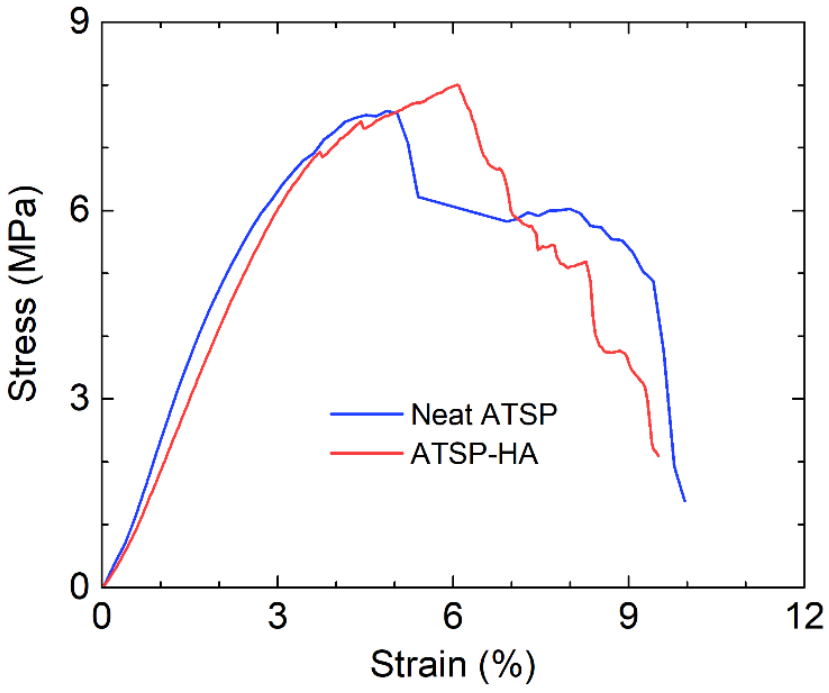

Figure 10.5 Characterization of mechanical performance. Representative compressive stress-strain curves of the neat ATSP and ATSP-HA nanocomposite foams.

Table 10.1 Compressive mechanical properties of the neat ATSP and ATSP-HA nanocomposite foams. The results are averaged over four specimens.

	Young's Modulus (GPa)	**Compressive Strength (MPa)**	**Density (Mg/m^3)**	**Relative Density**	**Strain-to-Failure (%)**
ATSP	0.27±0.04	7.62±0.5	0.54±0.03	0.42±0.03	5.34±1.10
ATSP-HA	0.23±0.04	8.31±0.3	0.55±0.01	0.43±0.01	6.29±0.70

We analyze glass transition behavior of the ATSP-HA nanocomposite to investigate the interfacial interactions of the HA particles and ATSP backbone chain. Note that the glass transition temperature is an exclusive feature of temperature-dependent structural relaxation characteristics of backbone chains for amorphous polymers, which hence can display chemical modifications induced in polymer network through nanofillers [29-31]. In Figure 10.6, neat ATSP parent material exhibits two characteristic peaks of sub-glass transition (β-transition) (T_β) at 79°C and glass transition (T_g) at 191 °C [21]. In comparison to the base form, the nanocomposite exhibits two distinct peaks within the glass transition domain. A low-temperature peak arises from the genuine structural relaxation of the matrix (the crosslinked network), which, in fact, slightly downshifts to ~158 °C for the reference base material. As well, a high-temperature peak forms due to suppressed segmental relaxation of the chains incurred through the presence of the HAs (refer to the Discussion section for detailed analysis of the glass transition characteristics). In the following part, we present results of chemical analyses on the nanocomposites to unveil the nature of interfacial attachment scheme between the HAs and ATSP.

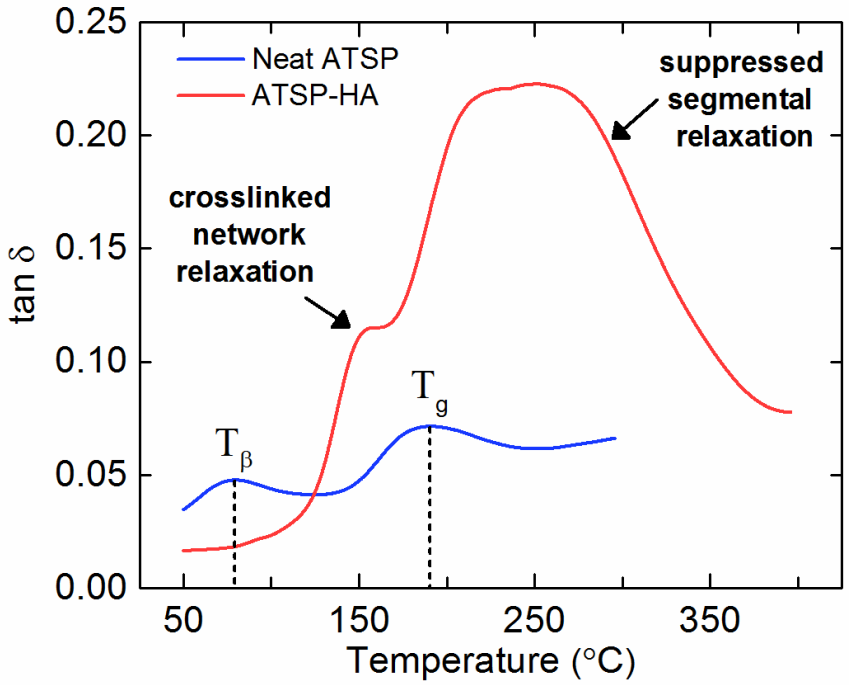

Figure 10.6 Characterization of polymer chain relaxation dynamics. Dynamic mechanical analysis (DMA) tangent delta (tan δ) profiles of the glass transition characteristics of the neat ATSP and ATSP-HA nanocomposite foams.

Solid-state Nuclear Magnetic Resonance (ssNMR) characterization is carried out to analyze the interfacial interactions between the HA particles and ATSP matrix. Figure 10.7 shows ^{1}H direct pulse magic-angle spinning (DPMAS), ^{13}C cross-polarization magic-angle spinning (CPMAS), and ^{31}P CPMAS spectra of the pristine HA, neat ATSP, and ATSP-HA nanocomposite formulations. First, the ^{1}H spectrum of the pristine HA demonstrates four peaks which are detected at -0.1 ppm, 1.0 ppm, 3.5 ppm, and 5.5 ppm (Figure 10.7.a). In particular, the peak at -0.1 ppm corresponds to hydroxyl ions (OH^-), and 5.5 ppm corresponds to absorbed water H_2O molecules [32]. The other sharp peaks (1.0 ppm and 3.5 ppm) may define apatitic functional groups in the HA structure. The neat ATSP shows a broad peak at 5.0 ppm with a linewidth of ~1640 Hz (Figure 10.7.d). The ATSP-HA nanocomposite exhibits a broad peak at 6.9 ppm with a linewidth of ~1844 Hz, which similarly reflects the matrix characteristics with a

notable line broadening (Figure 10.7.g). Also, we detect two small peaks at chemical shifts of -0.1 ppm and 3.5 ppm which are likely to come from the pristine HA. Second, the ^{13}C spectrum of the neat ATSP shows two characteristic peak groups corresponding to the aromatic backbone chains (C-C/C-H bonds) and the functional side-chains (C-O and C=O bonds) with a measured linewidth of ~860 Hz (Figure 10.7.e). For the nanocomposite, the linewidth increases to ~1428 Hz (over the highest intensity peak ~130 ppm) while preserving the original chemical configuration (Figure 10.7.h). Third, the ^{31}P spectrum of the pristine HA shows a characteristic peak at 2.7 ppm having a linewidth of ~95 Hz, as well a small broad secondary peak is identified around 5.5 ppm (Figure 10.7.c). In comparison, the nanocomposite displays a peak 2.9 ppm with a linewidth of ~125 Hz (Figure 10.7.i). We also perform ^{31}P anisotropy measurements using a higher-field ssNMR spectrometer (data not shown) and no significant difference is observed between the pristine HA and ATSP-HA composite.[33,34] As noticed, all the elemental spectra validate a significant peak broadening through the interactions with the HAs giving rise to peak broadening through ultimately altered structural relaxation behavior under a magnetic field of the backbone chains in the nanocomposite structure [35,36]. Particularly, such a peak broadening may be attributed to the interfacial entanglement of the polymer chains and the nanofiller particles causing electron mobility difference between highly crystalline HA particles amorphous ATSP chains.

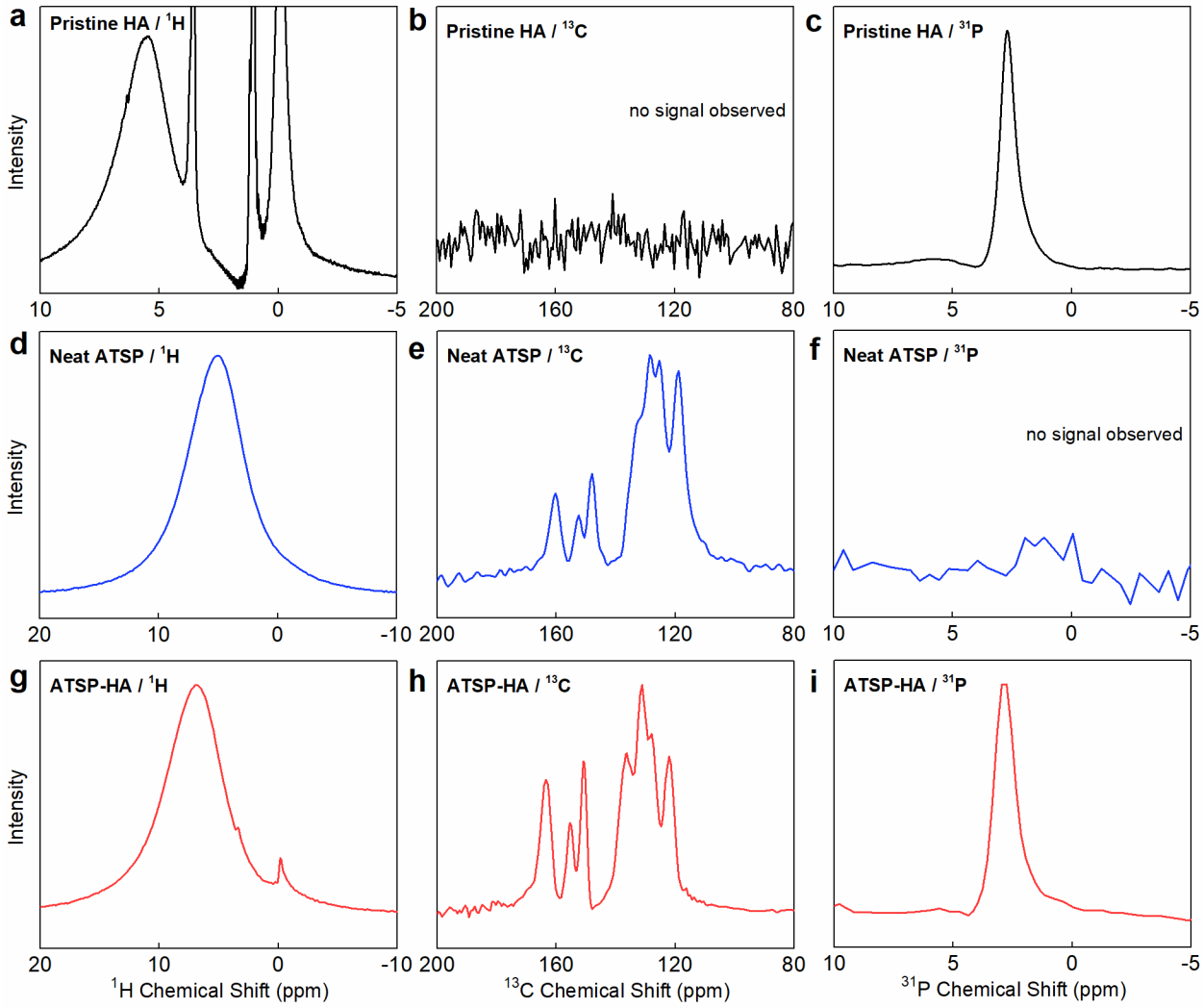

Figure 10.7 Characterization of interfacial interactions via Solid-state Nuclear Magnetic Resonance spectroscopy. Solid-state Nuclear Magnetic Resonance (ssNMR) ^{1}H direct pulse magic-angle spinning (DPMAS), ^{13}C cross-polarization magic-angle spinning (CPMAS), ^{31}P CPMAS spectra of the pristine HA particles (a, b, c), neat ATSP (d, e, f), and ATSP-HA nanocomposite (g, h, i) morphologies. No characteristic signals are observed in spectral windows of b and f. ^{1}H NMR spectra were processed using 1 Hz line broadening. ^{13}C and ^{31}P NMR spectra were processed using 25 Hz line broadenings.

Figure 10.8 demonstrates elemental spectra of O, C, P, and Ca obtained using X-ray Photoelectron Spectrometer (XPS) on the pristine HA, neat ATSP, and ATSP-HA nanocomposite. In the O 1s spectra (Figure 10.8. a-c), no additional oxygen-bonded peak formation is observed in the nanocomposite structure. Also, in the P 2p spectra (Figure 10.8. d, e), primitive phosphate form of the HAs is preserved within the nanocomposite. Similarly, in Ca

2p spectra (Figure 10.8. f, g), calcium does not form any further bonding with polymer chains. For the C 1s spectra (Figure 10.8. h, i), we likewise do not observe any additional bond peak developed with the backbone network.

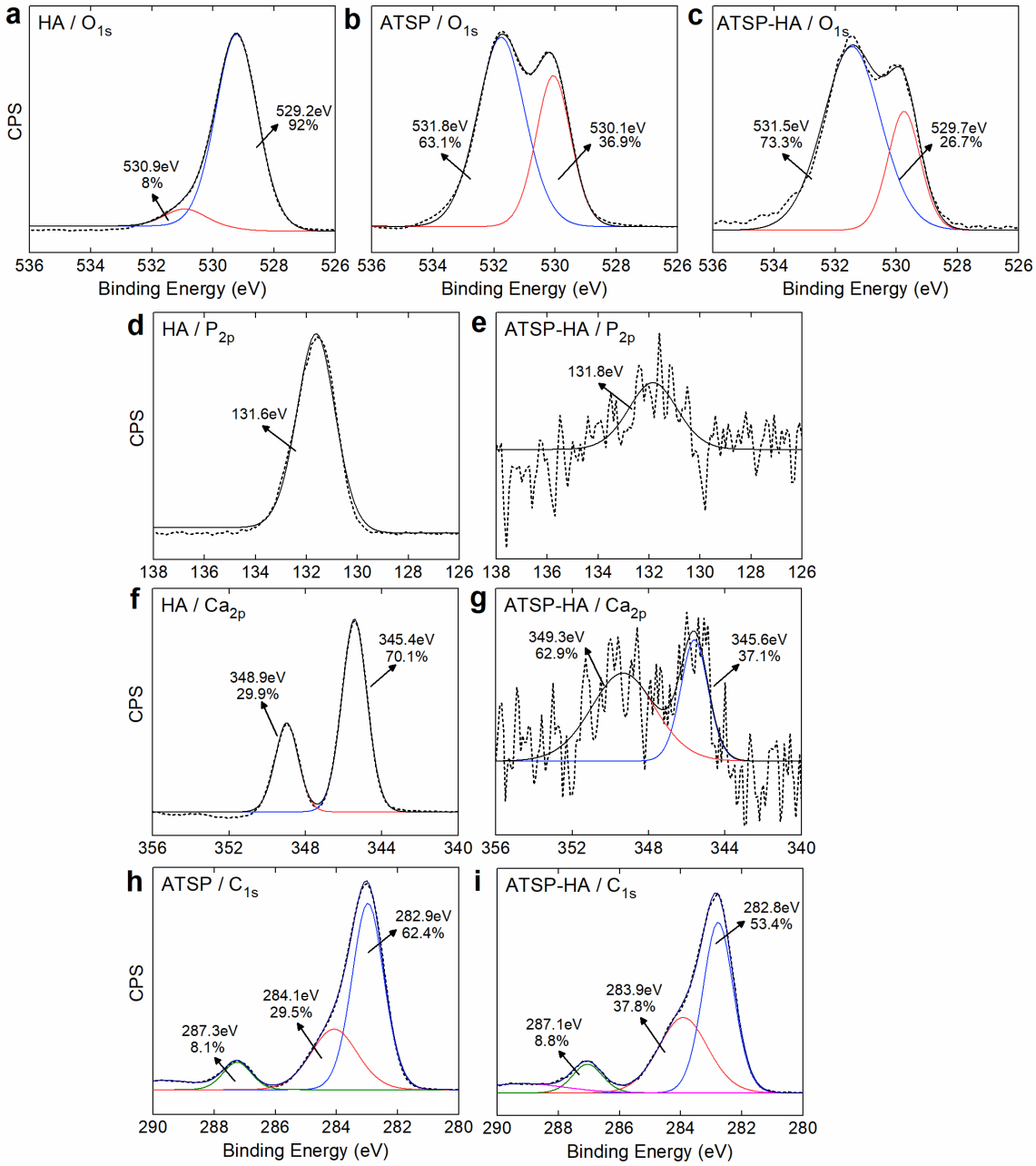

Figure 10.8 Characterization of interfacial interactions via X-ray photoelectron spectroscopy. X-ray photoelectron spectroscopy (XPS) O 1s spectra of the pristine hydroxyapatite (HA) (a), neat ATSP (b) and hydroxyapatite-ATSP nanocomposite (ATSP-HA) (c). P 2p spectra of the HA (d) and ATSP-HA (e). Ca 2p spectra of the HA (f) and ATSP-HA (g). C 1s spectra of the neat ATSP (h) and ATSP-HA (i).

10.4 Discussion

The prime feature of the solid-state mixing approach is to characteristically establish geometrical conformity between the HAs of ~5 μm and the oligomer particles of ~50-100 μm. Such an interparticle proportionality imminently develops short-range attractive forces between the HAs and precursor particles while subsiding the van der Waals forces that are inherently present within the pristine HA particle supply [23]. Hence, the *in situ* formed attractive forces draw the HAs and ATSP oligomer particles together which effectively breaks the primitive HA clusters apart enabling good distribution of the HAs within the powder oligomer domain. Furthermore, hydrodynamic forces coming into effect at elevated temperatures in molten oligomer medium in the course of the polymerization reaction enable the acetic acid blowing agent to advance in the viscous phase. Such relocation of the acetic acid bubbles facilitates rearrangement of the HAs prior to curing and ultimately contributes to nearly homogeneous distribution in the nanocomposite morphology [21,23,37].

Regarding the cure characterization of the precursor oligomers with the HAs, the broadening of the cure region observed in the DSC analysis may occur due to the increased melt viscosity of the oligomers caused by the presence of the HAs. The increase in viscosity consequently requires more energy input to carry out the crosslinking process, which thus stimulates early gelation of the crosslinked matrix [38,39]. Hence, the thermal relaxation peak forms due to devitrification of the matrix in the thermal process during which the glass transition temperature increases above the cure temperature [40]. Such a thermal response indicates that the degree of crosslinking is likewise considerably affected by the presence of the HAs, as also discussed in the glass transition characteristics. In the thermogravimetric response of the polymerization process, the delayed release of the acetic acid indicates notable modifications in

the reaction kinetics. It also concurs with the outcomes of the DSC analysis that completion of the curing extends beyond the nominal temperature.

Improvements in physical properties for the bionanocomposite structure are directly regulated by interfacial coupling of the reinforcement particles and host matrix. As observed in SEM images, the HAs behave as crack arresters within the polymer domain which impedes further fracture propagations. Eventually, such a particle-conjugated network yields a more deformation tolerant morphology with significantly increased material toughness. In correlation with the SEM analysis, several conclusions can be drawn from the compressive mechanical characterization results. For conventional polymer nanocomposites, improved mechanical properties generally cause a more brittle response [41,42]. However, the ATSP-HA nanocomposite maintains simultaneous increases in the fracture strength and strain, meaning improved material toughness. Hence, the nearly-preserved density of the structure, yet rather enhanced mechanical performance, indicate that HAs are very well incorporated into the matrix which develops an effective load transfer mechanism demonstrating significant improvements in the deformation tolerance. Earlier studies have reported increased Young's modulus for polymer nanocomposites with the incorporation of HAs, as also being conceivable due to significantly higher density and hardness values associated with the HAs [43,44]. However, the moderate decrease of Young's modulus in the ATSP-HA nanocomposites may be related to modifications induced either in the cellular morphology (e.g., porosity) or the chemical structure (e.g., crosslinked polymer chain configuration) that eventually lead to considerably softer nanocomposite structures, which are highlighted in the following chemical characterization part of the text. Hence, on the contrary to predictions introduced with analytical models, the mechanical property improvements observed in the ATSP bio-nanocomposites are directly

linked to an interfacial attachment scheme developed with the particles which effectively surpasses a mere reinforcement mechanism attainable with matrix-trapped ceramic particles [45]. Unparadoxically, the results of the mechanical characterization for the improved material toughness agree with the observations reported for the crack-arresting mechanism in the SEM microstructural analysis section.

According to the characterization of the glass transition temperature, particularly, for the low-temperature peak, in agreement with the characteristic features observed in the cure analyses, the presence of the HAs modifies the advancing crosslinking process during the polymerization process which, in this case, may promote longer polymer chains. The longer the polymer chains within the crosslinked network, the more degree of freedom is introduced to the chains which then develops a lower temperature glass transition peak [21]. Alternatively, the free volume occupied by the HAs may induce a lower glass transition temperature for the overall matrix [46]. In this case, the interfacial attachment between the HAs and the ATSP matrix is destroyed at elevated temperatures creating free volumes in the crosslinked network that gives rise to a lower glass transition relaxation. Regarding the formation of the second peak, the physical presence of the HAs forms a pseudo-rheological percolation behavior within the matrix facilitated through short inter-nanoparticle distances, which restricts the mobility of the chains, and subsequently increases the total chain relaxation time [29,30]. Overall, the double glass transition peak formation as a thermomechanical response of the nanocomposite structure also agrees with results shown in prior literature [47-50].

Supported by the XPS results, the interfacial bonding related line broadening observed in NMR may occur via *in situ* formed hydrogen-advanced bonds. Note that only ^{1}H ssNMR spectra of the nanocomposite backbone displayed additional peaks emerging from the chemical

configuration of the HAs. The precursor oligomers possess acetoxy and carboxylic acid functional groups that are composed of hydrogen bonds which can interact with the constituent elements in the HA structure [51]. Yet, hydrogen has no core electrons, but only valence electrons which participate in the chemical bonding. Thus, any XPS signal arising from hydrogen would overlap with signals from excitation of valence electrons of other constituent elements. Hence, it is technically impossible to distinguish between valence electrons of hydrogen and other elements. The hydrogen groups, via an interfacial attachment mechanism, are only viable until about 100°C which in fact causes a lower glass transition temperature, as observed in DMA analysis [31]. Due to bond scissions at elevated temperatures near glass transition region free volumes in the chain configuration are generated which then effectively downshifts the glass transition temperature. Yet, the H-driven bond is workable at room temperature, which in fact improves the mechanical performance of the nanocomposite participating in the crack-arresting deformation mechanism.

10.5 Conclusion

We demonstrate the hydroxyapatite (HA) particle reinforced aromatic thermosetting copolyester (ATSP) matrix bionanocomposite as a potential artificial bone replacement material. During the *in situ* endothermic polycondensation reaction, the matching oligomers form a robust crosslinked network of aromatic backbone having HAs distributed in the polymer domain, as validated through morphological analysis. The HAs offer a crack-arresting mechanism which develops an effective load transfer network along with enhanced material toughness. Glass transition characteristics of the bionanocomposite matrix are modified through nanofiller-immobilized local chain relaxation effects. ssNMR and XPS analyses on backbone chain of the nanocomposite exhibit the presence of a hydrogen bonding-based interfacial coupling between

the HAs and ATSP matrix through *in situ* formed hydrogen bonds. Future work may focus on systematical biocompatibility analysis of the ATSP matrix and ATSP bionanocomposites. This study may initiate further analyses of intermolecular interactions between the bioceramic particles and biocompatible polymer systems towards the improved physical performance of advanced synthetic bone bionanocomposites.

10.6 References

[1] Giannoudis, P. V., Dinopoulos, H. & Tsiridis, E. Bone substitutes: an update. Injury 36, 20-27, https://doi.org/10.1016/j.injury.2005.07.029 (2005).

[2] Van Heest, A. & Swiontkowski, M. Bone-graft substitutes. The Lancet 353, 28-29, https://10.1016/S0140-6736(99)90228-3 (1999).

[3] Campana, V. et al. Bone substitutes in orthopaedic surgery: from basic science to clinical practice. Journal of Materials Science. Materials in Medicine 25, 2445-2461, https://10.1007/s10856-014-5240-2 (2014).

[4] Schwartz, C., Liss, P., Jacquemaire, B., Lecestre, P. & Frayssinet, P. Biphasic synthetic bone substitute use in orthopaedic and trauma surgery: clinical, radiological and histological results. Journal of Materials Science: Materials in Medicine 10, 821-825, https://10.1023/a:1008944227417 (1999).

[5] Gupta, A. et al. Bone graft substitutes for spine fusion: a brief review. World Journal of Orthopedics 6, 449-456, https://10.5312/wjo.v6.i6.449 (2015).

[6] Daculsi, G. Biphasic calcium phosphate concept applied to artificial bone, implant coating and injectable bone substitute. Biomaterials 19, 1473-1478 (1998).

[7] Arner, J. W. & Santrock, R. D. A historical review of common bone graft materials in foot and ankle surgery. Foot & ankle specialist 7, 143-151 (2014).

[8] Bucholz, R. W., Carlton, A. & Holmes, R. E. Hydroxyapatite and tricalcium phosphate bone graft substitutes. The Orthopedic clinics of North America 18, 323-334 (1987).

[9] Kolk, A. et al. Current trends and future perspectives of bone substitute materials – from space holders to innovative biomaterials. Journal of Cranio-Maxillofacial Surgery 40, 706-718, https://doi.org/10.1016/j.jcms.2012.01.002 (2012).

[10] Darder, M., Aranda, P. & Ruiz-Hitzky, E. Bionanocomposites: a new concept of ecological, bioinspired, and functional hybrid materials. Advanced Materials 19, 1309-1319, https://10.1002/adma.200602328 (2007).

[11] Gasser, B. About composite materials and their use in bone surgery. Injury 31, 48-53, https://doi.org/10.1016/S0020-1383(00)80023-6 (2000).

[12] Wagoner Johnson, A. J. & Herschler, B. A. A review of the mechanical behavior of CaP and CaP/polymer composites for applications in bone replacement and repair. Acta Biomaterialia 7, 16-30, https://doi.org/10.1016/j.actbio.2010.07.012 (2011).

[13] Rezwan, K., Chen, Q. Z., Blaker, J. J. & Boccaccini, A. R. Biodegradable and bioactive porous polymer/inorganic composite scaffolds for bone tissue engineering. Biomaterials 27, 3413-3431, https://doi.org/10.1016/j.biomaterials.2006.01.039 (2006).

[14] Lee, H. J., Choi, H. W., Kim, K. J. & Lee, S. C. Modification of hydroxyapatite nanosurfaces for enhanced colloidal stability and improved interfacial adhesion in nanocomposites. Chemistry of Materials 18, 5111-5118, https://10.1021/cm061139x (2006).

[15] Verma, D., Katti, K. S. & Katti, D. R. Effect of biopolymers on structure of hydroxyapatite and interfacial interactions in biomimetically synthesized hydroxyapatite/biopolymer nanocomposites. Annals of Biomedical Engineering 36, 1024, https://10.1007/s10439-008-9483-2 (2008).

[16] Deng, X., Hao, J. & Wang, C. Preparation and mechanical properties of nanocomposites of poly(d,l-lactide) with Ca-deficient hydroxyapatite nanocrystals. Biomaterials 22, 2867-2873, https://doi.org/10.1016/S0142-9612(01)00031-X (2001).

[17] Lee, H. J. et al. The effect of surface-modified nano-hydroxyapatite on biocompatibility of poly(ε-caprolactone)/hydroxyapatite nanocomposites. European Polymer Journal 43, 1602-1608, https://doi.org/10.1016/j.eurpolymj.2007.02.030 (2007).

[18] Frich, D., Goranov, K., Schneggenburger, L. & Economy, J. Novel high-temperature aromatic copolyester thermosets: synthesis, characterization, and physical properties. Macromolecules 29, 7734-7739, https://10.1021/ma960862d (1996).

[19] Frich, D. & Economy, J. Thermally stable liquid crystalline thermosets based on aromatic copolyesters: preparation and properties. Journal of Polymer Science Part A: Polymer Chemistry 35, 1061-1067 (1997).

[20] Vaezian, B., Meyer, J. L. & Economy, J. Processing of aromatic thermosetting copolyesters into foams and bulk parts: characterization and mechanical properties. Polymers for Advanced Technologies 27, 1006-1013, https://10.1002/pat.3762 (2016).

[21] Bakir, M., Meyer, J. L., Economy, J. & Jasiuk, I. Heat-induced polycondensation reaction with self-generated blowing agent forming aromatic thermosetting copolyester foams. Macromolecules 49, 6489-6496, https://10.1021/acs.macromol.6b00971 (2016).

[22] Shi, F. F. & Economy, J. Moisture transport studies on newly developed aromatic and aromatic/aliphatic copolyester thin films. Journal of Polymer Science Part B: Polymer Physics 36, 1025-1035 (1998).

[23] Bakir, M., Meyer, J. L., Economy, J. & Jasiuk, I. Aromatic thermosetting copolyester nanocomposite foams: high thermal and mechanical performance lightweight structural materials. Polymer 123, 311-320, https://doi.org/10.1016/j.polymer.2017.07.030 (2017).

[24] Huang, Y. & Economy, J. Aromatic thermosetting copolyester (ATSP)/UHMWPE blends with improved wear properties and biocompatibility. MRS Proceedings 1063, https://10.1557/PROC-1063-OO09-09 (2011).

[25] Bakir, M. et al. Effects of environmental aging on physical properties of aromatic thermosetting copolyester matrix neat and nanocomposite foams. Polymer Degradation and Stability 147, 49-56, https://doi.org/10.1016/j.polymdegradstab.2017.11.009 (2018).

[26] Panda, R. N., Hsieh, M. F., Chung, R. J. & Chin, T. S. FTIR, XRD, SEM and solid state NMR investigations of carbonate-containing hydroxyapatite nano-particles synthesized by hydroxide-gel technique. Journal of Physics and Chemistry of Solids 64, 193-199, https://doi.org/10.1016/S0022-3697(02)00257-3 (2003).

[27] Chen, F., Wang, Z.-C. & Lin, C.-J. Preparation and characterization of nano-sized hydroxyapatite particles and hydroxyapatite/chitosan nano-composite for use in biomedical materials. Materials Letters 57, 858-861, https://doi.org/10.1016/S0167-577X(02)00885-6 (2002).

[28] Feng, P., Niu, M., Gao, C., Peng, S. & Shuai, C. A novel two-step sintering for nano-hydroxyapatite scaffolds for bone tissue engineering. Scientific Reports 4, 5599, https://10.1038/srep05599 (2014).

[29] Bansal, A. et al. Quantitative equivalence between polymer nanocomposites and thin polymer films. Nat Mater 4, 693-698 (2005).

[30] Oh, H. & Green, P. F. Polymer chain dynamics and glass transition in athermal polymer/nanoparticle mixtures. Nat Mater 8, 139-143 (2009).

[31] Liao, K.-H., Aoyama, S., Abdala, A. A. & Macosko, C. Does graphene change Tg of nanocomposites? Macromolecules 47, 8311-8319 (2014).

[32] Yon, M. et al. Solid-state 31P and 1H chemical MR micro-imaging of hard tissues and biomaterials with magic angle spinning at very high magnetic field. Scientific Reports 7, 8224, https://10.1038/s41598-017-08458-0 (2017).

[33] Rothwell, W., Waugh, J. & Yesinowski, J. High-resolution variable-temperature phosphorus-31 NMR of solid calcium phosphates. Journal of the American Chemical Society 102, 2637-2643 (1980).

[34] Braun, M., Hartmann, P. & Jana, C. 19F and 31P NMR spectroscopy of calcium apatites. Journal of Materials Science: Materials in Medicine 6, 150-154, https://10.1007/bf00120291 (1995).

[35] Chen, J. et al. Noncovalent engineering of carbon nanotube surfaces by rigid, functional conjugated polymers. Journal of the American Chemical Society 124, 9034-9035 (2002).

[36] Bain, A. D., Eaton, D. R., Hamielec, A. E., Mlekuz, M. & Sayer, B. G. Line broadening in the carbon-13 NMR spectra of crosslinked polymers. Macromolecules 22, 3561-3564, https://10.1021/ma00199a011 (1989).

[37] Yousefi, N. et al. Highly aligned graphene/polymer nanocomposites with excellent dielectric properties for high-performance electromagnetic interference shielding. Advanced Materials 26, 5480-5487, https://10.1002/adma.201305293 (2014).

[38] Tung, C.-Y. M. & Dynes, P. J. Relationship between viscoelastic properties and gelation in thermosetting systems. Journal of Applied Polymer Science 27, 569-574, https://10.1002/app.1982.070270220 (1982).

[39] Li, S. et al. The melt grafting preparation and rheological characterization of long chain branching polypropylene. Polymer 50, 6121-6128 (2009).

[40] Fraga, I., Montserrat, S. & Hutchinson, J. M. Vitrification during the isothermal cure of thermosets: comparison of theoretical simulations with temperature-modulated DSC and dielectric analysis. Macromolecular Chemistry and Physics 209, 2003-2011, https://10.1002/macp.200800217 (2008).

[41] Luong, N. D. et al. Enhanced mechanical and electrical properties of polyimide film by graphene sheets via in situ polymerization. Polymer 52, 5237-5242 (2011).

[42] Zhao, X., Zhang, Q., Chen, D. & Lu, P. Enhanced mechanical properties of graphene-based poly (vinyl alcohol) composites. Macromolecules 43, 2357-2363 (2010).

[43] Raja, S. N. et al. Influence of three-dimensional nanoparticle branching on the Young's modulus of nanocomposites: Effect of interface orientation. Proceedings of the National Academy of Sciences 112, 6533-6538, https://10.1073/pnas.1421644112 (2015).

[44] Loiola, L. M. D. et al. Thermal and mechanical properties of nanocomposites based on a PLLA-b-PEO-b-PLLA triblock copolymer and nanohydroxyapatite. Journal of Applied Polymer Science 133, 44187, https://10.1002/app.44187 (2016).

[45] Gibson, L. J. & Ashby, M. F. Cellular solids: structure and properties. (Cambridge university press, 1999).

[46] White, R. P. & Lipson, J. E. G. Polymer free volume and its connection to the glass transition. Macromolecules 49, 3987-4007, https://10.1021/acs.macromol.6b00215 (2016).

[47] Robertson, C. G. & Rackaitis, M. Further consideration of viscoelastic two glass transition behavior of nanoparticle-filled polymers. Macromolecules 44, 1177-1181, https://10.1021/ma102631h (2011).

[48] Fragiadakis, D., Pissis, P. & Bokobza, L. Glass transition and molecular dynamics in poly (dimethylsiloxane)/silica nanocomposites. Polymer 46, 6001-6008 (2005).

[49] Li, X. et al. Double glass transitions in exfoliated poly (methyl methacrylate)/organically modified MgAl layered double hydroxide nanocomposites. RSC Advances 6, 101941-101947 (2016).

[50] Chen, L. et al. Double glass transitions and interfacial immobilized layer in in-situ-synthesized poly (vinyl alcohol)/silica nanocomposites. Macromolecules 43, 1076-1082 (2009).

[51] Kerber, S. et al. The nature of hydrogen in x-ray photoelectron spectroscopy: General patterns from hydroxides to hydrogen bonding. Journal of Vacuum Science & Technology A: Vacuum, Surfaces, and Films 14, 1314-1320 (1996).

CHAPTER 11: GLASS TRANSITION BROADENING VIA NANOFILLER-CONTIGUOUS POLYMER NETWORK

11.1 Introduction

Polymer nanocomposites, incorporating various forms of nanofillers at low loading fractions, provide multifunctional properties, and thus bear a great potential to address a broad range of cutting-edge technological applications [1]. Ultrapermeable membranes, biocompatible artificial bone scaffolds, and electrically conductive electromagnetic shielding interference (EMI) materials are amongst the example nanocomposite configurations that drew wide interest [2-4] Particularly, with the objective of maximizing physical properties, a primary research thrust on polymer nanocomposites has been centered on efforts to realize robust interfacial attachment mechanisms between the nanofiller reinforcements and the backbone chains of host polymer matrices [5-7]. In this context, glass transition behaviors of the polymer nanocomposites have been extensively studied as tabulated in a comprehensive review [8]. So far, as glass transition temperature shifts are concerned, edge-or-surface-functionalized nanofillers have been shown to promote covalent conjugations with a broad spectrum of polymers via *in situ* polymerization processes [8-11].

This work was previously published: Bakir, M., Meyer, J.L., Sutrisno, A., Economy, J., and Jasiuk, I., Glass transition broadening via nanofiller-contiguous polymer network, 56 (24), 1595-1603 (2018).

Special thanks to Dr. Andre Sutrisno (NMR/ERP Laboratory, University of Illinois) for providing invaluable guidance and help on NMR analysis.

However, the nature of the functionalization process generates structural defect sites on nanoparticles, such as graphene and carbon nanotube, which deteriorate their physicochemical architectures [12]. Also, the temperature shifts are bound to intrinsic chain configurations of the host matrices while most polymer systems can only afford weak hydroxyl-group advanced intermolecular attachments with functionalized nanofiller particles [8]. Consequently, the state-of-the-art polymer nanocomposites have not demonstrated a strong interfacial coupling scheme which forms a robustly crosslinked network of nanofiller particles and polymer chains to realize ultimate physical property improvements [4,13].

Aromatic thermosetting copolyester (ATSP) was developed in the 1990s utilizing low cost, easily processable and readily crosslinkable oligomers to form a new high-performance polymer system [14]. The ATSP morphology comprises a crosslinked network of aromatic polyester backbone interconnected via covalent oxygen bonds, which hence enables superior physical properties (e.g., glass transition temperature) [15]. Additionally, chemistry-favored tailorable macromolecular architectures along with convenient reconfigurability into different physical forms (e.g., foam, coating, and adhesive) makes ATSP available for various nanocomposite applications [13, 16-18]. Herein, we demonstrate nanofiller-contiguous polymer network with ATSP nanocomposites, incorporating chemically pristine carbon nanofillers, which displayed remarkable glass transition temperature shift as well as a unique peak broadening effect [13, 15, 18] Chemical characterization of ATSP backbone chains exhibited the formation of a robust covalent coupling with the nanoparticles enabled through *in situ* polymerization reaction wherein precursor oligomers and nanofiller particles were concurrently present [19-20] Supported by further enhancements in thermophysical properties, ATSP chains crosslinked and

incorporated with the nanofiller particles forming a nanofiller-conjugated nanocomposite morphology, which extensively modifies the backbone configuration of the nanocomposites.

11.2 Materials and Methods

The carboxylic acid and acetoxy functional group constituent oligomers were synthesized using biphenol diacetate (BPDA), 4-acetoxybenzoic acid (ABA), isophthalic acid (IPA), and trimesic acid (TMA) (Sigma-Aldrich Co.) via melt-oligomerization as outlined in prior literature [15,18]. The ATSP nanocomposite foams were fabricated via *in situ* condensation polymerization reaction between carboxylic acid and acetoxy functional group precursor oligomers, which were initially mixed in the solid state as uncured powders with as-purchased GNP, CNT and CB nanofillers at 1 wt % and 5 wt % ratios. Upon polymerization, the ATSP nanocomposites obtained a nanofiller-crosslinked aromatic polyester backbone porous matrix [13]. CB (Vulcan XC72, Cabot Corp.) (bulk density: 264 kg/m^3), CNT (Industrial-Grade Multi-Walled Carbon Nanotubes, US Research Nanomaterials, Inc.) (outside diameter (OD): 10-30 nm, inside diameter (ID): 5-10 nm, length: 10-30 μm, bulk density: 2100 kg/m^3), and GNP (Grade M-5, XG Sciences) (flake diameter: ~5 μm, thickness: 6-8 nm, density: 2200 kg/m^3). The mixed combinations were subjected to a thermal cure cycle with two dwell stages at 200 °C for 90 minutes and 270 °C for 150 minutes, and a final cure stage at 330 °C for 90 minutes [18]. Densified ITR nanocomposites were fabricated using cured ATSP powder combined with 1 wt % GNP powder, which was sintered under temperature (330 °C) and pressure (~7 MPa) for 2 hours [15].

Scanning electron microscopy was operated in high-resolution and upper detector mode (10-15 kV, 10 μA) to analyze microstructures of the nanocomposite foams on fracture surfaces, and lower detector mode to image uncured oligomer and nanofiller mixtures (15 kV, 5 μA)

(Hitachi S-4800). The specimens were sputter-coated with Pd-Au for 40 seconds to minimize charging effects.

Transmission electron microscopy was operated in bright-field mode (200 kV, 102 μA) to analyze the GNP sheets (JEOL 2010LaB_6). Fabricated nanocomposite specimens were ground using a laboratory grinder, and the powder was settled in methanol solution for 10-15 min. Solution samples having floating particles were collected using a pipette and passed through a copper grid, which was then dried at 80 $^{\circ}$C for 1 hour.

Morphologies of the nanocomposite were characterized in powder form using X-ray diffractometer with Cu K-alpha source operated at 40 kV and 30 mA, and 0.15148 nm wavelength (Siemens/Bruker D-5000). Broad-range (2θ=10°-60°) nanocomposite scans were performed using nominal 1°/min scanning rate. Narrow-range (2θ=24°-28°) crystalline carbon peak nanocomposite scans were performed with 0.05 °/min slow scanning rate. Data analysis was done using JADE software (KS Analytical Systems, Ltd.)

Chemical compositions of the nanocomposites were analyzed using Kratos Axis ULTRA X-ray photoelectron spectroscopy (Kratos Analytical) operated at monochromatic Al source at 210 W with 1000 meV step size and 100 ms dwell time and 220 s total acquisition time. Data analysis was carried out using CasaXPS software.

Primary glass transition characterization of the nanocomposites was carried out using Dynamic Mechanical Analysis with a dual-cantilever beam (DCB) bending clamp fixture (Q800 TA Instruments). A temperature-ramp cycle was operated with a 3 °C/min heating rate. Specimens were in 35 x 10 x 5 mm^3 (length x width x thickness), and the tests were performed in air. Supplementary glass transition characterization with differential scanning calorimeter (DSC) (DSC 2500 TA Instruments) was obtained on ground neat and nanocomposite specimens (~5

mg) using aluminum pans. Two consecutive temperature-ramped heating cycles with a constant 5 °C/min heating rate were applied while an intermediary cooling cycle with the same temperature rate was implemented. The DSC tests were performed in air.

Direct current (DC) electrical conductivity measurements were performed on foam morphology specimens using a 4 point-probe method (6517 B, Keithley Instruments, USA). The specimens were in 5 x 5 x 12 mm^3 (width x thickness x length). The DC electrical conductivity results were averaged over four samples per loading fraction, and standard deviations were given by error bars, accordingly.

Solid-state nuclear magnetic resonance spectroscopy measurements were carried out using ground nanocomposite specimens (~50 mg) packed into NMR rotors (Varian Unity Inova 300 MHz and Agilent VNMRS 750 MHz spectrometers). ^{1}H and ^{13}C spectra were obtained using direct pulse (DP) and cross-polarized (CP) excitations, respectively. Specimens were spun at 10 kHz. Data analysis was performed using the MestreNova software.

Fourier transform infrared spectroscopy of the nanocomposites was obtained using DRIFTS fixture (Nexus 670 Thermo-Nicolet) FTIR where ground nanocomposite specimens were mixed with potassium bromide reference material (FTIR grade KBr) (Alfa Aesar).

Linear thermal expansion of the nanocomposite was measured using a horizontal digital dilatometer (Model 2010 B Edward Orton Jr Ceramic Foundation). The tests were performed in air. A temperature-ramp heating cycle was applied with a constant 3 °C/min heating rate until 200 °C. The samples had cylindrical shapes with a diameter of 1.27 cm and a height of 2.54 cm.

Thermal degradation stability temperatures of the nanocomposite foams were characterized using the TGA (TGA 2950 TA Instruments). A temperature-ramp heating cycle was applied with a constant 10 °C/min heating rate until 600 °C. Specimens weighed 10-15 mg.

Compressive mechanical properties of the nanocomposite foams were measured using a compressive load frame (4483 Load Frame Instron Testing Systems) with a constant crosshead speed of 6 mm/min. The specimens were cylindrical in shape with a diameter of 1.27 cm and a height of 2.54 cm. Materials toughness was calculated as the area under stress-strain curves until fracture points using Origin (OriginLab Corporation). The strain at fracture was defined as strain at maximum stress. Structural density was calculated as the ratio of measured weight to volume of the specimens. Relative density was calculated as the ratio of the measured structural density of the nanocomposite foam to the density of neat fully dense ATSP (1.27 Mg/m^3).

11.3 Results and Discussion

The ATSP nanocomposites were obtained through *in situ* polycondensation reaction between carboxylic acid- and acetoxy-terminated constituent oligomers wherein carbon nanofillers were also present [13]. The polymerization process generates a crosslinked polymer network while releasing acetic acid as a reaction by-product [13]. The acetic acid emerges in the gas form at elevated reaction temperatures (~200 °C), which hence acts as a blowing agent forming porous nanocomposite matrix [18]. Thus, the nanocomposites inherently acquired foam morphology upon the *in situ* polymerization process. First, we present results obtained from the characterization of glass transition behaviors of the ATSP nanocomposite foam structures using Dynamic Mechanical Analyzer (DMA) (Figure 11.1). *In situ* synthesized neat ATSP foam base material, having amorphous morphology, displayed two characteristic tangent delta (tan δ) peaks: sub-glass transition (β-relaxation) (T_β) at 79 °C and glass transition (α-relaxation) (T_g) at 191 °C, which defines its chain relaxation response [18]. In this respect, the nanocomposite structures, individually incorporating graphene nanoplatelet (GNP), carbon nanotube (CNT) and carbon black (CB) nanofiller particles, yielded increases in the T_g by ~80 °C along with

broadened glass transition peaks having breadths widened by ~100 °C (Figures 11.1a-c) (see Figure 11.2 for storage/loss moduli results). As well, the β-transition peak of the nanocomposite morphologies was suppressed in comparison to the parent form. These distinct changes within the glass transition regime indicated the occurrence of collective reconfiguration in the ATSP backbone chains upon interfacial interactions with the nanofillers wherein the degree of freedom for chain motion (chain orientation mode) was substantially modified. On the other hand, simple mixture of precured/crosslinked ATSP formulation (GNPs were not present during initial polymerization process) with the GNP particles by means of solid-state interchain transesterification reactions (ITR) using high-pressure and -temperature sintering process did not produce any deviations in the T_g peak position (Figure 11.1.d) (see Figure 11.3, and refer to references 15 and 21 for a detailed discussion on the ITR mechanism). The T_g peak breadth became slightly narrower as compared to the neat ATSP because of different material forms, as detailed below. Likewise, the β-transition peak of the consolidated nanocomposite was suppressed (see Figure 11.4 for storage/loss moduli results).

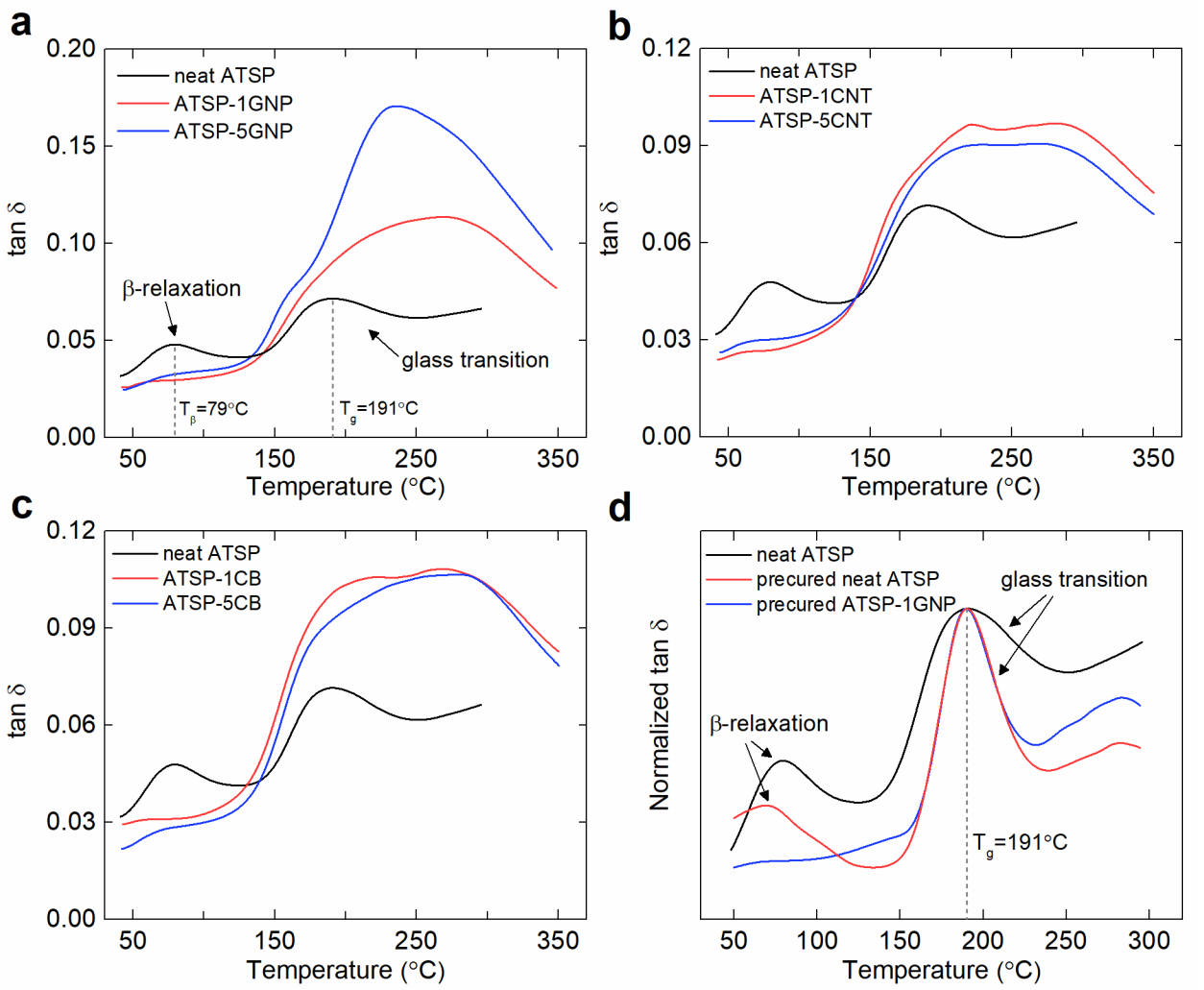

Figure 11.1 Dynamic mechanical analysis (DMA) tangent delta (tan δ) measurements of the *in situ* synthesized foam morphology nanocomposites demonstrated large peak temperature upshifts and significant peak broadenings in the glass transition regime. The sub-glass transition (β-relaxation) was suppressed within the nanocomposites. (a) Graphene nanoplatelet (GNP) nanocomposites. (b) Carbon nanotube (CNT) nanocomposites. (c) Carbon black (CB) nanocomposites. (d) Mixture of precured/crosslinked ATSP formulation (GNPs were not present during initial polymerization) with GNP particles by means of solid-state interchain transesterification reactions (ITR) using high-pressure and -temperature sintering process (see references 15 and 21, and Figure 11.4 with for the ITR mechanism) did not reveal any changes in the glass transition peak position for both neat and nanocomposite configurations. The figure is given in normalized tan δ scale to demonstrate the glass transition peak positions. Nanocomposites were named in accordance with weight fractions of the added nanofillers (1 wt % and 5 wt %).

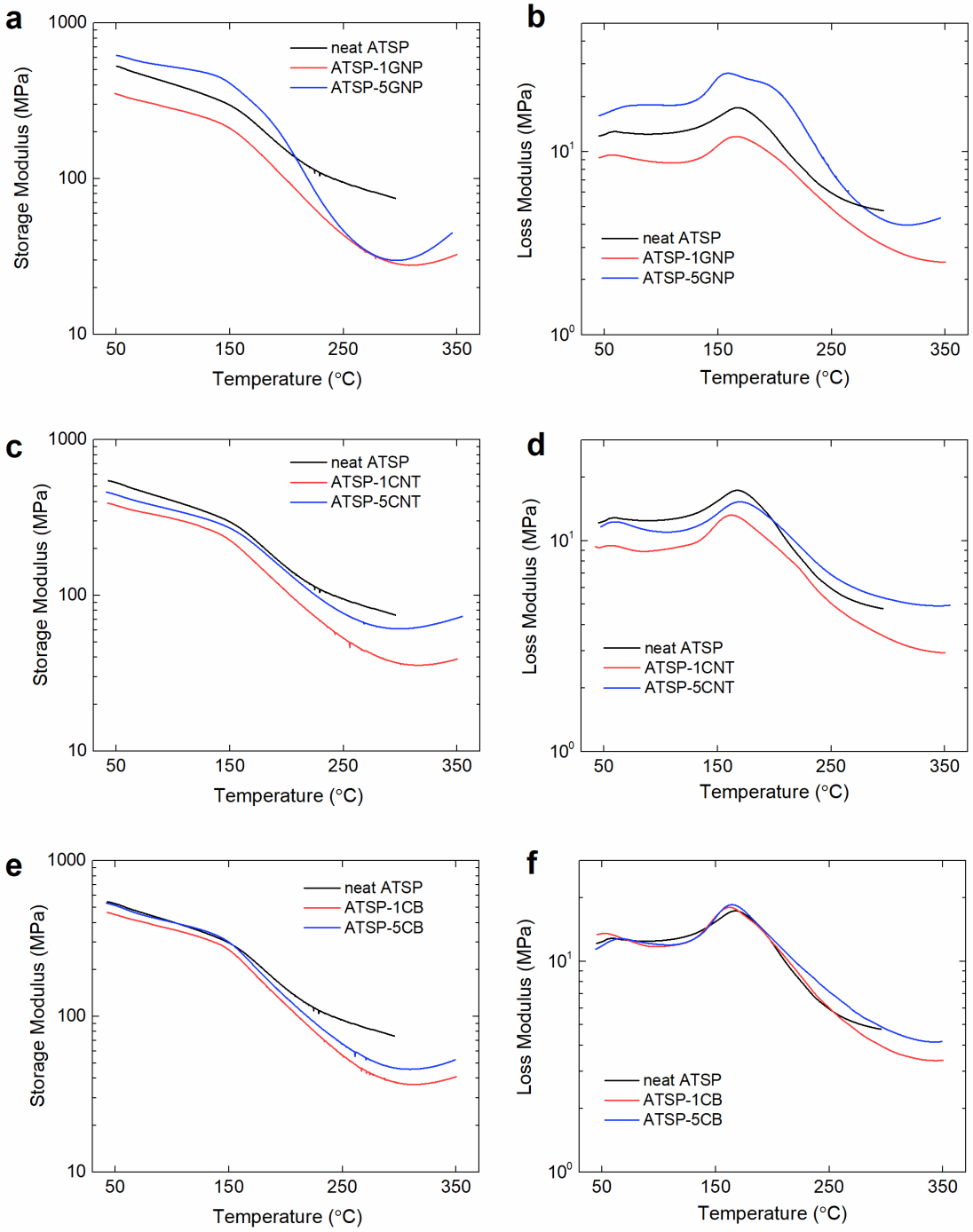

Figure 11.2 Dynamic mechanical analysis (DMA) thermomechanical property measurements of the *in situ* synthesized foam morphology nanocomposites with 1 wt % and 5 wt % nanofiller loadings. (a) Storage and (b) loss moduli of the graphene nanoplatelet (GNP) nanocomposites. (c) Storage and (d) loss moduli of the carbon nanotube (CNT) nanocomposites. (e) Storage and (f) loss moduli of the carbon black (CB) nanocomposites. Nanocomposites were named in accordance with incorporated weight fractions of the nanofillers.

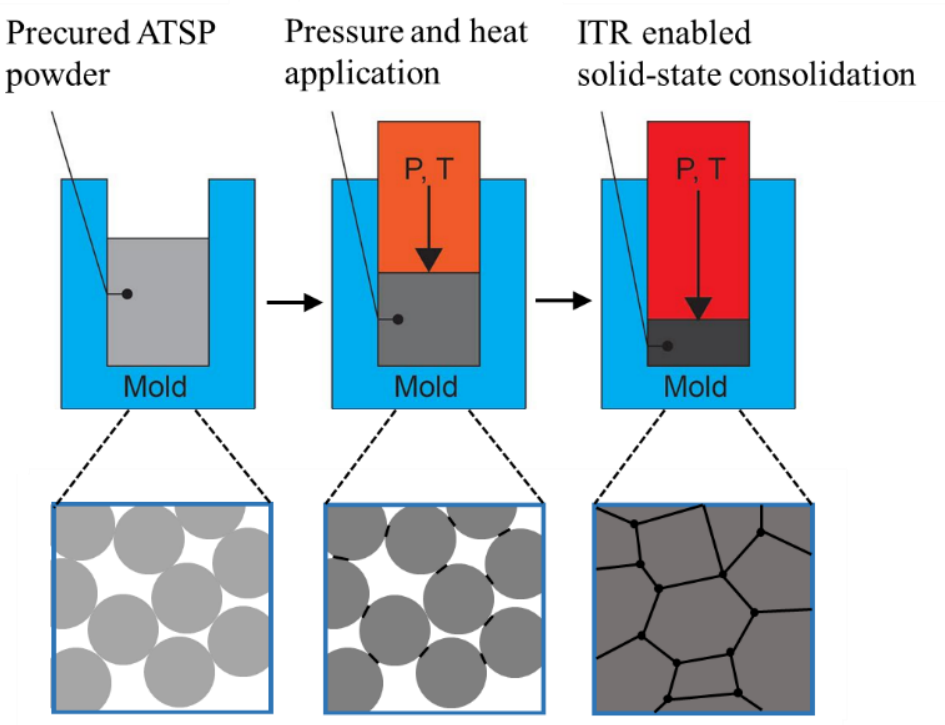

Figure 11.3 Schematic representation of interchain transesterification reactions (ITR) based solid-state consolidation of precured ATSP under applied heat and pressure. For the nanocomposites, the GNP nanofiller particles were mixed with the precured polymer particles in the solid state. Precured ATSP powder was packed into a mold where the polymer particles were loosely organized. Upon introduction of heat and pressure, the polymer powder particles were brought into contact as the ITR process progressed. Finally, diffusion-based solid-state consolidated fully dense ATSP nanocomposites were obtained. ITR process does not evolve any volatiles, on the contrary to the *in situ* polymerization process.

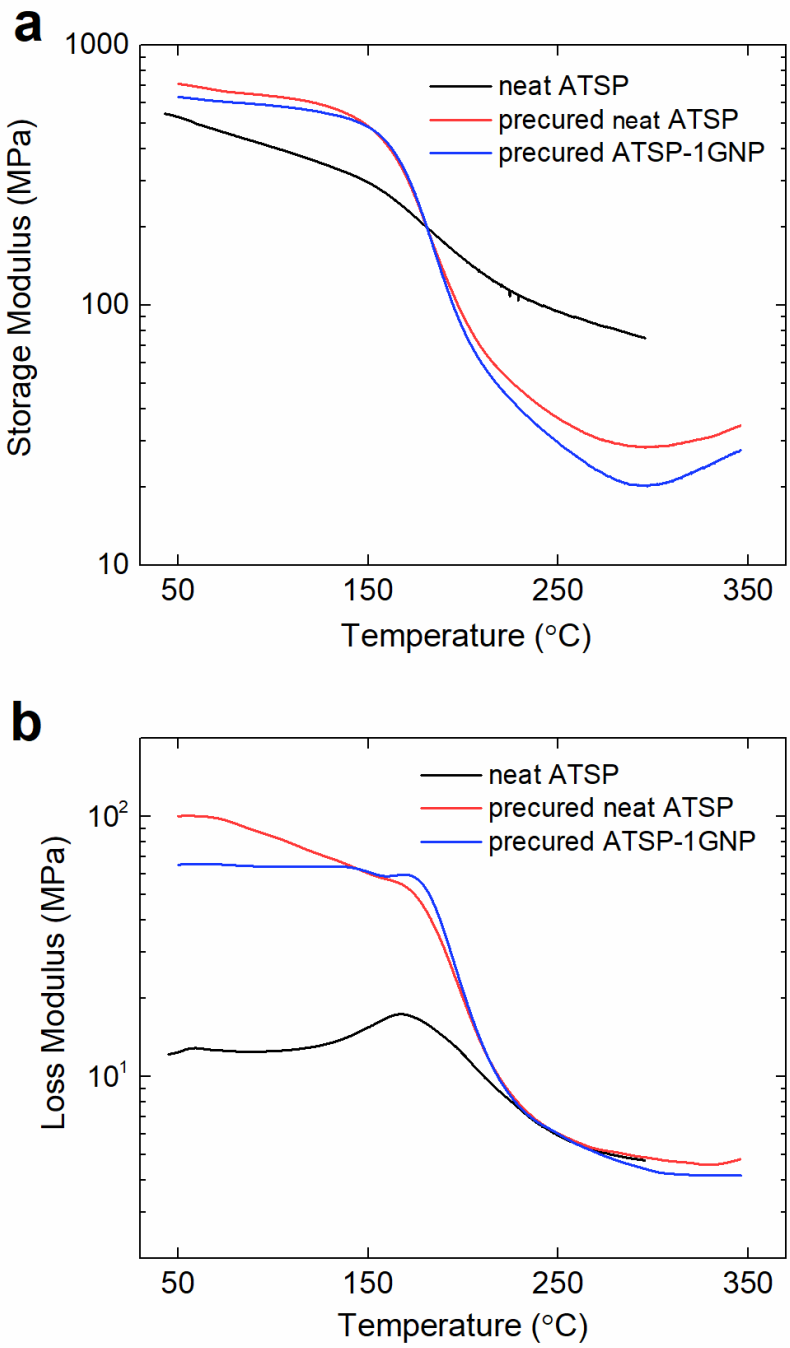

Figure 11.4 Dynamic mechanical analysis (DMA) thermomechanical property measurements of the interchain transesterification reaction (ITR) melt-consolidated precured/crosslinked chemistry ATSP and GNP nanofiller particles. Precured neat ATSP and 1 wt % GNP incorporated precured ATSP nanocomposites were compared to the *in situ* synthesized neat ATSP foam morphology. (a) Storage and (b) loss moduli were represented. Nanocomposite sample was named in accordance with an incorporated weight fraction of the GNP nanofiller. Neat ATSP data was taken from reference 18.

It is worthwhile to mention that the foam morphology possesses increased solid-air interface region (surface-area-to-volume ratio) with respect to a bulk (fully dense) specimen. Hence, testing environment may be conceived to affect chain relaxation dynamics at the interface [22]. In this regard, our recent study on the effects of environmental aging on physical properties of ATSP neat and nanocomposite foams showed only marginal changes in the glass transition temperatures following extended exposure periods [23]. Besides, the geometrical factor (spatial confinement effect) for the foam structures did not necessarily induce any substantial changes in the glass transition regime, as compared to the bulk specimen, owing to having scalable (macrocellular) porous morphology for which corresponding T_g peak positions were detected to be identical for both material forms (Figure 11.1.d) [24]. The moderately narrower glass transition peak breadths developed for the fully dense morphology due to the extent of the ITR mechanism which reconfigured the heterogeneity in chain mobility through exchanging chain segments during the transesterification process [21, 25]. The glass transition regime characteristics were also cross-checked using Differential Scanning Calorimeter (DSC), and corresponding temperature upshift and peak broadening effects were likewise observable with the supplementary method (see Figure 11.5 for DSC results). Besides, two successive DMA thermal cycles were carried out to verify integrity of the glass transition characteristics in which we observed that the temperature upshift and peak broadening features still held true, yet thermomechanical response of the nanocomposite structure was moderately weakened in the second cycle (with a reduced tan δ intensity) due to physicochemical aging-induced activation energy reduction during the first cycle (see Figure 11.6 for DMA reproducibility results) [26]. We note that the ATSP nanocomposites possessed fully cured matrices prior to the DMA/DSC analyses such that any further chemical reaction between the ATSP backbone chains and

nanofiller particles would not be necessarily induced in the course of the glass transition characterization measurements [13]. We highlight two key characteristics as previously reported on similar polymer systems, which hereby directly relate to the results obtained for the ATSP nanocomposites. First, increased crosslinking density in the thermosetting polymers induces chain immobility which then produces upshifted glass transition temperatures [27,28]. Second, strong repulsive interaction forces within well-ordered monomer components of gradient copolymers produce broadened glass transition peak regions [29]. Based on these findings, the nanofiller particles behaved as crosslinking agents during the polymerization reaction wherein a fraction of the functional groups of the oligomers reacted with the nanoparticles, which consequently reduced the fraction of the functional groups that participate in the ordinary crosslinking polymerization process. Hence, the nanoparticles effectively joined to the highly-crosslinked network of the ATSP matrix, which consequently developed a nanofiller-contiguous network morphology.

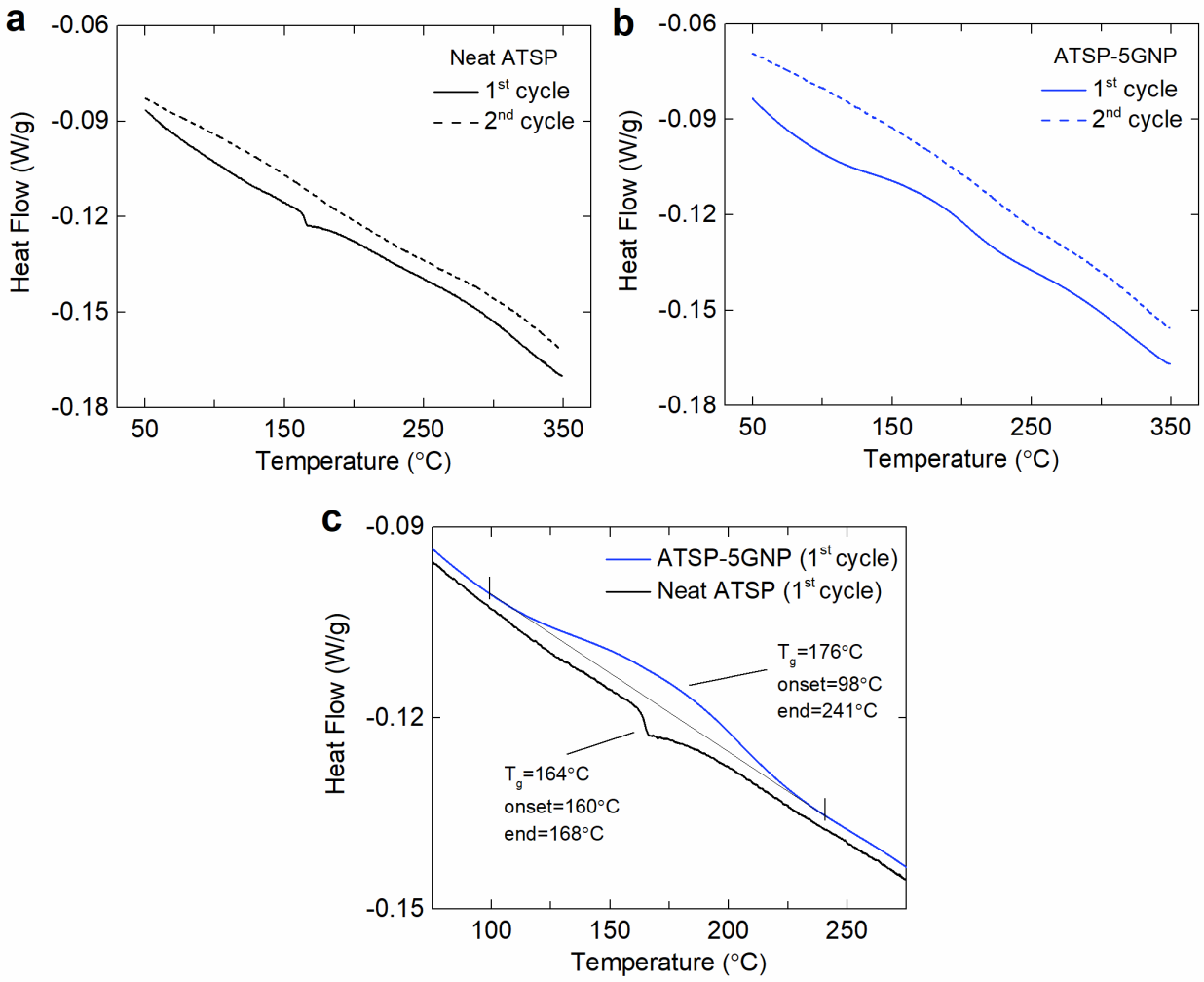

Figure 11.5 Characterization of glass transition behaviors via DSC. Differential scanning calorimetry (DSC) two consecutive glass transition temperature measurements of the *in situ* synthesized neat ATSP and ATSP-GNP nanocomposite displaying temperature upshift along with peak broadening effects. The second cycles do not reveal any characteristic peaks observed in the first cycles. (a) neat ATSP. (b) 5 wt % graphene nanoplatelet (GNP) incorporated ATSP nanocomposite. (c) Comparison of glass transition temperatures of the neat ATSP and ATSP-GNP nanocomposite. Nanocomposites were named in accordance with incorporated weight fractions of the nanofillers. Two consecutive temperature-ramped heating cycles with a constant 5 °C/min heating rate were applied while an intermediary cooling cycle with the same temperature rate was implemented. Note that the second cycles do not reveal any characteristic peaks observed in the first cycles for both material configurations due to induced physicochemical aging on already weak phase transitions detectable to DSC. The detected glass transition temperatures, as well as the nanofiller-induced glass transition regime characteristics in DSC, were slightly different than those obtained in DMA. The phase transition measurements in DSC relies on enthalpic changes in materials whereas DMA analyses utilize thermomechanical response of materials at a certain excitation frequency. On the basis of the proposed mechanism (Figure 2), the temperature upshift and peak broadening effects were still detectable. The measured T_g of the neat ATSP via DMA was 191°C along with ~120°C of peak breadth. The detected T_g of the ATSP-5GNP nanocomposite was 235 °C in DMA.

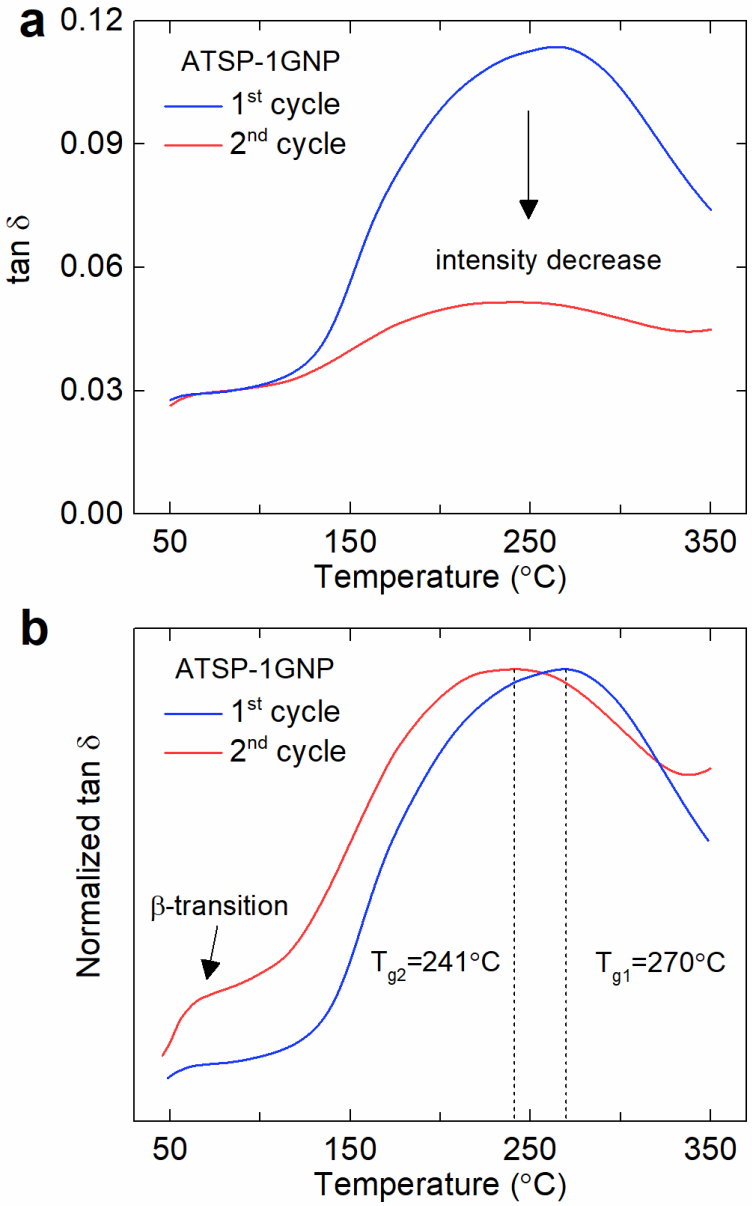

Figure 11.6 (a,b) Reproducibility of the glass transition characteristics. Dynamic mechanical analysis (DMA) two successive tangent delta (tan δ) measurements of the *in situ* synthesized nanocomposite foam morphology with 1 wt % graphene nanoplatelet (GNP) represented in normalized axis units showing that the glass transition temperature upshift is maintained (T_g of neat ATSP is 191°C) along with the formation of equivalently broad glass transition peak, yet yielding decreased tan δ intensity due to thermal stress and high temperature induced physical aging. From a thermodynamical point of view, during the first cycle, the polymer chains relax to an enthalpically favorable equilibrium state during which they dissipate energy while acquiring structural mobility around the glass transition temperatures. Upon a subsequent cooling cycle, the chains cannot completely recover the dissipated energy (enthalpic recovery). Hence, on a second thermal cycle, energy-wise weaker glass transition regimes were observed. This effect was also aggravated due to physicochemical aging (oxidative degradation) of the polymer structures at elevated temperatures in the presence of air. Yet, ATSP nanocomposites preserved modified glass transition characteristics (temperature upshift and peak broadening) on the second cycles.

It is well-acknowledged in the polymer nanocomposites literature that interfacially bonded nanofiller particles and polymer chains form a co-continuous network within nanocomposite matrix, which constitutes a rheologically percolated nanoparticle domain [5,10]. The formation of such biphasic hybrid morphology was demonstrated to induce increases in the glass transition temperature via imposing reduced mobility (confinement) on polymer chains [30]. However, the conjugation scheme (with mostly linear chain configurations) does not necessarily alter the intrinsic structural relaxation characteristics of the polymer backbones through physicochemical modification. With the ATSP nanocomposites, the nanofiller particles joined the cure advancing crosslinked polymer network that generates the nanofiller-contiguous morphology (Figure 11.7). The nanofiller-contiguous network displayed a thoroughly modified relaxation behavior for the backbone chain, rather than merely imposing a confinement effect, which hence reflected the collective response of the nanocomposite structure. In the following part, we discuss the formation mechanism of the modulations in the glass transition regime. Fourier Transform Infrared (FTIR) spectroscopy results of the ATSP-GNP nanocomposites showed moderate conformational modulations in the fingerprint domain of the ATSP chain configuration corresponding to modifications in the in-plane bending mode of the C-C bond of aromatic rings (see Figure 11.8 for IR spectroscopy). Therefore, the formation of the broadened glass transition peaks along with the significant temperature upshifts could require additional dynamic chain relaxation and deformation modes to come into effect [26]. In that vein, we postulate the following interpretation to explain this phenomenon. In the glass transition region, the nanofiller particles, while strongly tethered the polymer backbone, induced a pseudo-rheological percolation behavior facilitated through short inter-nanoparticle distances, which first restricted the mobility of wide-extending long chains, and then consecutively increased the

overall chain relaxation time [5-6] (Figure 11.7) (see Figure 11.9 for electron microscopy images). Herein, the pseudo-rheological percolation applies to a crosslinked thermoset polymer network wherein conjugated nanofiller particles generated a 'local jamming effect' over junction points to polymer chains during relaxation process (Figure 11.7). Note that the increase in storage modulus above 250 °C also validates such a confinement effect (Figure 11.2). On a similar concept, nanofiller particle surface immobilized polymer chains were reported to induce frequency-dependent strain lagging effects [31]. Note that the local confinement effect in the nanofiller-conjugated network did not require the formation of an absolute rheological percolation state in the whole matrix, as indicated by electrical conductivity measurements for the ATSP nanocomposites (Table 11.1). Thus, this mechanism is conceptually different than that of the molten domains of thermoplastic systems [32-33]. Meanwhile, temperature-driven intrinsic structural relaxation mechanism (α-relaxation) became effective for the backbone chains, which sought to release deformation energy, yet the energy was transiently restored within the chains due to the strain lagging (via stress σ) induced delayed relaxation schedules (τ) [34-35]. Consequently, this deformation mode generated such substantially broadened glass transition regions with upshifted glass transition temperatures (Figure 11.7). Additionally, we note that the ATSP resin forms a surface-induced liquid crystalline interlayer domain on carbonaceous surfaces upon thermal curing, which would also introduce a further stiffening mechanism into the short-range polymer chains that would increase the deformation energy (similar to stretching a stiffer spring with increased spring constant) [36-37]. Therefore, the modulated glass transition characteristics of the ATSP nanocomposites, as emerged from the unified response of the nanofiller-crosslinked network, are different than the double glass transition peak phenomenon wherein a separate peak, in addition to original glass transition

peak, forms at a higher temperature due to nanofiller particle induced immobilization effects on chain relaxation characteristics [31]. More importantly, the increased intensity of the glass transition peak for the nanocomposites highlighted that the larger amount of aromatic chain segments engaged in the relaxation process due in part to the interactions with the nanofiller particles. It also evinced that the nanofiller-crosslinked modified polymer network acquired a different backbone chain arrangement that resulted in enhanced chain mobility (indicated by smaller storage modulus than neat form in the rubbery state, see Figure 11.2) which hence displayed higher intensity glass transition peaks. Regarding the peak broadening effect, due to the formation of the nanofiller-contiguous network, the modified nanocomposite backbone structure forms shorter macromolecular chains at nanofiller interface, which thus caused heterogeneity in the chain distribution generating broader peaks. Note that the broadening effect was only observable until initiation of bond scissions through thermal degradation starting at 350-400 °C.

Table 11.1 Electrical conductivity results. Results of DC electrical conductivity measurements on the ATSP-GNP and ATSP-CNT nanocomposites with 1 wt % and 5 wt % nanofiller loadings. Nanocomposites were named in accordance with incorporated weight fractions of the nanofillers. DC electrical conductivity measurements were performed using a 4 point-probe method. The electrical conductivity results were averaged over independent measurements on four different specimens with given standard deviations.

	DC Electrical Conductivity (S/m)	**Standard Deviation**
Neat ATSP	4.1×10^{-13}	7.7×10^{-14}
ATSP-1GNP	3.4×10^{-13}	7.8×10^{-14}
ATSP-5GNP	3.1×10^{-2}	2.2×10^{-3}
ATSP-1CNT	2.4×10^{-13}	1.5×10^{-13}
ATSP-5CNT	3.0×10^{-1}	2.9×10^{-1}

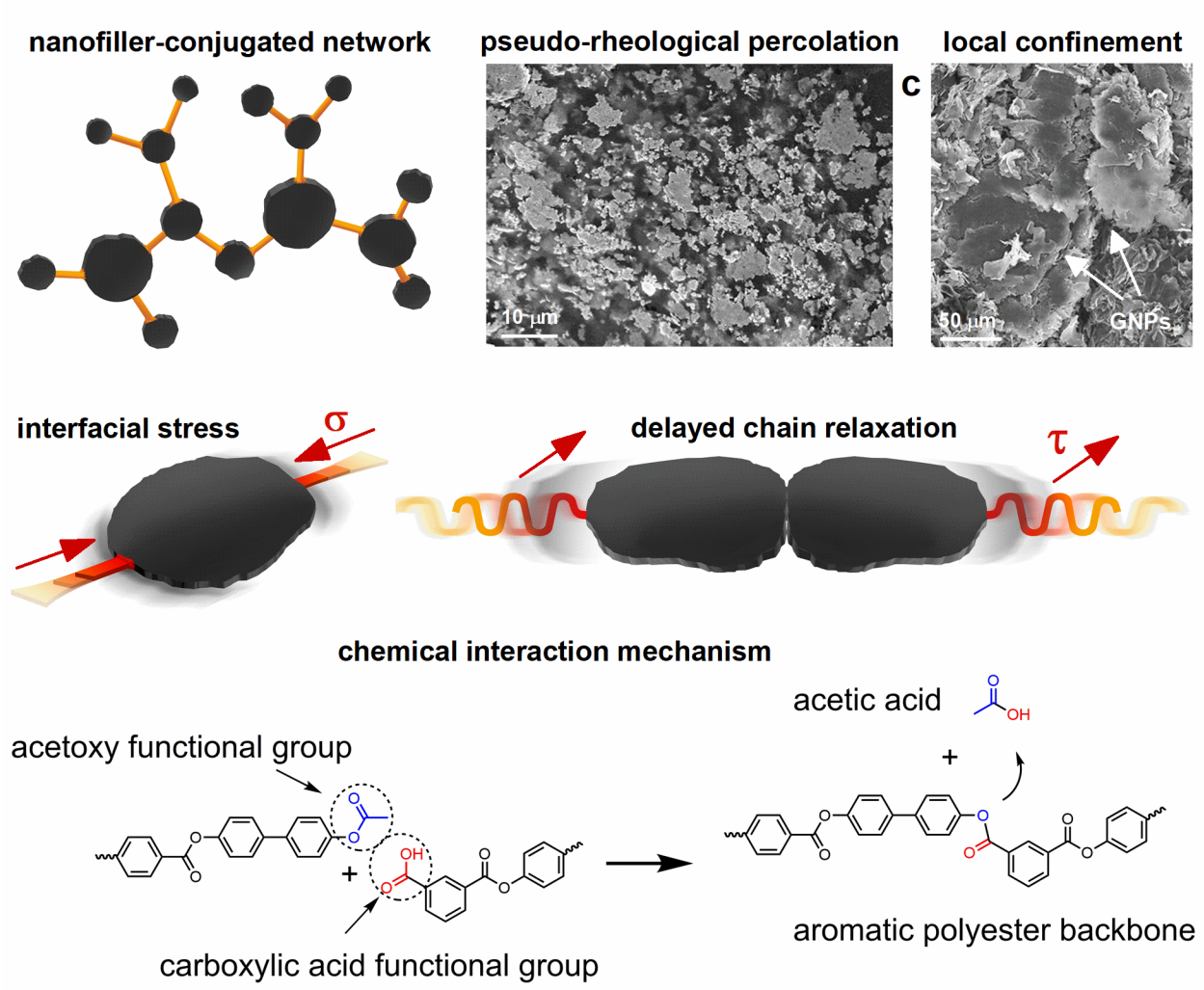

Figure 11.7 Graphical representation of the nanofiller-conjugated polymer network. Scanning electron microscope images obtained over a pore surface of the GNP nanocomposite demonstrating the formation of the pseudo-rheological percolation domain (GNPs appear brighter in darker ATSP matrix) and local confinement (jamming) effect. The polymer chains were covalently conjugated with the nanofiller reinforcements, which are applied interfacial stress (σ). Elongated relaxation time (τ) of the wide-extending ATSP chains due to the pseudo-rheological percolation of the nanofillers. Graphical representation of chemical interaction mechanism during the *in situ* polymerization reaction.

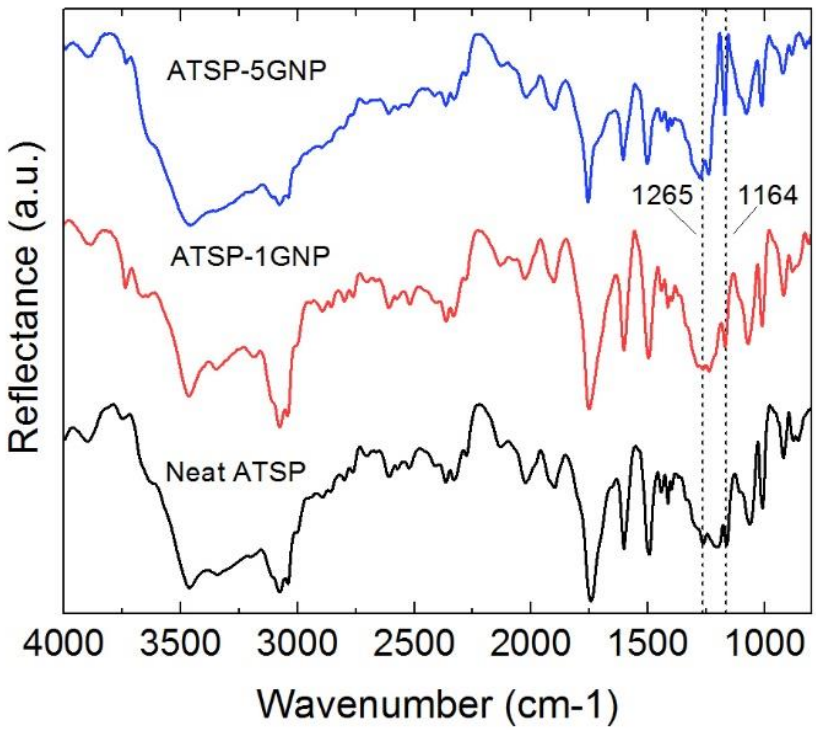

Figure 11.8 IR spectroscopy characterization. Fourier transform infrared spectra of the neat ATSP morphology, and the *in situ* synthesized 1 wt % and 5 wt % GNP incorporating nanocomposites. Nanocomposites were named in accordance with incorporated weight fractions of the nanofillers. Based on characteristic IR bands of the aromatic ring, peaks at 3040 cm^{-1} and 3080 cm^{-1} were assigned to stretching mode of C-H bonds. Additional bonds for stretching mode were observed at 1490 cm^{-1} and 1600 cm^{-1}, which denoted C-C bonds of the aromatic ring. The peak observed at 1745 cm^{-1} was attributed to stretching mode of C=O bonds. The peaks between approximately 1900 cm^{-1} and 2600 cm^{-1} were overtone bands of the aromatic ring. Within the fingerprint region, two peaks detected at 860 cm^{-1} and 920 cm^{-1} were attributed to out-of-plane bending modes of C-H bonds of the aromatic ring. More importantly, the peaks observed between 1000-1260 cm^{-1} defined in-plane bending modes of C-C bonds in the aromatic ring. Among these peaks, we observed the splitting of the peak at 1164 cm^{-1} from other grouping peaks at 1204 cm^{-1}, and 1265 cm^{-1} with respect increased GNP loadings, where it eventually became a separate peak with 5 wt % GNP nanocomposite structure. This result revealed significant conformational changes with respect to the in-plane motion of the polymer backbone, which could explain changes in the β-relaxation regime.

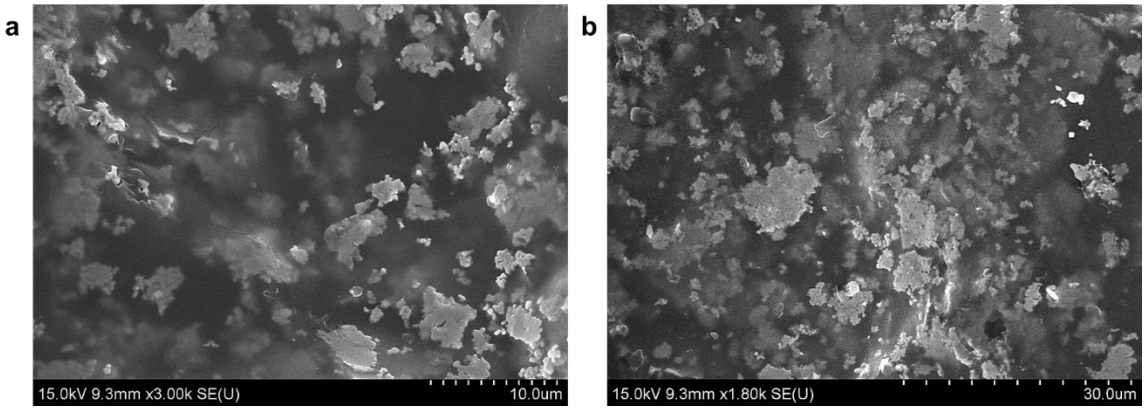

Figure 11.9 Microstructural images of GNP networks. Ultra high-resolution upper detector mode scanning electron microscopy images obtained on the ATSP-GNP nanocomposites over pore surfaces. a-b, GNP nanoparticle networks in the ATSP matrix domain. GNPs appear brighter in darker ATSP matrix. Visual transparency also highlighted effective surface wetting of the GNP nanofillers by the ATSP matrix.

Regarding the underlying chemical interaction and attachment mechanism that gave rise to such strong interfacial coupling, the *in situ* polymerization process involved acetoxy (-CH_3COO) and carboxylic acid (-COOH)-capped matching oligomer groups which carried out an esterification condensation reaction at sufficiently high temperatures (> 200 °C) (Figure 11.7) [18]. This reaction allowed the ether oxygen of the acetoxy-end-group oligomer to exchange with the hydroxyl groups of the carboxylic acid-end-group oligomer thereby forming a cross-linked network of the ATSP matrix while releasing acetic acid as a by-product [18]. Hence, the functionalized oligomers interacted with oxygen-containing polar sites (~3 at %) present on the GNP particles, which tethered the nanoparticles to the cure advancing crosslinked network of the ATSP backbone chains (see Figure 11.10 for chemical functional group surface spectroscopy results) [38-39]. Note that the high-temperature stability of the nanofiller-conjugated oxygen bonds of the functional groups of the oligomers enabled the broadening effect at elevated temperatures, which hence differs from the marginal temperature shifts enabled via hydroxyl-based coupling schemes in the literature [8]. Upon the GNP particles joining to the crosslinked

network of the ATSP backbone, the nanocomposite formed a nanofiller-contiguous morphology in which macroscopic thermomechanical behaviors of the nanocomposites were greatly altered by the orders of magnitude higher in-plane elastic properties of the GNP nanoparticles.

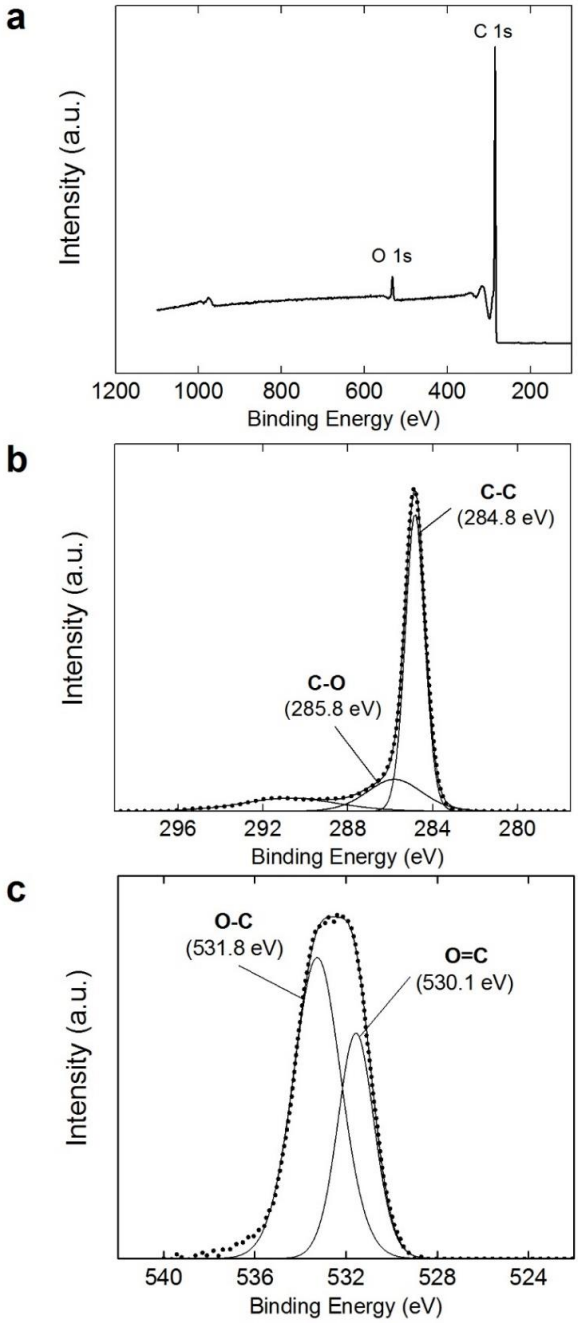

Figure 11.10 Chemical surface spectroscopy. X-ray photoelectron spectroscopy (XPS) spectra obtained on the pristine GNP. (a) survey scan. (b) C 1s spectra. (c) O 1s spectra. Results indicated native oxygen-functionalized sites on the GNP basal plane by ~3 at %, which facilitated chemical interaction with carboxylic acid and acetoxy-capped functional groups of the constituent ATSP oligomers.

Corresponding microstructural analysis revealed visual evidence for the presence of the interfacial attachment scheme between the GNP particles and the ATSP backbone chains (Figure 11.11). Scanning electron microscopy (SEM) analysis displayed three distinct features on fracture surfaces of the nanocomposites (Figure 11.11.a). First, the GNP particles were thickly coated by the ATSP matrix indicating their effective surface wettability enabled through the *in situ* attraction mechanism (see Figures 11.9 and 11.12 for additional electron microscopy images). Second, due to the strong coupling mechanism, surface cracks initiated over the ATSP-GNP junction sites, wherein the nanoparticles behaved as crack arresters within the nanofiller-crosslinked network to impede further fracture propagations, which eventually yielded increased strength and toughness in the nanocomposite morphology, as shown later in the text. Third, as the fracture propagation damaged the GNP particles, the broken nanoparticles remained embedded in the ATSP matrix while held in place by the robust interfacial adhesion. We underline that strength of the physicochemical coupling attenuated contact boundary slipping or surface debonding effects. To further illustrate the bonding effects, transmission electron microscopy (TEM) image is presented which displayed ATSP chain fragments (darker domains) while tethered on the GNP particles (Figure 11.11.b). The ATSP chains formed unique surface patterns smeared around the flakes that demonstrated molecular level extent of the coupling mechanism.

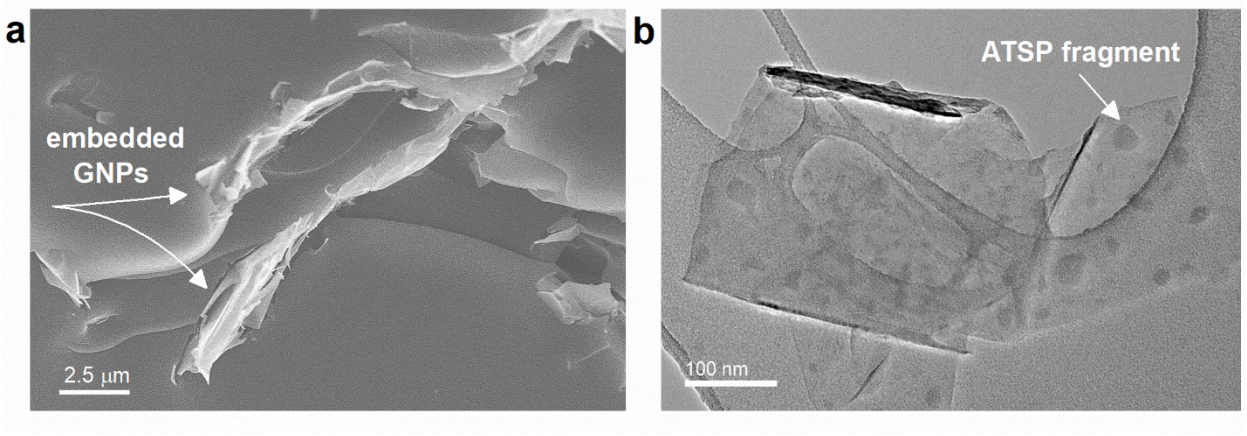

Figure 11.11 (a) Ultra high-resolution upper detector mode scanning electron microscope (SEM) image (10 kV, 10 μA) of fracture surfaces of the ATSP-GNP nanocomposites demonstrated matrix-wetted GNP particles forming robust interfacial bonding. The GNP particles remained embedded within the surrounding ATSP matrix upon fracture. (c) Bright-field transmission electron microscopy (TEM) image (200 kV, 102 μA) of the ATSP-GNP nanocomposite showed ATSP fragments (darker) while clung on the GNP flakes (brighter) clearly displaying extent of the effective attachment mechanism at the nanoscale.

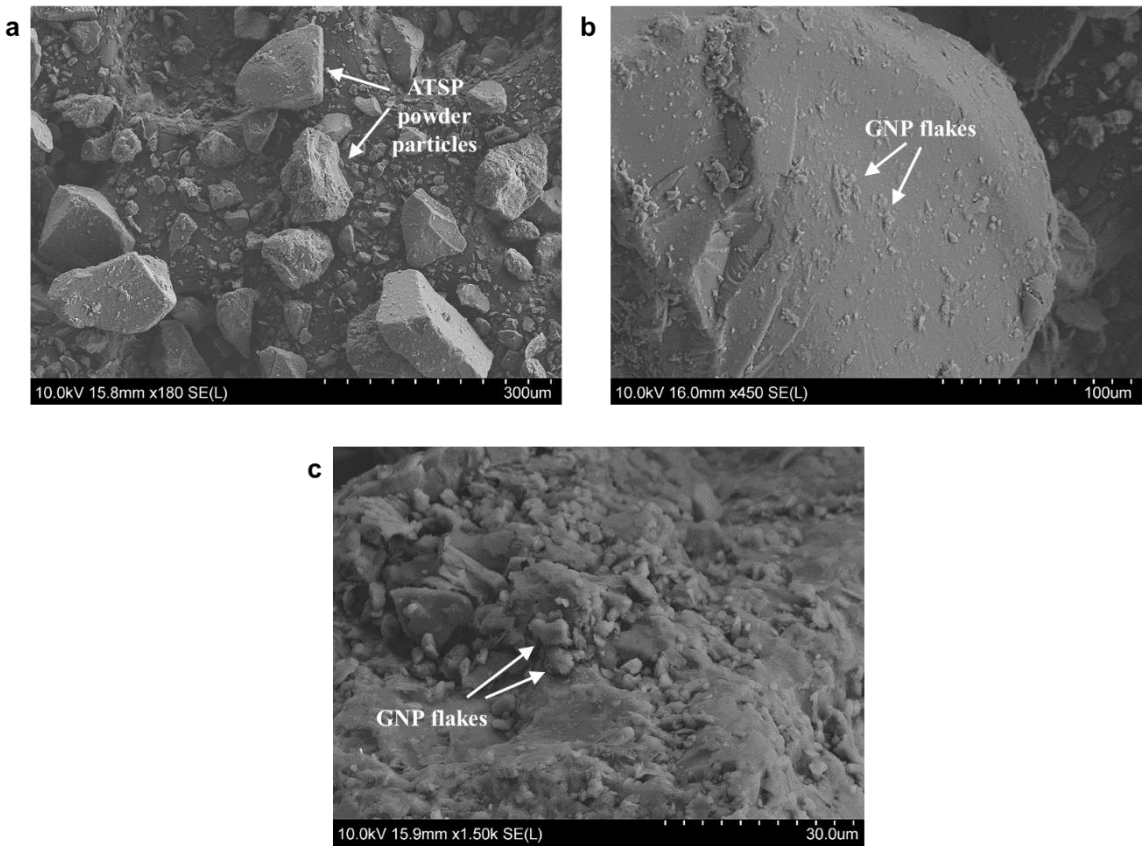

Figure 11.12 Microstructural images of uncured ATSP powder. Ultra high-resolution lower detector mode scanning electron microscopy (SEM) images of the uncured ATSP powder (combined carboxylic acid and acetoxy functional group oligomers) particles mixed in solid state with the GNP nanofiller particles. (a) Multiple ATSP powder particles (brighter) at different sizes distributed on carbon tape background (darker). Arrows indicate some of the powder particles. (b) GNP nanoparticles were effectively dispersed on an individual oligomer particle surface given at a magnified scale. Small particles on the surface represent the GNP flakes. Arrows highlight some of the GNP flakes. (c) A close-up image featuring effective precuring stage homogenous distribution of GNP flakes which hence facilitated good surface wettability in the course of the polymerization process. Arrows point some of the GNP flakes.

To elucidate the nature of the interfacial coupling mechanism at the molecular level, we performed comprehensive physicochemical analysis on the ATSP-GNP nanocomposites. X-ray photoelectron spectroscopy (XPS) results demonstrated that distinctive modifications developed in the polymer backbone chain configuration upon the chemical interactions with the GNP particles. In Figure 11.13.a, the characteristic peak of the sp^2-hybridized GNP structure (284.8 eV) was lumped into the C 1s spectra of the nanocomposites (see Figure 11.10 for surface spectroscopy results). As well, the aromatic ester backbone characteristic peak (283 eV)

downshifted, within a detectable range, to a lower binding energy of 282.7 eV with the 5 wt % GNP incorporation into the matrix. These two features highlighted that the GNP particles highly interacted with the ATSP backbone chains. Furthermore, the C 1s spectra exhibited markedly increased atomic concentration for the C-O functional group of the nanocomposite structures up to ~39 at % (ATSP-5GNP) as compared to ~27 at % of the base matrix. Similarly, the O 1s spectra displayed an *in situ* generated carbonyl functional group peak (~533 eV) within the nanocomposite structures, which evidenced the role of the reactive oxygen-bearing sites on the interfacial attraction and covalent conjugation with the GNP particles (Figure 11.13.b). Hence, referring to the previous argument on the interfacial interaction mechanism, the XPS results demonstrated that the GNPs and ATSP backbone covalently bonded through oxygen-bearing functional groups which were formerly present in both acetoxy/carboxylic acid-terminated precursor oligomer groups and oxygenated reactive sites on the GNPs. Besides, ^{13}C cross-polarization magic-angle spinning (CPMAS) solid-state Nuclear Magnetic Resonance (ssNMR) spectra of the neat ATSP structure showed two characteristic peak groups corresponding to the aromatic backbone chains (C-C/C-H bonds) and the functional side-chains (C-O and C=O bonds) (Figure 11.13.c). ^{13}C NMR spectra of the nanocomposites revealed broadened characteristic peaks with respect to incremented GNP loadings, wherein the linewidth was measured to increase from ~860 Hz (neat ATSP) to ~1045 Hz (ATSP-5GNP). The formation of peak broadening was due to the robust interfacial coupling, as also supported by the XPS spectra, which ultimately altered structural relaxation behavior of the backbone chains [40-42]. A similar peak broadening effect was also observed in the ^{1}H direct pulse magic-angle spinning (DPMAS) NMR spectra (Figure 11.13.d). The interfacial entanglement of the polymer chains and the nanofiller particles caused substantial electron mobility difference due to individually dissimilar

relaxation times, where the highly conductive GNP particles enabled fast electron transfer as opposed to the highly dielectric ATSP chains. We underline that the ^{13}C and ^{1}H NMR spectra of the nanocomposites did not exhibit any characteristic peaks arising from the pristine GNP structures within the given NMR spectra (see Figure 11.14 for NMR spectroscopy results). Figure 11.15 shows similar peak broadening effects over spinning side-bands (denoted by *) of the nanocomposite spectra obtained using a higher-field ssNMR spectrometer. In Figure 11.13.e, X-Ray diffraction (XRD) spectra of the nanocomposite structures demonstrated reduced interlayer spacing in the stacking morphology of the GNP sheets through higher diffraction angle shift for the (002) characteristic peak, while the polymer matrix retained its amorphous morphology (see Figure 11.16 for broad-range XRD spectroscopy results). Tensile strains were induced within the nanocomposites by cure stresses during the *in situ* thermal polymerization process, which effectively translated through the GNP structure through the covalent conjugation [43]. Via these multiple techniques, we observed that the aromatic polyester chains effectively adhered to and reacted with the GNP particles by means of the oxygen-bearing functional groups being inherently present in both the resin and the GNP particles.

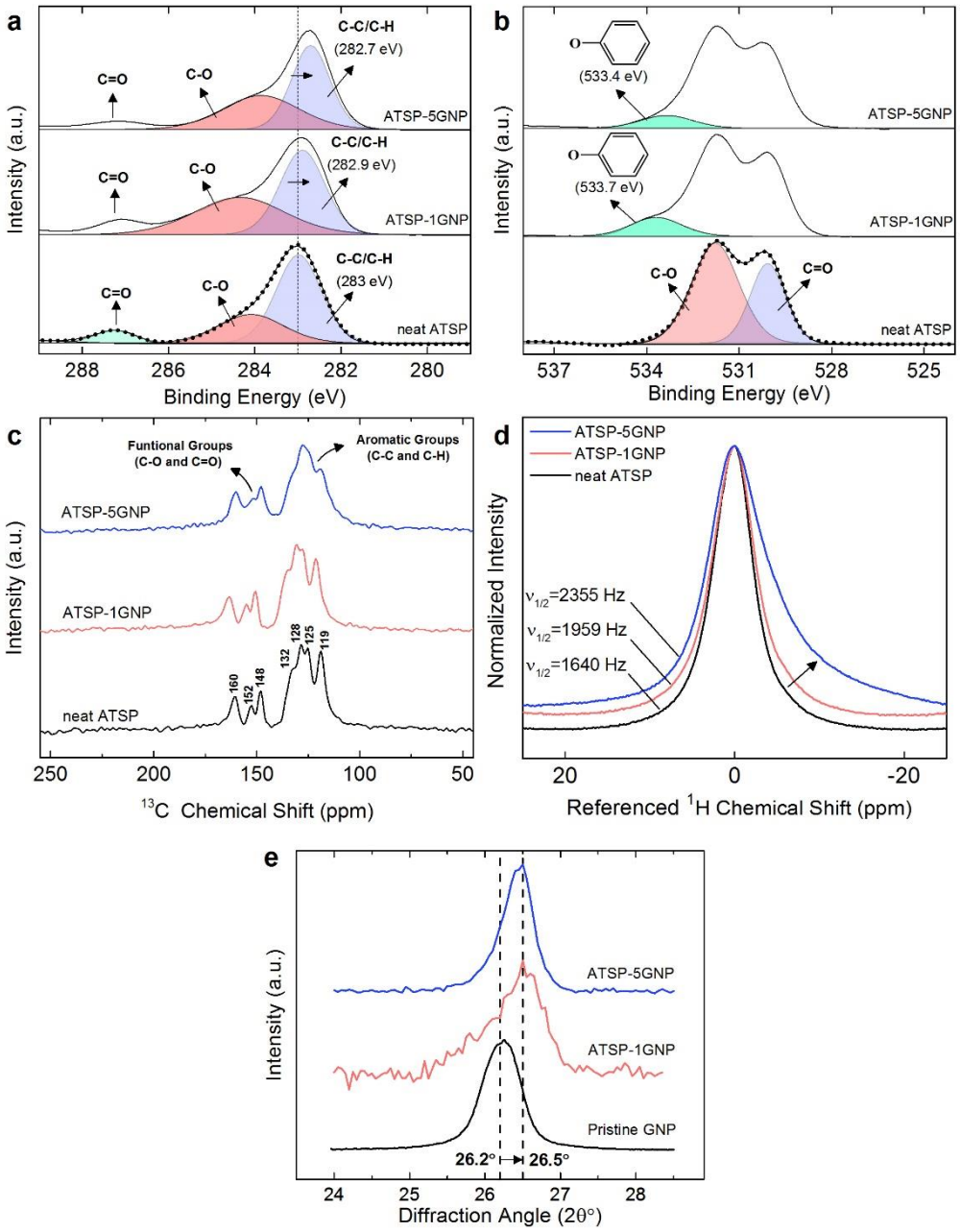

Figure 11.13 a) X-ray photoelectron spectroscopy (XPS) C 1s spectra of the nanocomposites demonstrated downshifts in the aromatic group peak domain and enhancements in the atomic concentration of carbonyl groups. (b) XPS O 1s spectra revealed *in situ* formed carbonyl group peak in the backbone chain configuration. (c) Solid-state Nuclear Magnetic Resonance (ssNMR) ^{13}C cross-polarization magic-angle spinning (CPMAS) spectra. (d) ssNMR ^{1}H direct pulse magic-angle spinning (DPMAS) spectra of the nanocomposites. ^{1}H and ^{13}C NMR spectra were processed using 1 Hz and 25 Hz line broadenings, respectively. ^{1}H spectra referenced to zero to display the peak broadening effect. (e) X-ray diffraction (XRD) spectra of the (002) characteristic peak of the GNP particles within nanocomposites showing reduced interlayer spacing distance through higher diffraction angle shifts.

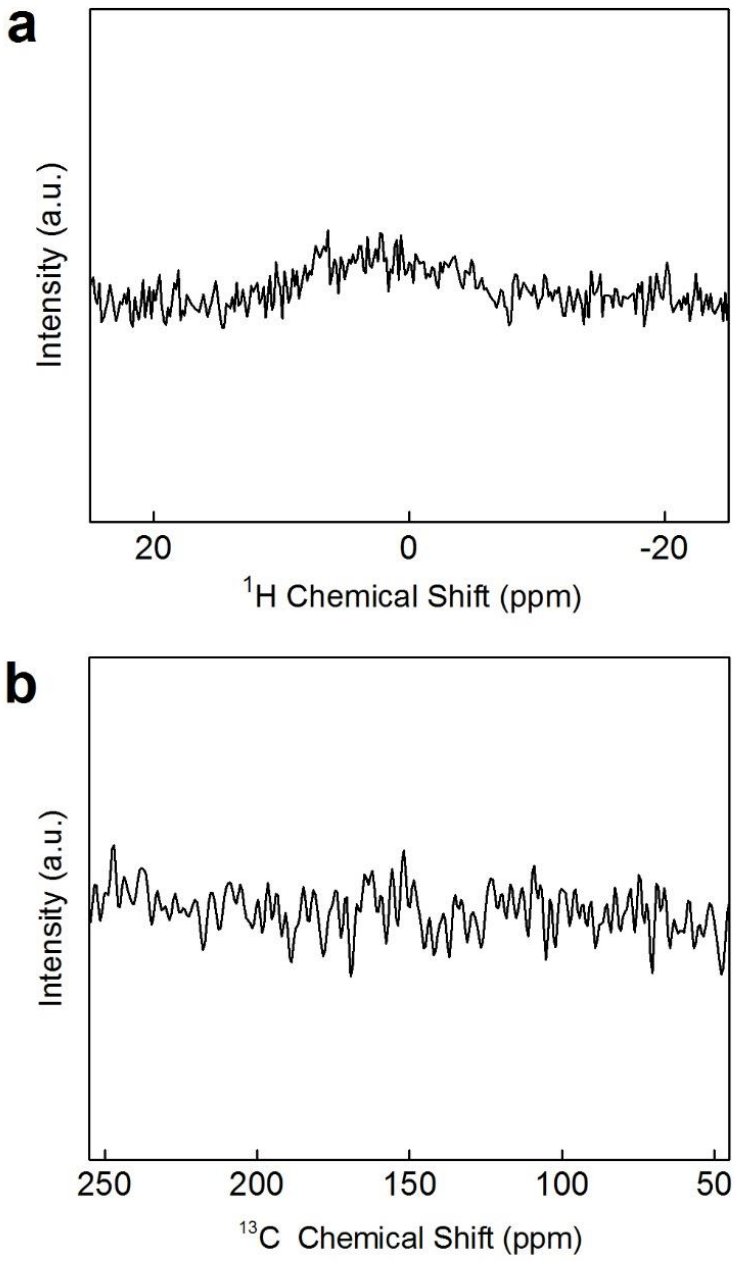

Figure 11.14 NMR spectroscopy of pristine GNP nanoparticles. Solid-state nuclear magnetic resonance (ssNMR) spectra of the pristine GNP particles. (a) ^{13}C cross-polarization magic-angle spinning (CPMAS). (b) ^{1}H direct pulse magic-angle spinning (DPMAS). Under the same operating conditions of the nanocomposites, the GNP did not display any characteristic peak neither in the ^{13}C nor the ^{1}H spectra. Spectra were obtained using Varian Unity Inova 300 MHz NMR spectrometer.

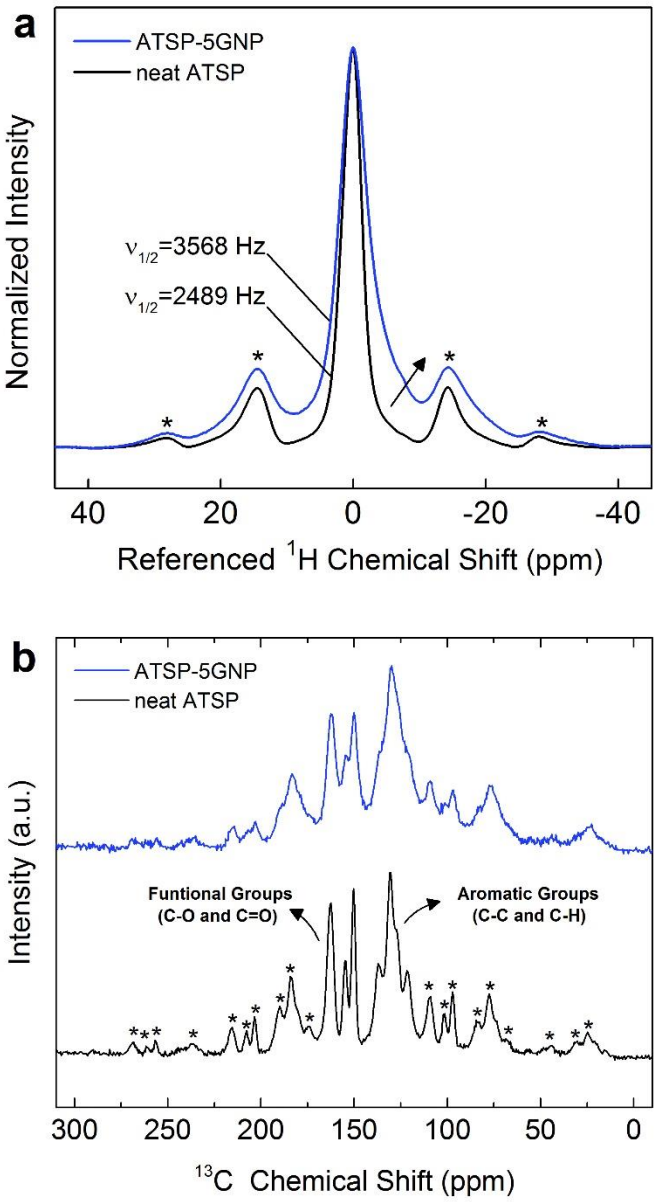

Figure 11.15 High-field NMR spectroscopy of nanocomposite. High-field solid-state nuclear magnetic resonance (ssNMR) spectra of neat ATSP and 5 wt % GNP incorporated ATSP nanocomposite. (a) ^{1}H direct pulse magic-angle spinning (DPMAS). (b) ^{13}C cross-polarization magic-angle spinning (CPMAS). Spectra were obtained using Agilent 750 MHz VNMRS spectrometer. * denotes spinning sidebands.

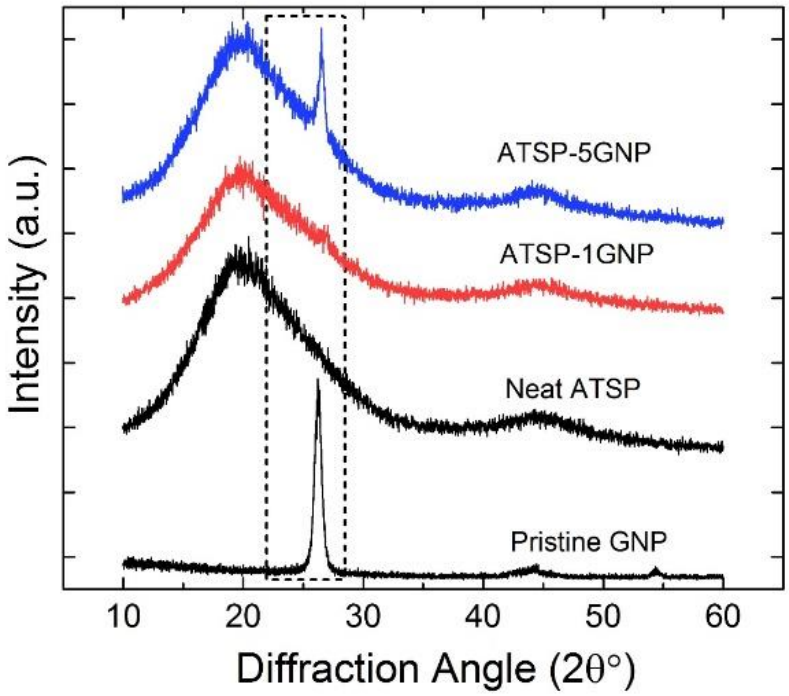

Figure 11.16 X-ray diffraction spectra. The crystalline form of the pristine GNP sheets was observed. The neat, 1 wt % GNP and 5 wt % incorporated samples displayed amorphous morphology of the polymer matrix. These scans were obtained using nominal scanning parameters. The GNP peak defines (002) characteristic peak of sp^2 crystalline carbon structure.

The unique chemical attraction mechanism enabled robust interfacial coupling further yielded significant enhancements in physical properties of the nanocomposites. The GNP incorporation considerably altered the porous morphology of the nanocomposites through the *in situ* rheological modulations during the polymerization process, which formed relatively higher-density structures. Thus, the increased density, with respect to incremented GNP loading, consecutively produced improved compressive strength and Young's modulus. Further analysis using mechanical property scaling relations (Gibson & Ashby method) likewise indicated a strong dependency on the density. Besides, calculated performance indices ($M = {}^{\sigma}/_{\rho}$) for mass minimization on a compressive strength against density chart displayed that the nanocomposite foams could provide equivalent strength to the neat foam for two-thirds of the given mass (see

Figure 11.17 and Table 11.2 for mechanical property scaling analysis) [44-46]. On top of this, the GNP nanocomposites exhibited simultaneous enhancement of the toughness along with the strain to failure, which was successfully enabled through effective load transfer mechanism within the GNP-conjugated network morphology (see Figure 11.18 and Table 11.3 for fracture toughness results). Enhanced deformation tolerance appears likewise to be a consequence of the mechanism producing the glass transition peak broadening [29]. The ATSP nanocomposites might shed light on strength versus toughness conflict in lightweight structural material designs [47]. In addition, the linear thermal expansion characteristics of the nanocomposites were similarly modulated by the chemical coupling mechanism as well as increased density such that the longitudinal elongation was measured as low as ~1 % (ATSP-5GNP) in comparison to ~1.5 % of the parent material at 200 °C, which translated into ~33 % reduced expansion (see Figure 11.19 for thermal expansion results). In this case, the segmental mobility of the ATSP backbone chains was restrained by the negative thermal expansion of the GNP particles, which eventually induced structural stiffening and dimensional stability [48]. Furthermore, the GNP particles, being homogeneously distributed within the nanocomposite morphology, marginally slowed thermal degradation processes on the ATSP backbone chains, for which higher thermal stability of the GNP sheets shielded the polymer chains against further bond scissions (see Figure 11.20 for thermogravimetric analysis results) [49].

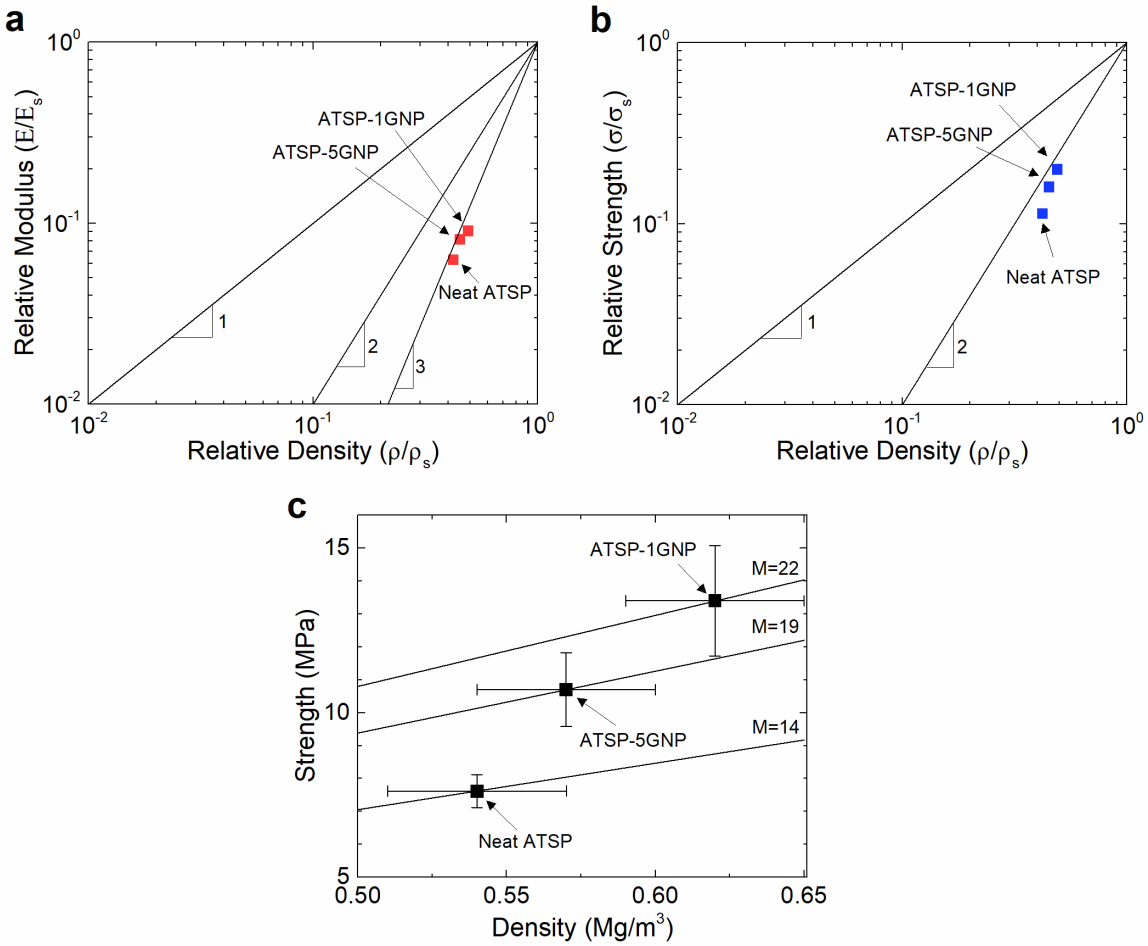

Figure 11.17 Mechanical property scaling relations. (a) Relative Young's modulus (E/E_s) of the neat ATSP and ATSP-GNP nanocomposite foams (1 wt % and 5 wt %) against relative density (ρ/ρ_s). E_s represents Young's modulus, and ρ_s defines the density of bulk ATSP, respectively. The ATSP foams lie around the slope of 3. (b) Relative compressive strength (σ/σ_s) of neat ATSP and ATSP-GNP nanocomposite foams (1 wt % and 5 wt %) against density (ρ/ρ_s). σ_s is the material strength of bulk ATSP. The ATSP foams populate near the slope of 2 which indicates elastic buckling failure mode rather than brittle crushing (slope of 3/2). (c) Compressive strength plotted against density for neat ATSP and ATSP-GNP nanocomposite foams (1 wt % and 5 wt %). M is defined as σ/ρ (σ and ρ are strength and density, respectively) which describes performance index for mass minimization of materials. ATSP nanocomposites foams could provide equivalent strength as the neat foam for two-thirds of the given mass. The mechanical property enhancements were beyond the estimation of predictive tools.

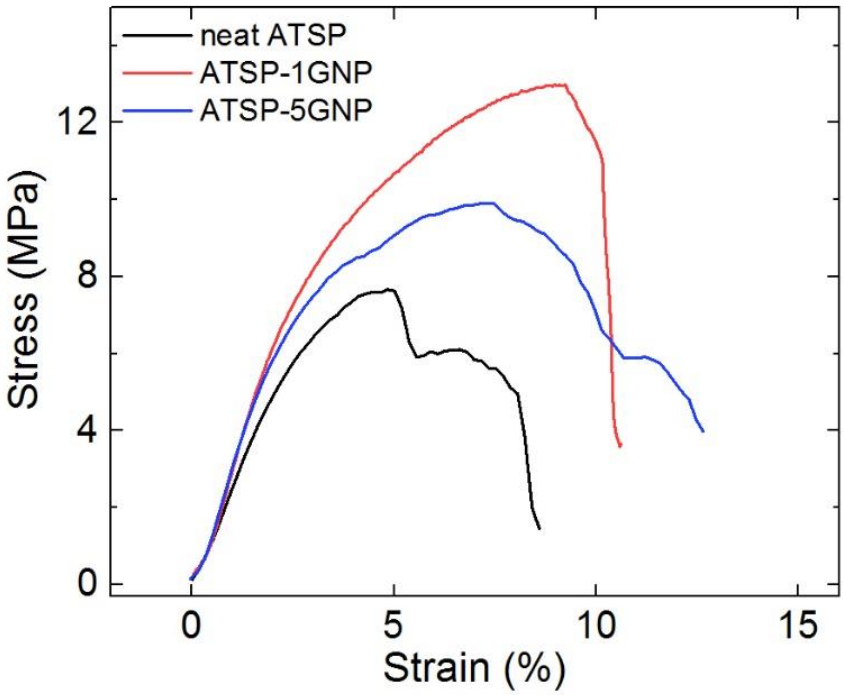

Figure 11.18 Compressive mechanical property characterization. Compressive mechanical behaviors of the nanocomposites demonstrated increased compressive strength and strain-to-failure generating a more deformation tolerant and tough material morphology.

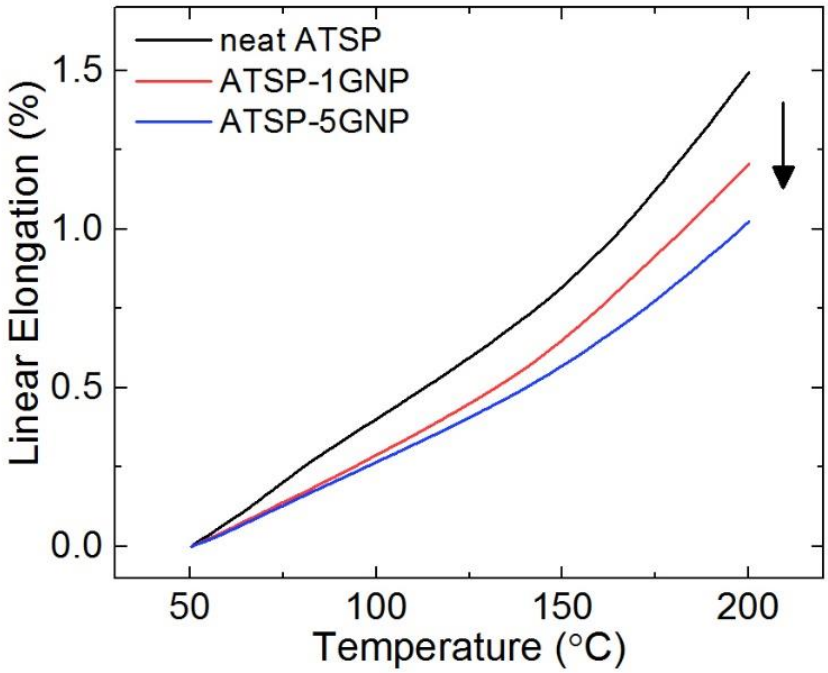

Figure 11.19 Thermal expansion characterization. Linear thermal expansion characteristics of the nanocomposites showed reduced elongation influenced by the negative expansion of the GNP sheets. The results also correlate with the glass transition behaviors.

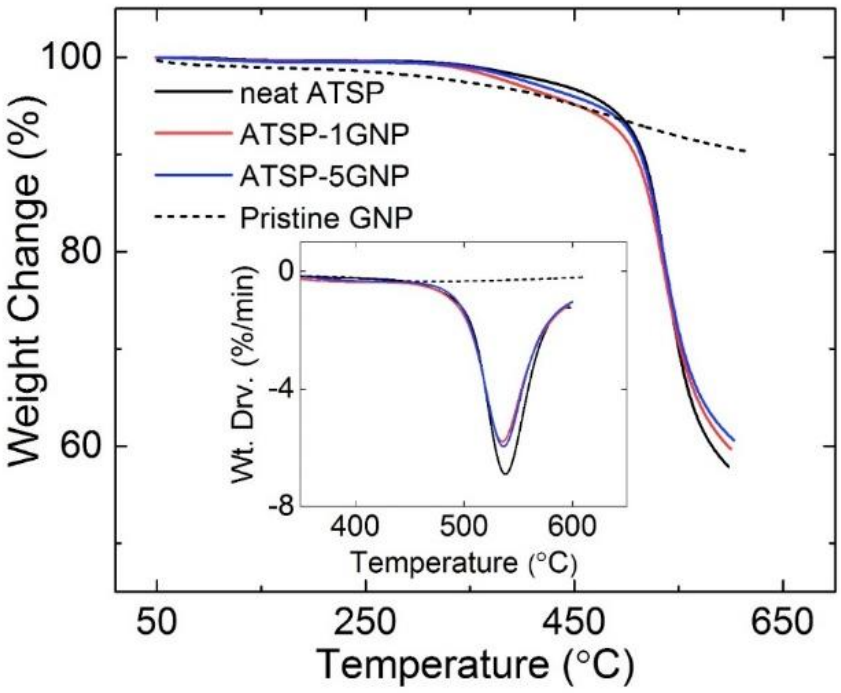

Figure 11.20 Thermogravimetric analysis results. Thermogravimetric and weight derivate thermal degradation analysis of the nanocomposites measured under dry nitrogen. The nanofiller-crosslinked network displayed similar characteristics to the pristine structure, while GNP particles reduced degradation process.

Table 11.2 Mechanical properties. Compressive mechanical properties of the neat ATSP and ATSP-GNP nanocomposite foams with 1 wt % GNP and 5 wt% GNP.

	Modulus (GPa)	**Std. Dev.**	**Strength (MPa)**	**Std. Dev.**	**Density (Mg/m^3)**	**Std. Dev.**	**Relative Density**	**Std. Dev.**
Neat ATSP	0.27	0.04	7.62	0.5	0.54	0.03	0.42	0.03
ATSP-1GNP	0.39	0.05	13.38	1.68	0.62	0.03	0.49	0.03
ATSP-5GNP	0.35	0.04	10.7	1.12	0.57	0.03	0.45	0.03

Table 11.3 Material toughness results**.** Material toughness of the neat ATSP and ATSP-GNP nanocomposite foams with 1 wt % GNP and 5 wt % GNP.

	Strength (MPa)	**Std. Dev.**	**Strain at Max. Stress (%)**	**Std. Dev.**	**Material Toughness (MJ/m^3)**	**Std. Dev.**
Neat ATSP	7.62	0.5	5.30	1.10	21.1	6.4
ATSP-1GNP	13.38	1.68	8.25	1.12	74.6	14.7
ATSP-5GNP	10.7	1.12	6.88	0.67	46.6	7.3

11.4 Conclusion

In conclusion, the aromatic polyester oligomers demonstrated strong interfacial covalent bonding with chemically pristine carbonaceous nanoparticles. Through the attachment mechanism between carboxylic acid and acetoxy functional end-groups of the constituent oligomers and the oxygen-bearing sites of the carbonaceous particles, thermomechanical chain relaxation characteristics of the backbone in the nanocomposite morphology was greatly altered yielding remarkably broadened (~100 °C) and significantly high temperature shifted (~80 °C) glass transition regimes. Within the nanofiller-contiguous polymer network, the backbone-conjugated nanofiller particles induced the pseudo-rheological percolation behavior during the glass transition via local immobilization by which chain relaxation schedules lagged behind causing transient energy buffering in the chains that accordingly generated substantially broadened glass transition regions with significantly upshifted peak temperatures. The ATSP nanocomposites demonstrate an advanced nanocomposite material technology to obtain ultimately enhanced multifunctional physical properties that may further help to address emerging application problems in the development of new materials.

11.5 References

[1] Jordan, J.; Jacob, K. I.; Tannenbaum, R.; Sharaf, M. A.; Jasiuk, I., Experimental trends in polymer nanocomposites—a review. Materials Science and Engineering: A 2005, 393 (1–2), 1-11.

[2] Merkel, T. C.; Freeman, B. D.; Spontak, R. J.; He, Z.; Pinnau, I.; Meakin, P.; Hill, A. J., Ultrapermeable, reverse-selective nanocomposite membranes. Science 2002, 296 (5567), 519-522.

[3] Darder, M.; Aranda, P.; Ruiz-Hitzky, E., Bionanocomposites: A new concept of ecological, bioinspired, and functional hybrid materials. Advanced Materials 2007, 19 (10), 1309-1319.

[4] Chen, Z.; Xu, C.; Ma, C.; Ren, W.; Cheng, H. M., Lightweight and flexible graphene foam composites for high-performance electromagnetic interference shielding. Advanced materials 2013, 25 (9), 1296-1300.

[5] Bansal, A.; Yang, H.; Li, C.; Cho, K.; Benicewicz, B. C.; Kumar, S. K.; Schadler, L. S., Quantitative equivalence between polymer nanocomposites and thin polymer films. Nat Mater 2005, 4 (9), 693-698.

[6] Oh, H.; Green, P. F., Polymer chain dynamics and glass transition in athermal polymer/nanoparticle mixtures. Nat Mater 2009, 8 (2), 139-143.

[7] Kim, H.; Abdala, A. A.; Macosko, C. W., Graphene/polymer nanocomposites. Macromolecules 2010, 43 (16), 6515-6530.

[8] Liao, K.-H.; Aoyama, S.; Abdala, A. A.; Macosko, C., Does graphene change Tg of nanocomposites? Macromolecules 2014, 47 (23), 8311-8319.

[9] Potts, J. R.; Lee, S. H.; Alam, T. M.; An, J.; Stoller, M. D.; Piner, R. D.; Ruoff, R. S., Thermomechanical properties of chemically modified graphene/poly(methyl methacrylate) composites made by in situ polymerization. Carbon 2011, 49 (8), 2615-2623.

[10] Ramanathan, T.; Abdala, A. A.; StankovichS; Dikin, D. A.; Herrera Alonso, M.; Piner, R. D.; Adamson, D. H.; Schniepp, H. C.; ChenX; Ruoff, R. S.; Nguyen, S. T.; Aksay, I. A.; Prud'Homme, R. K.; Brinson, L. C., Functionalized graphene sheets for polymer nanocomposites. Nat Nano 2008, 3 (6), 327-331.

[11] Fang, M.; Wang, K.; Lu, H.; Yang, Y.; Nutt, S., Covalent polymer functionalization of graphene nanosheets and mechanical properties of composites. Journal of Materials Chemistry 2009, 19 (38), 7098-7105.

[12] Boukhvalov, D. W.; Katsnelson, M. I., Chemical functionalization of graphene with defects. Nano Letters 2008, 8 (12), 4373-4379.

[13] Bakir, M.; Meyer, J. L.; Economy, J.; Jasiuk, I., Aromatic thermosetting copolyester nanocomposite foams: High thermal and mechanical performance lightweight structural materials. Polymer 2017, 123, 311-320.

[14] Frich, D.; Goranov, K.; Schneggenburger, L.; Economy, J., Novel high-temperature aromatic copolyester thermosets: synthesis, characterization, and physical properties. Macromolecules 1996, 29 (24), 7734-7739.

[15] Vaezian, B.; Meyer, J. L.; Economy, J., Processing of aromatic thermosetting copolyesters into foams and bulk parts: characterization and mechanical properties. Polymers for Advanced Technologies 2016, 27 (8), 1006-1013.

[16] Frich, D.; Economy, J.; Goranov, K., Aromatic copolyester thermosets: high temperature adhesive properties. Polymer Engineering & Science 1997, 37 (3), 541-548.

[17] Lan, P.; Meyer, J. L.; Economy, J.; Polycarpou, A. A., Unlubricated tribological performance of aromatic thermosetting polyester (ATSP) coatings under different temperature conditions. Tribology Letters 2016, 61 (1), 10.

[18] Bakir, M.; Meyer, J. L.; Economy, J.; Jasiuk, I., Heat-induced polycondensation reaction with self-generated blowing agent forming aromatic thermosetting copolyester foams. Macromolecules 2016, 49 (17), 6489-6496.

[19] Bakir, M.; Meyer, J. L.; Sutrisno, A.; Economy, J.; Jasiuk, I., Nanofiller-conjugated percolating conductive network modified polymerization reaction characteristics of aromatic thermosetting copolyester resin. RSC Advances 2018, 8 (9), 4946-4954.

[20] Bakir, M.; Meyer, J. L.; Hussainova, I.; Sutrisno, A.; Economy, J.; Jasiuk, I., Periodic functionalization of graphene-layered alumina nanofibers with aromatic thermosetting copolyester via epitaxial step-growth polymerization. Macromolecular Chemistry and Physics 2017, 218 (24), 1700338.

[21] Frich, D.; Hall, A.; Economy, J., Nature of adhesive bonding via interchain transesterification reactions (ITR). Macromolecular Chemistry and Physics 1998, 199 (5), 913-921.

[22] Kerle, T.; Lin, Z.; Kim, H.-C.; Russell, T. P., Mobility of polymers at the air/polymer interface. Macromolecules 2001, 34 (10), 3484-3492.

[23] Bakir, M.; Henderson, C. N.; Meyer, J. L.; Oh, J.; Miljkovic, N.; Kumosa, M.; Economy, J.; Jasiuk, I., Effects of environmental aging on physical properties of aromatic thermosetting copolyester matrix neat and nanocomposite foams. Polymer Degradation and Stability 2018, 147, 49-56.

[24] Ellison, C. J.; Torkelson, J. M., The distribution of glass-transition temperatures in nanoscopically confined glass formers. Nature Materials 2003, 2, 695.

[25] Frich, D. J., The effect of interchain transesterification reactions on the development of aromatic copolyesters. University of Illinois at Urbana-Champaign: 1996.

[26] Tsagaropoulos, G.; Eisenberg, A., Dynamic mechanical study of the factors affecting the two glass transition behavior of filled polymers. Similarities and differences with random ionomers. Macromolecules 1995, 28 (18), 6067-6077.

[27] Stutz, H.; Illers, K. H.; Mertes, J., A generalized theory for the glass transition temperature of crosslinked and uncrosslinked polymers. Journal of Polymer Science Part B: Polymer Physics 1990, 28 (9), 1483-1498.

[28] Yu, J. W.; Jung, J.; Choi, Y.-M.; Choi, J. H.; Yu, J.; Lee, J. K.; You, N.-H.; Goh, M., Enhancement of the crosslink density, glass transition temperature, and strength of epoxy resin by using functionalized graphene oxide co-curing agents. Polymer Chemistry 2016, 7 (1), 36-43.

[29] Kim, J.; Mok, M. M.; Sandoval, R. W.; Woo, D. J.; Torkelson, J. M., Uniquely broad glass transition temperatures of gradient copolymers relative to random and block copolymers containing repulsive comonomers. Macromolecules 2006, 39 (18), 6152-6160.

[30] Rittigstein, P.; Priestley, R. D.; Broadbelt, L. J.; Torkelson, J. M., Model polymer nanocomposites provide an understanding of confinement effects in real nanocomposites. Nature Materials 2007, 6, 278.

[31] Chen, L.; Zheng, K.; Tian, X.; Hu, K.; Wang, R.; Liu, C.; Li, Y.; Cui, P., Double glass transitions and interfacial immobilized layer in in-situ-synthesized poly(vinyl alcohol)/silica nanocomposites. Macromolecules 2010, 43 (2), 1076-1082.

[32] Kota, A. K.; Cipriano, B. H.; Duesterberg, M. K.; Gershon, A. L.; Powell, D.; Raghavan, S. R.; Bruck, H. A., Electrical and rheological percolation in polystyrene/MWCNT nanocomposites. Macromolecules 2007, 40 (20), 7400-7406.

[33] Pötschke, P.; Fornes, T. D.; Paul, D. R., Rheological behavior of multiwalled carbon nanotube/polycarbonate composites. Polymer 2002, 43 (11), 3247-3255.

[34] Williams, M. L.; Landel, R. F.; Ferry, J. D., The temperature dependence of relaxation mechanisms in amorphous polymers and other glass-forming liquids. Journal of the American Chemical society 1955, 77 (14), 3701-3707.

[35] Priestley, R. D.; Ellison, C. J.; Broadbelt, L. J.; Torkelson, J. M., Structural relaxation of polymer glasses at surfaces, interfaces, and in between. Science 2005, 309 (5733), 456-459.

[36] Parkar, Z., Design of unique composites based on aromatic thermosetting copolyesters. University of Illinois at Urbana-Champaign: 2011.

[37] Korbakov, N.; Harel, H.; Feldman, Y.; Marom, G., Dielectric response of aramid fiber-reinforced PEEK. Macromolecular Chemistry and Physics 2002, 203 (16), 2267-2272.

[38] Zhang, J.; Zou, H.; Qing, Q.; Yang, Y.; Li, Q.; Liu, Z.; Guo, X.; Du, Z., Effect of chemical oxidation on the structure of single-walled carbon nanotubes. The Journal of Physical Chemistry B 2003, 107 (16), 3712-3718.

[39] Peng, H.; Alemany, L. B.; Margrave, J. L.; Khabashesku, V. N., Sidewall carboxylic acid functionalization of single-walled carbon nanotubes. Journal of the American Chemical Society 2003, 125 (49), 15174-15182.

[40] Chen, J.; Liu, H.; Weimer, W. A.; Halls, M. D.; Waldeck, D. H.; Walker, G. C., Noncovalent engineering of carbon nanotube surfaces by rigid, functional conjugated polymers. Journal of the American Chemical Society 2002, 124 (31), 9034-9035.

[41] Lin, Y.; Zhou, B.; Shiral Fernando, K. A.; Liu, P.; Allard, L. F.; Sun, Y.-P., Polymeric carbon nanocomposites from carbon nanotubes functionalized with matrix Polymer. Macromolecules 2003, 36 (19), 7199-7204.

[42] Bain, A. D.; Eaton, D. R.; Hamielec, A. E.; Mlekuz, M.; Sayer, B. G., Line broadening in the carbon-13 NMR spectra of crosslinked polymers. Macromolecules 1989, 22 (9), 3561-3564.

[43] Shioya, H.; Craciun, M. F.; Russo, S.; Yamamoto, M.; Tarucha, S., Straining graphene using thin film shrinkage methods. Nano Letters 2014, 14 (3), 1158-1163.

[44] Gibson, L. J., Biomechanics of cellular solids. Journal of Biomechanics 2005, 38 (3), 377-399.

[45] Gibson, L. J.; Ashby, M. F., Cellular solids: structure and properties. Cambridge university press: 1999.

[46] Gibson, L. J., The hierarchical structure and mechanics of plant materials. Journal of The Royal Society Interface 2012, 9 (76), 2749-2766.

[47] Ritchie, R. O., The conflicts between strength and toughness. Nat Mater 2011, 10 (11), 817-822.

[48] Wang, S.; Tambraparni, M.; Qiu, J.; Tipton, J.; Dean, D., Thermal expansion of graphene composites. Macromolecules 2009, 42 (14), 5251-5255.

[49] Bao, C.; Song, L.; Xing, W.; Yuan, B.; Wilkie, C. A.; Huang, J.; Guo, Y.; Hu, Y., Preparation of graphene by pressurized oxidation and multiplex reduction and its polymer nanocomposites by masterbatch-based melt blending. Journal of Materials Chemistry 2012, 22 (13), 6088-6096.

CHAPTER 12: REVERSIBLE ADHESION OF AROMATIC THERMOSETTING COPOLYESTER FOR IN-SPACE ASSEMBLY

12.1 Introduction

Development of next-generation space structures [1,2] requires lightweight and multifunctional architectures, made from environment-compatible and model-based designed materials via versatile manufacturing processes, as highlighted in NASA's Technology Roadmap Technology Area 12 [3]. Future space missions are envisioned towards both sustainment of long-term on-mission space stations (e.g. ISS) [4], and, particularly, construction of on-site habitable structures beyond low-Earth orbit (e.g. Human Exploration of MARS) [2], which prompts need of innovative concepts for reconfigurable and reusable designs in response to changing mission needs. Specifically, NASA's Solar Electric Propulsion (SEP) project is sought to develop electrically propelled space shuttles having on-board multiple solar arrays (e.g. MegaFlex and Mega-ROSA concept designs) [5]. Likewise, Orbital Replacement Units (ORUs) are utilized to repair/replace malfunctioning segments of on-mission space systems (e.g. ISS) at present, and will soon be employed for building on-site space structures [6].

This work was performed performed under NASA Small Business Innovation Research (SBIR) Phase-I program (Contract Number: NNX17CL41P) with ATSP Innovations and NASA Langley Research Center (2017).

Herein, we demonstrate a conveniently reconfigurable joining approach to connect highly scalable multifunctional architectures with fiber-reinforced polymer composite links. A reversible solid-state bonding mechanism is enabled using a novel high-performance polymer resin, for which only physical contact and application of heat is required. Hence, the attachment scheme will be amenable to automated robotic assembly along with minimized mass usage and power consumption.

Joining approaches towards reversible assembly usually involve screw or snap-together mechanisms. A screw mechanism would require threaded units to be mounted on the unit elements which would add to weight and parts count. More importantly, primary concern should be to counter-balance the moments induced when the unit elements are rotated and tightened in microgravity. Existing screw-based devices often require bulky equipment in microgravity environments due to the need for unlubricated operation [7] which increases total launch weight. A disconnect or snap-on based joining approach (plug-and-play concept) likewise may increase total structural mass, and mitigation of this additional mass would have the technical complexity of finding an appropriate high temperature resin to construct the disconnects to reduce weight. Therefore, a bonding scheme based on reversible solid-state reactions is the most practical way to minimize mass for reconfigurable space architectures.

At a glance, state-of-the-art space frame construction technologies [8] rely on the use of metal-based unit elements [9,10], which are either permanently joined or connected via labor-intensive and difficult to automate joint mechanisms. Although such designs are readily used on low-Earth orbit space missions, their large weights and infeasibility of reassembly under space conditions becloud their implementations on future space missions. To address these problems, recent studies have employed fiber composite unit elements attached via mechanical interlocks to

build lightweight, high strength/stiffness cellular structures [11]. Even though such design concept addresses the above-mentioned issues and presents a reversible joint mechanism, the length scales are currently far below those of targeted technological applications, and joining requires complex mechanical interlocks which may inhibit a fully autonomous assembly. Present automation concepts for assembly of cellular structures [12] involve unit members that have a relatively low packing factor and specific mechanical properties and therefore would occupy launch volume and mass needlessly. Also, reconfigurable concepts which switch from one-unit cell type to another, have not been explored. Regarding bonding approach of primary structures, DARPA/Lockheed Martin X-55 Advanced Composite Cargo Aircraft demonstration paved the way through feasibility of building adhesively joined unitized composite skin for a fuselage structure [13]. Utilizing such an innovative approach, substantial weight savings on an aircraft frame were enabled by simply eliminating rivet and fastener use (more than 85%) along with significantly reduced material cost, time and labor for fabrication and assembly [14].

In this regard, Aromatic Thermosetting Copolyester (ATSP) intrinsically enables solid-state adhesive bonding possessing reformable bonds by virtue of the interchain transesterification reactions (ITR) [15]. The ITR bonding scheme is a chemical interfacial self-welding mechanism which effectively consolidates pre-cured ATSP parts forming a smooth continuous bond line. The ITR bonding is enabled via only application of heat and physical contact, which does not evolve any volatiles during such joining process. The ITR bonding is uniquely reversibly allowing repeatable bond/debond over the very same bond line without causing any visible physical damage. Continuous fiber ATSP composites was investigated under a NASA SBIR Phase I program for high temperature and cryogenic applications [16]. The results showed that ITR bonding between laminae produces excellent interlaminar properties. Shear strength,

modulus and fracture toughness were found to be comparable or superior to epoxy and polyimide carbon fiber composites [17-21] demonstrating the viability of ITR as a solid-state bonding scheme. Thermal fatigue tests showed that ATSP composites are resistant to microcracking, due to the resin's tendency of locally matching coefficient of thermal expansion (CTE) around the carbon fiber [21-23] and are capable of withstanding extreme hot and cold temperature cycles via cryogenic thermal cycling [16]. Additionally, they are durable [24,25], in-situ self-repairable [26], and maintain mechanical properties at elevated temperatures (Tg up to 307°C). Also, ATSP shows a unique capability for repair of interlaminar cracks on application of heat and pressure through ITR. Similarly, metal coupons bonded via ITR were observed to have a lap shear strength of up to 20 MPa [27]. Tailorable ATSP chemistry can be adapted to nearly any polymer processing technique by adjustments in oligomer structure.

There are several criteria for a practical reversible adhesive scheme relevant to missions in space. The first is that it be a fully reversible and all solid-state process as liquids generally have an unacceptably high vapor pressure in vacuum, which eliminates approaches that rely on uncured polymer [14] or a meltable interstitial phase [28]. The second is that the joint members of the structure and the reversible adhesive do not experience a glass or melt transition within the range of temperatures experienced by the structure during day/night cycles (-160 to 120 °C) [29] in conditions without thermal controls - which would induce undesirable adhesive reversion due to an uncontrolled change in phase and negate mechanical properties of the bonded interface [30-31]. This eliminates shape memory polymers [32] and some "gecko" adhesive [33-34] schemes which generally rely on polymers which have glass transitions below 120°C. Additionally, the reversible adhesive joint must be scalable and able to be implemented into complex geometries. This eliminates gecko adhesive schemes available in the literature [35] due to their reliance on

patterned fibrillar surfaces. While conventional bonding processes contingent on melting the resin phase exist for thermoplastic composites [36-39], ITR would offer the first viable composite welding scheme for fully cured thermoset composites. With a glass transition temperature of up to 310°C and the entire polymer backbone possessing thermally-activated labile ester bonds and therefore the complete structure accessible as a reversible adhesive, ATSP-based composites present a viable and possibly unique solution to minimize mass and reduce component numbers in reconfigurable structures.

12.2 Results and Discussion

ATSP coated metal specimens were utilized in this project. For the coating specimens, uncured matching oligomers of ATSP were sprayed onto aerospace-grade Al 7075 substrates employing an electrostatic powder technique. Figure 12.1 shows an example of a coated cylindrical sample. The coated samples were then cured in a convection oven at 270°C for about 30 min. Upon curing, ATSP coating thickness was measured to be around 40-60 μm by an eddy-current-based magnetic coating thickness gauge.

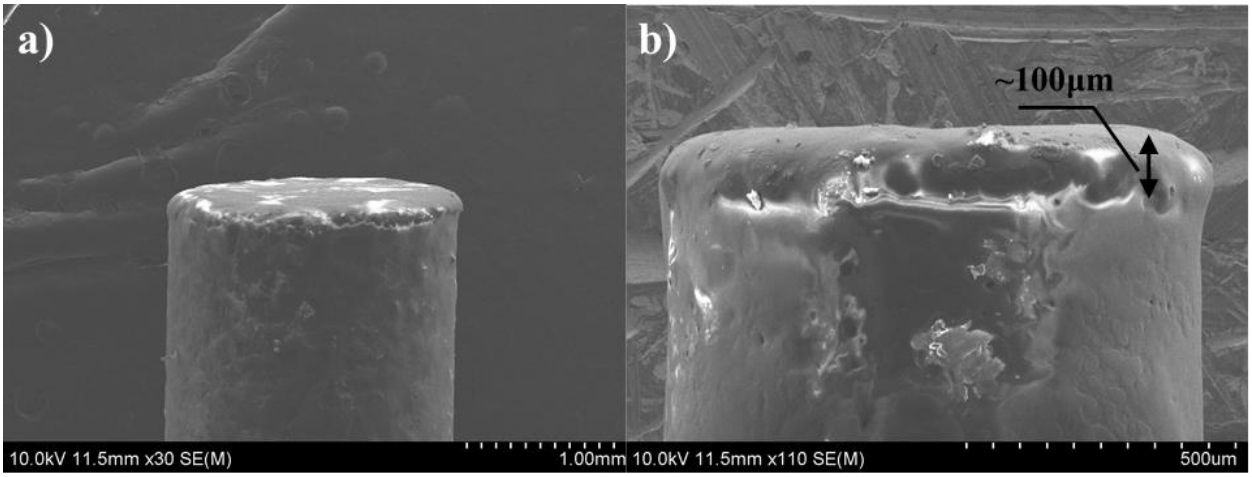

Figure 12.1 Scanning Electron Microscope (SEM) images of the ATSP-coated Al specimens prepared for DMA/ITR tests.

Operational parameters of temperature, time and pressure for the ITR bonding were assessed and characterized via Dynamic Mechanical Analysis (DMA) (Q800 TA Instruments) tests. A uniaxial fixture was operated in the DMA to enable compressive force (bonding force) during the ITR process and to apply tensile force (pull-off force) during the pull-off experiments. The DMA setup is limited to ±18 N in both modes. For the DMA experiments, Al pieces of 1 mm and 2 mm diameter circular heads, coated with ATSP and cured, were brought in contact with rectangular bases of 10 mm x 10 mm Al pieces (Figure 12.2). Upon enabling successful ITR bonding between the two pieces, pull-off tests were applied to measure strengths of the samples. Measured pull-off strengths were beyond the limits of the DMA fixture (18 N) for both 1 mm and 2 mm diameter heads. However, larger diameter heads are more likely to see misalignment between two parts, which causes partial bonding between the parts, while a smaller diameter causes full-scale bonding.

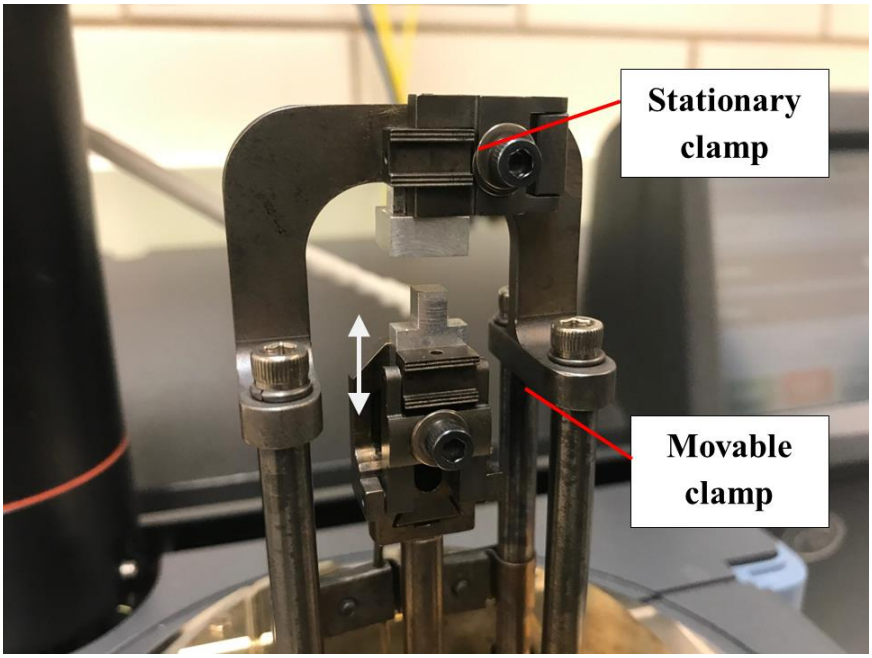

Figure 12.2 DMA uniaxial loading configuration showing ITR bonding setup with a movable clamp that enables both compressive and tensile forces applied on the stationary clamp.

We also obtained scanning electron microscopy (SEM) images of the ITR bonded samples (Figure 12.3). The samples with a smaller diameter (1 mm) still evidenced bonding strength that was beyond the force limits of the DMA. To fall into the force limit of the DMA, even smaller diameters were employed, yet due to mechanical properties of the metal parts coming into effect at smaller scales, we limited the smallest diameter size to 1 mm. Overall, with results of the DMA analysis, we have observed that 23 MPa, 30 min and 400 °C enables effective ITR bonding and can be considered an effective upper bound in terms of conditions necessary.

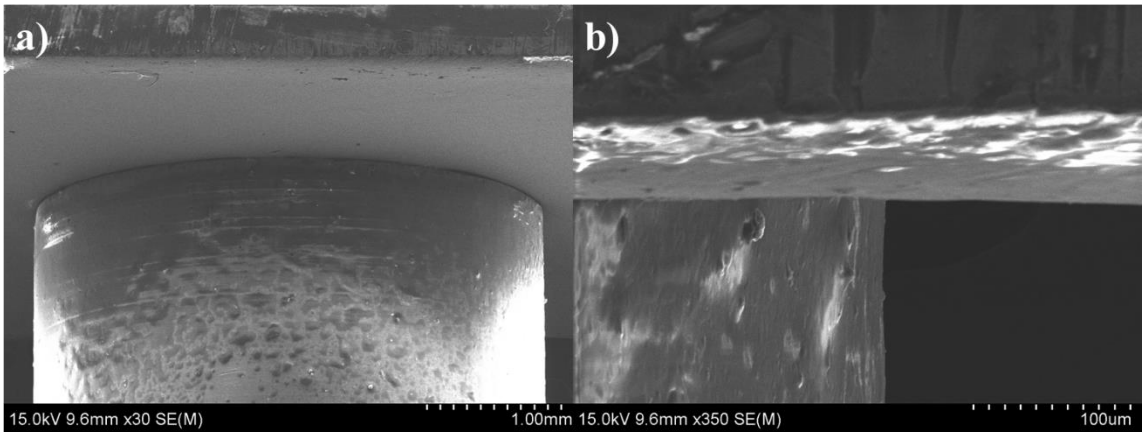

Figure 12.3 SEM images of the ATSP-coated Al specimens bonded via ITR.

We designed DMA cycles to realized debonding under elevated temperature and applied tensile force. Figure 12.4 shows a thermomechanical DMA cycle that enables reversible ITR debonding of already bonded two parts. In the cycle, the force is kept at 5N (6.4 MPa) with ramp up of temperature to 400°C; if the bond did not break, the temperature was held at 400°C and force was ramped up to 18N. The debonding temperatures at 5N are 336°C, 372°C and 392°C for C1A1, C2A2, and CBAB, respectively, for different formulations of ATSP.

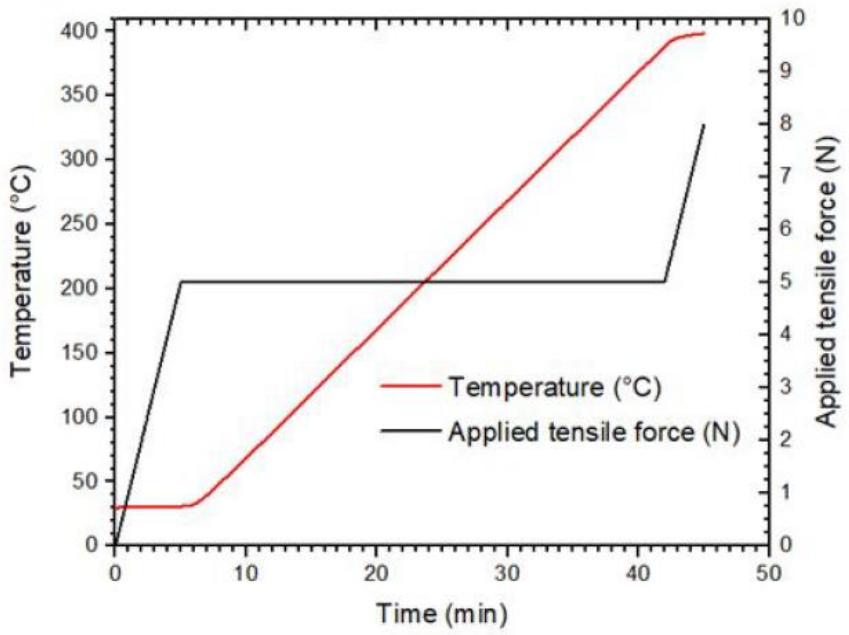

Figure 12.4 Thermomechanical DMA cycle to enable ITR reversible debonding of the two parts.

The high bond strength is well demonstrated at room and high temperature. However, in space the temperature can range from cryogenic to high temperature. Thus, as shown in Figure 12.5, a pull strength study was carried out from -150°C to 200°C and the results show that the bond strength is well maintained (~13 MPa) throughout this temperature range.

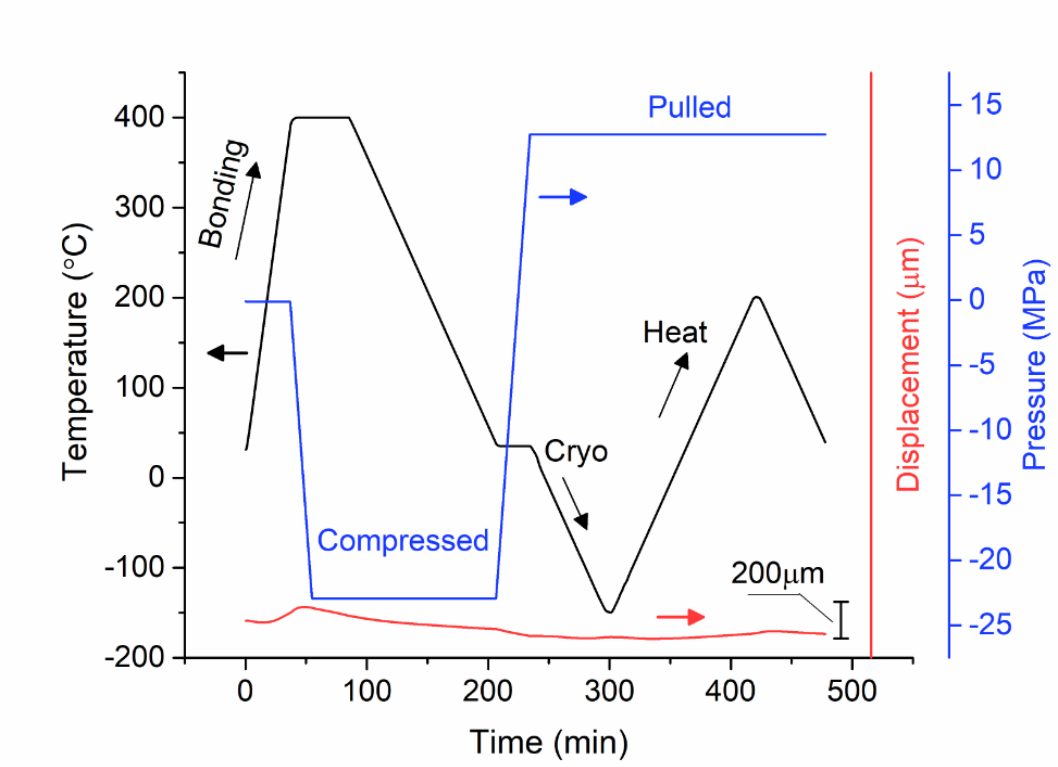

Figure 12.5 DMA thermomechanical cycle of ATSP-coated Al 7075 parts; first ITR bonding, second cryogenic cooling, and last high-temperature treatment.

Based on the thermomechanical results, shown in Figure 12.6, three consecutive cycles of reversible ITR bonding/debonding were successfully performed over the same bonding area using uniaxial loading fixture in DMA. The ITR cycles demonstrated quite repeatable trends with respect to displacement over the bond line at the given temperature and tensile stress (pressure) which effectively validated the reversibility concept of the ITR bonding. Another major finding is that the debonding, or reversibility, occurred in cohesive mode as the corresponding surface on the base substrate still contained polymer coating. As seen in SEM (Hitachi 4800) images in Figure 12.7, the applied ATSP coating remained on the metal substrate surface. Fracture surface clearly shows the evidence of ductile failure mode - fibrillation/drawing is clearly evident in the lower right close-up image, as compared to surface features of fractured

specimen at room temperature. Note the concave structure in Figure 12.7 was formed due to the extremely high bonding temperature (400°C) and applied compressive pressure (~13 MPa).

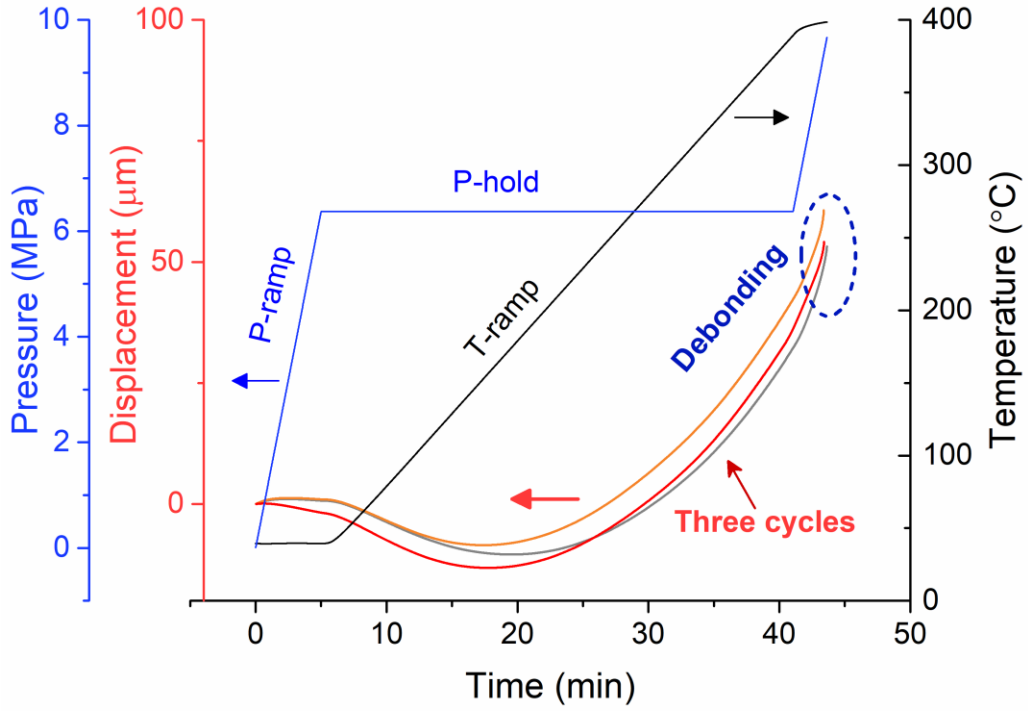

Figure 12.6 DMA three subsequent bonding/debonding cycles on the same bonding region showing highly repeatable debonding characteristics in terms of debonding displacement corresponding to close operation temperatures and effective pressure (Pressure is applied in tensile mode as tensile stress).

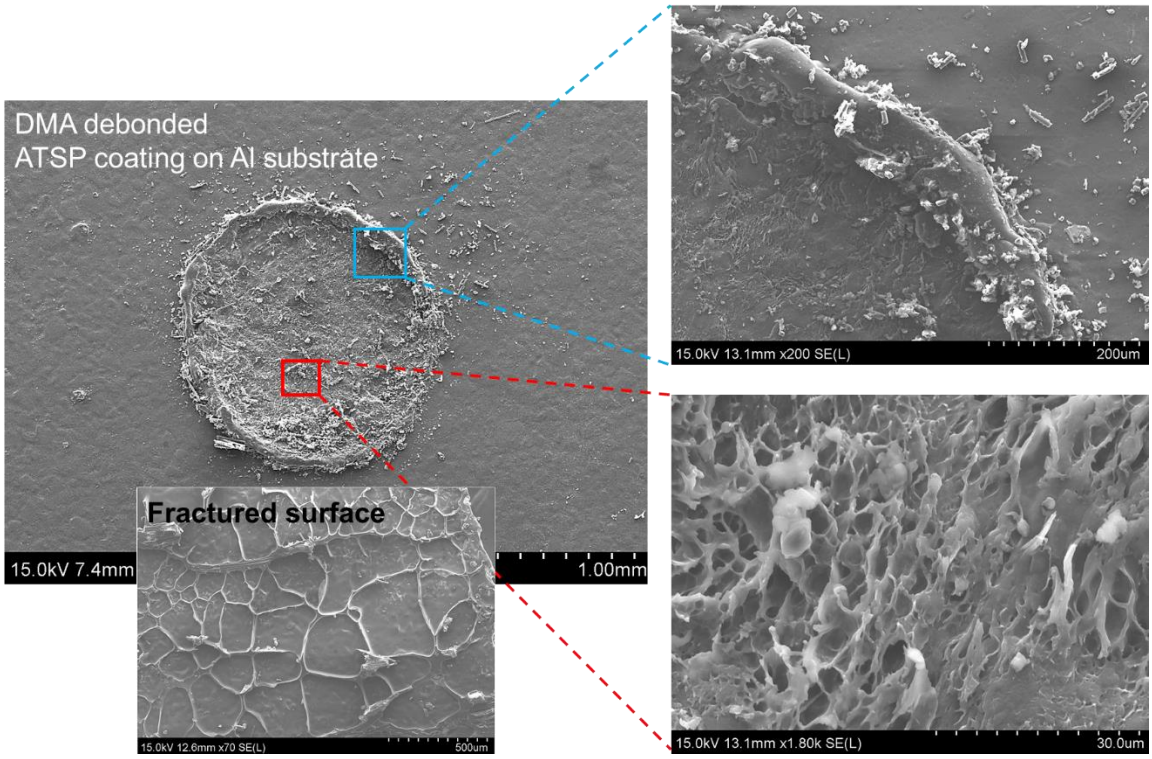

Figure 12.7 Figure 11. SEM images of reversibly debonded (three times) surface with close-up views of surface features. Fractured surface represents delaminated bonding at room temperature.

12.3 Conclusion

The NASA Technology Roadmap TA12 Materials, Structures, Mechanical Systems and Manufacturing describes the ability to reversibly join structural truss units capable of sustaining loads 100 - 500 N. The technology described in this report exceeds this force criteria by a factor of 6 even with a very small cone-shaped joint; with the same cone shape but similar dimension as struss, the force can reach 56760N (113 times of 500N) with contact area of 1290 mm 2 (2 square inches); from the parameters study, it is clear that various levels of bond strength can be obtained by optimizing the bond parameters of temperature, pressure, and time. Joint design concepts based around this technology can allow multifunctionality as electrical contacts as described in the roadmap and solicitation. Additionally, the reversibility scheme developed during this work has been shown to be reversible >50 times.

12.4 References

[1] NASA Authorization Act (2010).

[2] NASA Report, Voyages: Charting the Course for Sustainable Human Space Exploration.

[3] NASA Technology Roadmaps, TA 12: Materials, Structures, Mechanical Systems and Manufacturing (2015).

[4] B. Stockman, J. Boyle, and J. Bacon, International Space Station Systems Engineering Case Study, Air Force Center for Systems Engineering (2012).

[5] McGuire, M. L., Hack, K. J., Manzella, D. H., & Herman, D. A. (2014). Concept designs for NASA's Solar Electric Propulsion Technology Demonstration Mission. AIAA, 3717, 28-30.)

[6] Patterson, L. P. (2001). On-orbit maintenance operations strategy for the International Space Station-concept and implementation. NASA Technical Report.

[7] J. Paquin, "Mission to Hubble," NASA's Goddard Space Flight Center, http://www.nasa.gov/mission_pages/hubble/servicing/series/cats.html, (2008).

[8] NASA Report, Reference Guide to International Space Station (2010).

[9] S. Rawal, "Metal-Matrix Composites for Space Applications," Journal of Materials 53, 14-17 (2001).

[10] D.B. Miracle and B. Maruyama, "Metal Matrix Composites for Space Systems: Current Uses and Future Opportunities," Proc. National Space and Missile Materials Symp., ed. M. Stropki (Dayton, OH: Anteon Corp. (2000).

[11] K. C. Cheung and N. Gershenfeld, "Reversibly assembled cellular composite materials," Science 341, 1219-1221 (2013).

[12] MIT Center for Bits and Atoms Digital Materials and Assemblers, link: dma.cba.mit.edu

[13] Excerpted from http://www.amc.af.mil/News/Article-Display/Article/147235/advanced-composite-cargo-aircraft-makes-first-flight.

[14] Excerpted from http://www.compositesworld.com/articles/building-trust-in-bonded-primary structures.

[15] D. Frich, A. Hall and J. Economy, Nature of adhesive bonding via interchain transesterification reactions (ITR). Macromolecular Chemistry and Physics, 199(5), 913-921, 1998.

[16] B. Vaezian, J. Meyer, C. Mangun and J. Economy, "Aromatic thermosetting copolyester composites for high temperature and cryogenic applications," NASA SBIR Phase I NNX14CM10P – Final Report (2014).

[17] K.C. Chuang, J. Criss and E. Mintz, "Polyimide composites properties of RTM370 fabricated by vacuum assisted resins transfer molding (VARTM)," NASA Technical Report 20110008609, (2011).

[18] S. Ghose, K.A. Watson, R.J. Cano, S.M. Britton, B.J. Jensen, J.W. Connell, H.M. Herring, and Q.J. Lineberry, "High temperature VARTM using LARC-PETI-9 polyimide resin," High Performance Polymers 21, 653-672 (2009).

[19] R.J. Cano, B.W. Grimsley, B.J. Jensen, and C.B. Kellen, "Processing and characterization of PETI composites fabricated by high temperature VARTM," 36th International SAMPE Conference, 459-468 (2004).

[20] K.C. Chuang, D.M. Revilock, J.M. Pereira, J.M. Criss and E.A. Mintz, "High temperature RTM 370 composites fabricated by RTM," SAMPE Journal 49, 48-57 (2013).

[21] C. de Ruijter, E. Mendes, H. Boerstoel, S, Picken, "Orientational order and mechanical

properties of poly(amide-block-aramid) alternating block copolymer films and fibers," Polymer 47, 8517-8526 (2006).

[22] S. Bhama and S. Stupp, "Liquid crystal polymer-carbon fiber composites. Molecular Orientation," Poly. Eng. and Sci. 30, 228-234 (1990).

[23] T. Chung, Z. Gurion, and J. Stamatoff, "Induced orientational behavior of liquid crystal polymer by carbon fibers," Polymer Composites 6, 181-184 (1985).

[24] N. Demas, J. Zhang, A. Polycarpou, and J. Economy, "Tribological characterization of aromatic thermosetting copolyester–PTFE blends in air conditioning compressor environment," Tribol. Lett. 29, 253–258 (2008).

[25] J. Zhang, N. Demas, A. Polycarpou, and J. Economy, "A new family of low wear, low coefficient of friction polymer blend based on polytetrafluoroethylene and an aromatic thermosetting polyester," Polym. Adv. Technol. 19, 1105–1112 (2008).

[26] Z. Parkar, Design of unique composites based on aromatic thermosetting copolyester, PhD Dissertation, University of Illinois Urbana-Champaign (2011).

[27] D. Frich, J. Economy and K. Goranov Economy, J., & Goranov, K. Aromatic copolyester thermosets: High temperature adhesive properties. Polymer Engineering & Science, 37(3), 541-548 (1997).

[28] X. Luo, K. Lauber, and P. Mather, "A thermally responsive, rigid, and reversible adhesive," Polymer 51, 1169–1175 (2010).

[29] V. Pisacane, "Fundamentals of Space Systems," Johns Hopkins University Applied Physics Laboratory Series in Science & Engineering, 424 (2005).

[30] T. Xie, J. Hulway, and X. Xiao, "Shape memory polymer and adhesive combination and methods of making and using the same," US 8685528 B2 (2009).

[31] T. Xie, “Recent advances in polymer shape memory,” Polymer 52, 4985-5000 (2011).

[32] H. Mengand and G. Li, “A review of stimuli-responsive shape memory polymer composites,” Polymer 54, 2199-2221 (2013).

[33] M. Bartlett and A. Crosby, “High capacity, easy release adhesives from renewable materials,” Adv. Mater. 26, 3405-3409 (2014).

[34] D. King, M. Bartlett, C. Gilman, D. Irschick, and A. Crosby, “Creating gecko-like Adhesives for ‘Real World’ Surfaces,” Adv. Materials 26, 4345–4351 (2014).

[35] M. Bartlett, A. Croll, D. King, B. Paret, D. Irschick, and A. Crosby, “Looking beyond fibrillar features to scale gecko-like adhesion,” Adv. Materials 24, 1078-1083 (2012).

[36] A. Yousefpour, M. Hojjati, and J-P Immarigeon, “Fusion bonding/welding of thermoplastic composites,” J. Thermoplastic Compos. Materials 17, 303-334 (2004).

[37] I. Villegas, “High-speed spot welding of continuous fibre reinforced thermoplastic Composites,” CfK Valley Convention (2012)

[38] I. Villegas and H. Bersee, “Ultrasonic welding of advanced thermoplastic composites: an investigation on energy-directing surfaces,” Adv. in Poly. Tech. 2, 112-121 (2010).

[39] R. Rudolf, P. Mitschang, and M. Neitzel, “Induction heating of continuous carbon-fibre reinforced thermoplastics,” Composites A: App. Sci. and Manuf. 31, 1191-1202 (2000).

CHAPTER 13: SOLID-STATE BONDING OF AROMATIC THERMOSETTING COPOLYESTER AS A COMPOSITE WELDING MECHANISM

13.1 Introduction

Today, fiber reinforced polymer (FRP) composites are progressively being adopted for spacecraft applications replacing conventional metallic structures to realize future transportation technologies with minimized structural weight, yet uncompromised operational safety, as described in NASA's Roadmap Technology Area 12 [1]. In this regard particularly, composite cryotank technology will enable effective transportation of cryogenic liquid hydrogen (LH2) on Earth-departure weight critical architectures, and storage at in-space propellant depots to sustain next-generation deep space missions [2]. However, the explosion of the SpaceX Falcon 9 rocket, as recently announced to be caused by a supercooled liquid oxygen leak from a buckled composite overwrapped pressure vessel (COPV), have drawn attention to safety issues, as expressed by NASA advisory committee [3]. In that particular case, just before the explosion, a steep temperature gradient developed in leak-tight double-layer skin of the COPV as inner metal liner being subjected to warm helium while outer carbon fiber reinforced polymer (CFRP) composite wrap being exposed to cold oxidizer, which caused severe degradation in mechanical properties, and ultimately the failure [4].

This work was performed performed under NASA Small Business Innovation Research (SBIR) Phase-I program (Contract Number: NNX17CL40P) with ATSP Innovations and NASA Langley Research Center (2017).

Clearly, such rupture would occur due to a weak adhesive bonding between the CFRP and metal layers, being unable to equilibrate thermal expansion differences, causing delamination of the CFRP part from the metal surface, in which effects rippled out as combined with poor intrinsic thermomechanical performance of the CFRP wrapping part. That being given, adhesively bonded FRPs, in fact, can enable the most significant mass reduction in fuselage structure of launch vehicle systems yielding ultimately increased payload mass fraction, which is a critical need for all in-space systems. Thus, DARPA/Lockheed Martin X-55 Advanced Composite Cargo Aircraft demonstration paved the way through feasibility of building adhesively joined unitized composite skin for a fuselage structure [5]. Utilizing such an innovative approach, substantial weight savings on an aircraft frame were enabled by simply eliminating rivet and fastener use (more than 85% [5]) along with significantly reduced material cost, time and labor for fabrication and assembly [6]. Currently the most viable bonding technique to realize likewise structures is to use commercial adhesives, which also allow improvement in fatigue resistance, corrosion protection and uniform stress distribution for the composites. Yet, such adhesive application conceivably prompts bond line delamination under cyclic loads and thermal cycles during extended spaceflights, which undoubtedly raise safety concerns. Among plethora combinations of resin types, fiber grades and tow sizes, only proper FRPs possessing superior structural properties can meet such utmost demands towards ultimate performance.

Herein, we demonstrate carbon fiber reinforced high performance aromatic thermosetting copolyester (ATSP) resin composites (ATSP/C) being solid-state bonded to primary metal spacecraft structures in order to build lightweight elements with tailorable structural properties without necessitating additional uses of adhesives or mechanical joints.

In that regard, ATSP intrinsically enables solid-state adhesive bonding possessing reformable bonds by virtue of the interchain transesterification reactions (ITR) [7]. The ITR bonding scheme is a chemical interfacial (surface) self-welding mechanism which effectively consolidates pre-cured ATSP parts forming a smooth continuous bond line. The ITR bonding is enabled via only application of heat and physical contact, which does not evolve any volatiles. The ITR bonding is uniquely reversibly allowing repeatable bond/debond processes over the very same bond line causing no visible physical damage. Continuous fiber ATSP composites were investigated under a NASA SBIR Phase I program for high temperature and cryogenic applications [8]. The results showed that ITR bonding between laminae produces excellent interlaminar properties. Shear strength, modulus and fracture toughness were found to be comparable or superior to epoxy and polyimide carbon fiber composites [9-13] demonstrating the viability of ITR as a solid-state bonding scheme. Thermal fatigue tests showed that ATSP composites are resistant to microcracking, due to the resin's tendency of locally matching coefficient of thermal expansion (CTE) around the carbon fiber [13-15] and are capable of withstanding extreme hot and cold temperature cycles via cryogenic thermal cycling [8]. Additionally, they are durable [16,17], in-situ self-repairable [18], and maintain mechanical properties at elevated temperatures (Tg up to 307°C). Also, ATSP shows a unique capability for repair of interlaminar cracks on application of heat and pressure through ITR. Similarly, metal coupons bonded via ITR were observed to have a lap shear strength of up to 20 MPa [19]. As well, ATSP forms smooth and strongly bonded coating on metals upon curing [20, 21]. Tailorable ATSP chemistry can be adapted to nearly any polymer processing technique by adjustments in oligomer structure. Hence, building on these prior findings, we will produce one-

piece consolidated ATSP/C lamina and ATSP coated metal substrate via solid-state ITR bonding.

At a glance, state-of-the-art space frame construction technologies [22] have generally relied on use of metal-based unit elements [23,24], which are either permanently joined or connected via labor-intensive and difficult to automate joint mechanisms. Although such designs are readily used on low-Earth orbit space missions, their large weights and infeasibility of assembly under space conditions becloud their implementations on future space missions. To address these problems, recent studies have employed fiber composite unit elements attached via mechanical interlocks to build lightweight, high strength/stiffness cellular structures [25]. Even though these designs address the above-mentioned issues, the length scales are currently far below those of targeted technological applications, and joining requires complex mechanical interlocks which may inhibit a fully autonomous assembly.

With regard to application of bonding for composites, “co-curing” method enables bonding of partially cured composite parts by use of a curable adhesive, in which the adhesive chemically bonds on to the composite layers [26]. Yet, such uncured composite parts lack structural rigidity, and so this technique is unable to support bond assemble large parts with complex forms. Alternatively, “Co-bonding” method comprises a pre-cured composite part, which is connected to an uncured composite part through a curable adhesive as both the uncured part and the adhesive concurrently cure to bond [27]. However, this approach does not form a chemical bonding with the pre-cured composites, which could easily result in delamination, along with aforementioned handling problems with uncured parts. Hence, involving only pre-cured parts, “Secondary bonding” technique combines composites with use of adhesives. Though, such bonding only occurs by means of a mechanical interlocking on roughned

composite surfaces, which does not establish a strong chemical bonding [28]. Automated Fiber Placement (AFP) technology, being state-of-art composite manufacturing technique, enables prepregged carbon fiber tows to be automatically placed to build complex composite laminate, which was also utilized to build the aforementioned cryogenic fuel tanks. Yet, AFP partially utilizes cohesive bonding and consolidation features of thermoplastic resins (e.g. PEEK), which ultimately results in poor thermomechanical properties to withstand extreme operational conditions [29, 30]. Hence, state-of-the-art composite bonding approaches involve externally incorporated adhesive materials, which constitute a bottleneck in the FRPs causing delamination failure, as highlighted above. Herein, ITR mechanism allows a heat-induced a self-bonding of two pre-cured ATSP surfaces enabling a strong chemical interlocking mechanism facilitating assembly of large and complex composite parts.

The main objective of this project is to demonstrate a new solid-state bonding mechanism for similar/dissimilar carbon fiber reinforced polymer composites and primary metal components to produce lightweight aerospace structures without necessitating additional joining mechanisms, as highlighted in 2015 NASA Technology Roadmap under section of TA12 Materials, Structures, Mechanical Systems and Manufacturing. Herein, we utilized interchain transesterification reactions (ITR) driven adhesion mechanism of aromatic thermosetting copolyester (ATSP) to achieve solid-state bonding between fully cured ATSP-based parts within multimaterial (c-fiber composite ply/metal) configurations. We initially demonstrated proof-of-concept using a dynamic mechanical analyzer (DMA), thus joining ATSP coated (30-100 μm thickness) Al parts under 1 to 23 MPa pressure at temperatures beyond glass transition of the corresponding ATSP matrix (>300°C), as detailed in the report. Next, we adopted this approach to produce adhesively bonded upscaled specimens in a vacuum assisted hot press setup. It was

followed by physical characterization of the consolidated samples to quantify the bonding strength, adhesive/cohesive failure modes as well as analyzing performance of ITR bonded composite-metal multilayered structures in a broad temperature range. Overall, ITR bonding shows compatibility with prominent space-grade metals as well as fiber-reinforced composite plies. ITR bonding demonstrates thermomechanical reliability at a very broad temperature range that spans space operation criteria. Upon flexural analysis, ITR bonded composites displayed cohesive failure while mitigating structural delamination.

13.2 Results and Discussion

Operational parameters of temperature, time and pressure to obtain the ITR bonding were assessed and characterized via Dynamic Mechanical Analysis (DMA) tests. The DMA (TA Instruments Q800) is operated with a uniaxial fixture for the ITR process wherein two ATSP coated parts were held in contact under a compressive force (bonding pressure) for a certain duration (bonding time) at a given temperature (bonding temperature). Al pieces of 1 mm and 2 mm diameter circular heads (coated with ATSP) were brought in contact with rectangular bases of 10 mm x 10 mm Al pieces. Since the DMA setup is limited to ±18 N, max applied pressure was 23 MPa. The bonding cycle included both force-ramp and temperature-ramp processes within given durations, see Figure 13.1.a for details. Upon enabling successful ITR bonding between the two pieces, we obtained SEM (Hitachi 4800) and Micro-CT images of the bonded samples (Figure 13.1.b). Afterwards, pull-off tests were applied to measure bonding strengths of the samples. Measured pull-off strengths were beyond the limits of the DMA fixture (18 N) for both 1 mm and 2 mm diameter heads. Overall, from results of the DMA experiments, we have observed that 23 MPa of applied pressure, 30 min and 400°C enabled effective ITR bonding and can be considered an effective upper bound in terms of conditions necessary for effective

bonding. Subsequent alterations in at-temperature compliance of the total laminate and/or use of self-aligning geometries can drastically lower this input parameter.

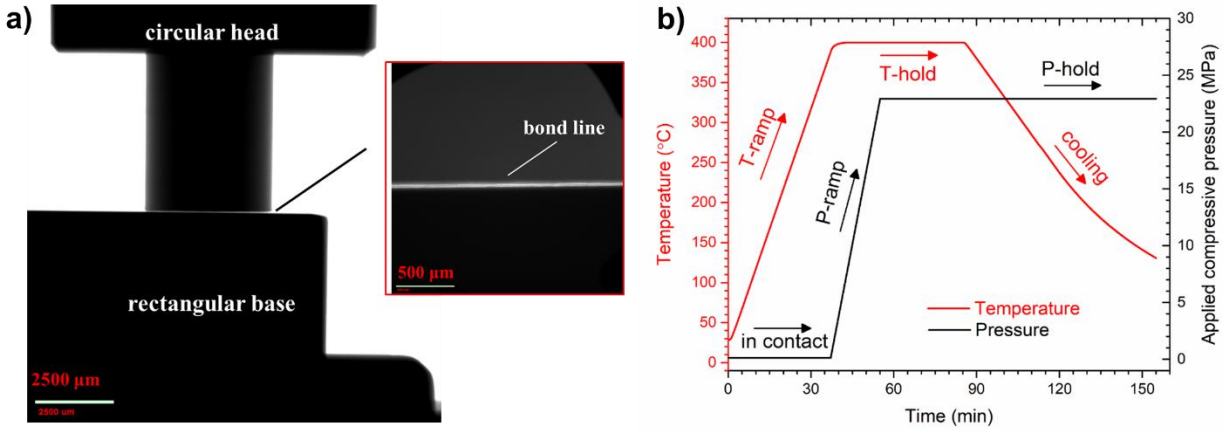

Figure 13.1 a) Micro-computed tomography (micro-CT) image of corresponding ITR bonded parts. b) A representative thermomechanical DMA cycle operated to enable ITR bonding between the two ATSP coated Al parts.

Regarding the fabrication of multimaterial configurations, we produced ATSP/C-fiber ply - Al7075 piece - ATSP/C-fiber ply three-layer composite form multimaterials utilizing ITR based adhesion mechanism (Figure 13.2.a). C-fiber plies were produced using C1A1-ATSP chemistry due to it having the lowest porosity among the ATSP resin composite (0.4% as measured by sulfuric acid digestion) and matched chemistry between the surfaces. To investigate the thermomechanical reliability of the structure, we applied a thermomechanical cycle on the specimen under 5 MPa static tensile load wherein the temperature was ranged between -150°C to 200°C. Phase transition temperatures of the polymeric matrix were detected around -95°C (cryogenic) and 181°C (heated) and it is notable that the specimen did not display delamination or failure throughout the applied temperature range (Figure 13.2.b). This experiment also helped to detect phase transition temperatures of the matrix within multimaterial configuration.

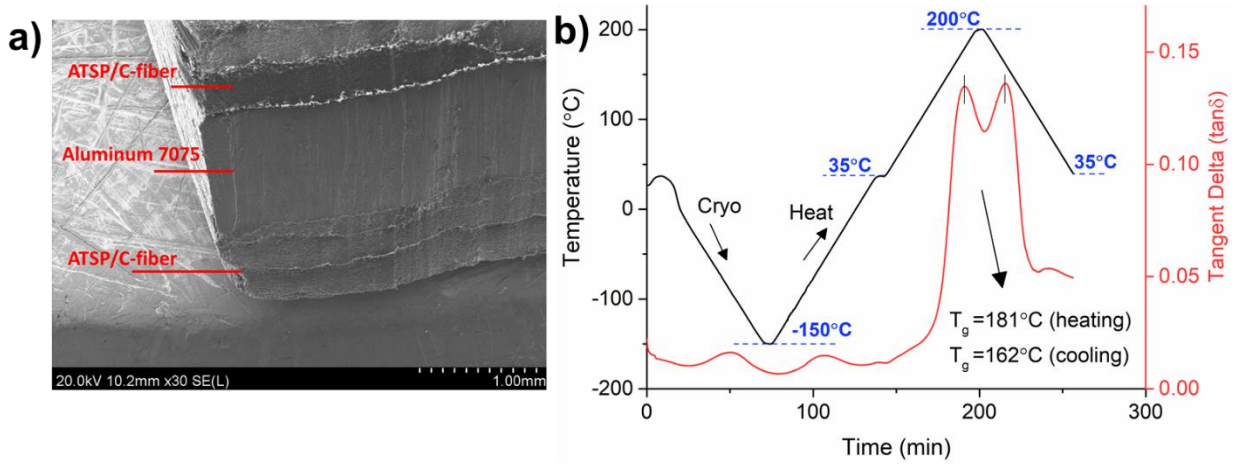

Figure 13.2 SEM image of ITR bonded ATSP/C-fiber plies (a) and Al 7075 part and DMA thermal cycle between -150°C and 200°C with demonstrated Tg phase transitions (b).

Similar to the metal-c-fiber ply multimaterial configuration, we also performed a broad temperature range thermomechanical cycle on both ITR bonded ATSP-coated Al7075 parts (Figure 13.3.a). Initially, ITR bonding was enabled as discussed earlier, then a cryogenic cooling (down to -150°C), and a subsequent heating (up to 200°C) processes were applied in which the specimen was subjected to a constant ~13 MPa tensile load. As observed over the displacement curve (red), the ITR adhered metal specimens did not break over the controlled thermal process. Additionally, test films composed of two plies of ATSP films bonded via ITR - using a DMA experiment, we found that the glass transition temperature was found to be at 215°C (Figure 13.3.b) for which the specimen was observed to maintain similar thermophysical features as corresponding individual parts. Based on these tests, we observed that ITR bonded multimaterials were thermomechanically reliable under extreme environmental conditions.

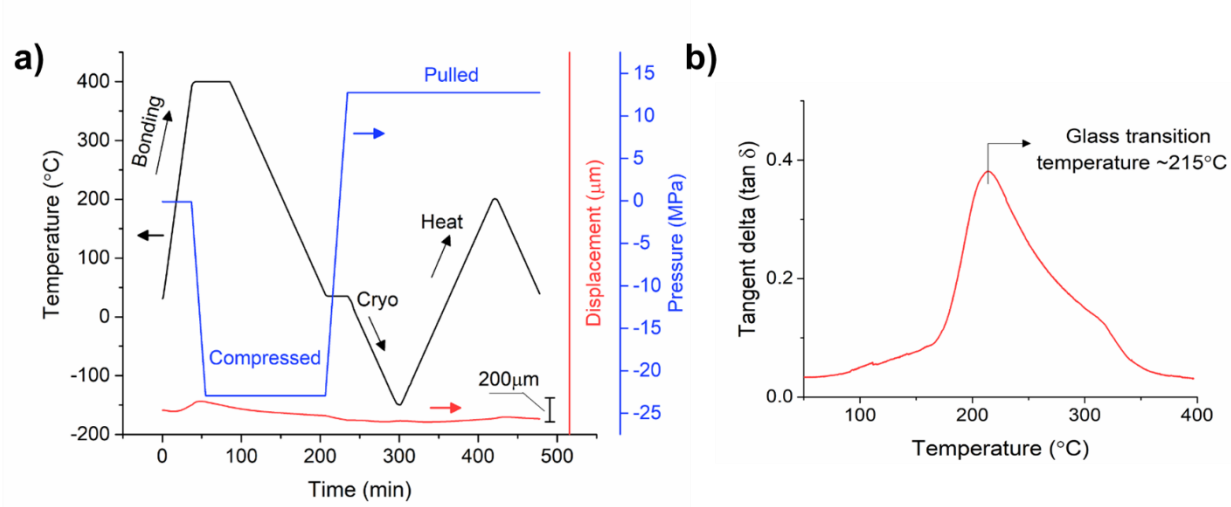

Figure 13.3 DMA cycle of ATSP-coated Al 7075 parts; ITR bonding, cryogenic treatment, and high-temperature treatment, respectively (a). DMA cycle of ITR bonded ATSP free-standing films (b).

We have fabricated a series of ATSP coated Al specimens for lap shear strength measurements. Based upon initial DMA tests performed on the ATSP coated Al samples, we performed a thermal ITR bonding cycle with a force of 6 MPa at 330°C for 3 hours. In contrast to the DMA tests, the lap shear coupons were produced under vacuum conditions. Upon fabrication of these samples, we performed lap shear strength measurements to compare performance of different ATSP chemistries and to check sufficiency of the experimental parameters to optimize the lap shear strength, in accordance with ASTM D3163 [8]. Experiments were conducted on an Instron test frame with wedge grips and a displacement controlled rate of 0.01 mm/sec. For Figure 13.4, the x-axis is the ATSP bondline thickness between the metal substrates and y-axis is the lap shear strength results. In general, Figure 13.4 shows higher thickness corresponding to higher lap shear strengths which indicates that we should deposit higher thickness of coatings to achieve higher lap shear strength.

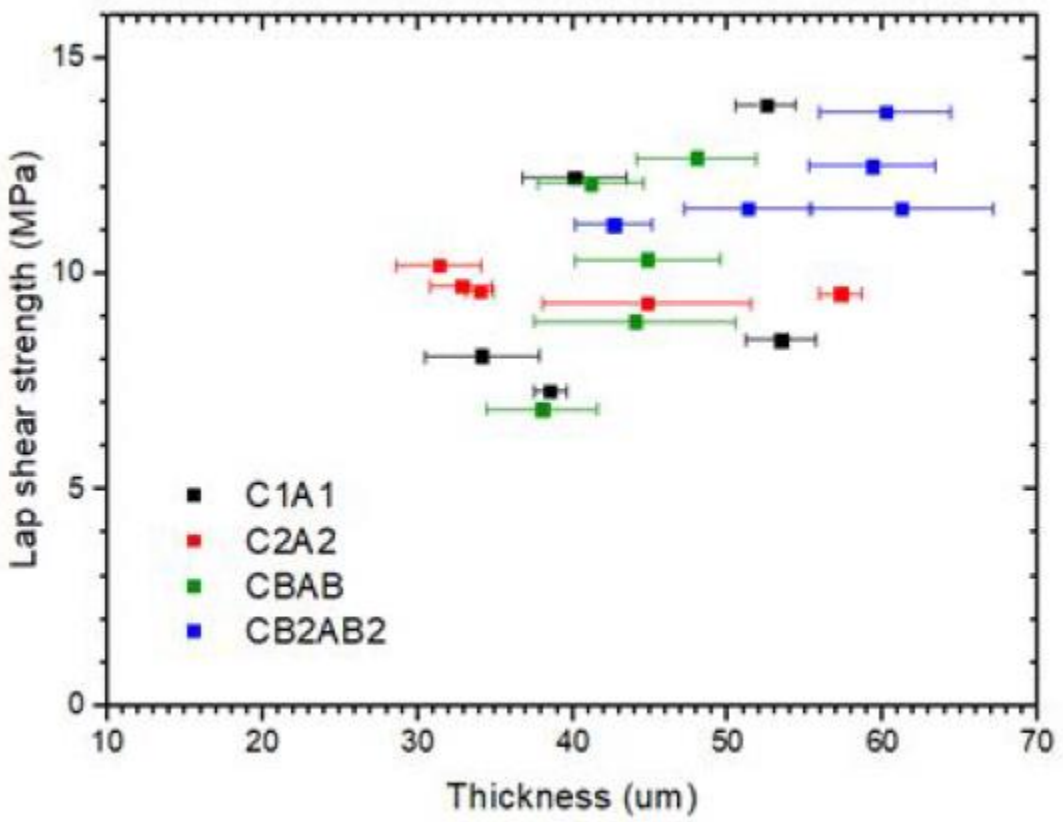

Figure 13.4 Characterized lap shear strengths with respect to the measured coating thicknesses of corresponding specimens for the four different ATSP chemistries.

Temperature is an important factor for materials in space applications. Thus, we did lap shear tests for CB2AB2 at different temperatures: -100 ℃, 25 ℃ and 100 ℃, and the results are shown in Figure 13.5. Figure 13.5.a illustrates that the stress vs. displacement curve at different temperatures has a very clear trend: when temperature increases, the slope of the curve decreases. The lap shear strength also decreases when temperature increases, as seen in Figure 13.5.b. However, there is no clear trend of cohesive failure percentage with respect to temperature.

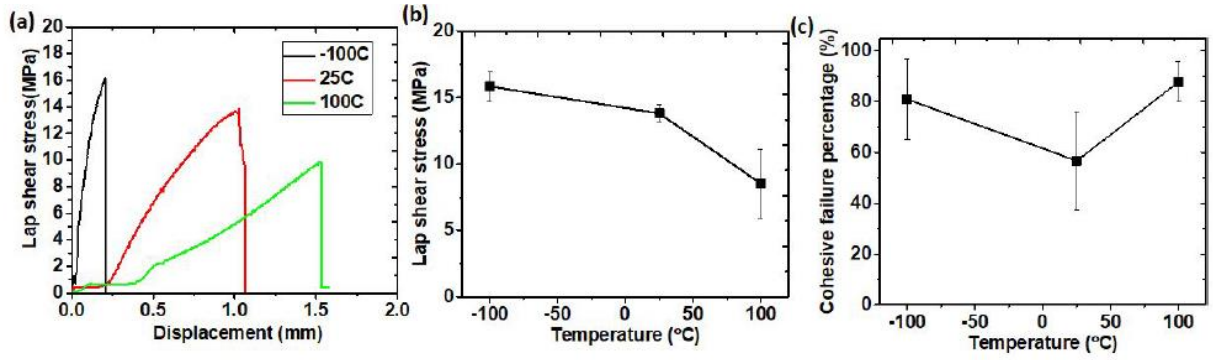

Figure 13.5 Temperature effects on lap shear strength, (a) lap shear stress vs. displacement plots, and (b) lap shear strength vs. temperature, (c) cohesive failure percentage vs. temperature.

Figure 13.6 are SEM images of delaminated ATSP/C-fiber and ATSP coated metal interlayer with broken fibers remaining on the surface (Figure 13.6.a) and cohesive debonding features (Figure 13.6.b) after the original sample tests. The SEM images did not show any adhesive failure of the coated aluminum samples, indicating a robust bond strength between the coating and aluminum substrate.

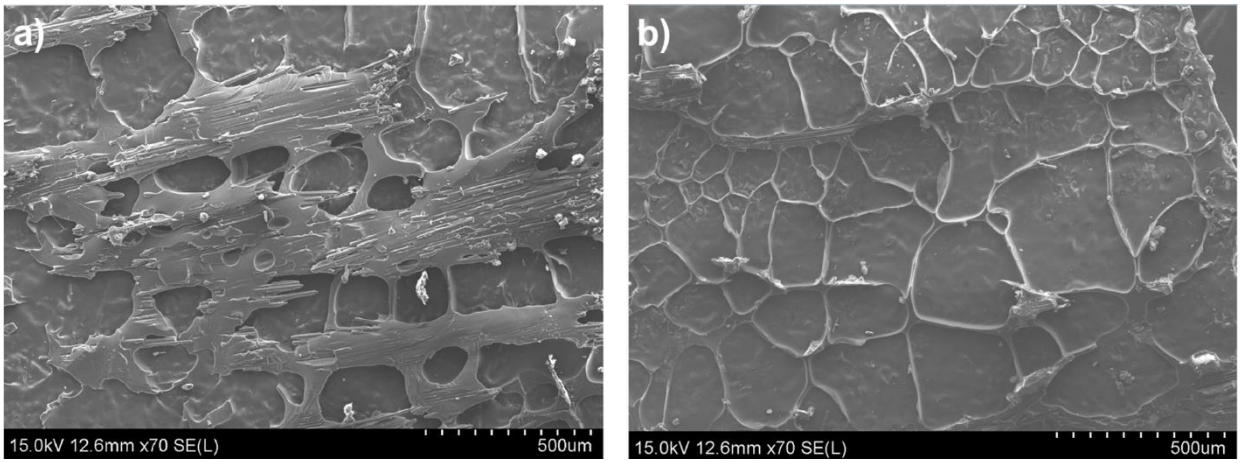

Figure 13.6 SEM images of delaminated ATSP/C-fiber and ATSP coated metal interlayer with broken fibers remaining on the surface (a) and cohesive debonding features (b).

SBS measurements were performed in accordance with ASTM D2344. Four point bending tests were carried out following ASTM D7264 protocol [11]. In all cases for both flexural [0_5/Al] (Figure 13.7) and SBS [0_4/Al/0_4] (Figure 13.8) layups at all ranges of

temperature, cryogenic temperature has the highest strength and other temperatures have slightly lower strength. Polymers have higher fracture strength at low temperatures; ATSP has a drastic storage modulus increase from 1.4 GPa to 14 GPa (from 25℃ to 140℃) due to the cross-linked molecular structure, thus it showed a higher strength in cryogenic temperature in the current study.

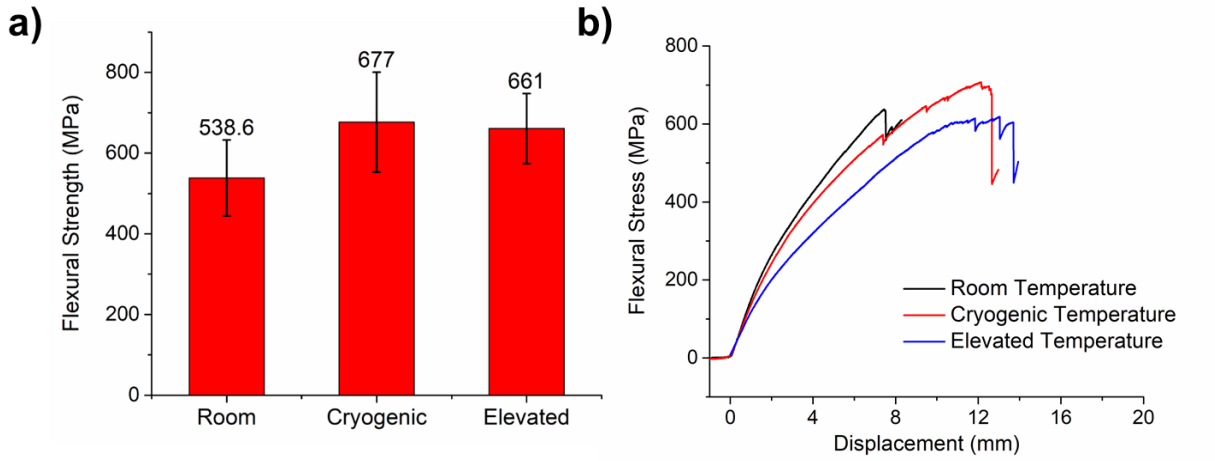

Figure 13.7 Four-point bending flexural stress averaged results at indicated temperatures. Cryogenic and elevated temperatures correspond to -100°C and 100°C, respectively.

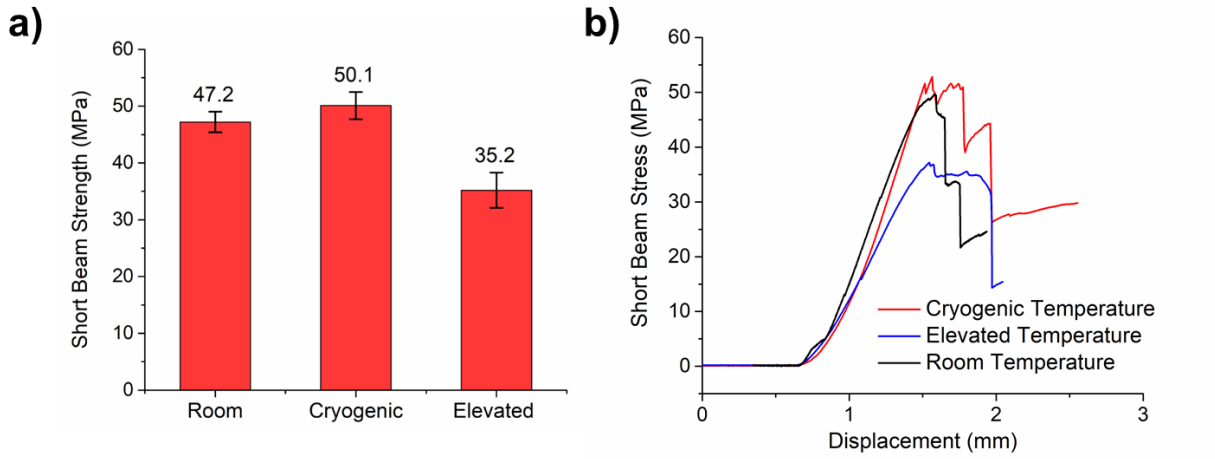

Figure 13.8 Short beam strength averaged results at indicated temperatures. Cryogenic and elevated temperatures correspond to -100°C and 100°C, respectively.

To expand on the multimaterial fabrication scheme, we will also develop and explore another multilayer structure assembly/production method utilizing a temperature-induced conformality feature of ATSP composites wherein availability of ITR bonding is essential, as demonstrated in Figure 13.9. In this process, a pre-shaped concave form Al part with ATSP coating (cured form) is consolidated with a fully cured (initially flat) ATSP/c-fiber ply in solid-state using ITR bonding mechanism via application of heat and pressure. Such a fabrication method is conveniently enabled through heating the overall mold to a temperature above the glass transition of the ATSP matrix (>300°C) in which the ATSP matrix softens and so can be reconfigured under an applied force to acquire the geometry of the preshaped Al substrate. The CT images obtained on a multimaterial structure of ATSP/C-fiber ply consolidated with Al7075 shows that the composite ply can effectively acquire the curved form of the Al piece. Moreover, close-up images provide precision to resolve interfacial bond line between metal and ply layers that no void formation was observed. As well, the c-fibers can be easily reformed within the ply without significant structural failures, which validates reconfigurability of the composite domain. Similarly, as demonstrated in the figure below (Figure 13.10), a three-layer (ply-metalply) flat multimaterial composite likewise shows smooth bondlines with no indication of voids or gaps. Similarly, another complex geometry of the multimaterial configuration, as shown below in computer tomography (CT) images (Figure 13.11), highlights the smooth bond lines between c-fiber plies with varied thicknesses consolidated with metal parts. Close-up SEM images provide micro-scale perspective on the bond line formation over the cross-section. Figure 13.12 shows an example of a novel repair approach based on ITR wherein a damage section had an Al7075 patch (coated with ATSP) applied under heat and pressure. Micro-CT experiments demonstrated

that the sample was intimately bonded and possessed no voids at the Al/composite interface, thereby imparting the high metal/composite adhesive strength.

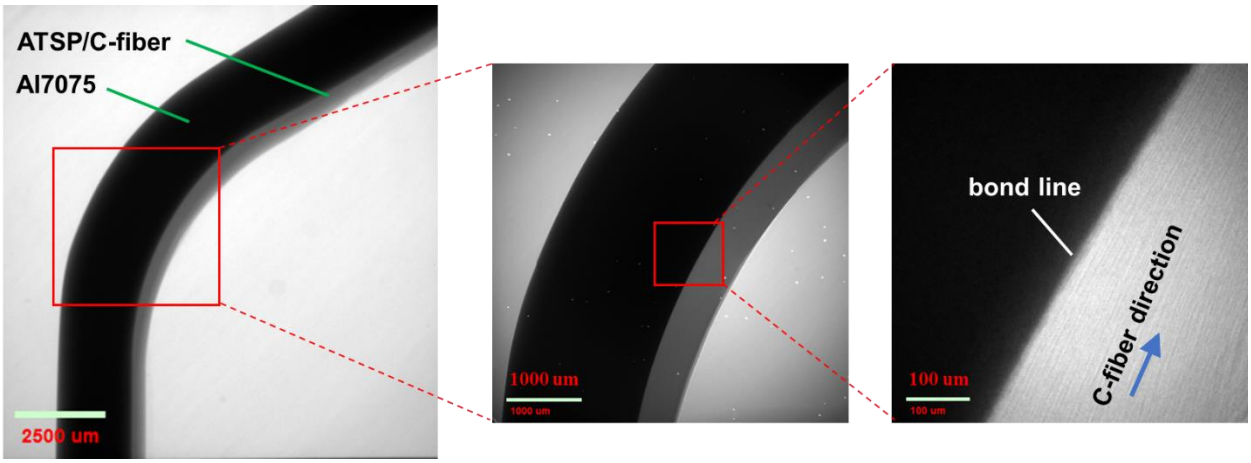

Figure 13.9 A representation of proof-of-concept to assemble complex-geometry multimaterial laminates using solid-state bond based on ITR. CT images of ITR bonded ATSP/C-fiber and Al7075 multimaterial configuration with curved geometry.

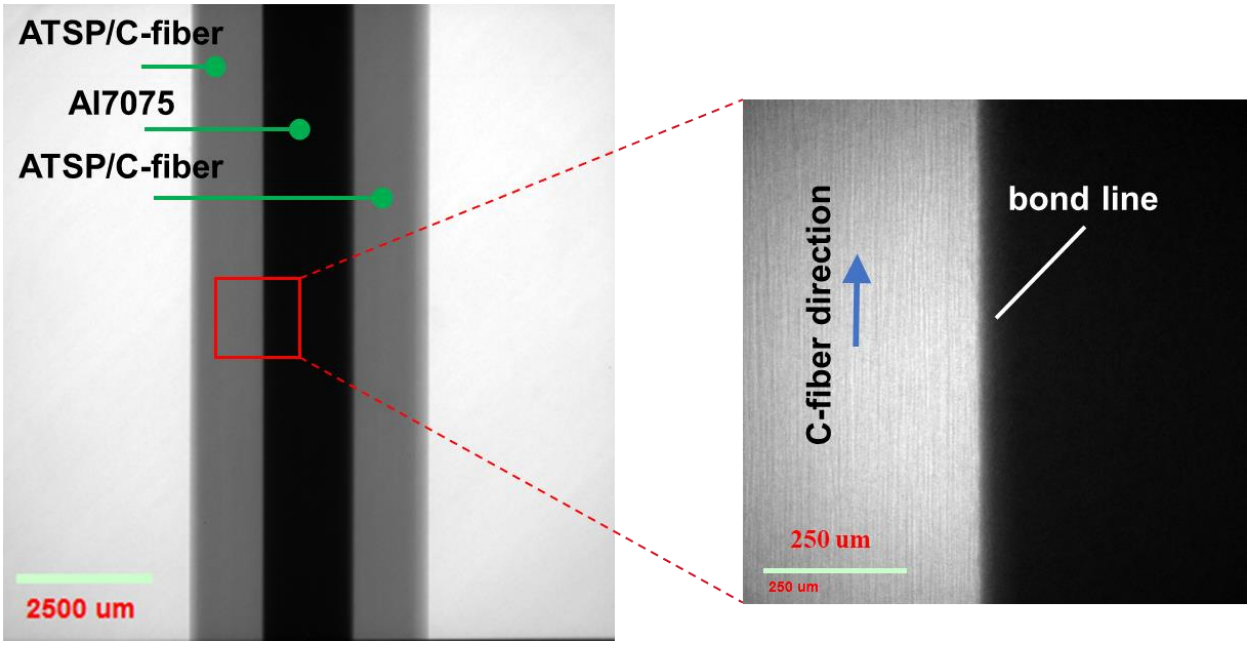

Figure 13.10 CT images of ITR bonded ATSP/C-fiber and Al7075 multimaterial configuration with flat geometry.

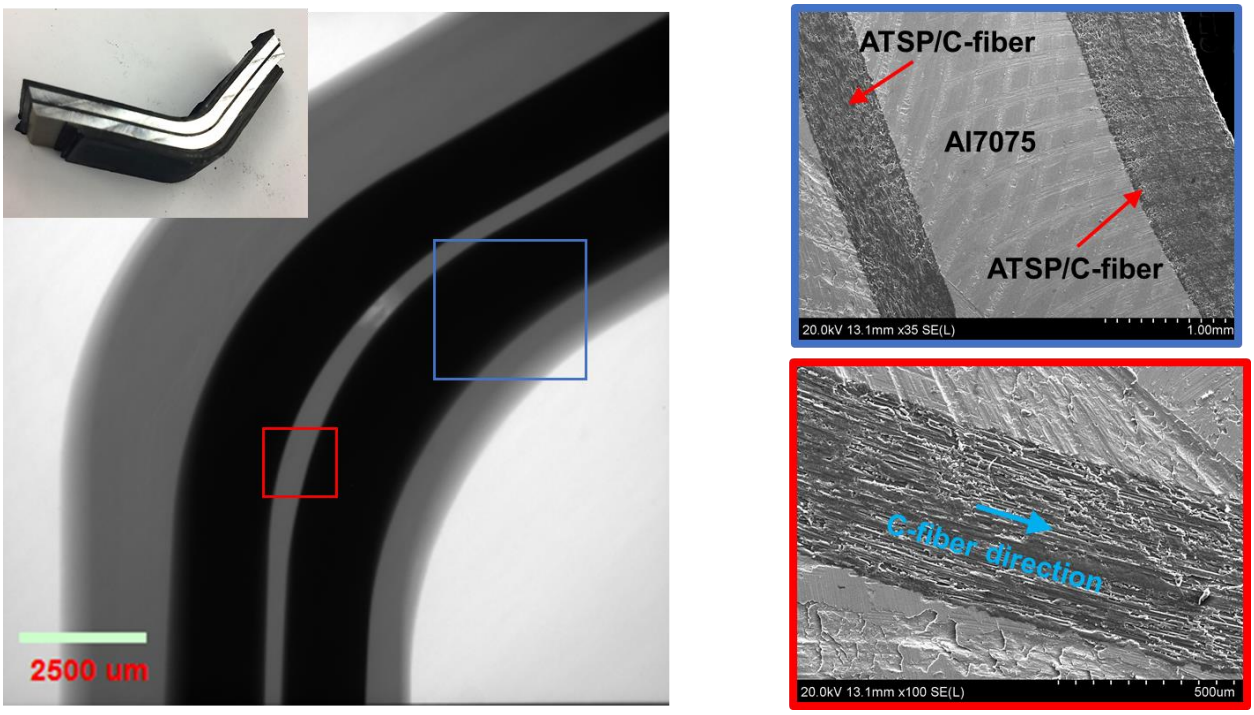

Figure 13.11 CT image of ITR bonded ATSP/C-fiber - Al7075 multimaterial configuration with curved geometry (left). SEM images of close-up over cross-section (right).

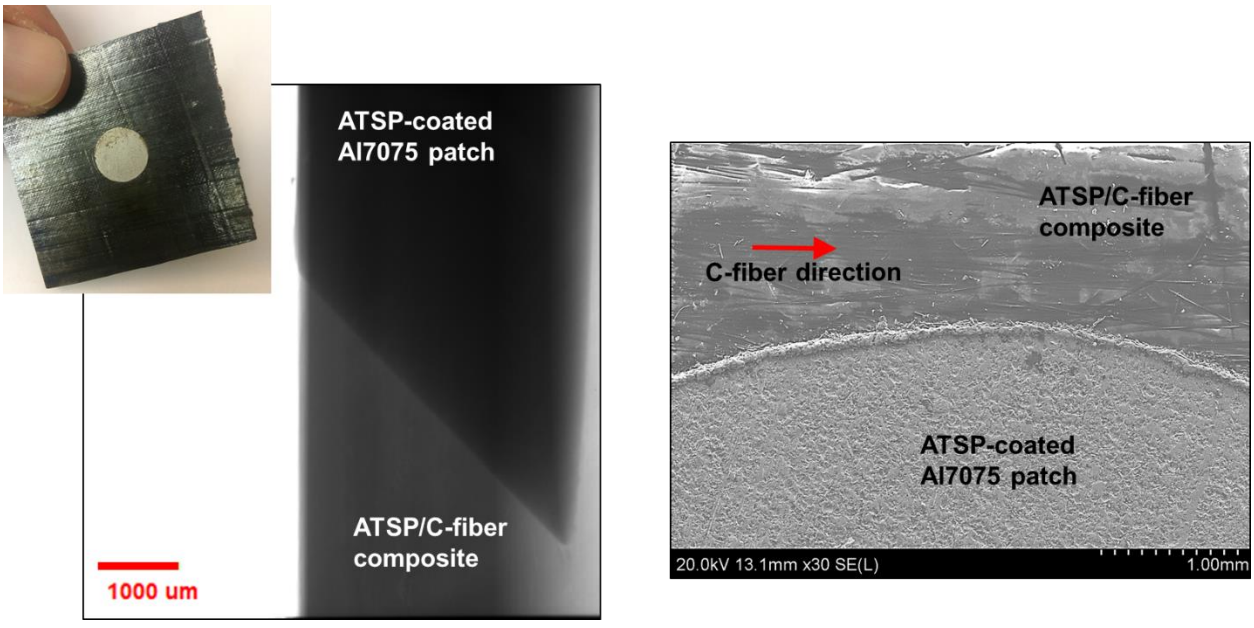

Figure 13.12 CT and SEM images of ITR repaired ATSP/C-fiber ply with ATSP-coated Al7075 cone shape patch.

13.3 Conclusion

Adhesively bonded FRPs can enable significant mass reduction in fuselage structure of launch vehicle systems yielding increased payload mass fraction, which is a critical need for all space systems. Utilizing such an innovative approach, substantial weight savings on an aircraft frame were enabled by simply eliminating rivet and fastener use (more than 85%) along with significantly reduced material cost, time and labor for fabrication and assembly. Currently the most viable bonding technique to realize likewise structures is to use commercial adhesives, which also allow improvement in fatigue resistance, corrosion protection and uniform stress distribution for the composites. Yet, such adhesive application conceivably prompts bond line delamination under cyclic loads and thermal cycles during extended spaceflight, which undoubtedly raise safety concerns. Among the plethora combinations of resin types, fiber grades and tow sizes, only proper FRPs possessing superior structural properties can meet such utmost demands towards ultimate performance. In this project, we demonstrated use of carbon fiber reinforced high performance aromatic thermosetting copolyester (ATSP) resin composites (ATSP/C) as bondable in the solid-state to primary metal spacecraft structures in order to build lightweight elements with tailorable structural properties without necessitating additional uses of adhesives or mechanical joints.

13.4 References

[1] NASA Technology Roadmap, 2015.

[2] J.R. Jackson, J. Vickers and J. Fikes, Composite cryotank technologies and development of 2.4 and 5.5M out of autoclave tank results, NASA Technical Report, 2015.

[3] Excerpted from http://www.wsj.com/articles/nasa-advisory-group-raises-concerns-about-spacex-rocket-fueling-plans-1477955860

[4] Excerpted from http://spaceflight101.com/falcon-9-amos-6/spacex-resorts-to-creative-testing-in-falcon-9-explosion-investigation/

[5] Excerpted from http://www.amc.af.mil/News/Article-Display/Article/147235/advanced-composite-cargo-aircraft-makes-first-flight

[6] Excerpted from http://www.compositesworld.com/articles/building-trust-in-bonded-primary-structures

[7] D. Frich, A. Hall and J. Economy, Nature of adhesive bonding via interchain transesterification reactions (ITR). Macromolecular Chemistry and Physics, 199(5), 913-921, 1998.

[8] B. Vaezian, J. Meyer, C. Mangun and J. Economy, "Aromatic thermosetting copolyester composites for high temperature and cryogenic applications," NASA SBIR Phase I NNX14CM10P – Final Report, 2014.

[9] K.C. Chuang, J. Criss and E. Mintz, "Polyimide composites properties of RTM370 fabricated by vacuum assisted resins transfer molding (VARTM)," NASA Technical Report 20110008609, 2011.

[10] S. Ghose, K.A. Watson, R.J. Cano, S.M. Britton, B.J. Jensen, J.W. Connell, H.M. Herring, and Q.J. Lineberry, "High temperature VARTM using LARC-PETI-9

polyimide resin," High Performance Polymers 21, 653-672, 2009.

[11] R.J. Cano, B.W. Grimsley, B.J. Jensen, and C.B. Kellen, "Processing and characterization of PETI composites fabricated by high temperature VARTM," 36th International SAMPE Conference, 459-468, 2004.

[12] K.C. Chuang, D.M. Revilock, J.M. Pereira, J.M. Criss and E.A. Mintz, "High temperature
RTM 370 composites fabricated by RTM," SAMPE Journal 49, 48-57, 2013.

[13] C. de Ruijter, E. Mendes, H. Boerstoel, S, Picken, "Orientational order and mechanical properties of poly(amide-block-aramid) alternating block copolymer films and fibers," Polymer 47, 8517-8526, 2006.

[14] S. Bhama and S. Stupp, "Liquid crystal polymer-carbon fiber composites. Molecular Orientation," Poly. Eng. and Sci. 30, 228-234, 1990.

[15] T. Chung, Z. Gurion, and J. Stamatoff, "Induced orientational behavior of liquid crystal polymer by carbon fibers," Polymer Composites 6, 181-184, 1985.

[16] N. Demas, J. Zhang, A. Polycarpou, and J. Economy, "Tribological characterization of aromatic thermosetting copolyester–PTFE blends in air conditioning compressor environment," Tribol. Lett. 29, 253–258, 2008.

[17] J. Zhang, N. Demas, A. Polycarpou, and J. Economy, "A new family of low wear, low coefficient of friction polymer blend based on polytetrafluoroethylene and an aromatic thermosetting polyester," Polym. Adv. Technol. 19, 1105–1112, 2008.

[18] Z. Parkar, Design of unique composites based on aromatic thermosetting copolyester, PhD Dissertation, University of Illinois Urbana-Champaign, 2011.

[19] D. Frich, J. Economy and K. Goranov Economy, J., & Goranov, K. Aromatic copolyester thermosets: High temperature adhesive properties. Polymer Engineering & Science, 37(3), 541-548, 1997.

[20] J. Economy, A. A. Polycarpou, and J. Meyer. "Polymer coating system for improved tribological performance." U.S. Patent Application No. 13/911,845

[21] P. Lan, J. L. Meyer, and J. Economy, A. A. Polycarpou, “Unlubricated Tribological Performance of Aromatic Thermosetting Copolyester (ATSP) Coatings Under Different Temperature Conditions. Tribology Letters, 61:10, 2016.

[22] NASA Report, Reference Guide to International Space Station, 2010.

[23] S. Rawal, “Metal-Matrix Composites for Space Applications,” Journal of Materials 53, 14-17, 2001.

[24] D.B. Miracle and B. Maruyama, “Metal Matrix Composites for Space Systems: Current Uses and Future Opportunities,” Proc. National Space and Missile Materials Symp., ed. M. Stropki (Dayton, OH: Anteon Corp., 2000.

[25] K. C. Cheung and N. Gershenfeld, “Reversibly assembled cellular composite materials,” Science 341, 1219-1221, 2013.

[26] L.A. MacAdams, D.K.Kohli, Bonding of composite materials, US Patent 20140144568 A1.

[27] P.N. Vines, A.G. Garcia, C.C. Pancorbo, Method for manufacturing elements of composite materials by the co-bonding technique, US Patent 6735866 B2.

[28] K. S. Kim, J. S. Yoo, Y. M. Yi and C. G. Kim. Failure mode and strength of uni-directional composite single lap bonded joints with different bonding methods. Composite structures, 72(4), 477-485, 2006.

[29] A.B. Hulcher, J.M. Marchello, J.A. Hinkley, N. J. Johnston and M.A. Lamontia, Dry ribbon for heated head automated fiber placement, 2000.

[30] Z. August, G. Ostrander, J. Michasiow and D. Hauber, Recent developments in automated fiber placement of thermoplastic composites, SAMPE J, 50(2), 30-37, 2014.

CHAPTER 14: NOVEL METAL-CARBON NANOMATERIALS: REVIEW ON COVETICS

14.1 Introduction

A decade ago Jason Shugart and Roger Scherer from Third Millennium Materials (TM2), LLC developed a new method to manufacture high carbon content metal compositions [1, 2]. These materials possess a single-phase morphology comprising of a nanocarbon in a metal lattice structure such that the carbon does not separate from the metal upon remelting and subsequent resolidification processes. This behavior has been attributed to the formation of an in-situ covalent bonding between the carbon and the metal. During the fabrication process, an electric arc induces a chemical conversion of amorphous activated carbon into crystalline carbon forms such that the carbon thereby interacts with the metal lattice and forms a new hybrid nanoscale morphology. This novel carbon-metal material was named "covetic" referring to a then hypothesized covalent bonding of the carbon atoms to the metallic crystalline structures. The covetics manufacturing method involves use of a conventional induction furnace, wherein metal is melted inside a graphite crucible. Then activated carbon particles are blended into the molten metal while it is being stirred and a sufficient electric current is applied via carbon electrodes to realize such chemical conversion reaction. So far, covetics were mainly demonstrated with use of amorphous activated carbon micron-sized particles as infused into about twenty metals including aluminum, copper, silver, zinc and tin [3].

This work was previously published: Bakir, M. and Jasiuk, I., Novel metal-carbon nanomaterials: review on covetics, *Advanced Materials Letters*, 8(9), 884-890 (2018).

Carbon incorporation into a metal matrix may yield improved properties as compared to base metals. For example, aluminum carbide, obtained through a chemical reaction between aluminum and carbon, possesses superior hardness and higher melting point than soft and low-temperature malleable parent aluminum. Also, steel, obtained through dissolving carbon in iron, attains better structural properties and oxidative corrosion resistance than iron. However, most metals pose chemical inertness to carbon which yields low, if not negligible, carbon solubility. Namely, copper is around 6-8 ppm [4], while nickel has about 1 wt.% carbon solubility [5]. Iron has higher solubility with steel having up to 2.14 wt.% and cast iron up to 6.7 wt%, as indicated by phase diagrams [6]. The covetics have been shown so far to have up to 15 wt.% carbon solubility which realizes a significant advancement for the metal-carbon materials.

Alternatively, to overcome the carbon solubility issue, metal-carbon composites have been fabricated by incorporating solid-phase carbon nanoparticles via various processing techniques which include chemical vapor deposition (CVD) [7], spark plasma sintering [8], melt processing [9] and thermal spraying [10], among others. Utilizing such methods, higher carbon contents can be realized in metal-matrix composites which in return may yield notable improvements in physical properties. For example, graphene was grown via CVD on copper powder and such compacted powder generated a composite material with 39% improvement in hardness, in comparison to a base copper [11]. Also, aluminum filled with carbon nanotubes, made using mechanical ball milling and hot pressing techniques, yielded five times higher hardness and seven times higher flexural strength [12]. In another work, 3 vol. % carbon nanotube infused aluminum matrix showed increased yield strength and hardness with higher carbon content [13, 14]. Also, copper with incorporated carbon nanotubes had almost equivalent conductivity to pure copper [15]. Graphene infused copper system displayed dislocation

inhibited strengthening effects [16]. However, metal oxide graphene compositions showed enhanced electrochemical capacitance which denoted their potential for energy storage applications [17].

Thus, enhancements in mostly mechanical material properties could be achieved by utilizing the above techniques by achieving higher carbon content in metal matrix composites. Yet, an interfacial bonding between the carbon fillers and the host metal matrix remains to be a challenge, which limits benefits which could be obtained from added carbon. Thus, the covetic materials enabling in-situ generated interfacial bonding and unique single-phase lattice structure should positively alter thermophysical properties. We hereon present experimental findings on the covetics in chronological order which highlight their promising prospects.

14.2 Recent Experimental Findings

The very first work on the covetics was published by Brown et al. in 2011 [18]. In that study, physical properties of a 3 wt.% carbon incorporated Al6061 covetic material were investigated in comparison to bare aluminum alloy parent material. Density was measured using a gas pycnometer where only an infinitesimal difference was observed between the parent and the covetic materials. Predicted by a rule of mixtures, the actual volume fraction of the carbon content was 1.17 vol.% with respect to as-manufactured ratio of 3.56 vol.% in the covetic material. Thus, the covetic materials can be described by either target carbon denoting carbon amount used during fabrication, or an actual carbon percentage measured via spectroscopic techniques. Yet, precise quantification of the carbon content in covetics remains to be a challenge. Vickers microhardness measurements yielded 23.4% higher average hardness values for the covetic material, which was attributed to presence of the carbon nanoparticles. It is worthwhile to mention that hardness was observed to increase towards outer regions of the

samples, indicating a nonuniform distribution of carbon. Following hardness measurements, images taken on indented regions displayed intact carbon aggregations, which were speculated to happen due to incomplete chemical conversion reaction. More importantly, electron beam backscatter diffraction (EBSD) analysis showed notable grain-size differences between the covetic and parent materials wherein the former had fine-grained (1-30 μm diameter) regions with strong orientation dependence, whereas the latter had 100-200 um diameter large grains with random orientations. Furthermore, four-probe method electrical conductivity measurements (according to ASTM B193) demonstrated that as-extruded covetic aluminum reached 67.3±3% IACS (International Annealed Copper Standard referring to 58 MS/m electrical conductivity of standard copper electrical conductivity). Upon T6 heat treatment, the electrical conductivity reduced to 47.81±3% IACS, which essentially became comparable to bare aluminum alloy with same heat-treatment. Quasi-static tensile tests showed that the yield strength of 91.10 MPa of the covetic material was 30% higher than that of base aluminum alloy wherein ultimate tensile strengths were closely equal (Figure 14.1). However, upon a T6 heat-treatment, although the material properties substantially increased, yet no noticeable differences were observed between the covetic and no-covetic materials. Split Hopkinson pressure bar (SHPB) measurements. which evaluate strain rate dependency of mechanical properties, showed no significant differences between the T6 conditioned covetic and parent materials. Lastly, differential thermal analysis (TGA) showed higher solidus temperature (619 °C) for the covetic material than the literature value of the parent T6-conditioned material (582 °C). These preliminary measurements demonstrated promising results for the covetic materials, yet underlying reasons were not comprehensively discussed.

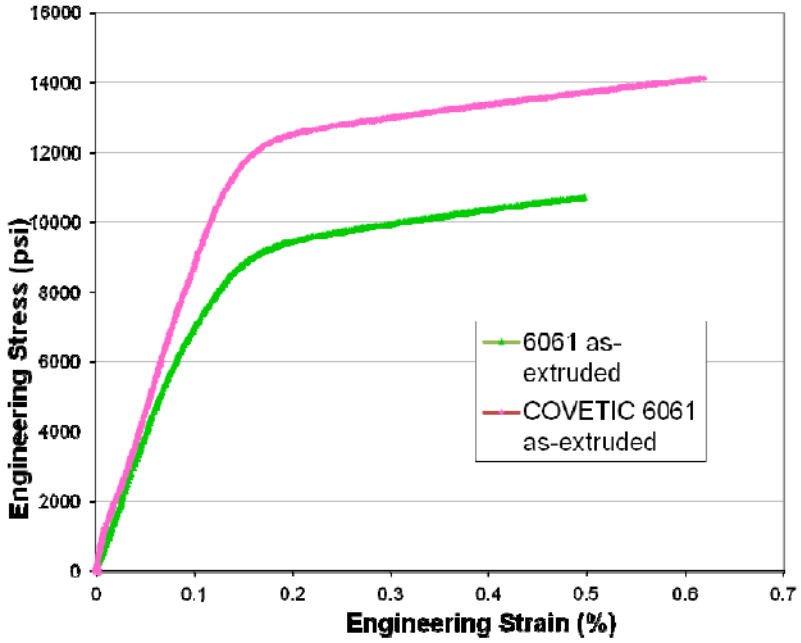

Figure 14.1 Tensile characteristics of parent and covetic materials where the covetic material obtained higher strength [18].

Following that study, Nilufar et al. [19] and Jasiuk et al. [20] presented results on characterization of warm-rolled (T0 conditioned) Al7075 covetic materials having 0, 3 and 5 wt.% target carbon compositions. They measured 0.8, 2.2 and 4 wt.% actual carbon contents for 0, 3 and 5 wt.% target compositions, respectively, using electron dispersive spectroscopy (EDS). Structural density measurements using the Buoyancy Technique did not show any significant differences among all three compositions, which was attributed to low actual carbon quantities. Yet, Vickers and Rockwell hardness tests of the covetics yielded improved properties where hardness increased by more than 30% with 5 wt.% target carbon content covetic samples (Figure 14.2). Similarly, local nanoindentation measurements displayed 43% increase in the hardness but no improvement in reduced modulus. Also, tensile measurements showed that covetic materials with 5 wt.% target carbon content could attain ultimate strength as high as bare T6-tempered Al 7075. In other words, about 40% strength increase was observed in the corresponding covetic material. Additionally, scanning electron microscopy (SEM) images revealed brittle fracture

formed with increased carbon content. The mechanical property results above were comparable to [18] showing notable improvements for the covetic materials.

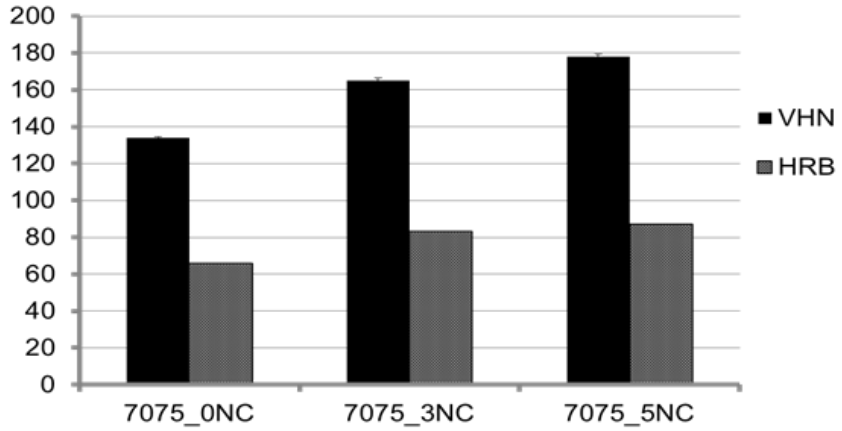

Figure 14.2 Vickers and Rockwell hardness measurements on Al7075 covetics [19].

Salamanca-Riba et al. [21] studied the form of carbon in covetics using several different techniques. In that study, they investigated 2 wt.% and 5 wt.% Cu110 covetics, 3 wt.% Ag covetics and 3 wt.% Al6061 covetics, as expressed by their target contents. Using SEM, two different carbon domain types were detected on 3 wt.% Al6061; 50-200 nm size "particle nano-carbon", and 5-100 nm size "lattice structure nanocarbon". Wherein, the former was amorphous and well distributed into the matrix, and the latter formed an inter-connected network. In that regard, high-resolution transmission electron microscopy (HRTEM) images of 5 wt.% Cu110 covetic sample displayed nanocarbon regions observed as weak satellite spots in diffraction patterns, where high carbon content was separately detected via EDS. As well, lattice structure nanocarbon yielded a stripe forms in the aluminum covetic, as detected through a high angle annular dark field (HAADF) technique. Similarly, HRTEM of Ag covetic demonstrated alternating graphene layers as formed in between (111) silver planes. Electron energy loss spectroscopy (EELS) data showed peak formations around 284 eV denoting sp^2 bonded carbon which indicates graphitic structures forming in all three covetic configurations. Supporting the

EELS results, Raman spectra on Al6061 covetic revealed characteristic D-band and G-band where the G-band defines graphene morphology. Also, an x-ray photoelectron spectroscopy (XPS) depth profiling of the Ag covetic showed a constant carbon content (0.71 wt.%) following a sputtering process. It is imperative to highlight that covetic surfaces were observed to contain hydrocarbon contaminations that after sputtering processes significantly reduced the initially detected carbon content. Finally, mechanical tests showed improved properties of Al covetics, validating earlier findings. This study demonstrated use of various spectroscopic techniques to analyze form of the carbon in the covetic structures, which paved way for further characterization of the carbon in covetics.

Then, Forrest et al. [22] investigated properties of Cu and Al covetics with various carbon contents. They reported that LECO and glow discharge mass spectroscopy (GDMS) methods were only able to detect trace amounts of the carbon, which corresponded to the unconverted carbon. XPS and EDS gave carbon quantities of 3.5 and 3.78 wt.% , respectively, for a 5 wt.% target amount in Cu covetics. Also, solidus temperatures of both Cu and Al increased as compared to literature values. Density of a 3.5 wt.% copper covetic, measured using a gas pycnometer, was lower than pure copper. Thermal conductivity of Cu covetic with actual 0.057 wt.% C was tested using two different techniques: steady state measurement (ASTM E1225) and laser flash diffusivity (ASTM E1461). The latter method demonstrated 50% higher thermal conductivity values than of the parent Cu material, while the former showed anisotropy in this thermal property. Electrical conductivity of 3 wt.% Al covetic was measured using the four-probe technique wherein as-extruded covetic yielded the highest electrical conducitivity, 67.3% IACS, higher than of a conventional Al 6061 alloy. Regarding mechanical properties, as-extruded 3 wt.% Al covetic possessed 30% higher yield strength than its parent material.

However, upon T6 heat treatment, both electrical and mechanical properties were very similar. It was concluded that resistance of as-extruded material to grain-coarsening resulted in the higher mechanical strength where heat treatment relaxed and minimized that effect.

Brown et al. compiled findings on physical, mechanical and electrical properties of 3 wt. % Al 6061 covetics [23]. They evaluated both parent and covetic materials being as-extruded (T0) and heat-treated to T6 condition. LECO analysis showed that an unconverted carbon content in the covetic material was 0.3 wt.% as compared to a nominal value 3 wt%. SEM images displayed nanocarbon particles ranging between 5-200 nm in diameter, where complementary EDS mapping revealed both converted and unconverted carbon sites. Similar to prior results, this work reported no significant density change in the covetics. Yet, in terms of hardness, as reported in [18], about 23 % hardness increase occurred in the T0 covetics which was correlated with the reduced grain size and coarsening effects. Regarding tensile properties, T0 covetic material demonstrated 29% higher strength than the parent material where yield strength was 30% greater. Following the tensile tests, the T0 covetics possessed brittle fracture surfaces, but heat treatment to T6 did not cause similar effects for covetic and parent materials. Electrical conductivity measurements showed 20% higher conductivity of T0 covetic than of its parent material. However, upon the T6 heat treatment such differences were removed. Yet quality of surface finishing increased the conductivity by about 8% in the T6 condition. Also, strain rate dependency measurements were conducted, similar to those in [18], where T0 covetic showed a 40% higher strength at increased strain rates correlating with prior findings. Wherein, T6 covetic did not reveal any dependence on strain rates.

On top of these pioneering works, researchers at University of Science and Technology (AGH) in Krakow first time independently synthesized copper covetics [24]. They utilized

activated carbon (0.83 and 2 wt.%.) and carbon nanotube (0.77 wt.%) reinforcements. Fabrication protocols and processing parameters are detailed in the study. Chemical analyses demonstrated very low oxygen content, and, more importantly, carbon contents of the samples were comparable with corresponding amounts added during the fabrication. Activated carbon incorporated covetics had lower density than the pure copper while CNT added covetics had similar density to the one of the pure copper. Hardness values of the covetics were lower than of the pure copper, which were not consistent with previous findings. Electrical conductivities of the three material types were close to pure copper, which was impressive as presence of impurities was reported. Using secondary-ion mass spectroscopy (SIMS), very small amount of carbon was detected in the CNT covetic, while carbon black covetic samples had more viable carbon content. Microstructural analysis showed secondary darker domains which were attributed to the presence of graphitic carbon.

In a follow-up work, the AGH researchers used a similar manufacturing method and they performed structural characterizations on as-cast covetic samples and extruded wire covetic samples [25]. During the fabrication process, argon gas protection was provided to prevent oxidation and combustion of the carbon at high temperatures. Covetic samples having 2-3 wt.% activated carbon were fabricated. The study provided detailed information regarding processing parameters for the fabrication. LECO-optical emission spectroscopy (OES) coupled analyses showed oxygen content at trace levels, with no carbon content detected. SIMS visually demonstrated presence and distribution of the carbon in the samples wherein lower carbon content and uneven distributions were also observed for different processing parameters. Densities of the samples were measured to be lower than pure copper. Hardness of the most carbon content sample was 20% lower than the lower carbon content samples, contradicting

previous findings. Electrical conductivity was measured as high as 100,17 % IACS inspite of impurities. Regarding the processed wires, tensile strength and yield strength were observed to decrease upon annealing which validated above findings that thermal treatment reduces mechanical properties. Yet, electrical properties were preserved upon annealing.

Salamanca-Riba et al. characterized Ag-covetics with 3 wt.% and 6 wt.% activated carbon [26]. X-ray photoelectron spectroscopy (XPS) depth profiling was utilized to analyze distribution of the carbon in the silver matrix (3 wt.%). They observed that after 1 min. of Ar ion sputtering, the carbon content remained almost constant at 1 wt%, indicating removal formation of hydrocarbon contaminations. X-ray diffraction (XRD) studies on 6 wt.% covetic sample showed that the silver lattice structure did not change with carbon infusion. It is important to note that no peaks of carbon or graphene (crystalline structure) were observed. Additionally, in TEM, they observed weak spots (patterns) between <220> Ag which indicated a carbon structure (Figure 14.3), as also validated by EELS. Through some calculations, interplanar distance of the weak spots was found to be closely comparable to $<10\bar{1}0>$ interplanar distance of graphite, yet with 13% strain applied on the carbon structure. Considering lattice and expansion coefficient mismatches between carbon and silver, it was concluded that such high strain formed due to epitaxial rearrangement of lattice structure in the covetics. Based on that it was concluded that carbon structure formed alternating layers of graphene between atomic planes of silver. Raman spectroscopy, of 6 wt.% Ag covetic showed presence of carbon via illustrative Dand G (disornanocrystalline graphite) characteristic peaks of sp2 bonding. The position of 1600 cm-1 as compared to 1540 cm-1 of pristine graphene, was attributed to highly disordered carbon forms in the metal as well as an induced strain. The D-band at 1334 cm^{-1}, on the other hand, corresponded to formation of a defective carbon structure. The carbon structure was also evidenced by XPS

spectra exhibiting a carbon peak at 284.4 eV. Additionally, EELS showed a slight peak at 284 eV corresponding to graphitic carbon. Adding carbon into the silver increased a melting temperature of the covetics by 15 °C (from 961.78 °C to 976.5 °C). Additionally, upon consecutive heating cycles, no further change in the melting temperature and materials weight were observed meaning that the carbon did not phase separate during heating/melting processes due to a strong bond to Ag matrix. Electrical conductivity of 6 wt.% covetic samples was measured to be 5.62 x 107 S/m as compared to 6.2 x107 S/m of the pure Ag.

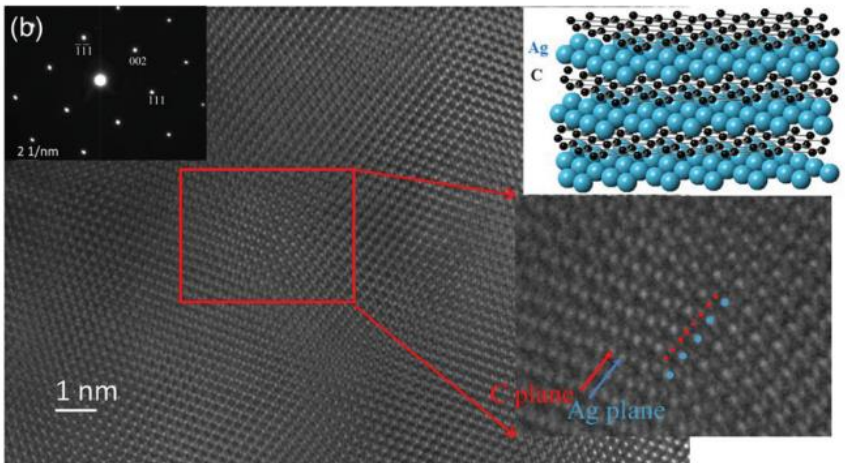

Figure 14.3 HRTEM image and diffraction pattern of 3 wt.% Ag covetic [26].

Isaacs et al. characterized copper covetics with 5 wt.% carbon [27]. $(01\bar{1})$ electron diffraction pattern displayed weak satellite spots, similar to the previous study [26], corresponding to modulation of 1.6 nm size, as observed in HRTEM along with detected high carbon content. It was concluded that during the covetics fabrication process, high-level of the current led to self-arrangement of the carbon structures in the copper matrix. XPS depth profiles and EDS demonstrated carbon content close to target value. Next, thin films (18 nm) of covetics on Si substrate were obtained using an e-beam deposition technique. Transmittance measurements revealed that copper covetics (with 5 wt.% carbon) are more transparent than the parent copper. Also, it was observed that as the carbon content increased, the thin films became

more transparent. This result was attributed to special interstitial placement of the carbon C in the Cu lattice that resulted in a lower reflection coefficient. With regard to electrical conductivity measurements, the covetic films showed lower and long-term stable resistivity than the pure copper film of the same thickness. The covetic films preserved their resistivity up to 80 days, while pure copper films were observed to degrade quickly. Wherein, the copper covetics inherently generated a resistance to oxidation due to the presence of carbon-silver bonds.

More recently, Ma et al. recently reported 3D nanoscale imaging of carbon features in the copper covetics with 0.21 wt.% C using synchrotron hard X-ray nanotomography [28]. SEM images displayed micron-size spherical features, having notable oxygen content and no difference in carbon content (Figure 14.4). Those features were attributed to form during the covetics fabrication process. In bright field TEMs, evidencing the SEM/EDS, the inclusions had higher oxygen content than the copper matrix. Scans of X-ray transmission micrographs revealed also formations of those features at various rotation angles. Additionally, X-ray radiographs clearly display those nanoscale features.

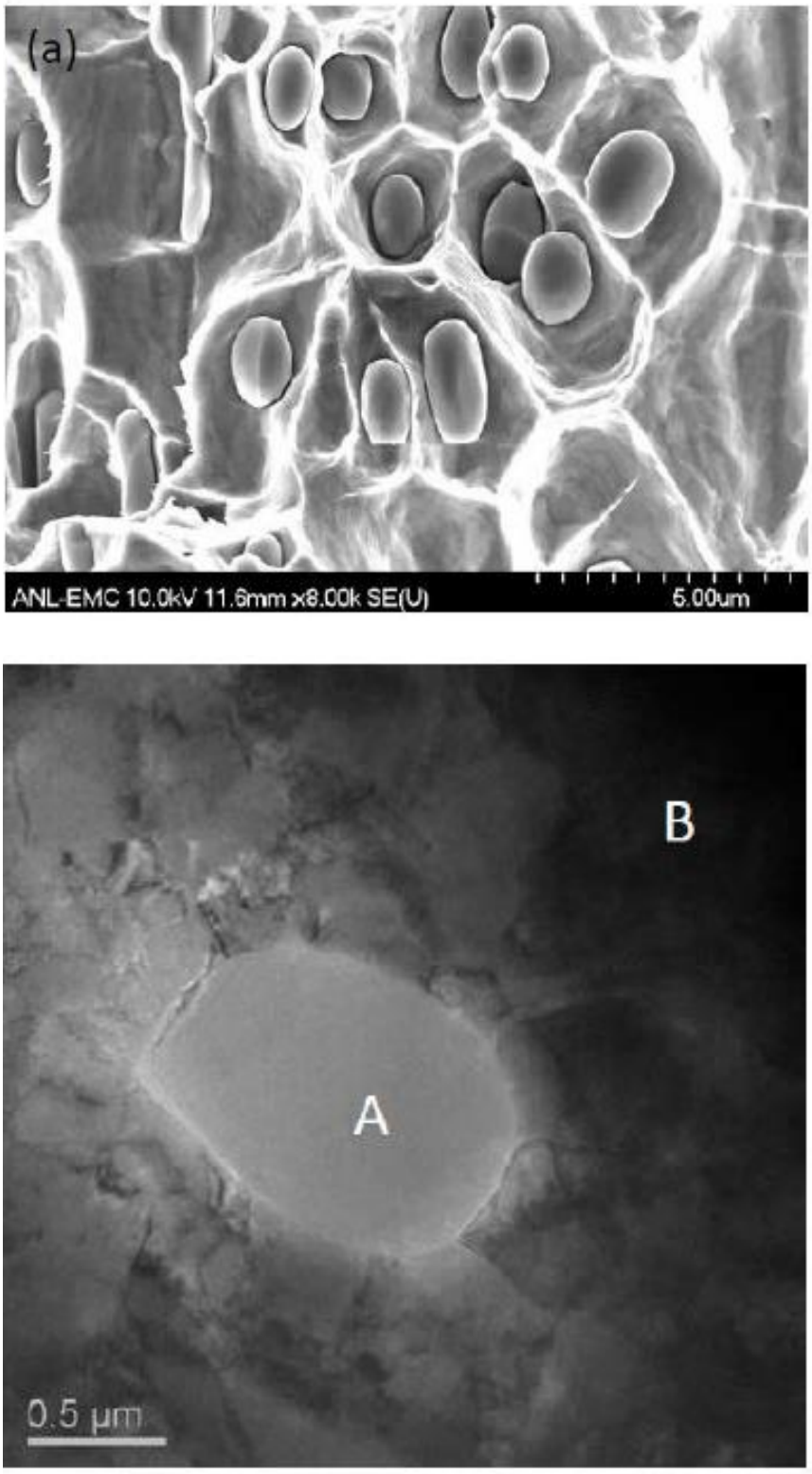

Figure 14.4 SEM (top) and TEM (bottom) images taken on the covetics [28].

Jaim et al. then studied the covetic structure, C-C bond forms, matrix dispersion of carbon, and bonding of carbon to aluminum matrix in aluminum covetics [29]. Using high angle HADDF mode in TEM, they demonstrated presence of folded ribbon-like structures with 3 wt.% Al 6061 matrix. The nanostructure was detected to have high concentration of carbon and oxygen using EDS. In TEM, weak spots were observed in diffraction spectra, as reported earlier, which were attributed to preferential orientation of carbon in the aluminum lattice. Note that, some amorphous carbon was also detected in the same spectra. EELS spectrum imaging confirmed presence of the sp2 bonding with a sharp edge at 284 eV evidencing conversion reaction. EELS C-K mappings also revealed presence of the nanoribbons. Additionally, Raman spectra taken on the aluminum covetics displayed strong peaks of D and G bands highlighting presence of carbon in the structure. Wherein, the intensity ratio between D and G peaks indicated formation of a graphitic disorder. They performed surface measurements on the covetics using AFM-KPFM technique that phase maps displayed darker spots with low surface potential corresponding to carbon nanoribbons being distributed in the matrix. Carbon content in the covetics was measured using XPS which again demonstrated carbon content being lower than the target carbon values. Regarding morphological analysis, XRD spectra, in particular, did not reveal any evidence of carbon or allotrope formations in the covetic structure (Figure 14.5). Yet, the covetic samples were polycrystalline having preferential orientations, as indicated by their changing indicial intensities with respect to different orientations. Also, it was observed that lattice constant as well as average crystallite size of the covetic structure was decreased with respect to an increased carbon content. Notable increases in ultimate tensile strength and hardness of the covetics were also observed.

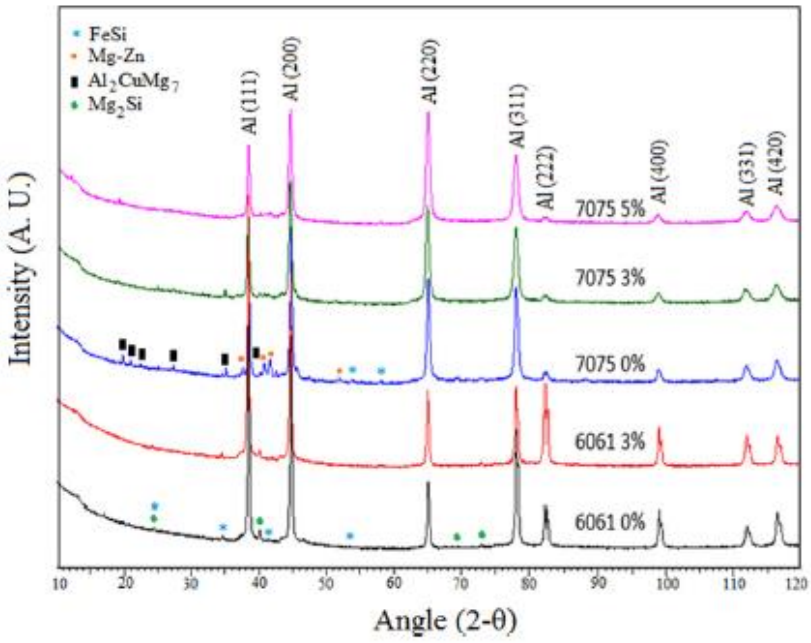

Figure 14.5 XRD spectra of covetics [29].

Additionally, Balachandran et.al. studied copper covetics with 3 wt.% carbon [30]. XRD results on both parent and covetic materials displayed impurities, wherein they also observed a Cu2O formation in the parent material, but not in the covetic material. Densities of the parent material and the covetic material were close, yet both were above the pure copper density. In SEM, both samples had similar grain sizes (~1 um). In DSC scans, they observed two peaks: low-temperature peak corresponding to solidus temperature of Cu2O, and higher temperature peak of copper. Regarding electrical conductivity, the parent material demonstrated 93.2% IACS while the covetic had 99.5% IACS. Parent copper and covetic materials exhibited similar thermal conductivities, where the covetic samples were 10% higher.

Jaim et al., in a follow up study, reported Raman studies on Al and Ag covetics analyzing sp2/sp3 bonding, strain, defects, oxidation and crystalline sizes of nanoribbons [31]. In Raman measurements, they confirmed that 3 wt.% Al covetic possessed the characteristic G and D

peaks, along with some amorphous carbon. Intensity variations observed through Raman mapping demonstrated unstrained condition for the G peak, whereas the D peak revealed strained carbon forms (Figure 14.6). Additionally, EELS imaging demonstrated formation of oxidation on the covetic samples. Through C mapping, nanoribbon like features were observed, at 284 eV, indicating sp2 carbon. Also, Raman spectra taken on the pure Ag and 6 wt.% Ag covetic samples displayed blue shifts observed in the G band which indicated compressive strains induced on the carbon. Interestingly, it was observed that strained regions were surrounded by unstrained regions wherein the highest strain was located in central carbon spots. As expected, variations in the D peak indicated presence of both sp2 and sp3. AFM/KPFM maps showed darker regions indicating presence of carbon along with some ribbon like structures having low surface potential. EELS of the 6 wt.% Ag covetic showed carbon rich regions along with the observed peaks at 284 and 290 eV indicating a sp2 carbon structure.

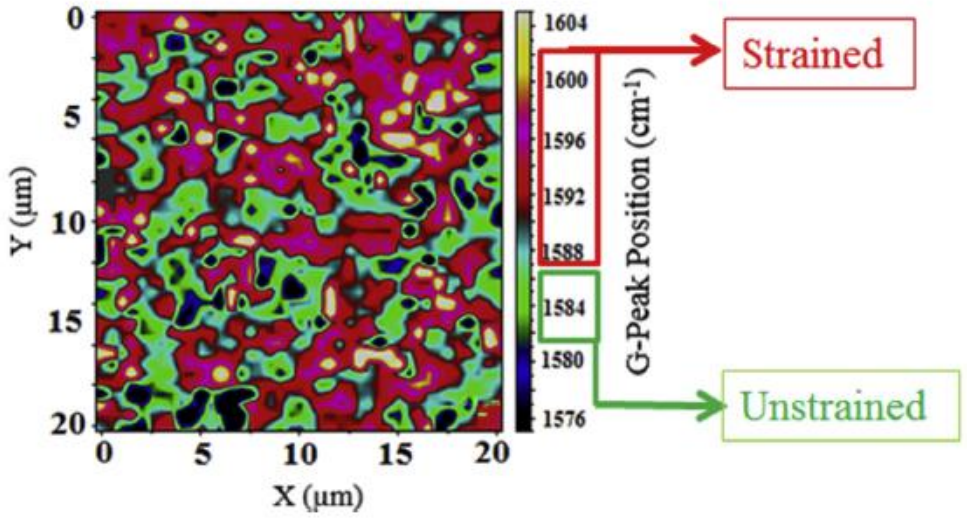

Figure 14.6 G-peak mapping of 6 wt.% Ag covetic [31].

14.3 Conclusions and Future Perspective

Macroscopic quantification of the carbon content is of key importance for determination of composition-structure-property relations of covetics. However, quantitative characterization of carbon content still remains a challenge. As discussed, target carbon contents utilized during processing are not necessarily the measured values on fabricated materials. So far, EDS and XPS measurements provided valuable information regarding the carbon content. Yet, those techniques are limited to local surface measurements. Hence, EDS/XPS are not sufficient to obtain the overall macroscopic carbon content in the covetics. Also, covetics are subjected to detector-originated carbon contaminations through the use of EDS/XPS. Thus, such measurements require simultaneous use of calibration samples to obtain accurate carbon content. Combustion based bulk techniques of LECO and GDMS did not provide valuable insights into the carbon content, which is attributed to strong bonding between carbon and metal in the covetic materials. Although density measurements appear to be a viable approach to quantify the carbon content, the predicted carbon contents via such method do not agree with the ones measured via spectroscopic techniques. Although that outcome is more likely due to porosity in the covetics, more detailed analyses could be pursued.

Furthermore, as XPS measurements demonstrated, surface hydrocarbon contamination is predominant in covetics. Although TEM and Raman measurements demonstrated crystalline carbon morphologies, XRD measurements so far did not validate such results, nor displayed characteristic carbon peaks. However, XRD provides consistent results with EBSD regarding the reduced grain size in the covetics.

SIMS [24] and x-ray micro-computed tomography (micro-CT) [28] techniques provided valuable information on imaging of carbon dispersion and they could be complementarily

utilized. Besides, the use of SIMS/X-Ray micro-CT could be further extended to quantification of the macroscopic carbon content.

Secondly, several studies provided valuable insight into form and bonding of carbon nanoparticles. Yet, comprehensive understanding of those outcomes and of the conversion reaction of the covetics is still lacking.

Another important issue is thermal stability of carbon nanoparticles (mostly activated carbon) in high melting temperatures of metals. Such high temperatures may cause rapid thermal decomposition of the carbon nanoparticles resulting in abrupt weight reductions. Wherein, thermal stability of the carbon nanoparticles should be analyzed with respect to processing temperature and time along with heating chamber ambient (air or vacuum). Indeed, lower values measured for carbon content would stem from decomposition of carbon nanoparticles during manufacturing.

Most studies showed improvement in mechanical properties of covetics. However, reasons for these improvements are not yet fully understood. Also, upon heat treatment, covetics were observed to loose such improved mechanical properties. So, to establish mechanical property comparison, both covetic and parent materials should be processed under same thermal conditions. In addition, not all studies confirmed previously reported improvements in electrical and thermal conductivities. Thus, further studies on electrical and thermal conductivities of covetics are needed.

Another pressing need is to understand effects processing parameters during the covetics manufacturing on covetics properties so these materials could reach their optimum performance.

In summary, covetics have promising physical properties surpassing bare traditional metals. With so far demonstrated characteristics, covetics possess potential to address needs in

cutting-edge applications. However, further research is needed before that can be fully accepted and used in industrial applications.

14.4 References

[1] Shugart, J. V.; Scherer, R. C.: Metal-carbon compositions. U.S. Patent 8541335 B2, 2013.

[2] Shugart, J. V.; Scherer, R. C.: Copper-carbon composition. U.S. Patent 20100327233 A1, 2010.

[3] Scherer, R. C.; Shugart, J. V.; Lafdi, K. New class of metallic nanocomposites - nanocarbon metals. Materials Science & Technology Conference and Exhibition 2009.

[4] López, G. A.; Mittemeijer, E. J. The solubility of C in solid Cu. Scripta Mater 2004, 51, 1-5. DOI: 10.1016/j.scriptamat.2004.03.028

[5] Lander, J. J.; Kern, H. E.; Beach, A. L. Solubility and diffusion coefficient of carbon in nickel: reaction rates of nickel-carbon alloys with barium oxide. Journal of Applied Physics 1952, 23, 1305-1309. DOI: 10.1063/1.1702064

[6] Speer, J.; Matlock, D. K.; De Cooman, B. C.; Schroth, J. G. Carbon partitioning into austenite after martensite transformation. Acta Materialia 2003, 51, 2611-2622. DOI: 10.1016/S1359-6454(03)00059-4

[7] He, C.; Zhao, N.; Shi, C.; Du, X.; Li, J.; Li, H.; Cui, Q. An approach to obtaining homogeneously dispersed carbon nanotubes in Al powders for preparing reinforced Al-matrix composites. Adv Mater 2007, 19, 1128-1132. DOI: 10.1002/adma.200601381

[8] Kwon, H.; Estili, M.; Takagi, K.; Miyazaki, T.; Kawasaki, A. Combination of hot extrusion and spark plasma sintering for producing carbon nanotube reinforced aluminum matrix composites. Carbon 2009, 47, 570-577. DOI: 10.1016/j.carbon.2008.10.041

[9] Hashim, J.; Looney, L.; Hashmi, M. S. J. Metal matrix composites: production by the stir casting method. Journal of Materials Processing Technology 1999, 92–93, 1-7. DOI: 10.1016/S0924-0136(99)00118-1

[10] Laha, T.; Agarwal, A.; McKechnie, T.; Seal, S. Synthesis and characterization of plasma spray formed carbon nanotube reinforced aluminum composite. Materials Science and Engineering: A 2004, 381, 249-258. DOI: 10.1016/j.msea.2004.04.014

[11] Koltsova, T. S.; Nasibulina, L. I.; Anoshkin, I. V.; Mishin, V. V.; Kauppinen, E. I.; Tolochko, O. V.; Nasibulin, A. G. New hybrid copper composite materials based on carbon nanostructures. Journal of Materials Science and Engineering B 2012, 2, 240-246.

[12] Kwon, H.; Lee, G.-G.; Kim, S.-G.; Lee, B.-W.; Seo, W.-C.; Leparoux, M. Mechanical properties of nanodiamond and multi-walled carbon nanotubes dual-reinforced aluminum matrix composite materials. Materials Science and Engineering: A 2015, 632, 72-77. DOI: 10.1016/j.msea.2015.02.057

[13] Choi, H. J.; Min, B. H.; Shin, J. H.; Bae, D. H. Strengthening in nanostructured 2024 aluminum alloy and its composites containing carbon nanotubes. Composites Part A: Applied Science and Manufacturing 2011, 42, 1438-1444. DOI: 10.1016/j.compositesa.2011.06.008

[14] Deng, C.; Zhang, X.; Wang, D.; Lin, Q.; Li, A. Preparation and characterization of carbon nanotubes/aluminum matrix composites. Materials Letters 2007, 61, 1725-1728. DOI: 10.1016/j.matlet.2006.07.119

[15] Subramaniam, C.; Yamada, T.; Kobashi, K.; Sekiguchi, A.; Futaba, D. N.; Yumura, M.; Hata, K. One hundred fold increase in current carrying capacity in a carbon nanotube–copper composite. Nature Communications 2013, 4, 2202. DOI: 10.1038/ncomms3202

[16] Kim, Y.; Lee, J.; Yeom, M. S.; Shin, J. W.; Kim, H.; Cui, Y.; Kysar, J. W.; Hone, J.; Jung, Y.; Jeon, S.; Han, S. M. Strengthening effect of single-atomic-layer graphene in metal–graphene nanolayered composites. Nature Communications 2013, 4, 2114. DOI: 10.1038/ncomms3114

[17] Wu, Z.-S.; Zhou, G.; Yin, L.-C.; Ren, W.; Li, F.; Cheng, H.-M. Graphene/metal oxide composite electrode materials for energy storage. Nano Energy 2012, 1, 107-131. DOI: 10.1016/j.nanoen.2011.11.001

[18] Brown, L.; Joyce, P.; Forrest, D.; Wolk, J. Physical and mechanical characterization of a nano carbon infused aluminum-matrix composite. Proceedings of the SAMPE Fall Technical Conference 2011.

[19] Nilufar, S.; Siddiqi, S.; Jasiuk, I. Multi-scale characterization of novel aluminum-carbon nanocomposites. Materials Science & Technology Conference and Exhibition 2012

[20] Jasiuk, I.; Nilufar, S.; Salamanca-Riba, L.; Isaacs, R.; Siddiqi, S. Novel aluminum-carbon materials. Technical Proceedings of the 2013 NSTI Nanotechnology Conference and Expo 2013.

[21] Salamanca-Riba, L.; Isaacs, R.; Mansour, A. N.; Hall, A.; Forrest, D. R.; LeMieux, M. C.; Shugart, J. V. A new type of carbon nanostructure formed within a metal-matrix. Proceedings of Nanotech Conference and Expo 2012.

[22] Forrest, D. R.; Jasiuk, I.; Brown, L.; Joyce, P.; Mansour, A.; Salamanca-Riba, L. Novel metal-matrix composites with integrally-bound nanoscale carbon2012.

[23] Brown, L.; Joyce, P.; Forrest, D.; Salamanca-Riba, L. Physical and mechanical characterization of a nanocarbon infused aluminum-matrix composite. 2014. DOI: 10.1520/MPC20130023

[24] Knych, T.; Kwaśniewski, P.; Kiesiewicz, G.; Mamala, A.; Kawecki, A.; Smyrak, B. Characterization of nanocarbon copper composites manufactured in metallurgical synthesis process. Metallurgical and Materials Transactions B 2014, 45, 1196-1203. DOI: 10.1007/s11663-014-0046-7

[25] Knych, T.; Kiesiewicz, G.; Kwasniewski, P.; Mamala, A.; Smyrak, B.; Kawecki, A. Fabrication and cold drawing of copper covetic nanostructured carbon composites/Otrzymywanie oraz ciągnienia kompozytów miedzianych typu covetic o strukturze nanometrycznej. Archives of Metallurgy and Materials 2014, 59, 1283-1286. DOI: 10.2478/amm-2014-0219

[26] Salamanca-Riba, L. G.; Isaacs, R. A.; LeMieux, M. C.; Wan, J.; Gaskell, K.; Jiang, Y.; Wuttig, M.; Mansour, A. N.; Rashkeev, S. N.; Kuklja, M. M.; Zavalij, P. Y.; Santiago, J. R.; Hu, L. Synthetic crystals of silver with carbon: 3D epitaxy of carbon nanostructures in the silver lattice. Advanced Functional Materials 2015, 25, 4768-4777. DOI: 10.1002/adfm.201501156

[27] Isaacs, R. A.; Zhu, H.; Preston, C.; Mansour, A.; LeMieux, M.; Zavalij, P. Y.; Jaim, H. M. I.; Rabin, O.; Hu, L.; Salamanca-Riba, L. G. Nanocarbon-copper thin film as transparent electrode. Applied Physics Letters 2015, 106, 193108. DOI: 10.1063/1.4921263

[28] Ma, B.; Winarski, R.; Wen, J.; Miller, D.; Segre, C.; Balachandran, U.; Forrest, D. Investigation of carbon nanostructure in copper covetics by x-ray nanotomography. Proceedings of the 2nd International Conference on Tomography of Materials and Structures 2015.

[29] Jaim, H. M. I.; Isaacs, R. A.; Rashkeev, S. N.; Kuklja, M.; Cole, D. P.; LeMieux, M. C.; Jasiuk, I.; Nilufar, S.; Salamanca-Riba, L. G. Sp2 carbon embedded in Al-6061 and Al-7075 alloys in the form of crystalline graphene nanoribbons. Carbon 2016, 107, 56-66. DOI: 10.1016/j.carbon.2016.05.053

[30] Balachandran, U.; Ma, B.; Dorris, S. E.; Koritala, R. E.; Forrest, D. R. Nanocarbon-infused metals: a new class of covetic materials for energy applications. Materials Science & Technology Conference and Exhibition 2016.

[31] Jaim, H. M. I.; Cole, D. P.; Salamanca-Riba, L. G. Characterization of carbon nanostructures in Al and Ag covetic alloys. Carbon 2017, 111, 309-321. DOI: 10.1016/j.carbon.2016.10.007

CHAPTER 15: INVESTIGATING THE CORROSION BEHAVIOR AND MECHANICAL PROPERTIES OF AL-ALLOY "COVETICS"

15.1 Introduction

The formation and processing of metal alloys allows significant enhancements in the desirable properties of the base metal. For example, the carburization of steel strongly influences its strength and ductility, and also increases its resistance to oxidation [1, 2]. Metal alloys are widely utilized in the building of infrastructure such as for the transmission of electricity in high-voltage power lines, for the fabrication of high-performance electronics, and for the construction of lightweight aerospace, naval, and automotive vehicles.

Aluminum (Al) and its alloys are of interest because of their increasingly significant role in applications requiring lightweight yet strong building materials that are resistant to chemical attack and degradation. The corrosion of many Al alloys has been investigated previously to understand the mechanism of corrosion and corrosion resistance. Typically, Al and its alloys undergo pitting corrosion in the presence of chlorine ions (Cl-) in which local breakdown of the metal-oxide passivation layer results in the dissolution of the Al surface [3-7]. Such pitting corrosion is of major concern due to the high Cl- levels found in the environments in which these metals are typically used, such as in seawater and on roadways.

This work was previously published: Varnell, J.A., Bakir, M., Chen, X., DiAscro, A.M., Nilufar, S., Jasiuk, I., Gewirth, A.A., Understanding the influence of carbon addition on the corrosion behavior and mechanical properties of Al-alloy "covetics", Journal of Materials Science, 54 (3), 2668-2679 (2018).

Special thanks to Jason Varnell (Chemistry, University of Illinois) for performing corrosion analysis.

For Al alloys, chromate conversion coating is commonly used to protect the surface [4]. However, this process involves the use of chromic acid which is toxic and highly regulated. Thus, alternative methods to protect Al alloys from corrosion are desirable [8].

Many attempts to manufacture composite materials by combining carbon fillers and metallic Al powders have recently been described [9]. These include mixing graphene and carbon nanotubes with powders of pure Al or Al-alloys and applying various processing techniques including ball milling, binder-assisted mixing, hot-pressing/sintering, high-pressure torsion, friction stir processing, and plasma spray forming [10-17]. The resulting composite materials consist of a mixture of carbon structures and Al particles because the solubility of carbon in Al is extremely low [18]. Additionally, the presence of a carbide phase, Al4C3, has been observed for manufacturing processes which involve high temperatures, generally above 600 °C. For all of these methods the resulting composite material typically consists of interdispersed carbon structures within the Al alloy.

Recently, a new method for incorporating carbon into Al alloys was developed by Third Millennium Materials, LLC, referred to as “electrocharging assisted bulk processing” [19, 20]. This process, which involves adding carbon to the molten metal and applying a high electrical current while stirring the mixture, was used to incorporate carbon into metals and alloys for which the predicted solubility of carbon is low, such as Ag, Cu, and Al [19-30]. It is hypothesized that the high currents used in this process result in the ionization of carbon atoms within the melt. This ionization might enable the formation of covalent bonds between the carbon and the metal, for which these “covetic” materials have been named. The formation of covetics in Ag, Cu, and Al has been studied by diffraction, electron energy-loss spectroscopy (EELS), Kelvin force-probe microscopy, and X-ray photoelectron spectroscopy (XPS) [19, 26,

27]. Additionally, multiple density functional theory (DFT) calculations have suggested the possibility of forming direct bonds between C and metal atoms, particularly for C atoms at defect sites and at the edge of graphene-like sheets [19, 26, 31].

The covetics obtained through the electrocharging process represent a new class of metallic/carbon nanostructured materials, in contrast to previously studied composite materials [32, 33]. It is expected that covetics, which ostensibly feature covalent bonds between the metal and carbon, could exhibit enhanced properties relative to the composites. Indeed, studies showed that covetic mechanical properties, such as hardness and tensile strength, are improved from the pure alloy upon carbon addition [21, 22, 25]. Covetics also exhibit higher thermal stability and a higher melting temperature compared to the pure alloy [19, 21, 22]. Efforts on the characterization of covetics and the enhanced properties of covetics are summarized in a recent review [2].

It has also been suggested that covetics could have the desirable properties of improved corrosion resistance and resistance to oxidation [28, 34]. Previous studies demonstrated that graphene can act as a barrier to prevent the oxidation of a Cu surface and a similar resistance to oxidation was observed for a Cu covetic [30, 35, 36]. However, a full experimental investigation of the corrosion properties and an understanding of how the covetic process influences these properties is lacking. As previously proposed, it is likely that the changes induced during the process used to make the covetics could affect their corrosion properties, particularly if the surface exhibits increased carbon content and/or there is a covalent interaction between the Al and any putative C [30, 37]. For typical Al alloys, the addition of alloying elements results in the formation of secondary phases which vary in composition from the bulk material [38]. The presence of these enriched phases is known to affect the corrosion properties of alloy materials

and anodic dissolution methods are sometimes employed to reveal the composition of different secondary phases [38, 39]. In this study, we present the results of corrosion tests for an Al 6061-based covetic with and without carbon added during the manufacturing process, and observe that the covetic with carbon exhibits a significant increase in corrosion potential. We also confirm improvements in the mechanical properties of the covetic with carbon added and provide detailed physical characterization to help reveal the origin of the observed changes in both mechanical properties and corrosion behavior.

15.2 Materials and Methods

Al 3003 samples were obtained from McMaster Carr (product number 8973K87). Al 6061-T6 (the parent material for the covetic) and the covetic Al 6061 samples were received from Third Millennium Materials (TMM) LLC, Waverly, OH. Covetic Al 6061 samples were prepared as described in previous work [2, 26, 27]. One material was prepared using the covetic process but without the addition of any carbon ("0% covetic", "AC 0% C") and one was prepared by adding 2.3 wt % carbon ("2.3% covetic", "AC 2.3% C") during manufacturing. We note that these carbon amounts are those reported by manufacturers and they may not be the actual carbon contents incorporated in the covetic materials. All samples were cut into disks with diameter = 1 cm. Before characterization and corrosion testing one surface of each sample was sanded using 220 grit aluminum oxide sandpaper to remove surface contamination and passive oxide layers followed by progressive polishing using 1.0 um to 0.25 um alumina polish. After polishing, samples were sonicated in Milli-Q (Millipore) water and thoroughly rinsed. Samples characterized after corrosion tests were first thoroughly rinsed with Milli-Q water.

Electrolyte solutions were prepared using NaCl (ACS reagent ≥99%, Sigma-Aldrich), H2O2 (ACS reagent, 30% solution, Macron), HCl (ACS reagent, Macron), and 18.2 MΩ·cm Milli-Q water (Millipore). All chemicals were used as received. For experiments following ASTM G69 ("oxygenated saltwater test"), 0.9 mL of 30% H2O2 (ACS reagent, Macron) was added to 100 mL of 1 M NaCl prior to beginning the corrosion test [40, 41]. For all experiments fresh electrolyte was used, taken from the same stock solution to ensure consistency in the results.

Corrosion tests were carried out at room temperature using a single compartment cell exposed to air with Al samples attached to a steel rod by conductive double-sided Cu tape and suspended using a hanging meniscus configuration. The Al samples were used as the working electrode with a Saturated Calomel Electrode (SCE, Koslow Scientific) used as the reference electrode and a graphite rod used as the counter electrode. Typically, the open circuit potential (OCP) was monitored and allowed to stabilize over a period of 30-60 minutes before data was collected [40]. Then OCP was recorded for 1 hour before beginning linear polarization (LP) testing. LP was performed using a potential range of ±250 mV of the OCP with a scan rate of 60 mV/min [42]. Tafel fitting was performed using EC-Lab software [43]. OCP measurements were taken using a CHI 760C (CH Instruments) and LP measurements were taken using a SP-150 (Biologic Science Instruments).

The compressive properties of the Al covetic samples were measured via a compressive test using a load frame (4483 Load Frame, Instron Testing Systems) with a constant crosshead speed of 0.05 mm/min. The samples were machined to cylindrical shapes with a diameter of 5 mm and a height of 10 mm. Three samples of each covetic material (0% and 2.3%) were tested. The measurements were carried out in accordance with the ASTM E9 standard [44]. Rockwell

hardness (HRB) was measured on both the longitudinal and transverse surfaces of the samples using a hardness tester (Wilson/ Rockwell Model 523). Vickers micro hardness (VHN) was also measured on both surfaces of the same samples by applying a load of 3000 grams for 15 seconds using a microhardness tester (Shimadzu HMV-M3 Newage Testing Instruments). The reported hardness values were the averages of the total of ten measurements made on the two orthogonal surfaces (longitudinal and transverse) of each sample.

Scanning electron microscopy (SEM) was carried out using a Hitachi A-4700 high resolution microscope with an emission gun capable of 2.5 nm resolution. Energy dispersive x-ray spectroscopy (EDS) was carried out using an Oxford Instruments ISIS EDS X-ray system with accelerating voltages of 5 keV and 20 keV. X-ray photoelectron spectroscopy (XPS) was performed with a Kratos AXIS Ulta spectrometer with a monochromatic Al Kα (1486.6 eV) X-ray source. X-ray diffraction was performed using an X-ray diffractometer (XRD) (Panalytical/Philips X'pert) with a Cu K-alpha source of 0.15148 nm wavelength operated at 45 kV/40 mA. The XRD spectra were obtained between diffraction angles of $2\theta=5°$ and $2\theta=100°$ with a scan step size of 0.05° and a dwell time of 2 s/step. For thermogravimetric analysis the covetic samples were cut into pieces weighing c.a. 50 mg, washed using isopropanol at least two times, and were allowed to dry. Then, they were placed in an alumina crucible and heating was carried out using TA Instruments Q-50 equipment with a temperature ramp heating cycle of 10 °C/min up to 800 °C under a constant N2 purge of 60 mL/min.

15.3 Results

In order to evaluate the corrosion behavior of the Al alloy and Al covetic samples we used linear polarization (LP) using the conditions for the "oxygenated saltwater test" and in acidic conditions using 0.1 M HCl. Figure 15.1 shows the linear polarization curves obtained for

the Al covetic (AC) samples and two reference samples: Al alloy (AA) 6061-T6 and AA 3003. The corrosion potential (E_{corr}) for each sample was determined from the polarization curves using Tafel fitting [42, 43]. From these results, we observe that the 2.3% covetic exhibits a Ecorr approximately 30-40 mV higher than the 0% covetic. The E_{corr} of the 2.3% covetic is also higher than the corresponding values measured for the Al 6061-T6 and Al 3003 samples.

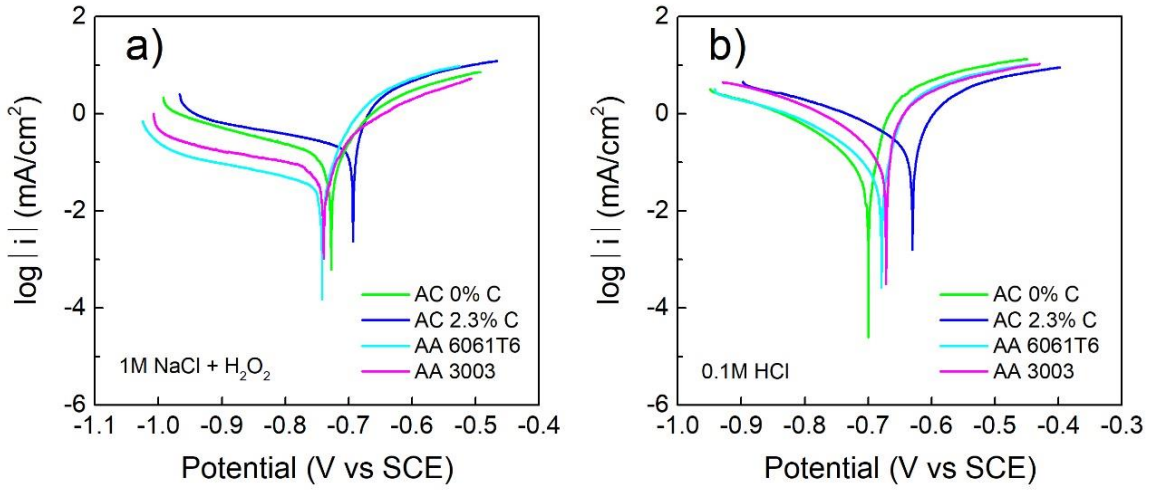

Figure 15.1 Linear polarization curves obtained for covetic materials and reference samples in the "oxygenated saltwater test" (1M NaCl + H_2O_2) (a) and 0.1M HCl (b).

To confirm the results of the LP tests, the open circuit potential (OCP) was recorded for a period of 60 minutes for each of the samples as shown in Figure 15.2 [40, 41]. The values of E_{corr} as determined from both the linear polarization curves and open circuit potentials agree closely. The values of E_{corr} obtained for the reference samples are consistent with the values reported in literature [40].

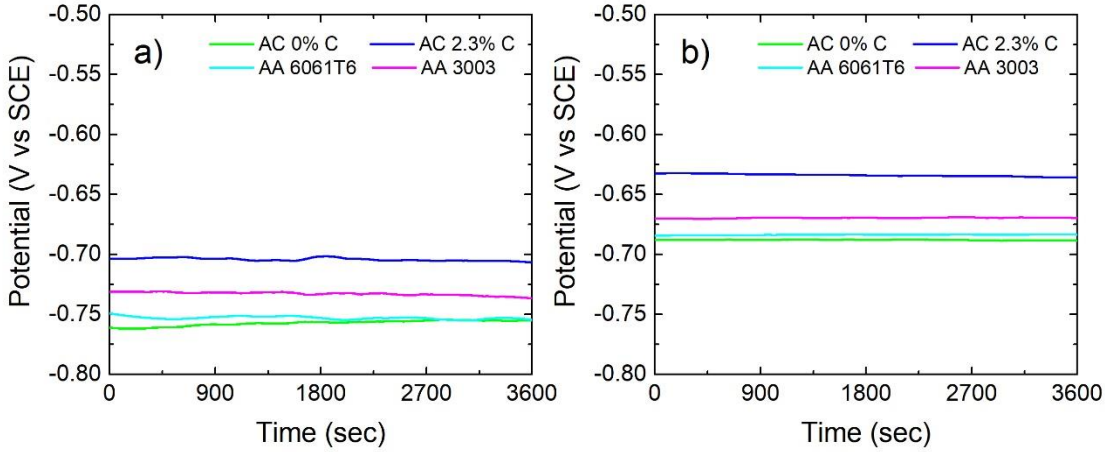

Figure 15.2 Open circuit voltage (OCV) recorded for 60 minutes in 1M NaCl (a) and 0.1M HCl (b).

To explain the difference in the corrosion behavior of the 2.3% covetic, we investigated the surface composition of the covetic samples. Figure 15.3.a and 15.3.b show SEM images of the covetics following the corrosion tests. The 0% covetic exhibits a crystalline etching pattern while the 2.3% covetic has a rougher-looking surface. To probe the elemental composition of the samples after corrosion, EDS was used at two different accelerating voltages as shown in Figure 15.3.c and 15.3.d. Interestingly, these results indicate that the surface of the 2.3% covetic after corrosion is enriched with Si, Cu, Mn, and Ti. In agreement with the EDS results, XPS also indicates that the surface of the 2.3% covetic contains Si, Cu and Mn. The elements found on the surface of the 2.3% covetic are all present in the Al 6061 parent material used to form the covetic [6]. The enrichment of these elements on the surface of the 2.3% covetic after corrosion suggests that the material is not homogeneous and that the composition of the material is altered. Since the 0% covetic does not exhibit the same increase in corrosion potential, it is evident that the addition of carbon to the covetic is necessary to promote this change in composition.

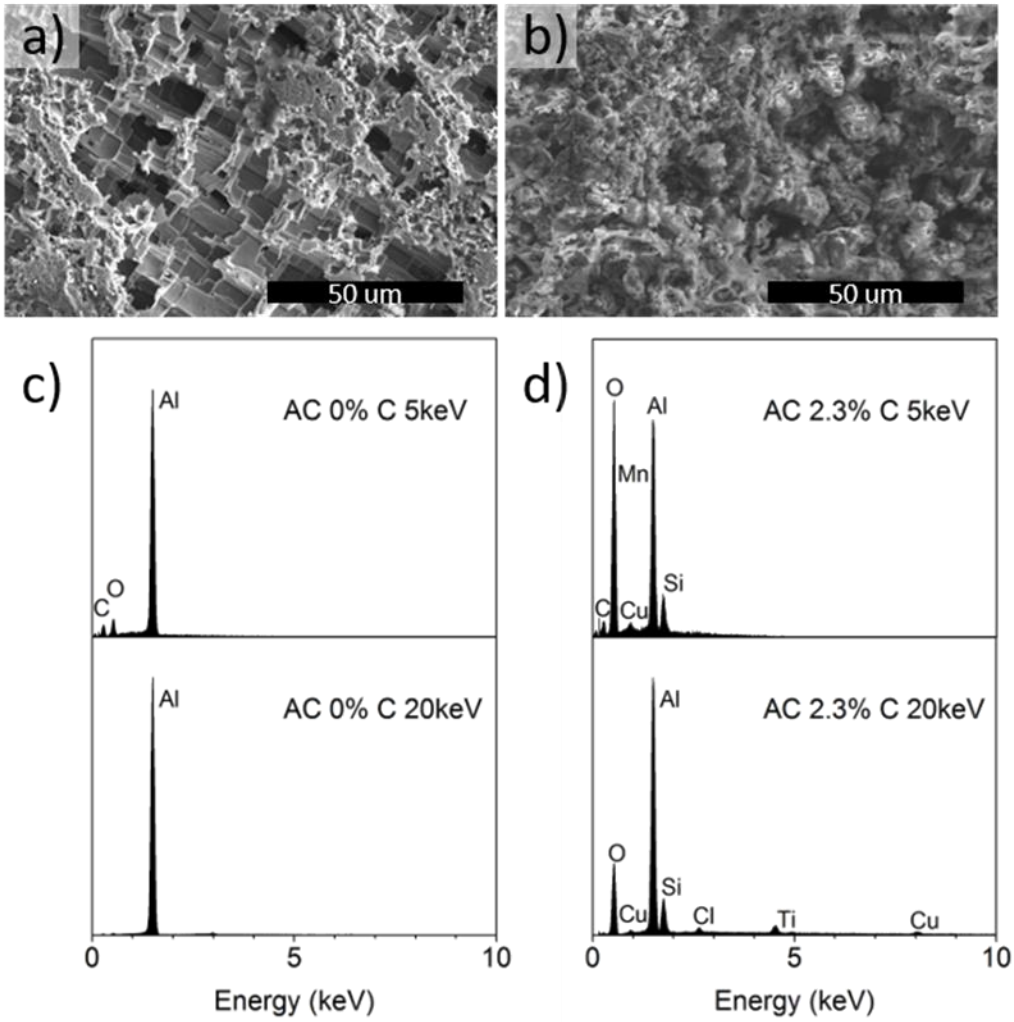

Figure 15.3 SEM images and EDS spectra of the 0% covetic (a, c) and the 2.3% covetic (b, d).

To further study the surfaces of the samples XRD was performed before and after corrosion. Figure 15.4 shows crystallographic morphologies of both 0% and 2.3% covetics. In both samples the crystal structure order of the base Al matrix was preserved. In addition, the 0% covetic demonstrated a polycrystalline morphology where the (111) peak intensity varied with respect to other peaks as the sample was rotated to different orientations. On the other hand, the 2.3% covetic possessed a preferred grain orientation where structural order did not display this modulation effect. Additionally, broadening in the (111) peak was observed for the 2.3%

covetic. The peak widths were used to determine the average grain sizes and lattice constants for each material by using the Scherer formula [36]. The average grain size for the 2.3% covetic was 170 ± 4 Å as compared to an average grain size of 232 ± 27 Å for the 0% covetic. From these values, it is clear that the surface of the 2.3% covetic has generally smaller grains than the 0% covetic. A previous study also observed smaller grain size resulting from the process used to make the covetics [22]. The presence of smaller grains also explains the preferential alignment of the grains in the 2.3% covetic [45, 46]. However, the lattice constants for the 2.3% and 0% covetics were determined to be 4.04524 ± 0.00121 Å and 4.04841 ± 0.00456 Å, respectively. These lattice constants are identical within error which suggests that the 2.3% and 0% covetics have a similar metallic-alloy structure. We note that no characteristic peaks for Al-carbides or for carbon were observed in the XRD spectra in any of the samples. For the case of the 2.3% covetic, this lack could indicate either that the carbon is well dispersed into the Al matrix via the electrocharging process, or that carbon is not present.

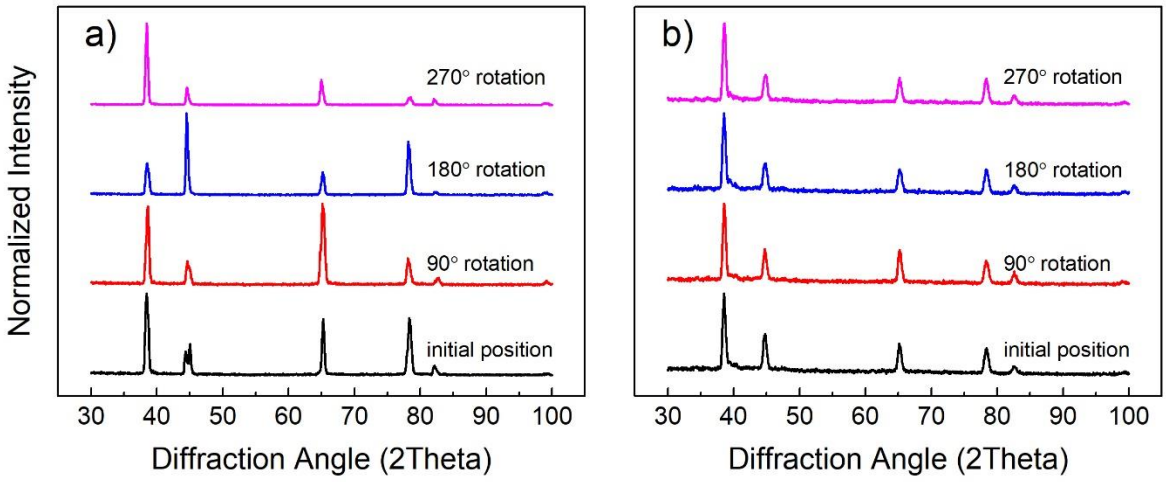

Figure 15.4 XRD spectra taken for the 0% covetic (a) and 2.3% covetic (b) following corrosion.

Finally, we carried out thermogravimetric analysis (TGA) on the 0% and 2.3% covetic samples. Figure 15.5 displays the temperature-ramp of the covetics carried out using TGA. The 0% covetic exhibited mass uptake with a small slope from the adsorption of N_2 at elevated temperature, which corresponds to ca. 0.1 % mass increase up until 800 °C. This trend was consistently reproduced through application of two subsequent heating cycles. However, the 2.3% covetic yielded significant mass reduction associated with thermal degradation until about 660 °C within the vicinity of melting point of the Al matrix. The mass loss was measured to be between 0.2 and 0.8 % of the initial mass of the sample. Decomposition started immediately during the thermal cycle, indicating that the observed mass loss is likely a consequence of the presence of water physically or chemically adsorbed to the transition metal oxides present in the 2.3% sample [47, 48]. Following the initial mass loss, the thermal curve took a positive slope similar to the 0% covetic. Likewise, a second cycle heating curve closely followed thermal behavior of the 0% covetic. We note that the TGA samples were freshly cut and not corroded before heating, so the observed mass loss likely corresponds to a phase found within the bulk composition and not only on the surface.

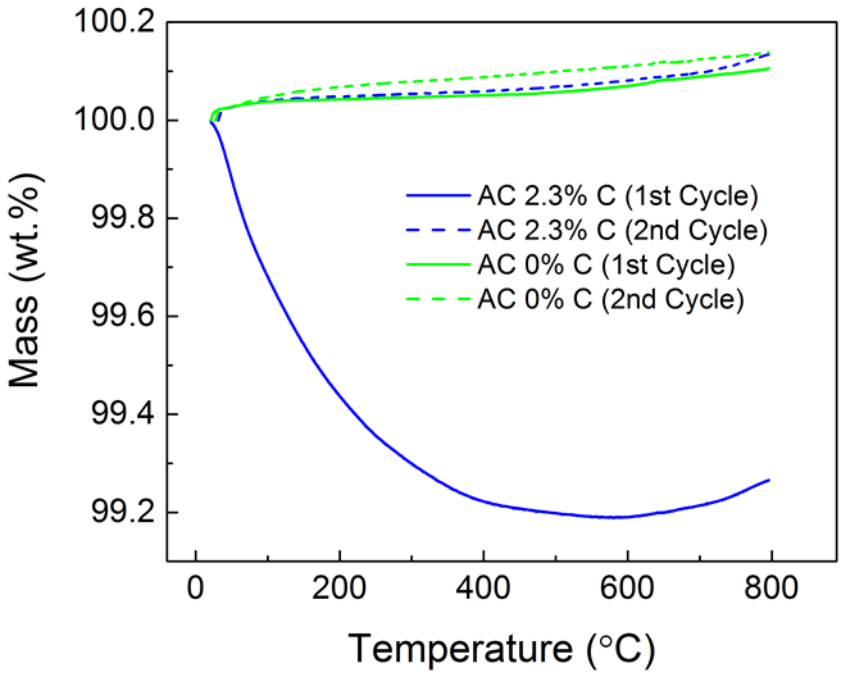

Figure 15.5 TGA curves for two heating cycles on the 0% and 2.3% covetic samples.

In addition to corrosion testing we also investigated mechanical properties of the covetic materials. Figure 15.6 shows representative compressive stress-strain curves of the 0% and 2.3% covetics. The 0% covetic displays a large plastic deformation domain following an initial elastic regime, which agrees well with the characteristic compressive behavior of Al samples [49]. The 2.3% covetic yielded substantially improved compressive strength relative to the 0% covetic. Increasing compressive stress applied on the 2.3% covetic was sustained until the formation of fracture at around 407.3 ± 25.4 MPa and 31.04 ± 5.8% strain-to-failure ratio. Hence, the 2.3% covetic enabled dramatically increased deformation energy absorption, as indicated by the toughness. The fracture formation under compression with the 2.3% covetic is a clear indication of a brittle morphology when compared to the completely plastic behavior of the 0% covetic. Additionally, both Rockwell and Vickers hardness values measured on the 2.3% covetic notably

increased with respect to the 0% covetic. Namely, the Rockwell and Vickers hardnesses improved by 10% and 51%, respectively, for the 2.3% covetic.

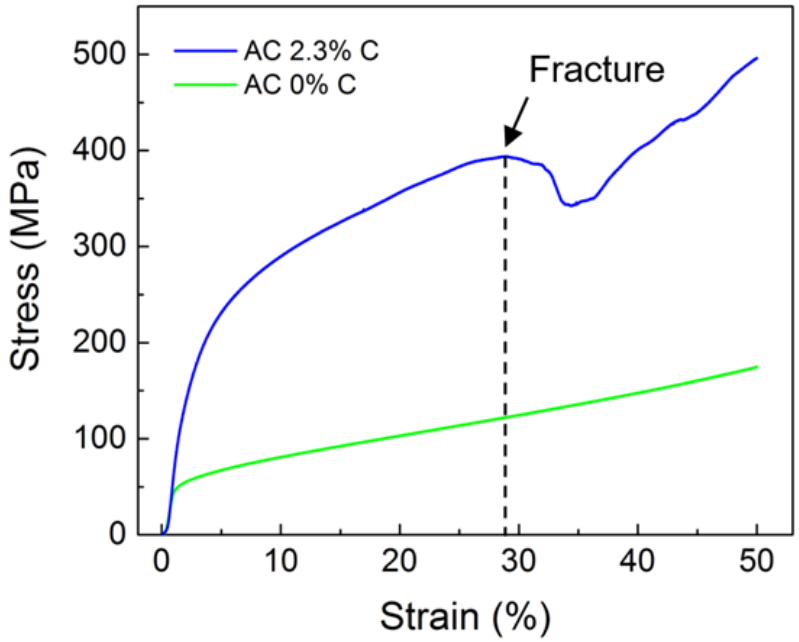

Figure 15.6 Compressive stress-strain curves for the 0% and 2.3% covetics.

The reduced grain size in the 2.3% covetic relates directly to the enhancement in mechanical properties through the Hall-Petch relation [50]. The Hall-Petch model suggests that increases in strength are expected to vary inversely with the square root of the grain size. Consequently, the prediction is that the 2.3% covetic should exhibit a strength slightly larger than that seen in the 0% covetic due to the marginally reduced grain size. However, the actual increases in the yield and ultimate strengths in the 2.3% covetic material are almost four-times until fracture. Thus, an additional strengthening mechanism is required to fully describe the large increase in compressive strengths observed for the 2.3% covetic.

15.4 Discussion

Our findings reveal that the corrosion potential is shifted to a more positive potential for the 2.3% covetic with carbon added via the electrocharging assisted process. Despite this shift, the corrosion current density at Ecorr is increased in the 2.3% covetic as compared to the 0% covetic and reference Al 3003 and Al 6061-T6 samples. Using several methods to study the materials before and after the corrosion tests we observe key differences between the 0% covetic and the 2.3% covetic. Surface characterization using SEM, EDS, and XPS indicates that the surface composition of the 2.3% covetic is different after corrosion, containing a higher concentration of several elements present in the parent material including Si, Ti, Mn, and Cu. The presence of these elements has been found to play a significant role in the corrosion behavior of Al alloys in agreement with the data that we report [6]. Additionally, previous work indicates that the presence of a secondary phase within an Al alloy containing Cu, Mn, and Si can greatly affect the corrosion properties of the material [39].

Additionally, we observe substantial improvements in the mechanical properties of the 2.3% covetic. In particular, the compressive strength is improved by four-fold in the covetic, which also dramatically enhanced the materials toughness. Additionally, the HRB and VHN hardness values of the covetics increased by 10% and 51%, respectively. We show that the average grain size for the 2.3% covetic is smaller than that of the 0% covetic. As expected, the reduction in grain size corresponds to an increase in the compressive strength and hardness for the 2.3% covetic, in agreement with previous reports [21,22,25]. However, the improvements in the mechanical properties observed for the 2.3% covetic are larger than would be expected from the decrease in grain size alone. From the corrosion studies and sample characterization, the

change in composition of the alloy phases present after addition of carbon further explains the increased strength and hardness of the 2.3% covetic [1,51].

Compositional differences within Al alloys are commonly observed due to secondary phase formation and as a result of processing, such as during heat treatments, aging, and welding [4, 38, 39]. Due to the high temperature and electrical current used to manufacture the covetic samples it is extremely likely that similar changes in the local composition of the alloy have occurred for the covetic samples. However, since the changes in corrosion potential, mechanical strength, and hardness are only observed for the 2.3% covetic it is apparent that the addition of carbon is required to facilitate these compositional changes. Carbon interacts strongly with oxygen and as carbon is added oxygen atoms may also be introduced into the molten covetic material. The O interacts strongly with the other elements present in the melt and as the covetic is cooled phase separation occurs. This results in changes to the phase composition within the material, increasing the presence of oxides of Al, Si, Mn, Ti, and Cu.

Previous studies on covetic materials suggest that carbon incorporation into the covetic material results in graphene-like nanoribbons, observed using techniques such as Raman and EELS mapping [19, 25-27]. Such possibilities have been supported by DFT studies which show that graphene-like carbon can be directly bonded to Al atoms in the alloy through the formation of covalent bonds between carbon and Al [19, 26, 31]. However, in our studies we did not specifically observe the incorporation of carbon into the 2.3% covetic. All of the samples examined by XPS exhibited a peak around 284 eV from carbon on the surface. The carbon peak was more pronounced before the corrosion tests, but was still present on all samples after corrosion, even those not intentionally doped with carbon. In our case, we attribute this peak to residual surface contamination, unrelated to the incorporation of carbon into the covetic

materials. For the covetic samples we studied any incorporated carbon would be difficult to quantify since the amount of carbon present is expected to be very close to or below the normal detection limits of XPS (ca. 2%) [52].

In summary, we show that changes in the composition of alloy phases with elevated amounts of O, Si, Ti, Mn, and Cu are induced by the addition of carbon during the electrocharging assisted process. We further show that these compositional changes are more evident on the surface of the material after corrosion testing, forming a layer which increases the corrosion potential but also the corrosion current density. Additionally, we observe that the mechanical properties including the compressive strength and hardness are also enhanced by the addition of carbon in the 2.3% covetic. We attribute the origin of these improvements to the altered phase composition within the covetic material and also to the smaller grain size. Understanding the corrosion behavior and mechanical properties of covetic materials is important for potential applications within manufacturing and construction industries. Our findings suggest that covetics prepared via the electrocharging-assisted process could be promising candidates for application as robust as lightweight building materials where corrosion may be an issue. We believe that further research to gain a better understanding of the processing and characteristics of covetic materials could lead to further control and improvement of their properties and help to accelerate their commercialization.

15.5 References

[1] R.E. Smallman, A.H.W. Ngan, Physical Metallurgy and Advanced Materials (7th Edition), Elsevier, 2007.

[2] M. Bakir, Jasiuk, I., Novel metal-carbon nanomaterials: A review on covetics, Advanced Materials Letters, 8 (2017) 884-890.

[3] P.M. Natishan, W.E. O'Grady, Chloride Ion Interactions with Oxide-Covered Aluminum Leading to Pitting Corrosion: A Review, J. Electrochem. Soc., 161 (2014) C421-C432.

[4] T.D. Burleigh, Corrosion of Aluminum and Its Alloys, in: Handbook of Aluminum, 2003, pp. 421-463.

[5] K. Hauffe, Chlorine and Chlorinated Water, in: R. Bender (Ed.) Corrosion Resistance of Aluminum and Its Alloys, Wiley, 2010.

[6] M.B. Rockel, Sodium Chloride, in: R. Bender (Ed.) Corrosion Resistance of Aluminum and Its Alloys, Wiley, 2010, pp. 367-465.

[7] P. Drodten, Seawater, in: R. Bender (Ed.) Corrosion Resistance of Aluminum and Its Alloys, Wiley, 2010, pp. 349-365.

[8] R.L. Twite, G.P. Bierwagen, Review of alternatives to chromate for corrosion protection of aluminum aerospace alloys, Progress in Organic Coatings, 33 (1998) 91-100.

[9] D.R. Forrest, Approaches to High Performance Conductors, Next Generation Electric Machines Workshop, (2015).

[10] J. Liao, M.-J. Tan, Mixing of carbon nanotubes (CNTs) and aluminum powder for powder metallurgy use, Powder Technology, 208 (2011) 42-48.

[11] S.F. Bartolucci, J. Paras, M.A. Rafiee, J. Rafiee, S. Lee, D. Kapoor, N. Koratkar, Graphene–aluminum nanocomposites, Materials Science and Engineering: A, 528 (2011) 7933-7937.

[12] M. Bastwros, G.-Y. Kim, C. Zhu, K. Zhang, S. Wang, X. Tang, X. Wang, Effect of ball milling on graphene reinforced Al6061 composite fabricated by semi-solid sintering, Composites Part B: Engineering, 60 (2014) 111-118.

[13] D. Jeyasimman, K. Sivaprasad, S. Sivasankaran, R. Narayanasamy, Fabrication and consolidation behavior of Al 6061 nanocomposite powders reinforced by multi-walled carbon nanotubes, Powder Technology, 258 (2014) 189-197.

[14] L. Zhao, H. Lu, Z. Gao, Microstructure and Mechanical Properties of Al/Graphene Composite Produced by High-Pressure Torsion, Advanced Engineering Materials, 17 (2015) 976-981.

[15] C.-H. Jeon, Y.-H. Jeong, J.-J. Seo, H.N. Tien, S.-T. Hong, Y.-J. Yum, S.-H. Hur, K.-J. Lee, Material properties of graphene/aluminum metal matrix composites fabricated by friction stir processing, International Journal of Precision Engineering and Manufacturing, 15 (2014) 1235-1239.

[16] T. Laha, A. Agarwal, T. McKechnie, S. Seal, Synthesis and characterization of plasma spray formed carbon nanotube reinforced aluminum composite, Materials Science and Engineering: A, 381 (2004) 249-258.

[17] T. Laha, Y. Chen, D. Lahiri, A. Agarwal, Tensile properties of carbon nanotube reinforced aluminum nanocomposite fabricated by plasma spray forming, Composites Part A: Applied Science and Manufacturing, 40 (2009) 589-594.

[18] C. Qiu, R. Metselaar, Solubility of carbon in liquid Al and stability of Al4C3, J. Alloys Compd., 216 (1994) 55-60.

[19] L.G. Salamanca-Riba, R.A. Isaacs, M.C. LeMieux, J. Wan, K. Gaskell, Y. Jiang, M. Wuttig, A.N. Mansour, S.N. Rashkeev, M.M. Kuklja, P.Y. Zavalij, J.R. Santiago, L. Hu, Synthetic Crystals of Silver with Carbon: 3D Epitaxy of Carbon Nanostructures in the Silver Lattice, Adv. Funct. Mater., 25 (2015) 4768-4777.

[20] J.V. Shugart, R.C. Scherer, R.L. Penn, Aluminum-carbon compositions, in, U.S. Patent US20120244033 A1, 2012.

[21] D.R. Forrest, I. Jasiuk, L. Brown, P. Joyce, A. Mansour, L. Salamanca-Riba, Novel Metal-Matrix Composites with Integrally-Bound Nanoscale Carbon, Nanotech 2012, (2012).

[22] L. Brown, P. Joyce, D. Forrest, J. Wolk, Physical and Mechanical Characterization of a Nano Carbon Infused Aluminum-Matrix Composite, Proceedings of the SAMPE Fall Technical Conference, Ft. Worth, TX, 17-20 October 2011, (2011).

[23] S. Nilufar, S. Siddiqi, I. Jasiuk, Multi-scale characterization of novel aluminum-carbon nanocomposites, in: Materials Science and Technology Conference and Exhibition 2012, MS and T 2012, 2012, pp. 701-707.

[24] I. Jasiuk, S. Nilufar, L. Salamanca-Riba, R. Isaacs, S. Siddiqi, Novel aluminum-carbon materials, in: Technical Proceedings of the 2013 NSTI Nanotechnology Conference and Expo, NSTI-Nanotech 2013, 2013, pp. 27-30.

[25] L. Salamanca-Riba, R. Isaacs, A.N. Mansour, A. Hall, D.R. Forrest, M.C. LeMieux, J. Shugart, A New Type of Carbon Nanostructure Formed Within a Metal-Matrix, Proceedings of Nanotech Conference and Expo 2012., (2012).

[26] H.M.I. Jaim, R.A. Isaacs, S.N. Rashkeev, M. Kuklja, D.P. Cole, M.C. LeMieux, I. Jasiuk, S. Nilufar, L.G. Salamanca-Riba, Sp2 carbon embedded in Al-6061 and Al-7075 alloys in the form of crystalline graphene nanoribbons, Carbon, 107 (2016) 56-66.

[27] H.M.I. Jaim, D.P. Cole, L.G. Salamanca-Riba, Characterization of carbon nanostructures in Al and Ag covetic alloys, Carbon, 111 (2017) 309-321.

[28] T. Knych, P. Kwaśniewski, G. Kiesiewicz, A. Mamala, A. Kawecki, B. Smyrak, Characterization of Nanocarbon Copper Composites Manufactured in Metallurgical Synthesis Process, Metallurgical and Materials Transactions B, 45 (2014) 1196-1203.

[29] T. Knych, G. Kiesiewicz, P. Kwasniewski, A. Mamala, B. Smyrak, A. Kawecki, Fabrication and Cold Drawing of Copper Covetic Nanostructured Carbon Composites/ Otrzymywanie Oraz Ciągnienia Kompozytów Miedzianych Typu Covetic O Strukturze Nanometrycznej, in: Archives of Metallurgy and Materials, 2014, pp. 1283.

[30] R.A. Isaacs, H. Zhu, C. Preston, A. Mansour, M. LeMieux, P.Y. Zavalij, H.M.I. Jaim, O. Rabin, L. Hu, L.G. Salamanca-Riba, Nanocarbon-copper thin film as transparent electrode, Applied Physics Letters, 106 (2015) 193108.

[31] D.-H. Lim, A.S. Negreira, J. Wilcox, DFT Studies on the Interaction of Defective Graphene-Supported Fe and Al Nanoparticles, The Journal of Physical Chemistry C, 115 (2011) 8961-8970.

[32] J.C. Reed, H. Zhu, A.Y. Zhu, C. Li, E. Cubukcu, Graphene-Enabled Silver Nanoantenna Sensors, Nano Lett., 12 (2012) 4090-4094.

[33] C. Subramaniam, T. Yamada, K. Kobashi, A. Sekiguchi, D.N. Futaba, M. Yumura, K. Hata, One hundred fold increase in current carrying capacity in a carbon nanotube–copper composite, Nat. Commun., 4 (2013) 2202.

[34] P.D. Jablonski, Melt Processing of Covetic Materials, U.S. DOE Advanced Manufacturing Office Program Review Meeting, (2015).

[35] J. Tian, H. Cao, W. Wu, Q. Yu, N.P. Guisinger, Y.P. Chen, Graphene Induced Surface Reconstruction of Cu, Nano Lett., 12 (2012) 3893-3899.

[36] R.A. Isaacs, H.M.I. Jaim, D.P. Cole, K. Gaskell, O. Rabin, L.G. Salamanca-Riba, Synthesis and characterization of copper-nanocarbon films with enhanced stability, Carbon, 122 (2017) 336-343.

[37] Y. Wang, M.G. Jiao, W. Song, Z.J. Wu, Doped fullerene as a metal-free electrocatalyst for oxygen reduction reaction: A first-principles study, Carbon, 114 (2017) 393-401.

[38] S.F. Cogan, F.W. Gayle, J.D. Klein, F.H. Cocks, M.L. Shepard, Extraction and X-ray analysis of phases in aluminium alloys, Journal of Materials Science, 13 (1978) 2687-2691.

[39] J. Li, J. Dang, A Summary of Corrosion Properties of Al-Rich Solid Solution and Secondary Phase Particles in Al Alloys, Metals, 7 (2017) 84.

[40] T.D. Burleigh, R.C. Rennick, F.S. Bovard, Technical Note: Corrosion Potential for Aluminum Alloys Measured by ASTM G 69, CORROSION, 49 (1993) 683-685.

[41] Standard Test Method for Measurement of Corrosion Potentials of Aluminum Alloys, in, ASTM International, 2012.

[42] G.S. Frankel, Fundamentals of Corrosion Kinetics, in: A.E. Hughes, J.M.C. Mol, M.L. Zheludkevich, R.G. Buchheit (Eds.) Active Protective Coatings: New-Generation Coatings for Metals, Springer Netherlands, Dordrecht, 2016, pp. 17-32.

[43] M. Stern, A.L. Geary, Electrochemical Polarization: I . A Theoretical Analysis of the Shape of Polarization Curves, J. Electrochem. Soc., 104 (1957) 56-63.

[44] Standard Test Methods of Compression Testing of Metallic Materials at Room Temperature, in, ASTM International, 2009.

[45] R. Sergiienko, E. Shibata, Z. Akase, H. Suwa, T. Nakamura, D. Shindo, Carbon encapsulated iron carbide nanoparticles synthesized in ethanol by an electric plasma discharge in an ultrasonic cavitation field, Materials Chemistry and Physics, 98 (2006) 34-38.

[46] S. Sivasankaran, K. Sivaprasad, R. Narayanasamy, P.V. Satyanarayana, X-ray peak broadening analysis of AA 6061100 − x − x wt.% Al2O3 nanocomposite prepared by mechanical alloying, Materials Characterization, 62 (2011) 661-672.

[47] R. Mueller, H.K. Kammler, K. Wegner, S.E. Pratsinis, OH Surface Density of SiO2 and TiO2 by Thermogravimetric Analysis, Langmuir, 19 (2003) 160-165.

[48] J. Cai, R. Liu, Research on Water Evaporation in the Process of Biomass Pyrolysis, Energy & Fuels, 21 (2007) 3695-3697.

[49] A.d.S. Scari, B.C. Pockszevnicki, J. Landre, P.A.A. Magalhaes, Stress-Strain Compression of AA6082-T6 Aluminum Alloy at Room Temperature, Journal of Structures, 2014 (2014) 7.

[50] N. Hansen, Hall–Petch relation and boundary strengthening, Scripta Materialia, 51 (2004) 801-806.

[51] J.E. Hatch, A. Association, A.S. Metals, Aluminum: Properties and Physical Metallurgy, American Society for Metals, 1984.

[52] D.A. Skoog, F.J. Holler, S.R. Crouch, Principles of instrumental analysis, 6th ed., Thomson, Belmont, CA, 2007.